Multi-messenger probes of dark matter, from radio to multi-frequency

Geoff Beck

A thesis submitted to the Department of Physics, University of the Witwatersrand in fulfilment of the academic requirements of the degree of Doctor of Philosophy.

Johannesburg, June 17, 2016

Abstract

The nature of dark matter remains one of the most significant problems in modern physics. One candidate hypothesis with strong theoretical motivation is a WIMP (Weakly Interacting Massive Particle) in the form of the supersymmetric neutralino. Although this lacks experimental evidence, supersymmetry may manifest in collider experiments and also has observable consequences in the emission of annihilation products from cosmic structures which would play host to large neutralino densities. Historically, interest has been focussed upon the direct detection of WIMPs, as well as indirect observation through γ-rays produced by pair-annihilation processes. In this work we present a detailed argument for a multi-frequency observational strategy. We motivate this by studying the redshift evolution of radio synchrotron radiation emitted by WIMP annihilation-product electrons. In so doing, we demonstrate the potential power of the SKA to probe the neutralino parameter space, being able to produce constraints several orders of magnitude better than current limits and distinguish between differing neutralino masses and annihilation channels. Furthermore, we motivate the SKA as a machine to study dark matter by discussing its ability to characterise cosmic magnetic fields through rotation measures and polarimetry, as well as resolve between non-thermal emissions produced by dark matter and those resulting from strictly baryonic processes, like star formation. These technical capabilities obviate the central uncertainties in the study of synchrotron radiation. Additionally, we highlight optimal laboratories for neutralino detection via the SKA, based on structures that might produce dark matter emissions with lower background synchrotron radiation. In particular we highlight galaxies and galaxy clusters at redshifts $z \sim 1$ and local dwarf spheroidal galaxies. Finally, we demonstrate the potential of X-rays, through the ASTRO-H mission, to compliment the SKA in a multi-frequency search. We then demonstrate our multi-frequency approach in the analysis of several prominent claims of signals compatible with dark matter-induced emissions. Showing that models designed to account for the AMS-2/Fermi/PAMELA anti-particle and galactic centre γ-ray excesses are incompatible with existing data as well as demonstrating that a dark matter interpretation of the Reticulum-2 γ-ray excess is untenable for a wide range of dark matter particle masses.

Contents

Preface and Declarations

The work described by this thesis was carried out at the University of the Witwatersrand, Department of Physics, from February 2013 until April 2016, under the supervision of Professor Sergio Colafrancesco.

This thesis is entirely, unless specifically contradicted in the text, the work of the candidate, Geoffrey Martin Beck, and has not been previously submitted, in whole or in part, to any other tertiary institution. Where use has been made of the work of others, it is duly acknowledged in the text.

Signed:  Name: Geoffrey Martin Beck

Date: 17 June 2016

Declaration - Plagiarism

I, Geoffrey Martin Beck declare that

1. The research reported in this thesis, except where otherwise indicated, is my original research.
2. This thesis has not been submitted for any degree or examination at any other university.
3. This thesis does not contain other persons' data, pictures, graphs or other information, unless specifically acknowledged as being sourced from other persons.
4. This thesis does not contain other persons' writing, unless specifically acknowledged as being sourced from other researchers. Where other written sources have been quoted, then:
    a. Their words have been rewritten but the general information attributed to them has been referenced.
    b. Where their exact words have been used, then their writing has been placed in italics and inside quotation marks, and referenced.
5. This thesis does not contain, text, graphics or tables copied and pasted from the Internet, unless specifically acknowledged, and the source being detailed in the thesis and in the References sections.

Signed: 

Declaration - Publications

Details of publications that form part and/or include research presented in this thesis. The candidate undersigned declares that following data is correct and accurate. Additionally, the candidate certifies that his contributions, as detailed here and in the introduction to each mentioned chapter, are accurate and true.

Signed: 

1.

Title: Evolution of Dark Matter Halos and their Radio Emissions

Status: Published: 2015, JCAP, **02**, 032C

Authors: S. Colafrancesco, P. Marchegiani & G. Beck

Contributions: Wrote software, produced all results, composed the majority text, as well as producing the analysis, arguments, and discussion expressed in the work. See Chapter 3 for a detailed description.

2.

Title: Probing the Nature of dark matter with the SKA

Status: Published: Proceedings of Science, *Advancing Astrophysics with the SKA*

Authors: S. Colafrancesco, *et al*, including G. Beck

Contributions: Produced majority of displayed results (Figs 2-5) and produced substantial passages of discussion as well as the analysis and arguments expressed therein. See Chapter 4 for a detailed description.

3.

Title: A Multi-frequency analysis of dark matter annihilation interpretations of recent anti-particle and γ-ray excesses in cosmic structures.

Status: Published: 2016, JCAP, **05**, 013P

Authors: G. Beck & S. Colafrancesco

Contributions: Wrote software, produced, all results, composed the text and logical substance of the expressed arguments, analysis, and discussion. See Chapter 5 for a detailed description.

Acknowledgements

Acknowledgement must go to Professor Sergio Colafrancesco, whose patient guidance and extensive knowledge have been key to the success of this work. Additionally thanks go out to all of those who collaborated on the publications included here, particularly Doctor Paolo Marchegiani, whose help and teaching were immensely appreciated. I also thank my wife Justine Tarrant, and the rest of my family for their support and encouragement. I acknowledge the funding support of the South African Square Kilometre Array Initiative through their post-graduate bursary programme. The conclusions reached here do not necessarily represent the positions of the SKA SA.

Chapter 1

Introduction

Dark matter (DM), originally hypothesised in the 1930's, by Jan Oort and Fritz Zwicky, to explain the orbital velocity of galaxies in clusters [1], has remained elusive ever since. Despite a lack of evidence as to the nature of dark matter itself, there is an abundance of modern astrophysical evidence [2, 3, 4, 5, 6] indicating its presence. Namely gravitational lensing, galaxy rotation curves, galaxy cluster masses, and cosmic microwave-background anisotropy data. All of which suggests that the majority of the matter content within the universe is in the form of dark matter and that this plays a vital role in the evolution of structure within the universe. The fact that all of this evidence is gravitational explains the lack of success in unmasking dark matter, as it does not allow us to learn any more detail about the behaviour of the bodies that might constitute it. This is problematic, as without some knowledge of its nature, dark matter remains merely a label attached to a set of anomalous phenomena, such nomic designations being empty of explanatory power.

Therefore, the nature of dark matter remains a major hiatus in the understanding of modern physics. Which has resulted in many contending models being proposed to account for this deficiency [7, 8, 9, 10, 11, 12, 13, 14, 15]. As well as many methods of both direct and indirect detection proposed [16, 17, 18, 19], and existing searches for dark matter candidates [20, 21, 22, 23, 125] being conducted. Dark matter forms a crucial component of the current cosmological framework, the so-called Λ-CDM model, as without the conjectured presence of dark matter, models based in the general theory of relativity cannot account for the state of the universe as we find it. Thus, the hunt for dark matter is one of the great scientific endeavours of our time, as its presence, or lack thereof, both stand to launch our understanding of the structure of the universe to unprecedented heights. In this work we focus upon one popular cold Weakly Interacting Massive Particle (WIMP) DM candidate: the so-called "neutralino", being the lightest particle from the minimal supersymmetric extension of the standard model (MSSM).

The neutralino is the lowest mass particle introduced by a minimal model of supersymmetry, a conjecture that particles occur in super-multiplets, often summarised as every boson is paired with a fermion and vice-a-versa (although it is more complicated). Under supersymmetry transformations all of the quantum numbers are preserved, barring the spin, which is changed by one half. Thus, a super-multiplet is a collection of particles related by supersymmetry transformations and differing only in their spins. Since the quantum numbers of the Higgs boson, photon, and Z boson are identical and all have a possible super-partner with the same quantum numbers and spin half, super-positions of these states will form a collection of "neutralino" mass eigenstates, with the lowest mass eigenstate being the neutralino of interest. Significantly, supersymmetry has the potential to cure many of the ills of the standard model, particularly issues of "naturalness" and "fine-tuning" [25] where only specific inexplicable choices of otherwise free parameters produce acceptable models. The neutralino forms an attractive model because it is neutral, weakly-interacting, and has viable mechanisms for the production of a thermal relic population [7]. Additionally, while there is currently no experimental evidence in favour of supersymmetry, supersymmetric effects may manifest unambiguously in collider experiments. With this

in mind, it seems that dark matter should be stalked exclusively within the confines of particle accelerators or direct scattering experiments. However, the possibility of indirect detection through astrophysical signatures remains a promising alternative, as the weakly interacting nature of the neutralino allows for mutual pair annihilation to produce a host of standard model particles which may then be ejected as cosmic rays or instead subsequently emit radiation themselves. Notably, neutralinos might annihilate to neutral pions which then decay into high-energy γ-rays. Such a WIMP might also annihilate into electrons/positrons, formed either directly or from charged pion decay, which subsequently produce synchrotron, inverse-Compton, or bremsstrahlung radiation in the highly magnetised environment of cosmic structure. This would result in non-thermal emissions, characteristic of the dark matter particle, from any structure that played host to a concentration of such particles. Additionally, the increasing sensitivity of astronomical measurements and the limitations of current ground-based direct detection experiments combine to elevate indirect detection methods to new levels of competitiveness when it comes to setting limits on the nature of dark matter.

In recent literature on indirect astrophysical detection, strong limits on possible WIMP models have been set by the study of the Cosmic Microwave Background (CMB) with the Planck satellite [26, 27], γ-ray studies of dwarf galaxies with the Fermi-LAT [28, 29, 30], as well as studies of radio emission in dwarf galaxies with the Australian Telescope Compact Array (ATCA) [31]. In addition to these limits there have also been several recent claims of the detection of excess signals compatible with WIMP-based emissions. Particularly from Fermi-LAT observations of the galactic centre, and PAMELA anti-proton excesses [32, 33, 34] which favour a neutralino with a mass of 35 GeV and cross-section $\langle \sigma V \rangle \sim 3 \times 10^{-26}$. These excesses are contentious, with several arguments for their existence without inference of a dark matter origin [35, 36, 37, 38, 39]. There are also the PAMELA and Alpha Magnetic Spectrometer (AMS) positron excesses [40, 41], which favour a neutralino with mass $\mathcal{O}(\text{TeV})$ and a cross-section $\langle \sigma V \rangle \sim 3 \times 10^{-24}$ cm^3 s^{-1} in order to reproduce observations via secondary anti-particle production [42], although the authors note this could also be explained via an unresolved pulsar population. Additionally, there is the claimed γ-ray excess from Fermi-LAT observations of the dwarf galaxy Reticulum-2 [43] purporting a 2.3σ excess above the background. Best-fit models in this case are ones with a mass around 40 GeV and $\langle \sigma V \rangle \sim 3 \times 10^{-26}$ cm^3 s^{-1} [44], however this is subject to uncertainties about the structure of this dwarf galaxy and is in some conflict with limits derived from Fermi-LAT observations of dwarf galaxies which included Reticulum-2 in the analysis [29]. Finally, there is the model derived from re-analysis of the AMS-2 positron data [45], arguing the excess to be compatible with DM models with cross-sections $\sim 2 - 8 \times 10^{-26}$ cm^3 s^{-1} and masses in the range $51 - 140$ GeV, depending on the annihilation channels studied.

All of the aforementioned dark matter models and limits are drawn from widely differing forms of observation. However, the universality of dark matter suggests that the consequences of any purported model should appear consistently across the spectrum in any environment that hosts large concentrations of dark matter particles. In order to study the diverse consequences of neutralino dark matter and ensure the resulting models are consistent with observations of any source that may play host to it, we will use this work to advocate a multi-frequency strategy for hunting dark matter. In order to justify this we will begin by arguing for the power of upcoming radio experiments, like the Square Kilometer Array (SKA), to hunt for neutralino-induced synchrotron emissions. We then supplement this with a study of the prospects of the ASTRO-H [46] X-ray satellite mission and demonstrate our multi-frequency approach in the comparison of excess-compatible dark matter models with available multi-frequency data.

While many authors have previously studied the high-energy products of WIMP pair annihilation [47, 48, 49, 50, 51, 52, 53, 54, 55], there has been some recent interest in the possibility of detecting radio emission resulting from the annihilation products of such particles [56, 57, 58, 59, 60, 61]. WIMP-induced radio emission takes the form of synchrotron radiation, which comes with the difficulty of disentangling the effects of the WIMP-produced electron spectrum and the magnetic field itself. This makes the accuracy of magnetic field

models, and characterisation of electron diffusion, within prospective radio sources highly important. This has commonly been seen as one of the central problems with radio dark matter detection and explains the bias towards γ-ray astronomy in this regard. However, experiments like the SKA, with the capability to do polarimetry and Faraday-rotation studies in order to characterise magnetic field structure [62, 63], are capable of obviating this difficulty. Moreover, the angular resolution of the SKA will open the possibility of obviating confusion between dark matter synchrotron radiation and strictly baryonic sources of such non-thermal emission. These points will be central to our motivation of the SKA as a vital ingredient in the continuing hunt for the nature of dark matter, particularly as a component of a multi-frequency strategy. We will motivate our argument for the SKA as a dark matter machine by studying the synchrotron emissions from a wide array of dark matter halo masses out to large redshifts. This will demonstrate that the SKA has the capability to observe dark matter-induced radio emissions and we highlight local dwarf galaxies and galaxy clusters at $z \sim 1$ as optimal detection laboratories. The potential constraints that the SKA can produce in an optimistic scenario are shown to be up to four orders of magnitude below the thermal relic density limit [7]. Both dwarf galaxies and high redshift clusters are structures that limit the possible synchrotron confusion, however, a multi-frequency strategy will be argued for as a means to obviate confusion with baryonic emission due to star formation etc. Significantly we will also use the SKA's ability to do polarimetry and rotation measures as motivation, as it can characterise magnetic fields with the same observations that hunt for dark matter. Moreover, the SKA is expected to have great power to characterise magnetic fields and is very well placed to measure regions of the WIMP/neutralino-induced spectra that are sensitive to variations in mass and annihilation channel. Additionally, by using projected sensitivity of the SKA [64] the optimal observation frequency for neutralino hunting in radio is shown to be ~ 1 GHz.

It has already been suggested that neutralino annihilation can result in electrons that produce radio-frequency synchrotron emission. However, these electrons can also result in inverse-Compton scattering of Cosmic Microwave Background photons [56]. Moreover, neutralinos annihilating into neutral pions produce γ-rays through the subsequent pion decay. This means that neutralinos produce observable consequences in frequencies from radio, through X-rays to γ-rays, making multi-frequency observation an excellent way to produce complementary or combined constraints on the properties of the neutralino. Importantly, we find that the signatures of the neutralino mass and dominant annihilation channel to be apparent in the each of the possible emission spectra, making multi-frequency characterisation a particularly powerful consistency check on any purported neutralino identification. Effects like star-formation, which stand to confuse neutralino detection in radio, or active galactic nuclei which emit in X-rays and γ-rays can be obviated by careful use of multi-frequency observations. This allows one to maximise the possible "optimal laboratories" where the chance of dark matter detection is highest. We particularly highlight the potential of ASTRO-H [46] to probe the X-ray region of the neutralino-induced spectrum. As, given target environments with favourable X-ray backgrounds, it is well placed to probe the WIMP parameter space and will be shown to cover a spectral region sensitive to variations in the neutralino mass and annihilation channel.

Finally, in order to demonstrate the effectiveness of multi-frequency analysis, as well as determine the prospects for the continuing dark matter hunt in a wide frequency band, we will examine all of the aforementioned claims of excesses compatible with neutralino dark matter using a multi-frequency strategy. In order to do so we select some target environments, about whom data or theoretical models are available. We then compare our multi-frequency dark matter spectra for each of these environments to available data and use this to determine the future detection prospects of the dark matter models favoured by the various detection claims. In particular we will cast doubt on the Reticulum-2 excess dark matter interpretation, by showing that recent Fermi-LAT limits derived from dwarf galaxies including Reticulum-2 are incompatible with available data in our target environments. The chosen environments are the Coma cluster, the M81 galaxy and the Draco dwarf galaxy. We will also show that the AMS dark matter models, which are largely ruled out by the Planck experiment [26] and Fermi limits [29], have their remaining parameter space ruled

out by multi-frequency data. While those models favoured by galactic centre excesses and the AMS-2 re-analysis are also in tension with multi-frequency observations of the target environments.

This means that the next generation of experiments, SKA and ASTRO-H in particular, will be vital to the formulation of a comprehensive multi-frequency strategy for dark matter detection. Finally, multi-frequency constraints can be made far more stringent, as in the case of the ICS and synchrotron, they serve to eliminate dependence on the thermal electron distribution within cosmic sources, the error/confusion then depends on the magnetic field which can be characterised by SKA polarimetry. Moreover, they represent a powerful consistency check, ensuring that purported dark matter models are consistent with observations in all frequency ranges.

This work begins with Chapter 2, a brief introduction to the problem of DM, including a review of observational evidence in favour of non-baryonic DM, a description of particle DM solutions, and an over-view of direct and collider dections methods, as well as a detailed examination of how multi-frequency spectra are calculated for the indirect detection of WIMP DM. The main argument presented in this work is laid out in three chapters: 3, 4, and 5, each being a stand-alone publication. The remaining structure of this thesis is therefore illuminated below, including details of how each publication contributes to the overall argument.

Chapter 3 consists of a peer-reviewed publication [65] in which we make an extensive study of the radio synchrotron emissions from dark matter halos while varying the neutralino mass, annihilation channel, halo mass and redshift, as well as using various dark matter density profiles such as Einasto, Burkert and Navarro-Frenk-White. In so doing, we scan the parameter space of structures hosting dark matter, extending from dwarf galaxies to galaxy clusters, with redshifts up to $z \sim 5$. The extension towards larger redshifts is of importance, as such conditions offer the potential of dark matter detection in more primitive structures. These objects make for good potential candidates given that they play host to reduced foreground contamination by strictly baryonic forms of synchrotron radiation, star formation for instance. The choice of a wide range of halo masses is vital to the aims of this chapter, as dwarf spheroidal galaxies are well known to be highly dark matter dominated, but produce faint emissions. While larger structures, like galaxy clusters, although displaying considerably more sources of baryonic emission, which may confuse DM detection, provide substantially stronger fluxes. Therefore, a survey of halos of varying mass is necessary to locate the best detection prospects for future telescopes like the SKA. The crux of this work is a discussion of the ability of the SKA to explore the neutralino parameter space and place constraints on the annihilation cross-section. The purpose of this analysis being a determination of “optimal laboratories” for neutralino detection via the SKA as well as to demonstrate that the SKA has the potential to produce upper-bounds on the cross section that are far more stringent than those from existing experiments, as found in [66, 67, 32], suggesting the SKA will be able to play a strong role in the quest to determine of the nature of dark matter.

Chapter 4 consists of a peer-reviewed publication [68] that places the work presented in chapter one in the full context of the case for the SKA as a machine to study dark matter. In this chapter the SKA is proposed as an instrument for use in the search for dark matter, making a case for this to be a key scientific project for SKA observations. The technical aspects of a dark matter search with the SKA are outlined, including its ability to characterise cosmic magnetic fields as well the specifications such as frequency range, angular resolution, and sensitivity that recommend it as an instrument for furthering the determination of the nature of dark matter. This chapter builds on the potential power of the SKA to probe the neutralino parameter space, outlined in Chapter 1, and also reviews strategies for the selection of observational targets, based on the results of Chapter 1, which would allow for the maximum potential for detection. Additionally, this work highlights the synergies of the proposed SKA dark matter search with high energy and multi-frequency searches, as well as the possibility of observing higher energy neutralino emissions via the proposed SKA phase 2.

Chapter 5 is a peer-reviewed publication [69] that examines the multi-frequency emis-

sions of neutralino models favoured by Fermi-LAT galactic centre observations as well as AMS-2/Fermi/PAMELA anti-particle excess models. This is done within the target environments of the Coma cluster, the Draco dwarf galaxy, and the galaxy M81. The source selection allows for concrete predictions to be derived from the given models, which are then compared to existing multi-frequency data. The purpose of the analysis is to eliminate models that are unsatisfactory as things stand, but also to determine the extent to which upcoming experiments like SKA and ASTRO-H will allow for the constraint of the neutralino across the spectrum. In the process we also briefly examine the prospects of the Cherenkov Telescope Array (CTA) and ASTROGAM mission in the continuing hunt for dark matter. From the results of this chapter we show that ASTRO-H has the potential to characterise a neutralino through X-ray observations that depend strongly on the neutralino mass and annihilation channel, provided there exist environments with favourable X-ray backgrounds. Additionally, we demonstrate that the DM interpretation of the reported Reticulum-2 γ-ray excess [43] are largely untenable, with consequences, in the studied environments, that are in conflict with existing multi-frequency measurements. The multi-frequency analysis also shows that the AMS-2/Fermi/PAMELA models as well as many of the galactic centre models are in tension with existing data. This chapter acts as a demonstration of the power of multi-frequency analysis of predicted DM spectra, using consistency across the spectrum to eliminate unsatisfactory models that are suggested by analysis of just one region of the spectrum. These results are used to motivate a multi-frequency dark matter search strategy incorporating next generation experiments like SKA and ASTRO-H that have great potential to hone in on the nature of dark matter.

Using these three publications we argue for a multi-frequency strategy for indirect dark matter detection, incorporating the SKA and ASTRO-H as vital components within the next decade.

Chapter 6 provides an outlook on what might be done, using 21-cm emissions and reionisation, to further the work presented here. Finally, Chapter 7 provides a concluding summary.

Chapter 2

How Do We Solve a Problem Like Dark Matter?

This chapter will provide an over-view of the problem of dark matter, particle solutions to the problem, and finally methods of detecting dark matter particles (with a particular focus on indirect detection). Section 2.1 begins with a brief outline of the observational evidence in favour of some as yet unidentified non-baryonic contribution to the energy density of matter in the universe. This is followed, in Section 2.2, by a discussion of particle solutions to the DM problem, with particular emphasis on Weakly Interacting Massive Particles (WIMPs). Finally, the manner in which WIMPs might be detected through direct, collider, and indirect searches is outlined in Sections 2.3.1, 2.3.2, and 2.3.3 respectively.

2.1 Observational Evidence of Dark Matter

As suggested in Chapter 1, clues as to the existence of dark matter have been around as far back as the 1930's when Jan Oort and Fritz Zwicky hypothesised it to explain the orbital velocity of galaxies [1]. As available observational data increased, the evidence has piled up in favour of this missing component of the universe. In 1970 Rubin and Ford [70] discovered that the rotation curves of galaxies are flat, meaning that the orbital velocity of stars within the galaxy remain constant out to large radii, rather than declining rapidly with radius as was expected. This was another hint that galaxies contained missing matter, as the mass of objects within the bright galactic disk is not sufficient to sustain such a rotation curve. However, in order to explain the data, the missing mass would have to be many times larger than the mass of the visible galaxy itself. This being a clue that most of the matter in the universe might be "dark". These rotation curve measurements are limited by the availability of stars or neutral hydrogen (emitting the 21-cm line), and thus can only trace the need for dark matter out to some 10's of kpc. Modern controversy over rotation curve measures stems from attempts to explain the flat nature of the curve via a small scale modification of gravity [71].

Further and better evidence for the existence of DM can be found in measurements of gravitational lensing, a well-confirmed consequence of general relativity [72, 73, 74]. This is a process whereby light reaching an observer must pass massive objects in the foreground. As it does so, the trajectories of the photons are curved. Given a symmetric object this can result in multiple images of the background source. The angle of deflection thus incurred is $\theta = \frac{2GM}{rc^2}$, where G and c are the standard universal constants, M is the object mass and r is the distance of approach for photons passing the massive object [75]. This means that the mass of lensing objects can be directly inferred from angles of deflection. Observations using NASA's Chandra [76, 77] satellite mission indicate that the so-called "Bullet" cluster, a pair of merging galaxy clusters, has visible emissions from inter-stellar gas uncorrelated with the regions which both host the most significant gravitational lensing effects and account for the majority of the mass of the cluster [78, 79]. In particular, this

merger has visible emissions around the centre of the merged cluster, with the strongest lensing found in two regions distant from visible emissions. This geometry is compatible with frictionless DM passing through the merger centre while the baryonic matter is slowed by friction. In addition to this, and despite the uncertainties inherent in lensing, there exists very strong lensing-based evidence that galaxies and galaxy clusters are dominated by dark matter [80].

Another powerful argument in favour of non-baryonic dark matter is found in the study of the Cosmic Microwave Background (CMB). The anisotropy of the CMB was found by the Cosmic Background Explorer (COBE), the Wilkinson Microwave Anisotropy Probe (WMAP), and the Planck mission [81, 82, 26] to be around the level of 1 part in 10^5. This sets up the size of the primordial density perturbations which eventually develop into cosmic structure. For these perturbations to grow into the highly non-linear structure we see today, from such small seeds, the data from these three experiments require that $\Omega_m \sim 0.3$, where $\Omega_m = \frac{\rho_m}{\rho_c}$, ρ_m is the matter density and ρ_c is the critical density of the universe (the energy density of a flat universe). This would allow the universe to become matter dominated earlier and thus accommodate greater growth of the density perturbations. Additionally, the second acoustic peak of the CMB power spectrum allows for a determination of the baryonic fraction of the universe from its amplitude, this places limitations of around $\Omega_b \sim 0.05$ [82, 26]. Thus indicating that a large non-baryonic matter component must account for the remaining value of Ω_m.

More evidence for non-baryonic dark matter comes from a combination of sources. The first ingredient to these arguments is derived from prediction of the abundance of low-mass elements produced via big-bang nucleo-synthesis. An approach of this nature allows for the use of observational data relating to current abundances of low-mass elements to constrain the total energy density contribution of baryonic matter to the universe. When compared to theoretical predictions, the observed elemental abundances suggest that baryonic matter can only constitute around 5% of the energy density of the universe, or $\Omega_b \sim 0.05$ [83, 84, 85, 86]. What follows below will be an examination of other observation evidence that, when combined with elemental abundances, suggests the existence of significant non-baryonic dark matter.

The first such argument for dark matter arises from type 1A supernovae measurements. This process uses these phenomena as standard candles with known luminosity. Fitting observed luminosities as a function of redshift allows for a determination of the geometry of the universe, which influences the redshift-distance relationship, and is dependent on the energy content of the universe. These analyses place the matter content of the universe at roughly $\Omega_m \sim 0.3$ [87] (for a flat universe). This determination of the matter fraction is orthogonal to the CMB measurements mentioned above [88]. Combined with the nucleo-synthesis arguments we have a strong indication that the matter content of the universe is overwhelmingly non-baryonic.

Another indication of the need for DM arises from the observation of galaxy clusters. Firstly the observed mass of clusters, as in the case of [1], observations of galactic rotation within Coma required a far larger mass than visible matter suggested. Then, if clusters are assumed a fair sample of matter to cosmological constant ratio in the universe, there are several means to estimate the fraction of the universe's energy density occupied by matter. One can use the mass-to-light ratios of clusters to estimate the apparent values of the matter fraction of the energy density [89], yielding a result of $\Omega_m \sim 0.2$. With the same fair-sampling assumption, the abundance of high-mass clusters as a function of redshift also requires a matter fraction $\Omega_m \sim 0.2$ [90]. Additionally, comparison of cluster and galaxy correlation functions requires that the matter fraction is around $\Omega_m \sim 0.25$ [91]. There is also the Sunyayev-Zel'dovich (SZ) effect, which causes a spectral distortion of the CMB through inverse-Compton scattering processes between CMB photons and free electrons within the intra-cluster medium. This dependence on hot electrons means that this effect can be used to estimate the ratio between the energy densities of baryons and all matter, provided the baryon fraction in clusters is a fair sampling of the cosmological fraction. Typical measurements made in this manner yield that the baryon fraction of matter is roughly $\frac{\Omega_b}{\Omega_m} \sim 0.1 - 0.2$ [92].

In summary we can see that a large amount of independent evidence favours the existence of a large non-baryonic matter component in the energy density of the universe. Interestingly, these disparate sources all seem to agree closely, and all favour a much larger component of matter in the universe than could possibly be supported based on the abundance of low-mass elements and nucleo-synthesis. Therefore, each of these sources alone provides a strong argument for existence of a non-baryonic matter component within the universe and additionally, that this component is greatly in excess of the baryonic contribution. Furthermore, because many of these forms of evidence are independent, collecting them all together yields a very powerful argument for the existence of some "dark", non-baryonic matter.

2.2 Particle solutions to the dark matter problem

The evidence presented above is indicative of one particular thing: that the present condition of the universe suggests that there is a large quantity of unobserved non-baryonic matter. However, the current observational data give us very little clue as to what form this matter might take, and the possibilities are bounded only by the imagination of scientists, as the shear variety of models mentioned in the Chapter 1 makes clear.

One seemingly simple solution is that this dark matter is constituted by some, as yet undiscovered, particle. These particles would constitute the missing mass in cosmic structure and thus reconcile cosmological and astrophysical models with the observations mentioned in Section 2.1. However, there are many types of particle that can be put forward to fill this role. As the requirements are simply that the particle be massive, that it interacts weakly with ordinary matter, and that there is a mechanism to produce a sufficient relic abundance of the particle to match the current cosmological estimates for present day dark matter densities. These requirements can understandably still admit a vast number of different possibilities. Thus, it is helpful to further sub-divide various particle models according to properties that have particular cosmological implications. One important division is according to the average velocity of the particles, models with ultra-relativistic DM particles being termed "hot", while highly non-relativistic cases are "cold". This property is a highly relevant cosmological point of division, in that it has a powerful impact on the formation of structure. Particles with extremely large velocities will understandably be unable to form structures whose sizes are smaller than their free-streaming length, which is of course strongly velocity dependent given that DM particles are almost frictionless in many models. Hot DM can take the form of low-mass particles called WISPs, or Weakly Interacting Slim Particles, like axions [93]. While a particularly popular paradigm for cold DM is that of the WIMP, or Weakly Interacting Massive Particle [94, 7]. There are also intermediate "warm" models, such as sterile neutrinos, proposed to mitigate the problem of observing cored DM density profiles within cosmic structures when cold DM models indicate that halos should be cuspy [95, 96] (see further discussion below). Models consisting purely of hot DM are widely considered to be unviable, as they cannot explain the formation of cosmic structure [97], however, hot DM species can be incorporated in so-called "mixed" DM scenarios, containing both hot and cold particles.

In this work we will focus upon cold WIMP dark matter. WIMPs have several important particle properties, being mass, lifetime, scattering cross-section with nucleons, and cross-section for pair annihilation. The annihilation cross-section is a measure of the rate of annihilation for WIMP pairs, while the scattering cross-section is a measure of the probability of a WIMP interacting with a nucleon. The last particle detail for WIMPs are the products into which they annihilate or decay. These particle properties will define whether or not we can observe WIMPs through their interaction with nucleons or their annihilation/decay into standard model particles (see Section 2.3 below). In this scenario of DM, WIMPs are produced thermally in the early universe and subsequently "freeze-out" of thermal equilibrium to leave an existing population of cold relic particles in the manner detailed by [7]. At this point WIMPs can proceed to annihilate/decay, producing standard model particles, leaving an abundance that matches the present-day observations of WMAP and Planck [82, 26].

This allows one to place limits on the annihilation cross-section or lifetime of the WIMP. The most commonly referenced limit of this sort is that the velocity-averaged cross-section must be such that $\langle \sigma V \rangle \lesssim 3 \times 10^{-26}$ cm^3 s^{-1} [7].

Being massive, WIMPs interact gravitationally leading to formation of dense "halos" of dark matter, providing the gravitational potential wells within which baryonic structure forms. The presence of the halo around visible structure accounts for the problem of the missing mass outlined in Section 2.1. The formation of a halo results from gravitational clustering around an initial density perturbation in the distribution of dark matter after inflation [98, 99]. If the density of the pertubation grows sufficiently above that of the background universe, it undergoes gravitational collapse until the point of virial equilibrium $U = -2K$, with U and K being potential and kinetic energies [99]. This establishes a virial radius r_{vir} at which collapse halts and the structure is stable, the mass contained with this radius is the virial mass M_{vir}. The properties of these halos are highly significant as the increase in WIMP density means that the probability of pairs of WIMPs annihilating there is considerably higher than in a smooth medium, as this will be proportional to the square of the DM density. The exact structure of WIMP halos has not yet been established, with numerical N-body simulations agreeing well with the cusped (density tends to infinity at zero radius) NFW profile [100, 101, 102]

$$\rho_N(x) = \frac{\rho_s}{x\left(1+x\right)^2} \, , \tag{2.1}$$

regardless of the epoch or cosmological parameters such as the matter density parameter Ω_m. Here ρ_s is characteristic halo density (ensuring normalisation to the virial mass) and $x = \frac{r}{r_s}$, where r_s is the scale-radius of the halo. This is related to r_{-2}, the radius at which the effective logarithmic slope of the profile is -2, as follows: $r_{-2} = x_{-2} r_s$. For NFW halos $x_{-2} = 1$. This value of r_{-2} is related to the virial radius through a parameter called the virial concentration $c_{vir} = \frac{r_{vir}}{r_{-2}}$. The relationship between c_{vir} and the virial mass has been explored extensively in the literature [103, 104, 105, 106] and several methods for relating these values are employed in the following chapters.

However, at least two other profiles have been shown to work at a phenomenological level, the Einasto profile [107]

$$\rho_E(x) = \rho_s \mathrm{e}^{-\frac{2}{\alpha}\left(x^\alpha - 1\right)} \, , \tag{2.2}$$

with $x_{-2} = 1$, and the Burkert profile [108, 109, 110], which, lacking a cusp, is referred to as cored

$$\rho_B(x) = \frac{\rho_s}{\left(1+x\right)\left(1+x^2\right)} \, , \tag{2.3}$$

where $x_{-2} \sim 1.52$. This last Burkert profile was derived to fit observations of dwarf galaxy rotation curves. In particular [108] concluded that baryonic processes would need to be too fine-tuned to account for slow rise of the rotation curve and that some additional intrinsic properties of dark matter clustering (i.e. forming a core) would be a better fit. However, later work [111] demonstrates that this fine-tuning argument is somewhat weakened, but many unknown astrophysical factors make definite cosmological conclusions about cusp/core issues in dwarf galaxies difficult. The fact that kinematics of dwarf galaxies are consistent with cored profiles [109, 110], and that the study of a large sample of so-called "low surface-brightness" galaxies also seem consistent with cores [112], suggests the existence of a discrepancy between cold WIMP clustering simulations and observations. This is known as the cusp/core problem, it can be summarised by noting that for radii above 0.1 kpc simulations agree well with the NFW profile [113], however, observational evidence points to the rotation curves of many halos being consistent with cored profiles.

A somewhat related problem in the field of cold DM halos is termed "too big to fail" (TBTF). This is the observation that dissipationless DM-only simulations show that predicted sub-halos within the milky-way galaxy are over-dense and do not match any known satellites [114]. However, this study was also predicated on the existence of steep cusps within the sub-halo density profiles. It has been shown that shallower cusps can alleviate this [115]. It is evident that the existence of cored sub-halos would also alleviate the TBTF

problem, however, this solution merely drives us back to the aforementioned cusp/core problem.

As was mentioned in the discussion of the TBTF problem, DM halos are expected to contain sub-halos [47, 114, 56]. These are smaller structures that are gravitationally bound within the parent halo yet have undergone their own collapse to virial equilibrium. These sub-halos are considerably denser than their parent halo [47] and so a population of such sub-halos can provide a considerable increase in the number of WIMP annihilations that occur within the halo. In this work there are two separate approaches to the calculation of the sub-halo contribution to fluxes from WIMP annihilation that will be explored.

The first method follows from [56] and is used in Chapter 3. We begin by delineating between the smooth and sub-halo contributions to the halo density profile

$$\rho_{tot}(r) = \rho_{sm}(r) + \rho_{sh}(r) \ , \tag{2.4}$$

where the total profile is

$$\rho_{tot}(r) = \rho_s g(r/r_s) \ , \tag{2.5}$$

with $g(x)$ being such as to reproduce the relevant density profile (NFW, Burkert or Einasto). Here ρ_{sm} and ρ_{sh} are respectively the smooth and sub-halo contributions to the mass density.

The substructure of the halo is characterised by f_s, the fraction of the halo mass concentrated within sub-halos

$$f_s \equiv \frac{M_{sub}^{tot}}{M_{vir}} \ , \tag{2.6}$$

and by the spatial density of sub-halos, assumed here to be given by same function as the total halo mass density but with a larger scale radius $r_s' \sim 7r_s$ to represent radial biasing of the distribution [116]

$$p_{sub}(r) = N g(r/r_s') \ , \tag{2.7}$$

with normalisation constant N determined by the requirement

$$4\pi \int_0^{r_{vir}} dr\, r^2 p_{sub}(r) = 1 \ . \tag{2.8}$$

An additional characteristic of the halo substructure is the sub-halo mass distribution. In order to account for this we consider the rate of change of the sub-halo number density with respect to sub-halo mass M_{sub} [47]

$$\frac{dn_s}{dM_{sub}}(M_{sub}) = \mathcal{M}_0 \widetilde{M}^{-\mu} \ , \tag{2.9}$$

with $\mu = 2$ where, for a given sub-halo mass scale M_*,

$$\widetilde{M} = \frac{M_{sub}}{M_*} \tag{2.10}$$

and $\mathcal{M}_0$ is the normalisation constant, such that the total sub-halo mass contribution is normalised to $f_s M_{vir}$. In choosing the limits for mass distribution, we follow the approach of [47] in setting $M_{min} = 1 \times 10^{-6} M_\odot$ and $M_{max} = 0.01 M_{vir}$. Our minimum mass has been chosen to correspond to the WIMP free-streaming scale, although it is possible for there to be contributions from even smaller masses within the wider SUSY frame-work: lower values of M_{min} could serve to increase the boosting factor which results from the increased density provided by sub-halos.
With this in hand one can determine the coefficient β

$$\beta = \int dM_s \, \frac{dn_s}{dM_s} \int dc_s' \, \mathcal{P}(c_s') \mathcal{F}(c_s') \ , \tag{2.11}$$

such that

$$\mathcal{N}_\chi^{sub}(r) \propto p_{sub}(r) \beta \ , \tag{2.12}$$

is the average sub-halo contribution to the local WIMP-pair density, χ will denote WIMPs in our notation. The function $\mathcal{P}(c_s)$ is a log-normal distribution in sub-halo concentration parameter

$$\mathcal{P}(c_s) = \frac{1}{\sqrt{2\pi}\sigma_c c_s} \exp\left(-\left(\frac{\log c_s - \log \bar{c}_s}{\sqrt{2\pi}\sigma_c}\right)^2\right), \tag{2.13}$$

with $\bar{c}_s$ is the average sub-halo concentration and $\sigma_c = 0.14$ [103, 47]. The limits of integration are chosen to ensure the whole Gaussian is captured. Additionally, we calculate the average concentration parameter of a sub-halo of mass $\widetilde{M}$ as being ~ 1.5 times greater than that of an isolated halo of equivalent mass, this is in order to account for the tendency for average sub-halo concentrations to exceed that of the parent halo [103, 56]. Finally, the function $\mathcal{F}$ is given by

$$\mathcal{F}(x) = 4\pi(r_s')^3 \int_0^x d\xi\, \xi^2 \left(\rho'(\xi)\right)^2 , \tag{2.14}$$

where $\xi = \frac{r}{r_s'}$ and we assume sub-halos have the same form as parent halo, with the sub-halo density profile $\rho'(\xi)$ given by

$$\rho'(\xi) = \rho_s(c_s) g\left(\xi\right) , \tag{2.15}$$

where $g(x)$ having its previous definition and r_s' being the scale-radius determined by the sub-halo mass M_{sub} and concentration c_s.

Now we can express the density of WIMP pairs $\mathcal{N}_\chi(r)$ as

$$\mathcal{N}_\chi(r) = \left(\left(\rho_{tot}(r) - f_s M_{vir} p_{sub}(r)\right)^2 + p_{sub}(r)\beta\right)/2m_\chi^2 . \tag{2.16}$$

We note that this expression is valid only when considering unresolved substructure and spherically averaged observables [56].

The second method of estimating the sub-halo boosting of annihilation fluxes follows [117] and will be used in Chapter 5. This formalism defines a boosting factor b which describes the increase in the number of annihilations as a result of the increased density of sub-halos. b is defined as follows

$$b(M_{vir}) = \frac{1}{L(M_{vir})} \int_{M_{min}}^{M_{vir}} \frac{dN}{dm} L(m) dm , \tag{2.17}$$

where $L(m) = 4\pi m c_{vir}^3(m)/f(c_{vir}(m))^2$ and $f(c) = log(1+c) - \frac{1}{1+c}$. $\frac{dN}{dm} = \frac{A}{M_{vir}}\left(\frac{m}{M_{vir}}\right)^{-\alpha}$, where $A = 0.012$ and $\alpha = 2$. We take $M_{min} = 10^{-6}$ $M_\odot$.

The structure of halos is not only vital for resolving possible DM emissions based on the density profile. Another aspect of the importance of halo structure is that halos play host to large-scale baryonic structure, thus the annihilation/decay products of DM will be exposed to a complicated astrophysical environment that is both highly magnetised and contains many low energy photons (from sources like the CMB). This especially relevant if the annihilation/decay results in long-lived charged particles like electrons/positrons which can emit both synchrotron radiation in the presence of the magnetic field, as well as resulting in inverse-Compton scattering when interacting with any lower energy photons present. Thus there are many additional astrophysical factors that contribute to possible DM-based emissions that may also be influenced by the structure of the halo that hosts them.

As the discussion around halo structure remains inconclusive, we will make use of each of three halo density profiles from Eqs.(2.1), (2.2), and (2.3) as phenomenological models, and compare the differing emissions that result from their adoption.

2.3 Detecting WIMPs

Having discussed particle solutions to the problem of dark matter, with particular emphasis on WIMPs, we proceed to how such particles might be detected. This section will cover

three different approaches. These being direct detection through WIMP scattering off nuclei in Section 2.3.1. This is followed, in Section 2.3.2, by detection within particle colliders through pair production of WIMPs that carry energy out of the detector. Finally, indirect detection through the search for annihilation/decay by-products within cosmic structures is discussed in Section 2.3.3. Special attention will be paid to the indirect searches, as these are the subject of this work.

2.3.1 Direct Detection

The most direct strategy that could be adopted in the attempt to detect WIMPs would be via the otherwise anomalous recoil of a target nucleus. This is most direct as it relies on extant dark matter particles, rather than their production in a collider, and their interactions with nucleons, unlike indirect detection via annihilation/decay products. The recoil energy of a nucleus that has undergone elastic scattering with a WIMP with masses between 10 GeV and 1 TeV would be in the range 1- 100 keV [118]. Since this energy is very small, precise knowledge of the variables contributing to the recoil is necessary, as well as experimental design to maximise the signal and to block out as much background noise as possible. This is typically done via locating the detector deep underground and designing elaborate cosmic-ray shielding techniques [119].

The differential recoil spectrum is given by [118]

$$\frac{dR}{dE}(E,t) = \frac{\rho_\chi}{m_\chi m_n} \int d^3v \; v f(\mathbf{v},t) \frac{d\sigma}{dE}(E,v) \; , \tag{2.18}$$

where E is the recoil energy, m_χ is the WIMP mass, v is the WIMP velocity in the detector frame, m_n is mass of the target nucleus, $\frac{d\sigma}{dE}$ is the differential scattering cross-section, ρ_χ is the local WIMP density, and $f(\mathbf{v},t)$ is WIMP velocity distribution in the detector frame.

The parameters that limit detection sensitivity are the energy detection threshold, the mass of the target material, and the exposure time. Using Eq. (2.18), there are several methods of exploiting the dependencies of this expression to enhance the ability of direct detection to discriminate a signal against background effects [119]. For instance, the velocity of the WIMPs in the detector frame is greatest in June and smallest in December [120]. This means that in June the number of recoils that exceed the energy threshold for detection is also the largest. Therefore, this effect modulates the rate of recoil event detections, thus allowing for better discrimination of WIMP-induced recoils over the background. The directional dependence of the recoil rate is also of importance, as this is modulated by the motion of the earth relative to the Milky-way. Thus, as the Earth rotates there will be an oscillatory pattern in the preferred recoil direction, allowing for improved discrimination of the WIMP recoil spectrum over the background [121, 122]. It is worth noting that direct detection is more sensitive to the spin-independent cross-section (derived from a scalar interaction operator) than the spin-dependent form (derived from an vector/axial-vector interaction operator).

The instrumental strategies used to detect recoil events come in several varieties. The central principal is that a large quantity of the detector medium is shielded from background effects, in order to maximise the possibility of observing a recoil event. The broad categorisation of detector media is into gas, liquid, and solid detectors. As well as two-phase detectors that use both liquid and gas. In liquid and gas detectors recoils are observed either through ionisation or scintillation. For instance XMASS [123] hunts for WIMP scattering scintillations within 800 kg of pure liquid Xenon. The DarkSide experiment [124] uses a 50 kg active-mass two-phase detector and has so far produced a limit of 6.1×10^{-44} cm^2 on the spin-independent WIMP-nucleon cross-section for a 100 GeV WIMP. In solid detectors the primary observation method is through the conversion of recoil excitation into lattice vibrations (phonons) [119].

The limits on WIMP-nucleon cross-section derived by the Xenon100 two phase detector [125] are displayed in Figure 2.1. These limits can be seen to begin to probe the regions favoured by constrained minimal models of supersymmetry in the grey shaded areas. Similarly, recent results from the Large Underground Xenon (LUX) detector [135] are

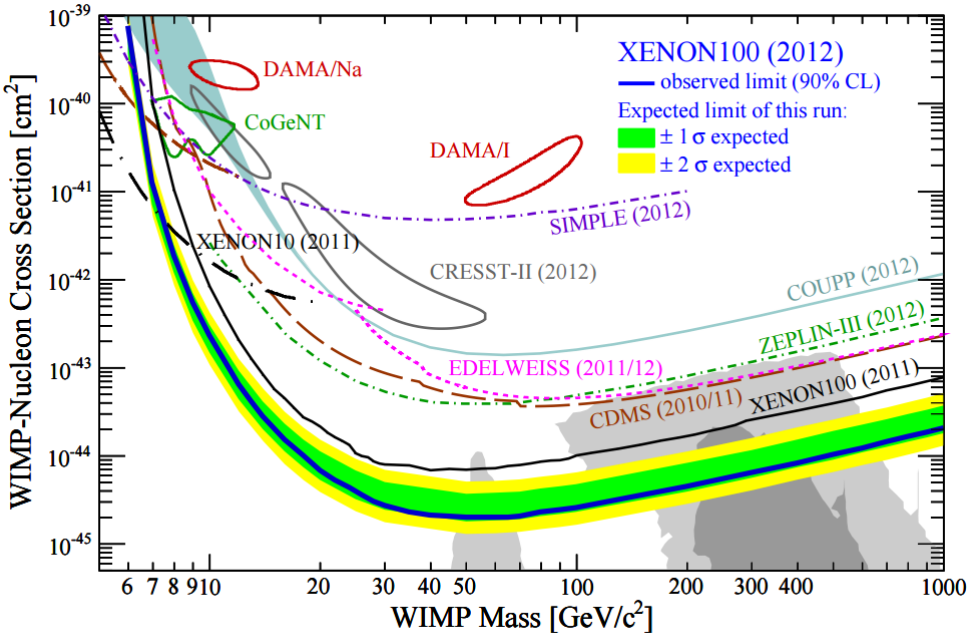

Figure 2.1: Figure from [125], displaying the WIMP-nucleon cross-section limits set by Xenon100 and other experiments [126, 127, 128, 129, 130, 131, 132, 133, 134]. The grey regions are favoured by the constrained minimal supersymmetric standard model [125].

displayed in Fig. 2.2, taken from [135], where it is evident that these substantially improve upon the Xenon100 limits. These limits on the WIMP-nucleon cross-section can be translated into those on the WIMP annihilation cross-section only through careful consideration of the particle physics of a chosen WIMP model.

In the area of solid detectors, a notable recent result was that from the DAMA experiment [142]. This experiment uses low-radioactivity sodium iodide crystals and has observed a signal modulation that, if interpreted as a result of elastic scattering with WIMPs, favours 10-15 GeV WIMPs if the scattering is from sodium, and 60-100 GeV for iodine [141]. Confirmation experiments are needed in order to eliminate the possibility of unforeseen systematics [141]. It is also apparent that it is difficult to reconcile the DAMA events with a WIMP, due to inconsistency between DAMA, LUX, and Xenon100 (as seen in Figs. 2.1 and 2.2).

Should a direct detection experiment locate a signal that is consistent with a WIMP, the next step is to reconstruct the mass and scattering cross-section. However, the dependence of direct detection upon astrophysical factors, like the WIMP velocity distribution, weakens its ability to perform this reconstruction, as there are considerable uncertainties in values of $f(\mathbf{v}, t)$ and ρ_χ [143, 144]. However, there is the possibility of improving the reconstruction by using results from multiple different direct detection experiments together. In [145] the authors argue that the use of data from hypothetical Argon, Xenon, and Germanium detectors would greatly increase the mass and cross-section reconstruction potential (reducing uncertainties by a factor of 2). This is due to the fact that each of these forms of detector are sensitive to differing regions of the m_χ–σ parameter space. The authors then demonstrate that this differing sensitivity allows the data to be used in a complementary fashion, reducing the impact of astrophysical uncertainties.

2.3.2 Collider Detection

A second detection approach is in the use of particle colliders. These can act as dark matter detectors if the beams are sufficiently energetic to result in the production of WIMP

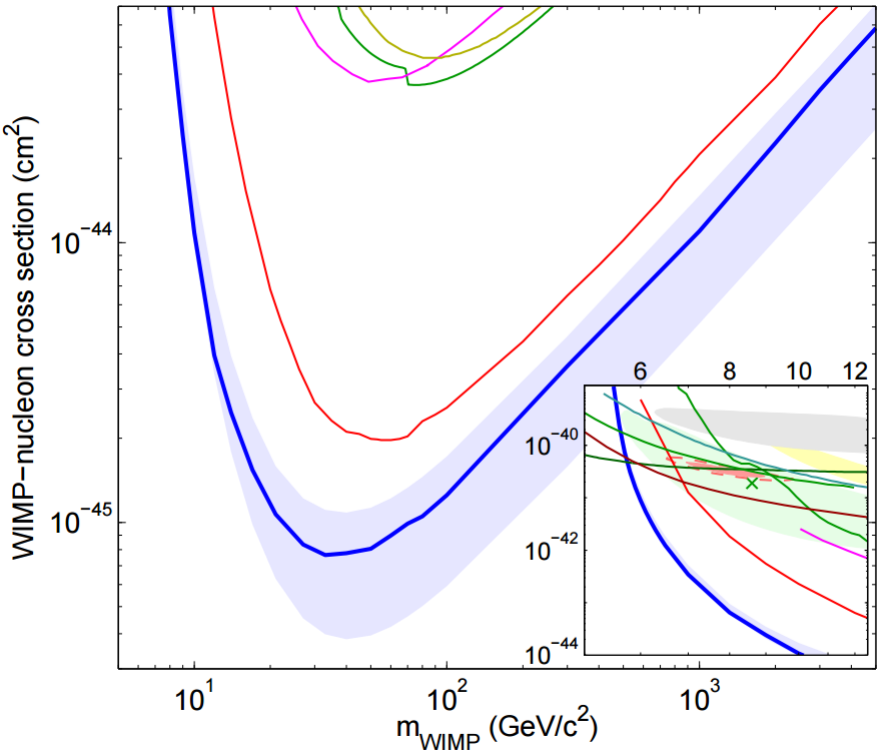

Figure 2.2: Figure from [135], displaying the cross-section limits set by LUX in the solid blue curve with 1σ shading. This figure also shows limits from Edelweiss II [130] (dark yellow line), CDMS II [129, 136] (green line), ZEPLIN-III [133] (magenta line), CDMSlite [137] (dark green line), XENON10 S2-only [131] (brown line), SIMPLE [132] (light blue line) and XENON100 100 live-day [138] (orange line), and 225 live-day [125] (red line) results. The inset (same axis units): CoGeNT [126] (light red, shaded), re-analysis of CDMS II data [139] (upper green line), CDMS II silicon detectors [140] (green shaded), 90% allowed region from CRESST II [128] (yellow shaded) and DAMA/LIBRA allowed region [141] interpreted by [127](grey shaded).

pairs. In which case the WIMPs carry away energy, leaving a net imbalance in momentum transverse to the beam axis. Additionally, WIMPs created in this way will scatter off other particles created in the same process (jets, electro-weak bosons, and heavy quarks), resulting in recoil of these Standard Model (SM) particles against WIMPs invisible to the particle detectors. Thus, the missing transverse energy correlated with anomalous recoil energy of possibly co-produced SM particles is a signature of WIMP production within an accelerator. One reason for historical and theoretical optimism in the collider search is the so called "WIMP miracle", where the assumption that the WIMP is a particle involved in electro-weak symmetry-breaking results in a prediction of the correct order of magnitude for the relic abundance [146]. This is significant as the scale explored by modern colliders is the regime of electro-weak symmetry-breaking. There is also the fact that stable neutral particles are common ingredients in theories devised to solve gauge heirachy problems [147].

This form of detection has certain advantages over the direct methods from Section 2.3.1 and the indirect methods discussed below in Section 2.3.3. In that, the direct and indirect methods both lose sensitivity as the WIMP mass decreases, as interactions thus involve less energy. In contrast to this, lower mass WIMPs are much easier to produce in collider scenarios, as their threshold for pair-production is more easily attained. However, heavier WIMP production in colliders is parton distribution suppressed, whereas indirect and direct methods are very effective at probing larger mass scales. This suppression becomes significant above a few hundred GeVs [147]. Additionally, collider searches have another significant uncertainty. This is that WIMP candidates produced in a collider might only be stable on the collider time-scale, thus being an "imposter" particle, rather than stable on cosmological time-scales which is needed for dark matter. The uncertainty occurs because collider experiments cannot easily discriminate between these two outcomes (see [148] and references therein), due to an imperfect ability to fully reconstruct all of the properties of the WIMP [149]. One remedy for this could be a bigger and better collider. However, the uncertainties in the nature of the WIMP can be mitigated through the combination of an ansatz that the local WIMP density scales with the cosmological relic abundance Ω_χ, and the use of collider data in a complementary fashion with that of direct detection experiments [149].

Collider experiments have historically focussed upon other particle physics aspects of theories believed to yield dark matter candidates. However, a new approach [150] which focuses more directly upon dark matter detection has recently been adopted. In order to do this as broadly as possible many model independent methods have been devised. The general framework is one of WIMP interactions with the standard model being mediated by a vector field. Some of these approaches involve constructing effective field theories with exhaustive operators for WIMP-SM interactions [151] with the simplification that the couplings to the mediator particle are perturbative to first order. Constraints can then be applied to each interaction operator by tagging the associated SM particles in the detector and searching for correlated missing energy. Another approach is to construct simplified models where the mediator is low mass [152, 153, 154, 155, 156], this approach has also been adopted by the CMS collaboration [157]. These simplified approaches operate under the minimal assumption set that only two particles are added to the SM, the WIMP and the mediator particle. This means that all of the WIMPs interactions with the SM are mediated through a single field. It is possible, as seen in [158], that this is too simple for general WIMP particle physics, as supersymmetric WIMPs, for instance, interact through multiple mediators.

Some existing limits on the WIMP-nucleon cross section, produced by the CMS experiment [159], are shown in Fig. 2.3 and demonstrate that the CMS detector probes a low mass region untouched by direct experiments. In the case of the spin-independent cross-section the limits in larger mass regions are substantially weaker than direct experiments. However, in the right panel the spin-dependent cross-section limits are substantially stronger than the displayed direct and neutrino indirect limits. Additionally, Fig. 2.4 shows results produced from ATLAS experiment [163] monojet data [164]. These are converted via the method of [165], under the assumption that the WIMP couples equally to all quarks, to display the consequences for the WIMP annihilation cross section. It is apparent that,

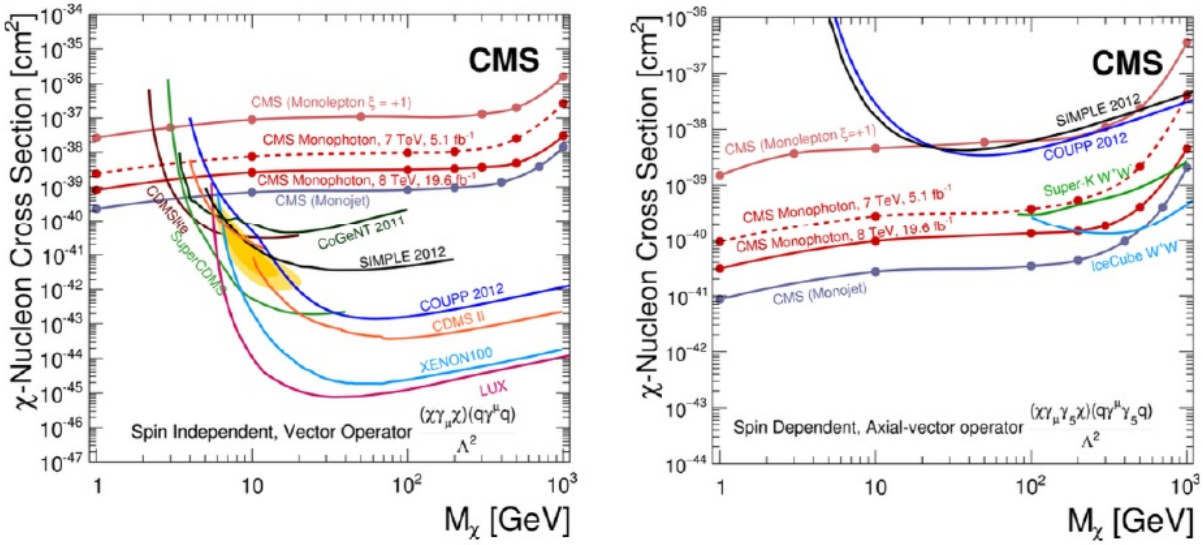

Figure 2.3: Figure from [160] displaying WIMP-nucleon cross-section limits set by the CMS experiment. Also shown are limits from direct detection experiments for comparison [137, 126, 134, 129, 125, 135, 132] as well as neutrino experiments [161, 162].

in the low mass region, these limits are highly competitive with the displayed Fermi-LAT limits [166] (it should be noted that this Fermi-LAT data is out of date), although comparison should be cautious as the WIMPs tested by ATLAS in this figure are Dirac fermions, whereas those considered by Fermi-LAT are Majorana particles.

2.3.3 Indirect Detection

Indirect detection is the process of inferring the characteristics of a WIMP by detecting its annihilation/decay by-products. Given that the annihilation cross-section (or decay rate) must be small to produce a sufficient thermal relic population [7], this form of search will need to be concentrated in targets that are expected to host large WIMP densities, such as the halos described in Section 2.2, or possibly within bodies like the sun. This section will cover, in detail, the methods of determining the expected photon spectra that result from SM particle production by WIMP annihilation and decay within cosmic structure. The increased detail is due to the focus of this work being on indirect detection, rather than the direct or collider searches of the preceding Sections 2.3.1 and 2.3.2. Additionally, there be a brief over-view of indirect detection via neutrino astronomy at the end of this section.

We will parameterise WIMP-induced particle injection with a source function Q, depending on radial position in the halo r and the product energy E. For annihilation processes this will take the form

$$Q_i(r, E) = \langle \sigma V \rangle \sum_f \frac{dN_i^f}{dE}\bigg|_E B_f \left(\frac{\rho_\chi(r)}{m_\chi} \right)^2 , \tag{2.19}$$

where f runs over the kinematically allowed annihilation states, each with branching ratio B_f, once again χ denotes the WIMP. $\langle \sigma V \rangle$ is the non-relativistic velocity-averaged WIMP annihilation cross-section at 0 K. The factor $\frac{dN_i^f}{dE}$ gives the number of particles i with energy E produced per annihilation per unit energy, while $\left(\frac{\rho_\chi(r)}{m_\chi} \right)^2$ characterises the number density of WIMP pairs. Thus Q_i has the units of number of i particles injected per unit energy per unit volume per second.

For decaying WIMPs the source function will be proportional to the decay rate and the

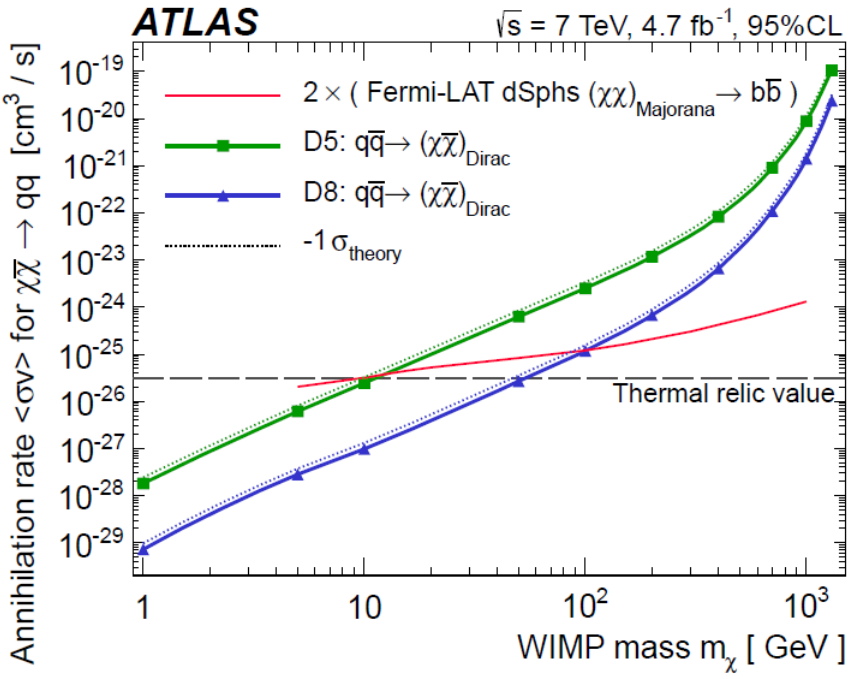

Figure 2.4: Figure from [147] with data sourced from [164] using the method from from [165], displaying WIMP annihilation cross-section limits set by the ATLAS experiment. This assumes the WIMP annihilates equally into each type of quark. The red line shows limit from Fermi-LAT dwarf spheroidal observations [166], while the green and blue lines display ATLAS limits for different WIMP-SM interaction operators (see [147]).

WIMP density

$$Q_i(r,E) = \frac{1}{\tau_\chi}\sum_f \frac{dN_i^f}{dE}\bigg|_E B_f \frac{\rho_\chi(r)}{m_\chi} \ , \tag{2.20}$$

where f runs over the kinematically allowed decay states, each with branching ratio B_f. τ_χ is the lifetime of the WIMP and the factor $\frac{dN_i^f}{dE}$ gives the number of the particles i produced per decay.

In this work we will be studying WIMPs that annihilate only, and the spectra $\frac{dN_i^f}{dE}$ will be found using the PYTHIA Monte-Carlo routines in DarkSUSY [167, 168]. For the neutralinos we study we will consider three allowed product states: bottom quarks $b\bar{b}$, τ leptons $\tau^+\tau^-$, and weak W-bosons W^+W^-. These can proceed to promptly decay or annihilate into further standard model particles.

If the particles being produced are photons Q_γ, then the spectrum of emission is dictated simply by annihilation product spectra $\frac{dN_\gamma^f}{dE}$, with the properties of the halo entering only into the radial dependence of Q. This means that pure photon production (through possible intermediary states) can be characterised by two separable factors, one astrophysical factor drawn from the halo, and the other dictated by the particle physics of the WIMP. We could then write the flux of such emissions as a product

$$\Phi(E_\gamma, D_L) = J_{halo}(D_L)\psi_{\chi\chi\to\gamma\gamma}(E_\gamma) \ , \tag{2.21}$$

where D_L is the luminosity distance and

$$\begin{aligned} J_{halo}(D_L) &= \int_0^{r_{vir}} dr^3 \ \frac{\rho_\chi^2(r)}{4\pi m_\chi^2 D_L^2} \ , \\ \psi_{\chi\chi\to\gamma\gamma}(E_\gamma) &= E_\gamma\langle\sigma V\rangle \sum_f \frac{dN_\gamma^f}{dE}\bigg|_{E_\gamma} B_f \ . \end{aligned} \tag{2.22}$$

Such a spectrum will evidently be non-thermal, as it depends only on the prompt emission functions $\frac{dN_\gamma^f}{dE}$ and their branching ratios, which are all matters of fundamental particle properties only. The typical energy of these photons will be dictated by the mass-energy of the WIMP, with WIMPs above keV mass-energies producing X-ray and γ-ray photons. The maximum γ-ray frequency thus produced is $\sim 10^{20}$ MHz for a 1 TeV mass-energy WIMP.

However, as mentioned in Section 2.2, there are more complex astrophysical possibilities should other stable particles result from WIMP annihilation/decay. In this case we want the equilibrium distributions of the stable particles, rather than their prompt emission function Q. For many sources of radiation electrons are the primary emitter, so we will look at the electron/positron equilibrium distributions $\frac{dn_{e^+}}{dE}$ and $\frac{dn_{e^-}}{dE}$. These are stationary solutions to the equation

$$\frac{\partial}{\partial t}\frac{dn_e}{dE} = \boldsymbol{\nabla}\left(D(E,\mathbf{x})\boldsymbol{\nabla}\frac{dn_e}{dE}\right) + \frac{\partial}{\partial E}\left(b(E,\mathbf{x})\frac{dn_e}{dE}\right) + Q_e(E,\mathbf{x}) \ , \tag{2.23}$$

where Q_e is the electron source function, $D(E,\mathbf{x})$ is the diffusion coefficient, and $b(E,\mathbf{x})$ is the energy-loss factor. This equation represents an injection of electrons via the function Q which then diffuse spatially under the influence of a turbulent magnetic field and lose energy via a variety of radiative and Coulomb processes. It is also apparent from Eq. (2.23) that $\frac{dn_{e^\pm}}{dE}$ has dimensions of electrons/positrons per unit energy per unit volume.

In order to simplify the solution of Eq. (2.23), we will assume spherical symmetry and that D and b depend only on average values of B and thermal electron density n_{th}. Then the diffusion coefficient is defined following [169]

$$D(E) = \frac{1}{3}cr_L(E)\frac{\overline{B}^2}{\int_{k_L}^\infty dk P(k)} \ , \tag{2.24}$$

where $P(k)$ is the magnetic field power spectrum, $\overline{B}$ is the average magnetic field in the halo, r_L is the Larmour radius of a relativistic particle with energy E and charge e, and $k_L = \frac{1}{r_L}$. We then require that

$$\int_{k_0}^{\infty} dk P(k) = \overline{B}^2 \ , \tag{2.25}$$

with $k_0 = \frac{1}{d_0}$, d_0 is smallest scale on which the magnetic field is uniform. This leads us to the result that

$$D(E) = D_0 d_0^{\frac{2}{3}} \left(\frac{\overline{B}}{1\mu\text{G}}\right)^{-\frac{1}{3}} \left(\frac{E}{1\text{GeV}}\right)^{\frac{1}{3}} \ , \tag{2.26}$$

where $D_0 = 3.1 \times 10^{28}$ cm^2 s^{-1}. Finally, the energy-loss factor is found via [56]

$$\begin{aligned} b(E) =& b_{IC} E^2 (1+z)^4 + b_{sync} E^2 \overline{B}^2 \\ &+ b_{Coul} \overline{n}_{th} (1+z)^3 \left(1 + \frac{1}{75} \log\left(\frac{\gamma}{\overline{n}_{th}(1+z)^3}\right)\right) \\ &+ b_{brem} \overline{n}_{th} (1+z)^3 \left(\log\left(\frac{\gamma}{\overline{n}_{th}(1+z)^3}\right) + 0.36\right) \ , \end{aligned} \tag{2.27}$$

where $\overline{n}_{th}$ is given in cm^{-3} and b_{IC}, b_{synch}, b_{col}, and b_{brem} are the inverse-Compton, synchrotron, Coulomb and bremsstrahlung energy loss factors, taken to be 0.25, 0.0254, 6.13, and 1.51 respectively in units of 10^{-16} GeV s^{-1}. Here E is the energy in GeV and the B-field is in μG.

Under the preceding assumptions, the stationary solution of Eq. (2.23) is found by method of images to be [170, 171, 56]

$$\frac{dn_e}{dE}(r, E) = \frac{1}{b(E)} \int_E^{m_\chi} dE' \, G(r, E, E') Q_e(r, E') \ , \tag{2.28}$$

where $G(r, E, E')$ is a Green's function. This function is expressed as

$$\begin{aligned} G(r, E, E') =& \frac{1}{\sqrt{4\pi\Delta v}} \sum_{n=-\infty}^{\infty} (-1)^n \int_0^{r_h} dr' \, \frac{r'}{r_n} \\ &\times \left(\exp\left(-\frac{(r'-r_n)^2}{4\Delta v}\right) - \exp\left(-\frac{(r'+r_n)^2}{4\Delta v}\right)\right) \frac{n_\chi^2(r')}{n_\chi^2(r)} \ , \end{aligned} \tag{2.29}$$

where r_h is the maximum radius considered for spatial diffusion, $n_\chi^2(r)$ is WIMP pair density at position r, $r_n = (-1)^n r + 2nr_h$ are the image charge positions, and

$$\Delta v = v(u(E)) - v(u(E')) \ , \tag{2.30}$$

with

$$\begin{aligned} v(u(E)) &= \int_{u_{min}}^{u(E)} dx \, D(x) \ , \\ u(E) &= \int_E^{E_{max}} \frac{dx}{b(x)} \ . \end{aligned} \tag{2.31}$$

These last equations constitute a similar change of variables to those used by [170, 171] to solve Eq. (2.23).

The stable particle species i can then produce electromagnetic radiation through interactions within the halo environment. A spectrum of this sort will arise from the injection of particles of species i into the halo environment, which proceed to interact with another species j, with some cross-section $\sigma_{i,j}$ giving the effective interaction area, to produce a photon of energy E_γ. In order to determine the resulting energy output, the spectral function will need to contain the product of the density for the species j, the particle distribution $\frac{dN_i}{dE}(r, E)$ (from Eq. (2.28) for instance), the cross-section $\sigma_{i,j}$, and the resulting output photon energy. To make this as general as possible, the density of j will be expressed as a

differential density with respect to energy E_j, and the cross-section will also be expressed in differential form with respect to energy. This will require that we integrate over the possible energies for E_j as well as the injection energies E_i, with the cross-section depending, in principle, on all three energies E_i, E_j, and E_γ. The resulting photon spectrum might then take the form

$$\zeta_{(i|k)}(E_\gamma, r) = cE_\gamma \sum_j \int dE_i \int dE_j \; \sigma_{(i,j|k)}(E_i, E_j, E_\gamma) n_j(E_j, r) \frac{dN_i(r)}{dE}\bigg|_{E_i} . \tag{2.32}$$

Here $\zeta_{(i|k)}$ is a spectral function for a process k with particles i with energy E_i, the sum runs over all the species j (with energy E_j) within the halo environment, $\sigma_{(i,j|k)}(E_i, E_j, E_\gamma)$ is the cross-section per unit energy for the k-process interaction between i and j producing a photon with energy E_γ, and $n_j(E_j, r)$ is the number density per unit energy of species j. ζ is thus expressed in dimensions of photons per unit volume per second. The case for prompt photon production will be $\zeta_{(\gamma|\gamma)} = E_\gamma Q_\gamma$.

The function $\zeta_{(i|k)}(E_\gamma, r)$ can be used to calculate the resulting flux at luminosity distance D_L:

$$\Phi(E_\gamma, D_L) = \int dr^3 \; \frac{\zeta_{(i|k)}(E_\gamma, r)}{4\pi D_L^2} , \tag{2.33}$$

where this is expressed in dimensions of photons per unit area per second. It is this flux that forms the primary means of indirectly detecting WIMPs via their annihilation/decay products, as it can be detected by sufficiently sensitive telescopes tuned to the appropriate frequency range.

An example of a process that can be modelled according to Eq. (2.32) is inverse-Compton scattering. In this case a high-energy electron produced by WIMP annihilation scatters a lower energy photon, imparting energy to the photon. For this process there will only be one species j, this being the population of low energy photons in the halo, often take simply as that of the CMB. The species i is then the electrons/positrons produced by WIMP annihilation, with $\frac{dN_i}{dE}(r, E) = \frac{dn_e^-}{dE}(r, E) + \frac{dn_e^+}{dE}(r, E)$, and $\sigma_{(e^\pm,\gamma|IC)}$ is the cross-section of inverse-Compton scattering [172]:

$$\sigma_{(e^\pm,\gamma|IC)}(E_e, E_{\gamma,in}, E_{\gamma,out}) = \frac{3\sigma_T m_e^2 c^4}{4E_{\gamma,in}E_e^2} G(q, \Gamma_e) , \tag{2.34}$$

where σ_T is the Thompson cross-section, E_e is the electron energy, $m_e c^2$ is the electron mass-energy, $E_{\gamma,in}$ is the starting photon energy, $E_{\gamma,out}$ is the photon energy after scattering, and

$$G(q, \Gamma_e) = 2q \ln q + (1 + 2q)(1 - q) + \frac{(\Gamma_e q)^2 (1 - q)}{2(1 + \Gamma_e q)} , \tag{2.35}$$

with

$$\begin{aligned} q &= \frac{E_{\gamma,out}}{\Gamma_e (E_e + E_{\gamma,out})} , \\ \Gamma_e &= \frac{4E_{\gamma,in}E_e}{m_e^2 c^4} . \end{aligned} \tag{2.36}$$

For WIMPs with mass-energies considerably larger than the mass-energy of an electron, this process will result in CMB photons being up-scattered to X-ray and even soft γ-ray spectral regions. This can be seen from the fact that the average frequency of inverse-Compton photons is given by [172]

$$\langle \nu_{out} \rangle = \nu_{in} \frac{4}{3} \left(\frac{E_e}{m_e c^2} \right)^2 . \tag{2.37}$$

Thus, for $z = 0$, the average up-scattered frequency of a CMB photon is $\langle \nu_{out} \rangle \sim \left(\frac{E_e}{\text{GeV}} \right)^2 10^{12}$ MHz. So for any WIMP with a mass larger than the electron mass, this frequency will be outside the radio region. The maximum photon frequency is only 3 times larger than

$\langle \nu_{out} \rangle$ [172], which means the spectrum is steeply peaked and will tail-off before 10^{18} MHz provided the WIMP mass is below 1 TeV. Therefore, it is apparent that inverse-Compton scattering of CMB photons will produce emissions in the X-ray and soft γ-ray frequency ranges.

Another example process is bremsstrahlung, whereby an electron is scattered off another particle and releases photons as it is decelerated. The species i will once again be the electrons/positrons produced by DM annihilation, with $\frac{dN_i}{dE}(r,E) = \frac{dn_e^-}{dE}(r,E) + \frac{dn_e^+}{dE}(r,E)$. The sum j will run over all the species present in the halo medium. The cross-section of this process $\sigma_{e^\pm,j|Brem}$ is given by [172]

$$\begin{aligned} \sigma_{e^\pm,j|Brem}(E_\gamma, E_e) &= \frac{3\alpha_e \sigma_T}{8\pi E_\gamma}\left[\left(1+\left(1-\frac{E_\gamma}{E_e}\right)^2\right)\phi(\Delta E) - \frac{2}{3}\left(1-\frac{E_\gamma}{E_e}\right)\phi(\Delta E)\right] , \\ \phi(\Delta E) &= 4\log(\Delta E) - \frac{1}{2} , \\ \Delta E &= 2E_e \frac{E_e - E_\gamma}{m_e c^2 E_\gamma} , \end{aligned} \tag{2.38}$$

with α_e being the fine-structure constant, E_e is the incident electron/positron energy, and E_γ is the bremsstrahlung photon energy. As the bremsstrahlung cross-section is independent of E_j, the following simplification holds $\int dE_j \; n_j(E_j, r) = n_j(r)$, where this is the species j number density in the halo. Again, for WIMPs with mass-energies considerably larger than the mass-energy of an electron, this process will result in the production of photons in the X-ray and even soft γ-ray spectral regions. The maximum bremsstrahlung emission frequency is determined by assuming all of the electron's kinetic energy is converted to a photon, thus this frequency will be slightly smaller than the maximum γ-ray production frequency. For the supersymmetric WIMPs studied here, the frequency with the largest flux occurs roughly an order of magnitude below the WIMP mass, below this frequency the spectral function ζ tails off approximately like a power-law. The resulting spectrum will fall between that of inverse-Compton scattering and photon pair-production.

A complete multi-frequency spectrum would constructed by enumerating all the processes k and finding the sum of their respective ζ functions for each species i produced by the WIMP annihilations. It is evident that even if the distributions n_j are thermal, the resulting spectra will be non-thermal, as their shape will be affected by the prompt emission spectra $\frac{dN_i^f}{dE}$ and details of fundamental particle physics which are quite independent of temperature.

If WIMP annihilation gives rise to charged particles like electrons/positrons, then, in the magnetised environment of cosmic structure there is the possibility of non-thermal synchrotron radiation being produced. This radiation occurs as charged particles trace out a helical trajectory under the influence of the force induced by the magnetic field component perpendicular to its velocity. This form of radiation is a vital aspect of a prospective multi-frequency WIMP-induced emission spectrum as it can result in radio frequency emission even for WIMPs with very large mass energies, in contrast to processes like direct photon production and inverse-Compton scattering. This can be seen by examining the formula for the characteristic/peak frequency for synchrotron radiation [172, 173]

$$\omega_c \approx 1.5 \times 10^2 \left(\frac{B}{1\mu\text{G}}\right)\left(\frac{E_e}{1\text{GeV}}\right)^2 \text{ MHz} , \tag{2.39}$$

where B is the magnetic field strength and E_e is the electron energy. Thus if our magnetic field is $\mathcal{O}(\mu\text{G})$ then we require $E_e \lesssim 10^2$ GeV to keep the synchrotron peak below 10 GHz. This means that if $m_\chi \lesssim 10^2$ GeV, we can expect a synchrotron spectrum tailing off above 10 GHz.

The spectral function for synchrotron radiation will differ somewhat from Eq. (2.32), as there is no secondary particle species j involved in the interaction. In fact, given that a number of photons $n_{synch}(E_\gamma, E_e, B)$ with energy E_γ are produced per electron with energy

E_e per second in a magnetic field of strength B, the spectral function takes the form

$$\zeta_{(e^+e^-|synch)}(E_\gamma, r) = E_\gamma \int dE \left(\frac{dn_{e^+}}{dE}(E, r) + \frac{dn_{e^-}}{dE}(E, r) \right) n_{synch}(E_\gamma, E, B(r)) \ , \quad (2.40)$$

where $\frac{dn_{e^+}}{dE}$ and $\frac{dn_{e^-}}{dE}$ are the WIMP-induced positron and electron equilibrium densities per unit energy respectively, see Eq. (2.28). Since the factor $E_\gamma n_{synch}(E_\gamma, E_e, B(r))$ is equivalent to synchrotron power per electron we can find it from [172]

$$E_\gamma n_{synch}(E_\gamma, E_e, B(r)) \propto \int_0^\pi d\theta \, \frac{\sin\theta^2}{2} 2\pi\sqrt{3} r_e m_e c \nu_g F_{synch} \left(\frac{\kappa}{\sin\theta} \right) \ , \quad (2.41)$$

where m_e is the electron mass, $\nu_g = \frac{eB}{2\pi m_e c}$ is the non-relativistic gyro-frequency - this being the frequency with which a non-relativistic electron orbits in the magnetic field, $r_e = \frac{e^2}{m_e c^2}$ is the classical electron radius, and the quantities κ and F_{synch} are defined as

$$\kappa = \frac{2\nu_\gamma (1+z) m_e^2 c^4}{3\nu_g E_e^2} \left(1 + \left(\frac{E_e \nu_p}{m_e c^2 \nu_\gamma (1+z)} \right)^2 \right)^{\frac{3}{2}} \ , \quad (2.42)$$

with $\nu_p \propto \sqrt{n_{th}}$ being the plasma frequency where $n_{th}(r)$ is the thermal electron density in the halo, and

$$F_{synch}(x) = x \int_x^\infty dy \, K_{5/3}(y) \simeq 1.25 x^{\frac{1}{3}} \mathrm{e}^{-x} \left(648 + x^2 \right)^{\frac{1}{12}} \ . \quad (2.43)$$

In summary there are several processes which can contribute to DM-induced photon production, with Eq. (2.32) providing a generalised spectral function. Significantly for WIMPs with masses much greater than the electron mass, only synchrotron radiation results in emissions below the X-ray band. Inverse-Compton emissions fall largely within the X-ray band, for WIMPs between 1 GeV and 1 TeV. The bremsstrahlung spectrum has a higher maximum frequency than that of inverse-Compton, but falls short of that from the production of photon pairs, which provides the highest-energy WIMP annihilation emissions. The final spectrum will be found as combination of synchrotron, inverse-Compton, bremsstrahlung, and direct photon emission. All of these emission forms are non-thermal as they depend on the energy distributions of the products of prompt WIMP annihilation/decay processes. This means that a search for such non-thermal emissions via γ-rays, X-rays, or radio would stand a chance at detecting the signatures of WIMP annihilation. This possibility will be explored in greater detail in the following chapters of this work. It must be noted that this summary of indirect detection methods is by no means complete, a particular method that was not discussed was the use of the CMB power spectrum to constrain the annihilation cross-section [26].

Some current limits from indirect detection are displayed in Figs. 2.5 and 2.6, taken from [69] and [31] respectively. In Fig. 2.5 the limits on the WIMP annihilation cross-section from the Planck experiment [26] are displayed in blue for two values of the dark matter energy deposition efficiency parameter f_{eff}. Additionally, this plot shows the limits from the Fermi-LAT observations of dwarf spheroidal galaxies [29] for WIMP annihilations via b quarks and τ leptons. Comparison should be made between the Fermi-LAT curves and the $f_{eff} = 0.2$ line for Planck (this matches the efficiency of the $b\bar{b}$ and $\tau^+\tau^-$ channels). It is evident that the constraints of Fermi-LAT, though spanning a smaller region, are considerably stronger than those of Planck for masses above 10 GeV. The sensitivity of Fermi-LAT weakens considerably for lower mass WIMPs, where Planck produces superior results. The green region shows the area favoured by models accounting for the AMS/Fermi/PAMELA positron excesses [42]. While the red area shows the region favoured by Fermi-LAT observations of excess γ-rays from the galactic centre [32, 33, 34]. The points are representative models used for testing in [69]. Although not shown, the HESS experiment [174], has produced limits that improve on Fermi-LAT for τ lepton annihilation and masses above 1 TeV [175]. The comparison of the curves in Figs. 2.5 and 2.6 demonstrate the great potential of the

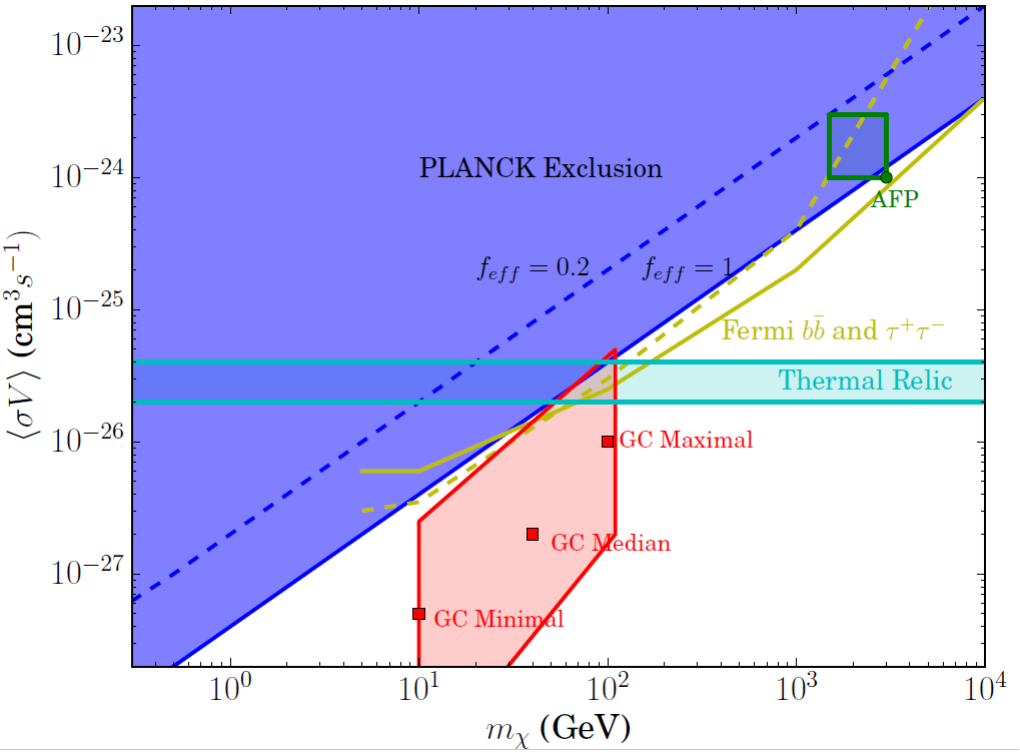

Figure 2.5: Figure from [69] showing the annihilation cross-section constraints from Planck (blue) and Fermi-LAT (yellow). As well as regions favoured by positron excesses (green) and galactic centre γ-ray excesses (red). f_{eff} refers to the DM annihilation energy deposition efficiency factor (note that $b\bar{b}$ and $\tau^+\tau^-$ annihilation channels have $f_{eff} \sim 0.2 - 0.3$)

indirect γ-ray and radio observation, both having potential to better Planck in different parts of the WIMP mass range. Figure 2.6 shows the limits on the WIMP annihilation cross-section derived from radio observation of dwarf spheroidal galaxies using the Australian Telescope Compact Array (ATCA). The three panels show three scenarios for diffusion characteristics within the halo, being optimistic on the left, pessimistic on the right, and with the average in between.

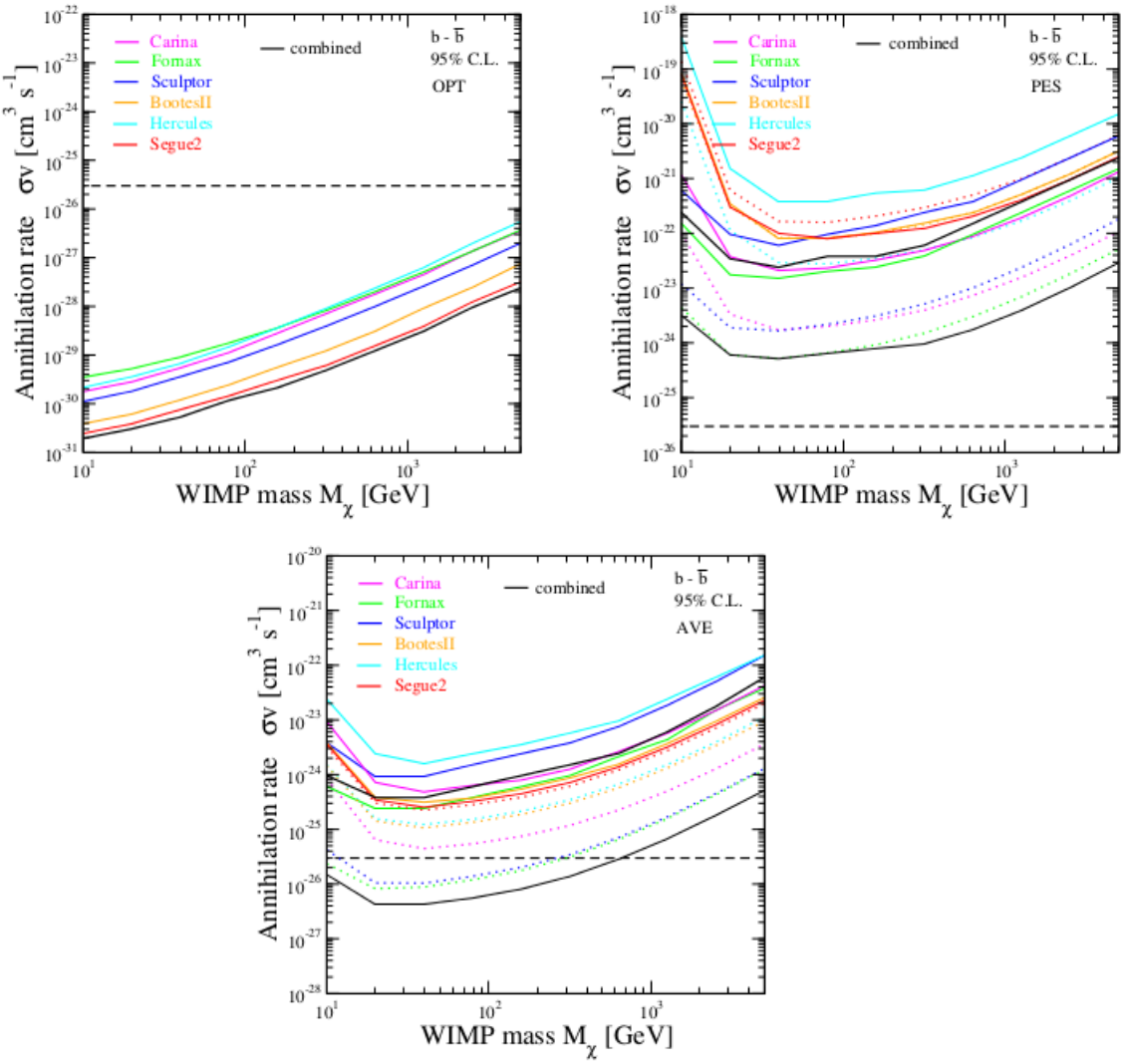

Figure 2.6: Figure from [31] showing limits on the WIMP annihilation cross-section from radio observation of dwarf galaxies. The three panels show differing diffusion scenarios. *Top Left*: optimistic, *Top Right*: pessimistic, and *Lower Middle*: average between the upper two. The dashed line is the thermal relic bound on the annihilation cross-section.

Neutrinos

Another indirect detection strategy might be to search for neutrinos produced by WIMP annihilation within the sun. This would occur as a result of WIMPs scattering against nucleons within the sun, losing energy, and becoming gravitationally bound. As the sun proceeds to capture more WIMPs, the annihilation probability increases with the WIMP density until an equilibrium is established between capture and annihilation rates. This is summarised in

the Riccati equation [7]

$$\frac{dN}{dt} = C_\odot - C_A N^2 - C_E N \,, \tag{2.44}$$

where N is the number of captured WIMPs, $C_\odot$ is the capture rate of the sun, $C_A N^2$ is twice the annihilation rate, and $C_E N$ is the rate of escape. If the WIMP mass is in excess of 10 GeV the escape rate is negligible [176], so this has the solution

$$C_A N^2 = C_\odot \tanh^2 \left(\sqrt{C_\odot C_A} t \right) . \tag{2.45}$$

For long times the term $\tanh^2 \left(\sqrt{C_\odot C_A} t \right) \to 1$, so that this results in $C_A N^2 = C_\odot$. Which implies that the neutrino flux emitted by WIMP annihilation in the sun is independent of the annihilation cross-section and depends only on the nucleon scattering cross-section through $C_\odot$.

Experiments conducted with the IceCube neutrino detector instrument [20] have so far detected no signals above the expected solar background [177, 162]. Figure 2.7, taken from [178], displays the limits imposed by IceCube on the spin-dependent WIMP-nucleon cross-section [162]. It is evident from this figure that neutrino experiments like IceCube are sensitive only to higher mass WIMPs. A comparison of IceCube, as well as Super-Kamiokande [161], to direct and accelerator limits was displayed in the right panel of Fig. 2.3. The effects of IceCube data on minimal models of supersymmetric WIMPs are displayed in Figure 2.8, taken from [162]. These results show that IceCube has eliminated further models that were not affected by the LUX experiment (these models are shown in red crosses). Models already eliminated by LUX appear as faded red crosses.

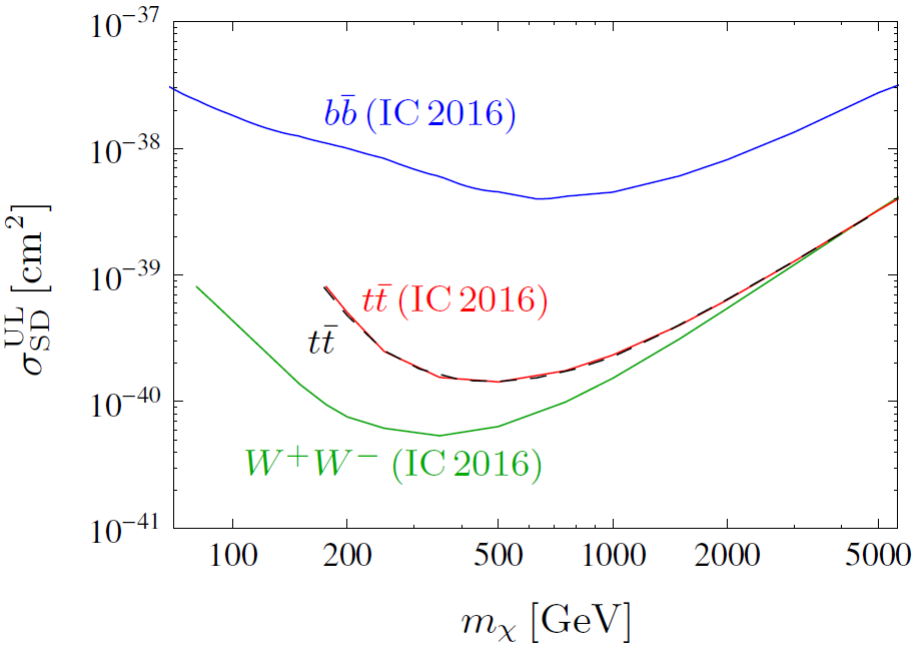

Figure 2.7: Figure from [178] using data from [162], displaying the 90% C.L. limits on the spin-dependent WIMP-nucleon cross-section set by IceCube. Annihilation is assumed to be 100% into either b quarks (blue), weak W bosons (green), or τ leptons (red).

Finally, another aspect of neutrino experiments is in their ability to aid direct detection experiments to reconstruct the mass and cross-section from a detected signal. In this regard, it has been shown that IceCube has the potential to complement future direct detection searches, allowing for a reduction in the uncertainty introduced by astrophysical factors [183]. Additionally, this improvement also occurs for constraints if a null-result is achieved.

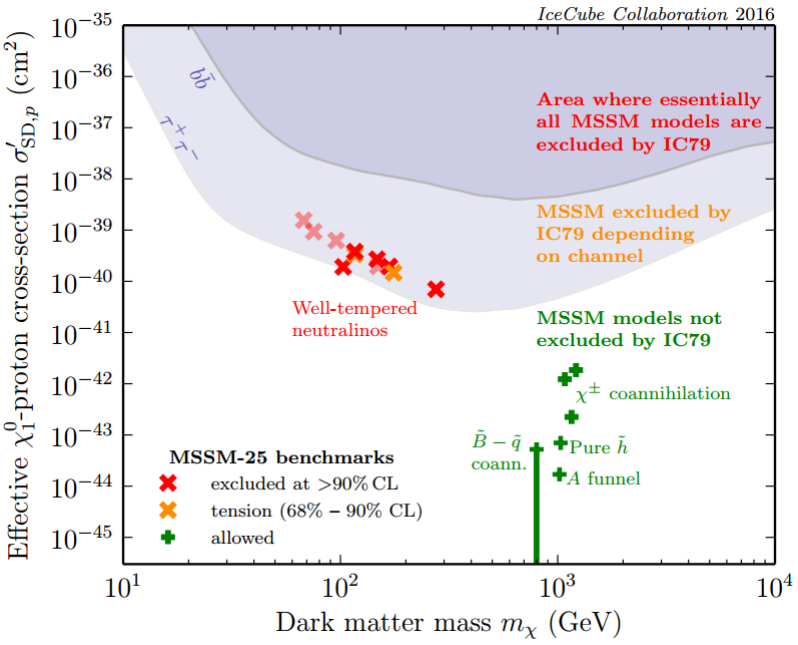

Figure 2.8: Figure from [162] (IC79), displaying the IceCube exclusion limits on the models of minimal supersymmetry. Models shown with solid red crosses are excluded by IceCube [162]. Faded red symbols are also excluded by LUX spin-dependent bounds [179, 180]. Orange crosses are in tension with IC79 results. Green pluses are unconstrained, and labelled according to the characteristic setting their relic density. The models are drawn from the MSSM-25 and MSSM-19 [181, 182].

Chapter 3

Dark Matter Halo Radio Emissions

This chapter consists of a survey of the radio emission from dark matter halos and the influence of redshift and halo mass upon this. These emissions are compared to the sensitivity of the SKA and non-detection constraints are derived for the case where the SKA fails to locate any such emissions. These constraints are several orders of magnitude better than existing results and demonstrate the potential power of the SKA to hunt dark matter. We also show the dependence of these constraints on the magnetic field within the halo and demonstrate that the SKA is sensitive to a spectral region that carries signatures of the neutralino mass and annihilation channel.

This contributes to our argument for multi-frequency strategies by showing that an experiment like the SKA can strongly contribute to future dark matter searches on a level that is extremely competitive with γ-ray experiments. We leave discussion of the ability of the SKA to deal with the magnetic field and confusion limit uncertainties, that would weaken the results shown here, to Chapter 4, while an exploration of the effects of background radio emissions is made in Chapter 5.

This chapter was published in the Journal of Cosmology and Astroparticle Physics. The contribution of the candidate was significant, including writing the software necessary for all the calculations (with guidance from Dr P. Marchegiani). Additionally, the candidate used the created software to produce all of the data needed for the figures displayed in the work (as well as the figures themselves). The candidate also selected the results to be displayed in the furtherance of the arguments in the work. Furthermore, apart from a section on magnetic fields extending from halfway down page 6 to halfway down page 7, as well as a segment beginning near the bottom of page 23 and ending two-thirds of the way down page 25, the candidate composed all of the text (with editing and suggestions from co-authors). This composition includes the formulation of the argumentation strategy expressed within the work as well as performing all the necessary analysis of the results.

Prepared for submission to JCAP

Evolution of Dark Matter Halos and their Radio Emissions

S. Colafrancesco,[a,1] **P. Marchegiani,**[a] **G. Beck**[a]

[a]School of Physics, University of the Witwatersrand, Private Bag 3, WITS-2050, Johannesburg, South Africa

E-mail: sergio.colafrancesco@wits.ac.za, paolo.marchegiani@wits.ac.za, geoff.m.beck@gmail.com

Abstract. Radio synchrotron emission is expected as a natural by-product of the self-annihilation of super-symmetric dark matter particles. In this work we discuss the general properties of the radio emission expected in a wide range of dark matter halos, from local dwarf spheroidal galaxies to large and distant galaxy clusters with the aim to determine the neutralino dark matter detection prospects of the Square Kilometre Array (SKA). The analysis of the SKA detection of dark matter(DM)-induced radio emission is presented for structures spanning a wide range of masses and redshifts, and we also analyze the limits that the SKA can set on the thermally averaged neutralino annihilation cross-section in the event of non-detection. To this aim, we construct a model of the redshift evolution of the radio emissions of dark matter halos and apply it to generate predicted fluxes from a range of neutralino masses and annihilation channels for the dark matter halos surrounding dwarf galaxies, galaxies and galaxy clusters. Using the available SKA performance predictions and its ability to determine an independent measure of the magnetic field in cosmic structures, we explore both the detailed detection prospects and the upper-bounds that might be placed on the neutralino annihilation cross-section in the event of non-detection. We find that the SKA can access a neutralino parameter space far larger than that of any preceding indirect-detection experiment, also improving on the realistic CTA detection prospects, with the possibility of setting cross-section upper-bounds up to four orders of magnitude below the thermal relic density bound. Additionally, we find that neutralino radio emissions carry redshift-independent signatures of the dominant annihilation channel and of neutralino mass, offering therefore a means to identify such non-thermal emissions within the observing frequency range of the SKA.

[1]Corresponding author.

Contents

1 Introduction

Modern astrophysical evidence, namely gravitational lensing, galaxy rotation curves, galaxy cluster masses, and cosmic microwave-background anisotropy data suggests that the majority of the matter content within the universe is in the form of dark matter and that this plays a vital role in the evolution of structure within the universe. The nature of dark matter remains a major hiatus in the understanding of modern physics, with many contending models proposed to account for this missing puzzle-piece [6, 27, 29, 41, 51, 58] and with many methods of both direct and indirect detection proposed [4, 14, 21, 31]. In this study we focus on one of the current favourites in the dark matter candidate zoo: the so-called "neutralino", being the lightest particle from the minimal super-symmetric extension of the standard model (MSSM). While there is no experimental evidence yet supporting super-symmetry, the model is attractive as super-symmetric effects may manifest unambiguously in collider experiments. Clearly then, direct detection provides the cleanest route to discovery. However, the possibility of indirect detection through astrophysical signatures remains, as the weakly interacting nature of the neutralino allows for mutual pair annihilation to produce standard model particles which may then be produced as cosmic rays or instead subsequently emit radiation. Additionally, the increasing sensitivity of astronomical measurements and the limitations of current ground-based direct detection experiments combine to make indirect detection methods increasingly attractive and competitive when it comes to setting limits on the nature of dark matter. While many authors have previously studied the high-energy products of neutralino pair annihilation [5, 22, 30, 32, 33, 43, 52, 59, 60], there has been some recent interest in the possibility of detecting radio emission resulting from the annihilation products of such particles [19, 44, 66, 69, 72]. However, this interest has been largely confined to single source studies, looking at either the galactic centre or towards specific, dark matter-dominated, sources. We therefore present here a detailed study of the radio emissions that result from the mutual pair annihilation of neutralinos within the dark matter halos that surround cosmic structures ranging from dwarf galaxies to galaxy clusters observable at various distances from the local environment (e.g. dwarf spheroidal galaxies) to redshifts of $z \sim 5$ (galaxies and galaxy clusters). In this context, we make a thorough survey to determine how dark matter-induced radio emissions depend upon the mass and annihilation channel of the neutralino, and how they evolve with redshift, with an additional focus on the potential detection capabilities of the upcoming Square Kilometre Array (SKA) telescope. Such a comprehensive study, especially one making special reference to the SKA as a "dark matter machine", is currently absent from the literature. In this paper we make an extensive study of the radio emissions from dark matter halos varying the neutralino mass, annihilation channel, as well the mass and redshift of the halo while using various dark matter density profiles such as Einasto, Burkert and Navarro-Frenk-White profiles. We scan the parameter space of structures hosting dark matter, extending from dwarf galaxies to galaxy

clusters with redshifts between 0.01 and 5. The relatively large redshifts examined are important as they might offer the chance to detect dark matter in structures that are more primitive, having fewer baryon-related astrophysical mechanisms that produce additional foreground synchrotron emissions which make unambiguous dark matter detection more difficult. The choice to examine the halos of both large and small structures is crucial, as dwarf spheroidal galaxies are well known to be highly dark matter dominated but produce faint emissions, while larger structures, even though not immaculate test-beds for dark matter emissions, provide substantially stronger fluxes. This means that a survey of halos of varying mass is essential to locate the best detection prospects for future telescopes like the SKA. In order to model the radio emission we confine our approach to the synchrotron radiation produced by the secondary electrons (we refer to electrons and positrons collectively as 'electrons') resulting from the annihilation of super-symmetric neutralinos that compose the halo. In so doing, we model the diffusion of secondary electrons following [19]. In the interest of comprehensiveness we utilise several neutralino masses, varying between 10 and 500 GeV in the annihilation channels $b\bar{b}$, $\tau^+\tau^-$ and W^+W^-, using data sourced from the DarkSUSY package [34]. The model we employ to track the redshift evolution of dark matter halos is based on the work of [11, 19, 20, 24, 26]. For our cosmological framework we consider a flat ΛCDM universe with $\Omega_m(0) = 0.315$ and $H_0 = 67.3$ km s^{-1} Mpc^{-1} in accordance with the PLANCK results [3]. Additionally we assume the primordial power spectrum to be scale invariant and normalised to the value $\sigma_8 = 0.897$. We also examine three models of the magnetic field radial dependency within galaxy clusters: *i*) a model following the density of the intra-cluster medium, *ii*) a power-law model in accordance with results in [7, 62] which suggest a flatter magnetic field radial profile than that of the thermal gas, and *iii*) a constant field model. In the case of galaxies and dwarf galaxies we use only the constant magnetic field model.

With this approach we examine the general properties of the neutralino-induced synchrotron radiation over the given parameter space and demonstrate that differing annihilation channels leave distinct signatures upon the observed flux from the halo and that these signatures are both redshift and halo mass independent. Additionally we used these results, in conjunction with the expected sensitivity of the SKA, to determine the bounds on the annihilation cross-section that might be imposed by non-detection with the SKA. These bounds are computed as functions of the neutralino mass and annihilation channel as well as the strength of the magnetic field present within the halo. Finally we discuss the exclusion plane that determines the combinations of halo mass and redshift that would be observable to the SKA for thermally-averaged cross section values of 3×10^{-26} cm^3 s^{-1} or lower. In so doing we determine the ideal cases for SKA detection of neutralino-induced synchrotron emission and demonstrate that the SKA has the potential to produce upper-bounds on the cross section that are far more stringent than those from existing experiments, as found in [1, 8, 38], suggesting the SKA will have a relevant role in determining the nature of dark matter. Moreover, the difficulty of disentangling the effects of the electron spectrum and the magnetic field itself in synchrotron radiation makes the accuracy of magnetic field models within prospective radio sources highly important. It is therefore of considerable advantage to radio searches for dark matter that the SKA will be also capable of determining magnetic field structures through both polarisation and Faraday Rotation measurements.

A breakdown of this paper is as follows: we first present a discussion of the models and assumptions employed in our work in sections 2, then we present the results of our synchrotron flux calculations for varying halo masses, redshifts and neutralino properties in section 3, following this we present the non-detection constraints derived from SKA sensitivity data and finally we discuss the implications of these results in section 4.

2 Radio Emission from Dark Matter Halos

2.1 Dark Matter Halos

In the study of dark matter halo structures we will make use of the prominent halo density profiles, i.e. the Navarro-Frenk-White (NFW) [55], Burkert [12], and Einasto [25] models. These are given

respectively by

$$\rho_N(r) = \frac{\rho_s}{\frac{r}{r_s}\left(1+\frac{r}{r_s}\right)^2} ,$$
$$\rho_B(r) = \frac{\rho_s}{\left(1+\frac{r}{r_s}\right)\left(1+\left(\frac{r}{r_s}\right)^2\right)} , \tag{2.1}$$
$$\rho_E(r) = 0.25\rho_s \mathrm{e}^{-\frac{2}{\alpha}\left(\left(\frac{r}{r_s}\right)^\alpha - 1\right)} ,$$

with r_s being the scale radius of the profile, with $\alpha \approx 0.18$ giving profiles similar to NFW in the outer halo while differing in the inner regions, and ρ_s is the halo characteristic density (the factor of 0.25 accounts for the difference between $\rho(r_{-2})$ and ρ_s where r_{-2} is the radius at which the logarithmic slope of halo density profile is equal to -2.). We then define the virial radius R_{vir}, of a halo with mass M_{vir}, as the radius within which the mean density of the halo is equal to the product of the collapse over-density Δ_c and the critical density ρ_c, where

$$\rho_c(z) = \frac{3H(z)^2}{8\pi G} , \tag{2.2}$$
$$M_{vir} = \frac{4}{3}\pi\Delta_c\rho_c R_{vir}^3 , \tag{2.3}$$

with $H(z)$ being the Hubble parameter. The density contrast parameter at collapse is given in flat cosmology by the approximate expression

$$\Delta_c \approx 18\pi^2 - 82x - 39x^2 , \tag{2.4}$$

and, in the Einstein/de-Sitter universe, by [10]

$$\Delta_c \approx 18\pi^2 - 60x - 32x^2 , \tag{2.5}$$

with $x = 1.0 - \Omega_m(z)$, where $\Omega_m(z)$ is the matter density parameter at redshift z given by

$$\Omega_m(z) = \frac{1}{1+\frac{\Omega_\Lambda(0)}{\Omega_m(0)}(1+z)^{-3}} . \tag{2.6}$$

The concentration parameter for the halo can then be defined as

$$c_{vir} = \frac{R_{vir}}{r_{-2}} . \tag{2.7}$$

Furthermore, we make the identification $r_s = r_{-2}$ for all of the Einasto, Burkert and NFW dark matter density profiles. In the following work we make use of the method discussed in [11] to determine the concentration parameter as a function of halo mass

$$c_{vir} = K\frac{1+z_c}{1+z} = \frac{c_{vir}(M, z=0)}{1+z} , \tag{2.8}$$

with $K = 4$ providing a good fit for ΛCDM models [26], and z_c is the collapse redshift of the halo, defined by

$$G(z_c)\sigma(FM_{vir}) = 1.686 , \tag{2.9}$$

with F being a free parameter (we take $F = 0.01$ in accordance with ref. [11]), $G(z)$ being the linear perturbation growth factor and $\sigma(M)$ is the present-day rms density fluctuation of spheres containing the mass M [57]. We note here that there are more recent results in the virial concentration mass relations [53] indicating larger values of the virial concentration parameter in the case of galaxy cluster-type halos. These in turn result in an amplification of the radio fluxes calculated here for this class of halo (within the redshift $z \leq 1$ range), while for higher redshifts (and smaller halos) there

is no substantial difference between the two approaches. This implies that the c_{vir} model used here provides slightly conservative estimates on the radio emission from more local DM halos.
The dimensionless characteristic density contrast $\frac{\rho_s}{\rho_c}$ can then be defined in terms of c_{vir}, following ref. [49],

$$\frac{\rho_s(c_{vir})}{\rho_c} = \frac{\Delta_c}{3} \frac{c_{vir}^3}{\ln(1+c_{vir}) - \frac{c_{vir}}{1+c_{vir}}} \ . \tag{2.10}$$

In this work we will explore three classes of dark matter halo. Those around galaxy clusters, with masses $M_{vir} > 10^{14} M_\odot$, around galaxies, with $10^{11} M_\odot \leq M_{vir} \leq 10^{12} M_\odot$, and finally the halos of dwarf spheroidal galaxies with $M_{vir} < 10^9 M_\odot$.

2.2 Halo Substructure

In order to account for the effect of substructure within a dark matter halo we will divide the total density profile into smooth and sub-halo components

$$\rho_{tot}(r) = \rho_{sm}(r) + \rho_{sh}(r) \ , \tag{2.11}$$

where the total profile is

$$\rho_{tot}(r) = \rho_s g(r/r_s) \ , \tag{2.12}$$

with $g(x)$ being such as to reproduce the relevant density profile (NFW, Burkert or Einasto). Here ρ_{sm} and ρ_{sh} are respectively the smooth and sub-halo contributions to the mass density.

The substructure of the halo is characterised by f_s, the fraction of the halo mass concentrated within sub-halos

$$f_s \equiv \frac{M_{sub}^{tot}}{M_{vir}} \ , \tag{2.13}$$

and by the spatial density of sub-halos, assumed here to be given by same function as the total halo mass density but with a larger scale radius $R_s \sim 7 r_s$ to represent radial biasing of the distribution [54]

$$p_{sub}(r) = N g(r/R_s) \ , \tag{2.14}$$

with normalisation constant N determined by the requirement

$$4\pi \int_0^{R_{vir}} dr\, r^2 p_{sub}(r) = 1 \ . \tag{2.15}$$

An additional characteristic of the halo substructure is the sub-halo mass distribution. In order to account for this we consider the rate of change of the sub-halo number density with respect to sub-halo mass M_{sub} [60]

$$\frac{dn_s}{dM_{sub}}(M_{sub}) = \mathcal{M}_0 \widetilde{M}^{-\mu} \ , \tag{2.16}$$

with $\mu = 2$ where, for a given sub-halo mass scale M_*,

$$\widetilde{M} = \frac{M_{sub}}{M_*} \tag{2.17}$$

and $\mathcal{M}_0$ is the normalisation constant, such that the total sub-halo mass contribution is normalised to $f_s M_{vir}$. In choosing the limits for mass distribution, we follow the approach of [60] in setting $M_{min} = 1 \times 10^{-6} M_\odot$ and $M_{max} = 0.01 M_{vir}$. Our minimum mass has been chosen to correspond to the WIMP free-streaming scale, although it is possible for there to be contributions from even smaller masses within the wider SUSY frame-work: lower values of M_{min} could serve to increase the boosting factor which results from the increased density provided by sub-halos.
With this in hand one can determine the coefficient β

$$\beta = \int dM_s \frac{dn_s}{dM_s} \int dc_s' \, \mathcal{P}(c_s') \mathcal{F}(c_s') \ , \tag{2.18}$$

such that

$$\mathcal{N}_\chi^{sub}(r) \propto p_{sub}(r)\beta \,, \tag{2.19}$$

is the average sub-halo contribution to the local WIMP-pair density. The function $\mathcal{P}(c_s)$ is a log-normal distribution in sub-halo concentration parameter

$$\mathcal{P}(c_s) = \frac{1}{\sqrt{2\pi}\sigma_c c_s} \exp - \left(\frac{\log c_s - \log \bar{c}_s}{\sqrt{2}\sigma_c} \right)^2 \,, \tag{2.20}$$

with $\bar{c}_s$ is the average sub-halo concentration from (2.8) and $\sigma_c = 0.14$ [11, 60]. The limits of integration are chosen to ensure the whole Gaussian is captured. Additionally, we calculate the average concentration parameter of a sub-halo of mass $\widetilde{M}$ as being ~ 1.5 times greater than that of an isolated halo of equivalent mass, this is in order to account for the tendency for average sub-halo concentrations to exceed that of the parent halo [11, 19]. Finally, the function $\mathcal{F}$ is given by

$$\mathcal{F}(x) = 4\pi (r_s')^3 \int_0^x d\xi \, \xi^2 \left(\rho'(\xi)\right)^2 \,, \tag{2.21}$$

where $\xi = \frac{r}{r_s'}$ and we assume sub-halos have the same form as parent halo, with the sub-halo density profile $\rho'(\xi)$ given by

$$\rho'(\xi) = \rho_s(c_s) g\left(\xi\right) \,, \tag{2.22}$$

where $g(r)$ having its previous definition and r_s' being the scale-radius determined by the sub-halo mass M_{sub} and concentration c_s.

Now we can express the density of WIMP pairs $\mathcal{N}_\chi(r)$ as

$$\mathcal{N}_\chi(r) = \left(\left(\rho_{tot}(r) - f_s M_{vir} p_{sub}(r)\right)^2 + p_{sub}(r)\beta \right) / 2M_\chi^2 \,. \tag{2.23}$$

We note that this expression is valid only when considering unresolved substructure and spherically averaged observables [19].

2.3 Electron Source Functions From Neutralino Annihilations

In this paper we assume dark matter to be composed of the lightest neutralino from the minimal supersymmetric extension to the standard model, following the model used by the DarkSUSY package [34]. The source function for the production of a stable particle i, produced promptly by neutralino annihilation or ancillary processes is given by

$$Q_i(r, E) = \langle \sigma V \rangle \sum_f \frac{dN_i^f}{dE} B_f \mathcal{N}_\chi(r) \,, \tag{2.24}$$

where $\langle \sigma V \rangle$ is the thermally-averaged neutralino annihilation cross-section at 0 K, the index f labels kinematically justified annihilation final states with branching ratios B_f and spectra $\frac{dN_i^f}{dE}$, and $\mathcal{N}_\chi(r)$ is the neutralino pair density at a given halo radius r.

The chosen particle physics framework will dictate both $\langle \sigma V \rangle$ and the set of branching ratios. Since the neutralino is a Majorana fermion, light fermion final states are suppressed in favour heavy fermions and Higgs bosons. In keeping with standard procedure in indirect detection studies we will focus on one annihilation channel at a time and assume a branching ratio of 1 for the channel of interest. In this study we have focussed on the $b\bar{b}$ annihilation channel, but have also considered W^+W^- and $\tau^+\tau^-$, and employed the results of the Pythia [68] DarkSUSY MonteCarlo routines in order to determine the spectra $\frac{dN_i^f}{dE}$ for electron production from the decay of neutralino annihilation products. Finally, the neutralino pair density will be calculated in accordance with eq.(2.23).

2.4 Magnetic Field and Thermal Plasma Models

In order to treat the diffusion of WIMP annihilation products, as well as resulting synchrotron radiation, we must account for the presence of both magnetic fields and a thermal plasma within host halos.

For the thermal plasma density we assume it follows a radial scaling of the form

$$n(r) = n_0 \left(1 + \left(\frac{r}{r_s}\right)^2\right)^{-q_e} , \tag{2.25}$$

with the central value n_0 and the scaling exponent q_e being specified as parameters. Then $\overline{n}$ is simply the volume average of $n(r)$ assuming spherical symmetry.

In the case of the magnetic field, we then assume it is subject to Kolmogorov-type turbulence, in accordance with previous work on the diffusion of secondary electrons from WIMP annihilation [19, 20]. In this case the power spectrum is thus given by [17, 70]

$$P(k) = P(k_0) \left(\frac{k}{k_0}\right)^{-\delta} , \tag{2.26}$$

where δ is the spectral index of the turbulence, $k = \frac{1}{d}$ where d is a uniformity scale for the magnetic field. Setting $\delta = \frac{5}{3}$ yields the spectrum of Kolmogorov turbulence. We assume that the smallest length-scale at which the field is uniform $d_0 = 20$ kpc.

We will examine three different magnetic field models here. The first being a constant field, the second model being one decreasing in magnitude with radius with a profile that mimics that of the thermal plasma

$$B(r) = B_0 \left(1 + \left(\frac{r}{r_s}\right)^2\right)^{-q_b} , \tag{2.27}$$

where B_0 is the central magnetic field strength and q_b is scaling exponent chosen to be 0.5. Our final magnetic field model will be an attempt to obtain a self-consistent description of the spatial shape of the magnetic field within a galaxy cluster. To do this we take into account the results of several experiments, simulations and analytical calculations, according to which a magnetic field can be written as $\vec{B} = \vec{B_0} + \vec{b}$, where $\vec{B_0}$ is the mean magnetic field (i.e. the smooth component), and $\vec{b}$ is representing the fluctuations component. It has been shown (see, e.g., [74] and references therein) that, while the power spectrum of the fluctuating component is expected to have a Kolmogorov shape (i.e. $\delta = \frac{5}{3}$), the smooth component is expected to have a spectrum of the type

$$\tilde{B_0}(k) \propto k^{-w} \quad \text{for} \quad k_{min} \leq k \leq k_{max}, \tag{2.28}$$

with $w \sim 1/3$. We can derive the radial shape of the magnetic field $B(r)$ by taking the inverse Fourier transform of eq.(2.28), and by assuming $k_{min} = R_{max}^{-1}$, where $R_{max} = R_{vir}$ is the maximum radius of the halo, and $k_{max} = R_{min}^{-1}$, where R_{min} is the minimum radius after which the magnetic field can be considered smooth, while under this radius the fluctuations component is dominant (so, it corresponds to the d_0 length introduced before). The normalization of the spectrum in eq.(2.28) is linked to the normalization of the magnetic field (as the effect of the Parseval's theorem, see also [17]) and to the values of k_{min} and k_{max}. For this reason, since we have the possibility to choose the value of the mean magnetic field from other considerations (i.e., the results of hydrodynamical simulations or Faraday Rotation measurements in galaxy clusters) we impose either a central or average value on the field and determine the appropriate normalisation thereafter. Thus we derive the required radial shape of the magnetic field, and then will set the normalization of B_0 by imposing that energy density of the magnetic field is less than the thermal energy density of the hot gas within the cluster

$$\frac{\langle B^2 \rangle}{8\pi} \leq \overline{n} k_b T , \tag{2.29}$$

where CGS units are used, k_b is the Boltzmann constant, $\langle B^2 \rangle$ represents a volume average and T is the intra-cluster medium temperature, or using the virial result [65]

$$k_b T = \frac{1}{2} \mu_{mp} \frac{G M_{vir}}{R_{vir}} \, , \tag{2.30}$$

with G being the Newton's constant and μ_{mp} being the mean molecular mass in the intra-cluster medium.

For a spectrum as in eq.(2.28), with $0 < w < 1$, the inverse Fourier transform is proportional to r^{w-1}, and so we obtain that the radial shape of the magnetic field is given by

$$B(r) = B_0 \left(\frac{r}{R_{min}} \right)^{w-1} \quad \text{for} \;\; R_{min} \leq r \leq R_{max}, \tag{2.31}$$

and the normalization is fixed by imposing the condition in eq.(2.29) and eq.(2.30). For $r < R_{min}$, the magnetic field is dominated by the fluctuations; so we can consider the smooth component as a constant in this region ($B(r) \sim B_0$), superimposed to which the fluctuations can increase the synchrotron emission [18]. For $r > R_{max}$, the magnetic field is assumed to decrease quickly to zero. The normalization in eq.(2.30) results in a condition, for a general value of $0 < w < 1$, given, where $R_{max} >> R_{min}$, by:

$$B_0^2 \leq \frac{8\pi}{3} (2w+1) \left(\frac{R_{vir}}{R_{min}} \right)^{2-2w} \overline{n} k_b T. \tag{2.32}$$

We note that for $w = 1/3$ we obtain a radial shape $B(r) \propto r^{-2/3}$, which is flatter than the one usually found in the literature for the thermal gas in galaxy clusters; this is in agreement with the results obtained from studies of Farady Rotation measurements in galaxy clusters (see, e.g., [7] for the Coma cluster case). We note also that [62] obtained in several galaxy clusters an almost flat profile for the magnetic field until large radii ($\sim 7 r_s$); however, we remind that the same authors pointed out that in their paper there is an error in the analysis of sources that may have affected the conclusions relative to the homogeneous component of the magnetic field.

It is clear from Figure 1, where we show the variance of the radio flux with magnetic field model, that each of the magnetic field models yields results similar to the constant field case, at most accounting for a difference of less then an order of magnitude at $\nu \approx 100$ Ghz and at redshift $z = 5$ in the case of the power-law model of eq.(2.31). However, this is largely due to a lack of a good model for the evolution of the B-field normalisation with redshift. Indeed the most notable differences incurred by eq.(2.31) occur only at energies beyond the range of frequencies observable by the SKA and thus are not of importance in the application examined here. Thus it is adequate for the purposes of modelling detection by the SKA to employ constant field models. The reason for the similarity in the predictions of these models is down to their behaviour within the core radius r_s, as the high electron density within this region is responsible for most of the observed synchrotron emission and within this region all the field models predict similar average magnetic field strengths, the weak radial dependence of eq. (2.31) ensures that its radial variation in this region is not large enough to impose significant differences although the increased high-frequency flux is caused by it predicting larger values for the field near the centre of the cluster. An additional consideration is the behaviour of synchrotron radiation with increasing B-field strength, where the output power increases until a saturation point, with the rate of power gain being inversely proportional to rate of increase in field strength as is evident in Figure 36 (presented in section 3 below). For each halo examined we will consider two different magnitudes for the constant magnetic field strength. The first has $\overline{B} = 5$ μG while the second is given by $\overline{B} = 1$ μG. For the thermal plasma we will assume that values of n_0 scale with the mass of the halo, using values of $n_0 = 10^{-3}$ cm^{-3} for large halos ($M_{vir} \geq 10^{14} M_\odot$) and $n_0 = 10^{-6}$ cm^{-3} for smallest halos ($M_{vir} \sim 10^7 M_\odot$) with intermediate mass halos taking values between these extremes.

2.5 Diffusion of Secondary Electrons

In order to take into account the effects of the magnetic field and thermal plasma on electron diffusion we take average values for the field strength and thermal plasma density, being $\overline{B} \equiv \sqrt{\langle B(r)^2 \rangle}$ and

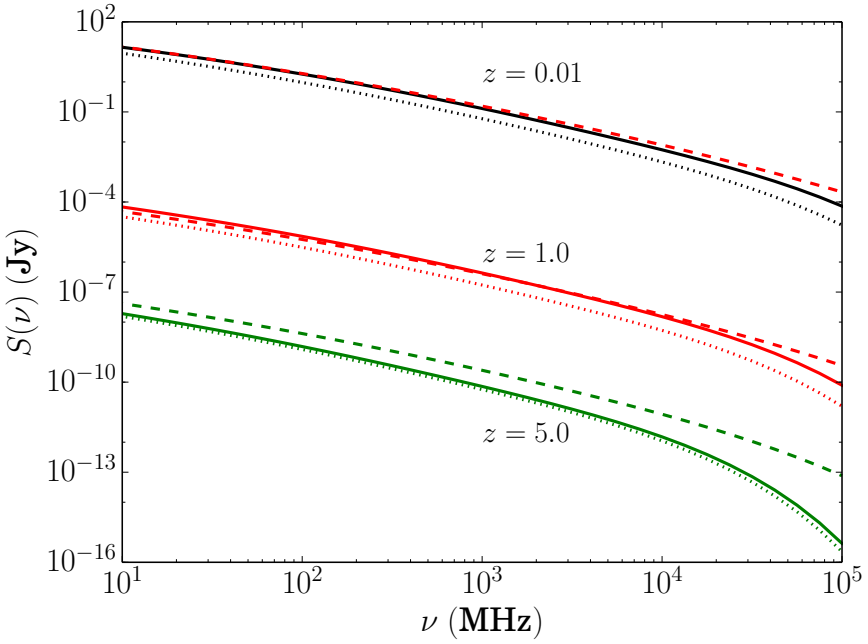

Figure 1. The effect of various magnetic field models on the radio flux, calculated according to eq.(2.43), for a galaxy cluster halo ($M = 10^{15}$ M$_\odot$). The solid lines are constant magnetic fields with magnitude 5 μG, dotted lines have central strength 5 μG but scale according to the thermal model in eq.(2.27) and the dashed lines represent the model in eq.(2.31) normalised to 0.1 of the thermal energy in the cluster at redshift zero. Black lines correspond to $z = 0.01$, red lines to $z = 1$ and green lines to $z = 5$.

$\overline{n} \equiv \langle n(r) \rangle$, respectively. We then define the spatial diffusion coefficient as [17]

$$D(E) = \frac{1}{3} c r_L(E) \frac{\overline{B}^2}{\int_{k_L}^{\infty} dk P(k)} \,, \tag{2.33}$$

where r_L is the Larmour radius of a relativistic particle with energy E and charge e and $k_L = \frac{1}{r_L}$, and require that

$$\int_{k_0}^{\infty} dk P(k) = \overline{B}^2 \,. \tag{2.34}$$

This leads us to the result that

$$D(E) = D_0 d_0^{\frac{2}{3}} \left(\frac{\overline{B}}{1\mu\text{G}} \right)^{-\frac{1}{3}} \left(\frac{E}{1\text{GeV}} \right)^{\frac{1}{3}} \,, \tag{2.35}$$

where $D_0 = 3.1 \times 10^{28}$ cm^2 s^{-1}. It is worth noting that the diffusion coefficient is assumed to be lacking radial dependence. While it is possible to implement diffusion without this simplification, we present results here under the assumption we can substitute the averaged value of the magnetic field in the diffusion coefficient as it is evident that the weak radial dependence of the field and the weak dependence of the diffusion coefficient on the field strength imply that our approximation is not unwarranted.

The diffusion equation for electrons within the halo is then taken to be

$$\begin{aligned} \frac{\partial}{\partial t} \frac{dn_e}{dE} = & \boldsymbol{\nabla} \left(D(E, \mathbf{x}) \boldsymbol{\nabla} \frac{dn_e}{dE} \right) + \frac{\partial}{\partial E} \left(b(E, \mathbf{x}) \frac{dn_e}{dE} \right) \\ & + Q_e(E, \mathbf{x}) \,, \end{aligned} \tag{2.36}$$

where $\frac{dn_e}{dE}$ is the electron equilibrium spectrum, $D(E, \mathbf{x})$ is the spatial diffusion function, $b(E, \mathbf{x})$ is the energy-loss function and $Q_e(E, \mathbf{x})$ is the electron source function. A detailed analysis of the solution to this equation in the case of electron production via neutralino annihilation can be found in [19]. The solution in the case of spherical symmetry and assuming the energy-loss and diffusion functions have no spatial dependence (as in eq.(2.35)) will be of the form

$$\frac{dn_e}{dE}(r, E) = \frac{1}{b(E)} \int_E^{M_\chi} dE'\, G(r, E, E') Q_e(r, E') \,, \tag{2.37}$$

where $G(r, E, E')$ is a Green's function which will reduce to unity in the case of larger halos at zero redshift [19]. However, in smaller halos the diffusive effects in $G(r, E, E')$ will become significant. Following [20] we take $b(E)$ to be

$$\begin{aligned} b(E) =& b_{IC} E^2 (1+z)^4 + b_{sync} E^2 \overline{B}^2 \\ &+ b_{Coul} \overline{n} (1+z)^3 \left(1 + \frac{1}{75} \log\left(\frac{\gamma}{\overline{n}(1+z)^3}\right)\right) \\ &+ b_{brem} \overline{n} (1+z)^3 \left(\log\left(\frac{\gamma}{\overline{n}(1+z)^3}\right) + 0.36\right) \end{aligned} \tag{2.38}$$

where $\overline{n}$ is given in cm^{-3} and b_{IC}, b_{synch}, b_{col}, and b_{brem} are the Inverse Compton, synchrotron, Coulomb and Bremsstrahlung energy loss factors, taken to be 0.25, 0.0254, 6.13, and 1.51 respectively in units of 10^{-16} GeV s^{-1}. Here E is the energy in GeV and the B-field is in μG.

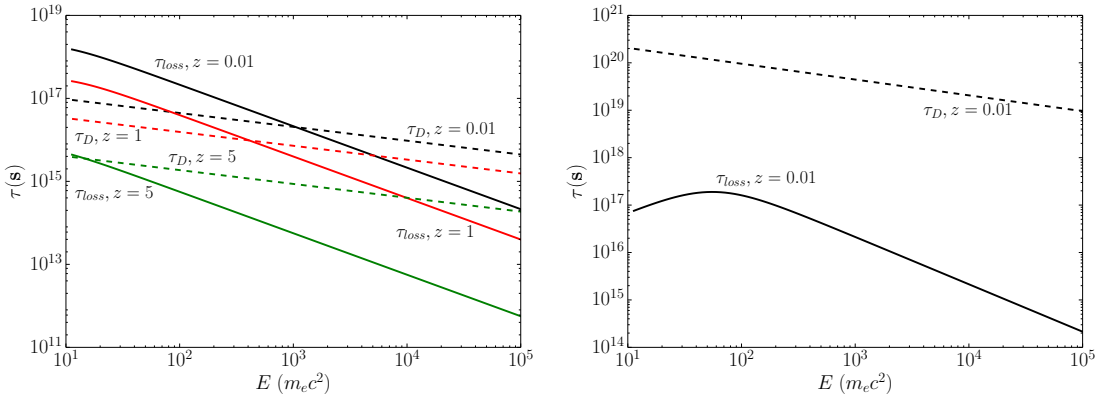

Figure 2. Time scales τ as electron energy E is varied. Left: Halo mass 10^7 $\mathrm{M}_\odot$, where black lines correspond to $z = 0.01$, red lines to $z = 1.0$ and green lines to $z = 3$. Right: Halo mass 10^{12} $\mathrm{M}_\odot$ at $z = 0.01$.

The time-scales of both diffusive and energy-loss effects are displayed in Figure 2. It is worth noting that as the redshift increases the energy-loss time-scale rapidly decreases, as the inverse-Compton (IC) process comes to dominate energy-loss and to accelerate the loss time-scale to levels that make diffusive effects irrelevant, as these only scale with the dimension of the halo, which shows far weaker redshift dependence than the IC terms. The right-hand panel of Fig. 2 shows how drastically insignificant diffusion time-scales become for larger halos. This conclusion very nicely corroborates the assertions made in [19] on this matter.

2.6 Synchrotron Emission

The average power of the synchrotron radiation at observed frequency ν emitted by an electron with energy E in a magnetic field with amplitude B is given by [48]

$$P_{synch}(\nu, E, r, z) = \int_0^\pi d\theta \frac{\sin\theta^2}{2} 2\pi\sqrt{3} r_e m_e c \nu_g F_{synch}\left(\frac{\kappa}{\sin\theta}\right) \,, \tag{2.39}$$

where m_e is the electron mass, $\nu_g = \frac{eB}{2\pi m_e c}$ is the non-relativistic gyro-frequency, $r_e = \frac{e^2}{m_e c^2}$ is the classical electron radius, and the quantities κ and F_{synch} are defined as

$$\kappa = \frac{2\nu(1+z)}{3\nu_0\gamma^2}\left(1+\left(\frac{\gamma\nu_p}{\nu(1+z)}\right)^2\right)^{\frac{3}{2}} , \tag{2.40}$$

and

$$F_{synch}(x) = x\int_x^\infty dy\, K_{5/3}(y) \simeq 1.25x^{\frac{1}{3}}\mathrm{e}^{-x}\left(648+x^2\right)^{\frac{1}{12}} . \tag{2.41}$$

The local synchrotron emissivity can then be found as a function of the electron and positron equilibrium distributions as well as the synchrotron power

$$j_{synch}(\nu, r, z) = \int_{m_e}^{M_\chi} dE\left(\frac{dn_{e^-}}{dE}+\frac{dn_{e^+}}{dE}\right)P_{synch}(\nu, E, r, z) . \tag{2.42}$$

Once one has determined this quantity, it can be used to find all of the observables relevant to our study, namely the flux densities and surface brightnesses of the dark matter halo. The flux density spectrum within a radius r is found via

$$S_{synch}(\nu, z) = \int_0^r d^3r'\,\frac{j_{synch}(\nu, r', z)}{4\pi D_L^2} , \tag{2.43}$$

where D_L is the luminosity distance to the halo. Then the azimuthally averaged surface brightness is given by

$$I_{synch}(\nu, \Theta, \Delta\Omega, z) = \int_{\Delta\Omega} d\Omega \int_{l.o.s} dl\,\frac{j_{synch}(\nu, l, z)}{4\pi} , \tag{2.44}$$

where the integrals are performed over a cone given by the solid angle $\Delta\Omega$ and an axis along the line of sight (l.o.s) which makes an angle Θ with the direction of the halo centre.

3 Results

Throughout this work the SKA sensitivity is drawn from [23] and represents the SKA MID and LOW frequency ranges for the SKA phase 1.

In Figures 3 to 30 we show the results of an exhaustive study of the neutralino induced synchrotron emissions from dark matter halos with three different masses (10^7, 10^{12} and 10^{15} $M_\odot$), two different magnetic field values (1μG and 5μG), and five different redshifts (0.01, 0.1, 1.0, 3.0 and 5.0). We also investigate the $b\bar{b}$, $\tau^+\tau^-$, and W^+W^- annihilation channels for neutralinos of mass 60 and 500 GeV. As a reference, a thermally-averaged, zero-temperature cross section value of $\langle\sigma V\rangle = 3\times10^{-26}$ cm^3 s^{-1} is assumed. This value is chosen to coincide with the thermal relic abundance upper bound given by [41]

$$\langle\sigma V\rangle \leq \frac{3\times10^{-27}}{\Omega_\chi h^2}\ \mathrm{cm}^3\ \mathrm{s}^{-1} , \tag{3.1}$$

where Ω_χ is the present day density parameter for neutralino dark matter, $\Omega_\chi h^2 \approx 0.1$, and h is the reduced Hubble constant in units of 100 km s^{-1} Mpc^{-1}.

A common theme in these results is that diffusion only plays a role at very small redshift and for very small halo masses, as can be seen in Figs. 3, 13, 19, and 25 for the calculation of flux within the virial radius. This conclusion is very nicely reinforced by Figure 2 which demonstrates that the diffusion time-scale is only comparable to that of energy-loss processes for the small mass halos at small redshift.

In general, from Figs. 3, 13, 19, and 25 we note that dwarf galaxy halos with masses around 10^7 $M_\odot$ will at most be marginally detectable at the 1σ c.l. with the sensitivity of the SKA for 1000 hours of integration time at redshift $z = 0.01$. This place restrictions on mass-redshift combination of halos that can be used for robust detection/constraint of dark matter annihilation processes via the SKA.

Larger halos, however, show promising detection of fluxes from within redshifts below one, as can be seen in Figs. 4, 14, 20, 26, 5, 15, 21, and 27. For higher redshifts ($z \geq 3$) we note that all the halos fall below the 1σ c.l. detection with the SKA sensitivity.

In the case of the weaker field, as in Figs. 10, 23 and, 30, we see an overall reduction in flux from the similar Figs. 3, 20 and 27. This is due to the fact that the synchrotron power depends upon the magnetic field strength. However, the weaker field has a particular effect that is prominent for the lighter neutralino masses: this is the expected suppression of the production of electrons with energies above a threshold dictated by the neutralino mass and magnetic field strength which results in a dramatic spectral steepening at high frequencies. The cut-off frequency, resulting from the suppression of higher energy electron production, then exhibits a trivial redshift dependence, as seen in Figs. 16, 17 and 18.

It is worth noting that there is little difference between the emissions of the Einasto and NFW profiles as seen in the comparison of Figures 7, 8 (for the Einasto case) and 9 with their NFW case counterparts in Figs.3, 4 and 5. This similarity is due to the choice of α, however, the effect of the sub-halos results in a slightly higher magnitude for the spectra of halos with Einasto profile. We also show in Figure 6 that in the case of dwarf galaxies there is little change to our results from the adoption of a cored profile, in this case a Burkert profile (see eq.(2.1)). The exploration of this case is significant since dwarf galaxy kinematics are also compatible with shallower cored profiles [2, 75].

Importantly, the different choices of neutralino annihilation channel affect the shape of the spectra. In the 60 GeV case comparing the $\tau^+\tau^-$ and $b\bar{b}$ spectra we find that the former is shallower and there is a crossing of the spectra typically at frequencies around 1 GHz, evident in Figure 31 or through comparison of Figs. 4 and 14 (or any similar pairing). The differences between the two spectra can amount to several orders of magnitude in the extremes of the frequency range shown. In the 500 GeV case, comparing the $b\bar{b}$ and W^+W^- channels embodied by Figs. 20 and 26 respectively, we see very similar spectra, with a slightly larger magnitude in the $b\bar{b}$ case but also a steeper slope at high frequency than that of W^+W^-. It is important to note that, in the ν range we consider, the differences in spectral shape resulting from differing annihilation channels are found to be redshift independent and do not depend upon the mass of the halo or the mass of the neutralino. However, the overall spectral shape is trivially dependent on redshift as previously discussed, thus the redshift dependency of the flux spectrum is influenced only by the neutralino mass and the magnetic field strength. This means that the dominant annihilation channels can be deduced from the shape of the observed spectrum, regardless of the redshift of the source or the mass of the neutralino in question. For sources at redshifts of $z = 1$ or lower it is evident that the optimal frequency for comparison of annihilation channel is around 1 GHz or lower, placing it well within the low frequency range of the SKA-MID.

The different choices of neutralino mass have an effect on the magnitude of the spectrum, as is evident in Figure 32. More importantly, the choice of neutralino mass, together with magnetic field strength, dictates the cut-off behaviour of the higher frequency regions of emission spectrum, as can be seen in the aforementioned Figure 32 or from comparison of Figs. 22, 23 and 24 with their counterparts in Figs. 10, 11 and 12. In the former set of figures, the larger neutralino mass means there is a far shallower slope to the spectrum than in the latter trio despite the fact that both use the same conditions otherwise. However, this high-frequency spectral steepening is also seen to be affected by the magnetic field strength and thus higher-frequency observation must be accompanied by studies of the magnetic field in target sources in order to lift this degeneracy. The mass dependence of the cut-off frequency means that higher frequency observations between 5 and 20 GHz, while somewhat less optimal for cross-section constraints, are still important to exploring the mass axis of the neutralino parameter space.

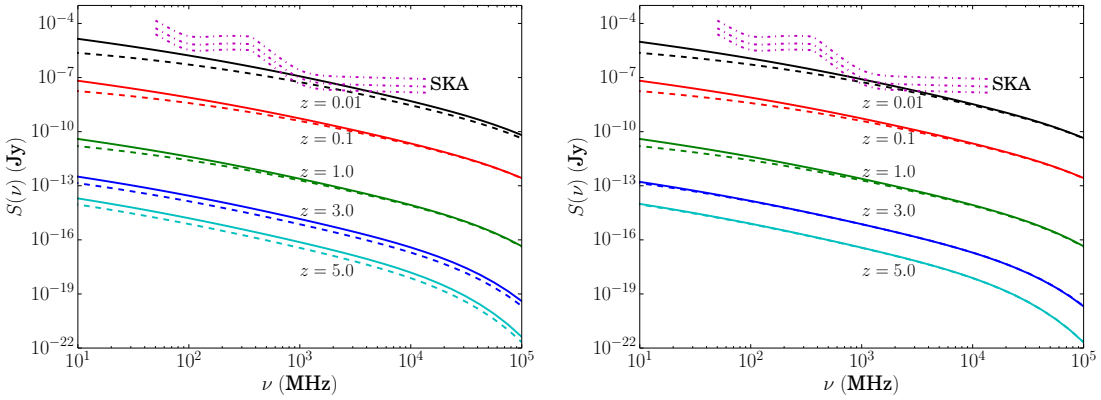

Figure 3. Flux densities for dwarf spheroidal galaxies ($M = 10^7 \mathrm{M}_\odot$), the halo profile is NFW and $\langle B \rangle = 5$ μG. WIMP mass is 60 GeV and the composition is $b\bar{b}$. Black lines represent $z = 0.01$, Red signifies $z = 0.1$, Green $z = 1$, Blue $z = 3$, and Cyan $z = 5$. Solid lines are without diffusion, dotted are with diffusion. The pink dash-dotted lines are SKA 1σ sensitivity limits for 30, 240, and 1000 hour integration times, respectively. The first (left) plot is the flux within an arcmin of the halo centre and the second (right) is within the virial radius.

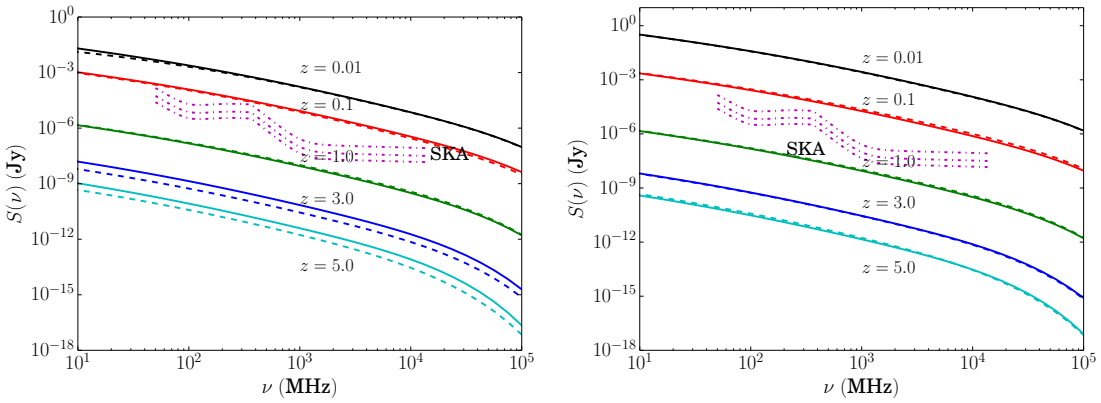

Figure 4. Flux densities for galaxies ($M = 10^{12} \mathrm{M}_\odot$), the halo profile is NFW and $\langle B \rangle = 5$ μG. WIMP mass is 60 GeV and the composition is $b\bar{b}$. See the caption of Figure 3 for legend.

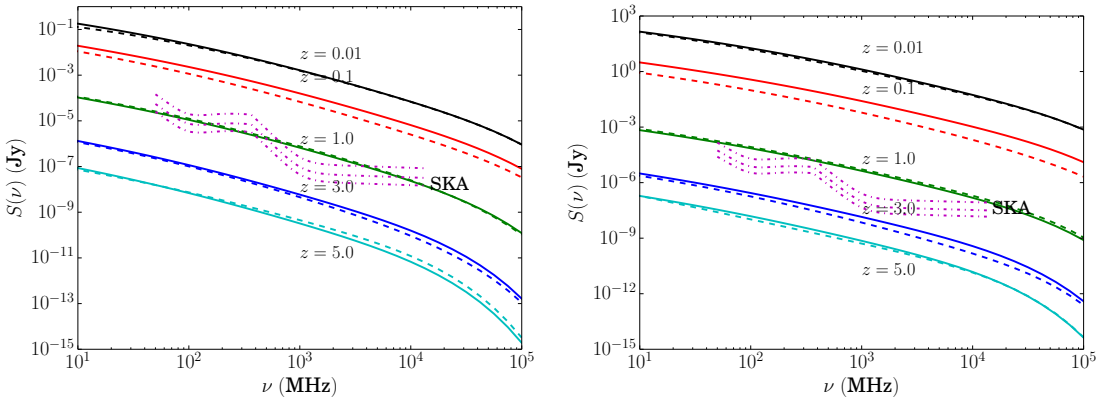

Figure 5. Flux densities for galaxy clusters ($M = 10^{15} \mathrm{M}_\odot$), the halo profile is NFW and $\langle B \rangle = 5$ μG. WIMP mass is 60 GeV and the composition is $b\bar{b}$. See the caption of Figure 3 for legend.

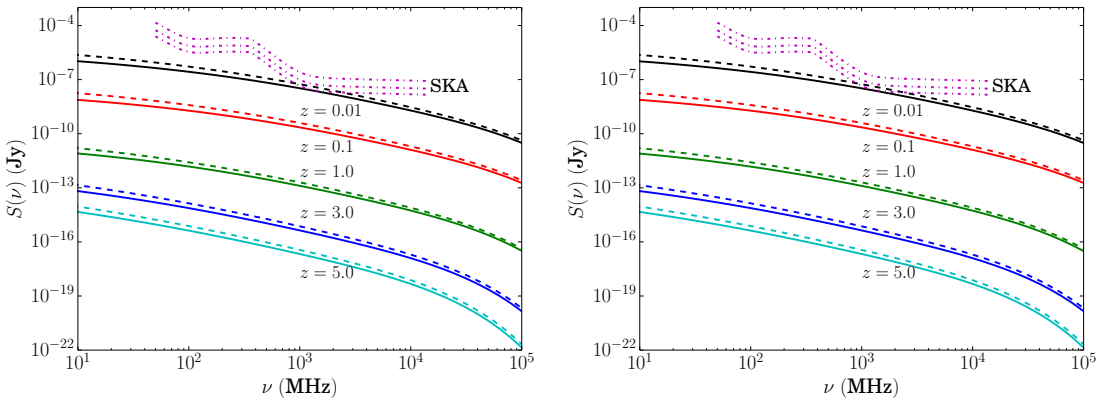

Figure 6. Flux densities for dwarf spheroidal galaxies ($M = 10^7 \mathrm{M}_\odot$), comparing halo profiles NFW (solid lines) and Burkert (dashed lines) with $\langle B \rangle = 5$ μG. WIMP mass is 60 GeV and the composition is $b\bar{b}$. See the caption of Figure 3 for legend (all plots include diffusion).

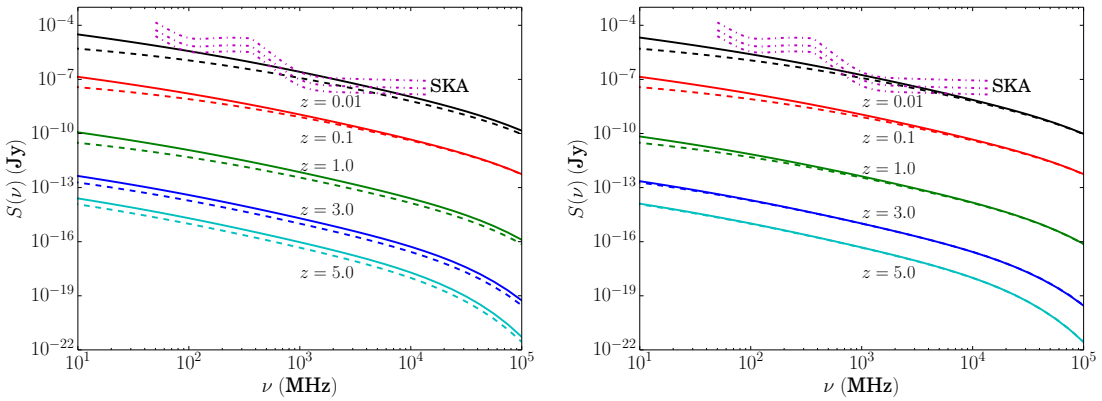

Figure 7. Flux densities for dwarf spheroidal galaxies ($M = 10^7 \mathrm{M}_\odot$), the halo profile is Einasto ($\alpha = 0.18$) and $\langle B \rangle = 5$ μG. WIMP mass is 60 GeV and the composition is $b\bar{b}$. See the caption of Figure 3 for legend.

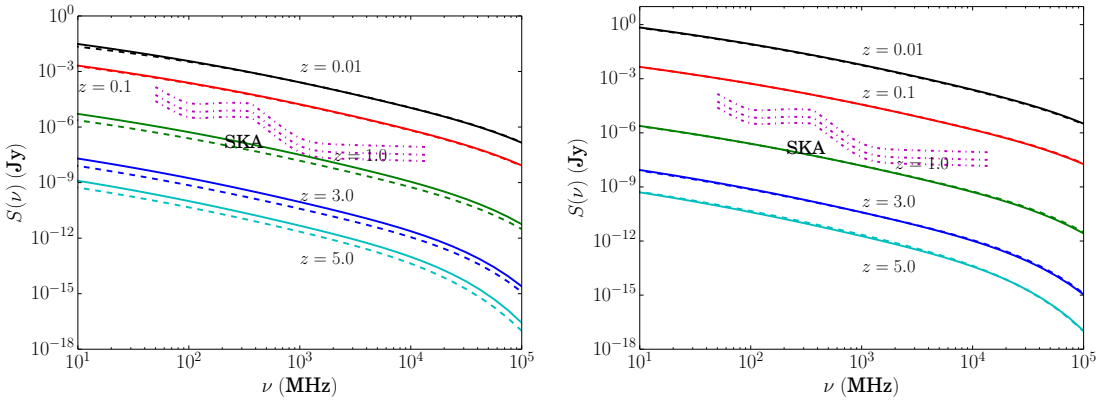

Figure 8. Flux densities for galaxies ($M = 10^{12} \mathrm{M}_\odot$), the halo profile is Einasto ($\alpha = 0.18$) and $\langle B \rangle = 5$ μG. WIMP mass is 60 GeV and the composition is $b\bar{b}$. See the caption of Figure 3 for legend.

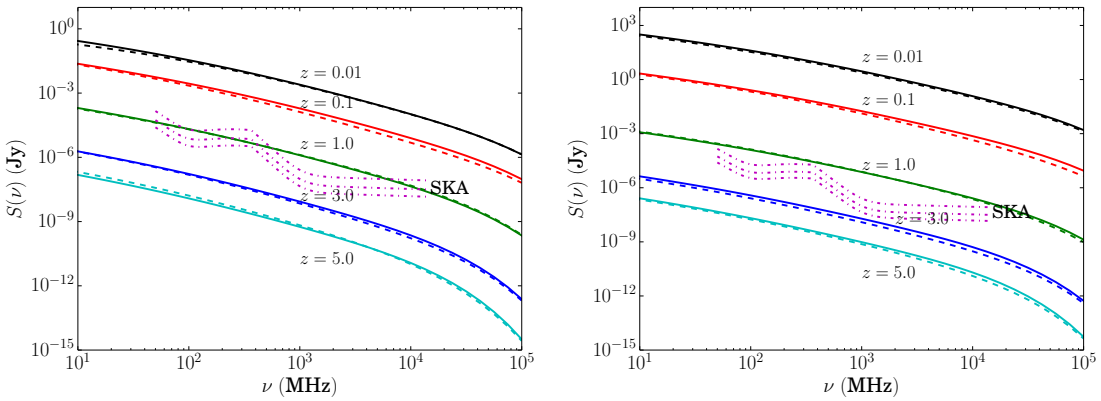

Figure 9. Flux densities for galaxy clusters ($M = 10^{15}\mathrm{M}_{\odot}$), the halo profile is Einasto ($\alpha = 0.18$) and $\langle B \rangle = 5$ μG. WIMP mass is 60 GeV and the composition is $b\bar{b}$. See the caption of Figure 3 for legend.

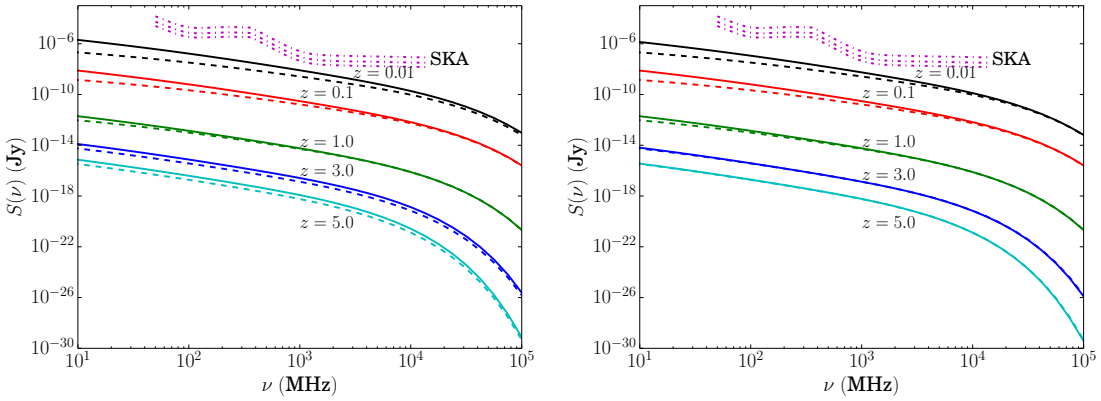

Figure 10. Flux densities for dwarf spheroidal galaxies ($M = 10^{7}\mathrm{M}_{\odot}$), the halo profile is NFW and $\langle B \rangle = 1$ μG. WIMP mass is 60 GeV and the composition is $b\bar{b}$. See the caption of Figure 3 for legend.

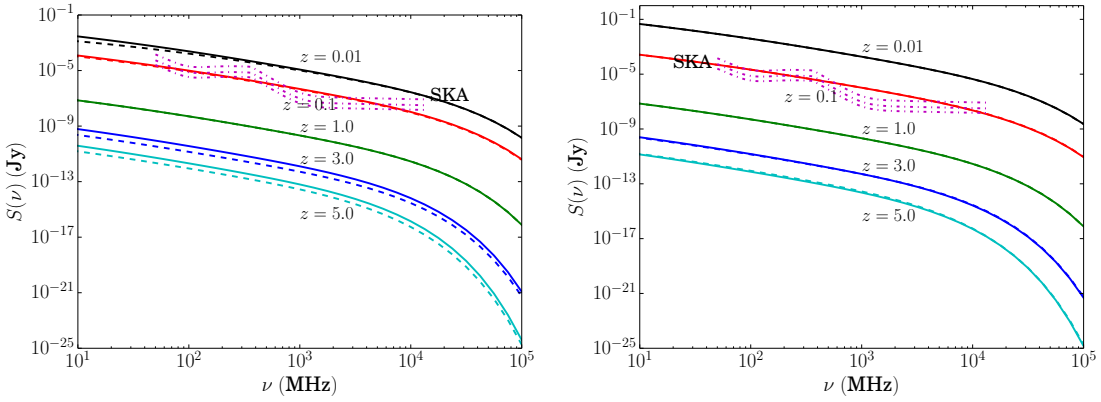

Figure 11. Flux densities for galaxies ($M = 10^{12}\mathrm{M}_{\odot}$), the halo profile is NFW and $\langle B \rangle = 1$ μG. WIMP mass is 60 GeV and the composition is $b\bar{b}$. See the caption of Figure 3 for legend.

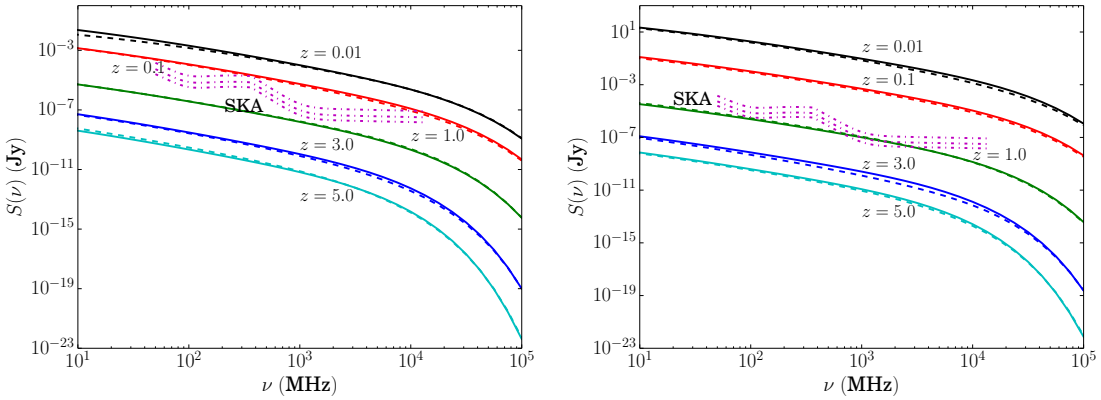

Figure 12. Flux densities for galaxy clusters ($M = 10^{15}\mathrm{M}_{\odot}$), the halo profile is NFW and $\langle B \rangle = 1$ μG. WIMP mass is 60 GeV and the composition is $b\bar{b}$. See the caption of Figure 3 for legend.

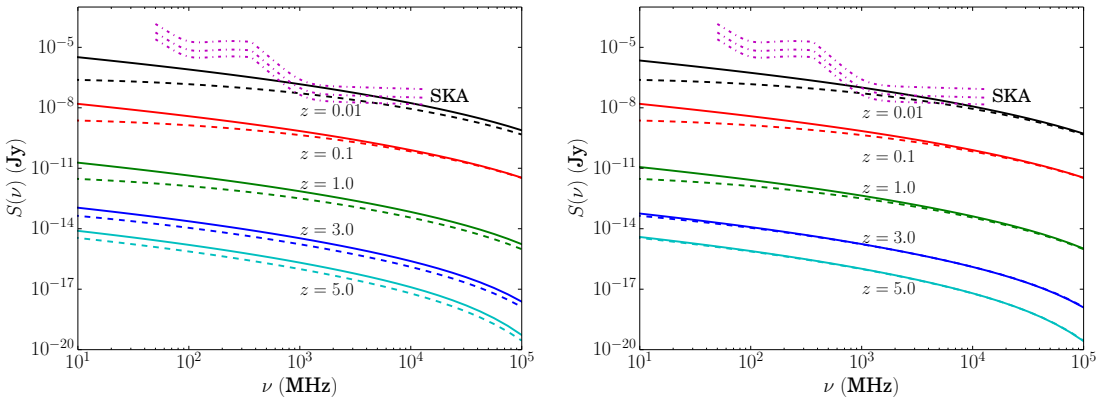

Figure 13. Flux densities for dwarf spheroidal galaxies ($M = 10^{7}\mathrm{M}_{\odot}$), $\langle B \rangle = 5$ μG. WIMP mass is 60 GeV and the composition is $\tau^{+}\tau^{-}$. See the caption of Figure 3 for legend.

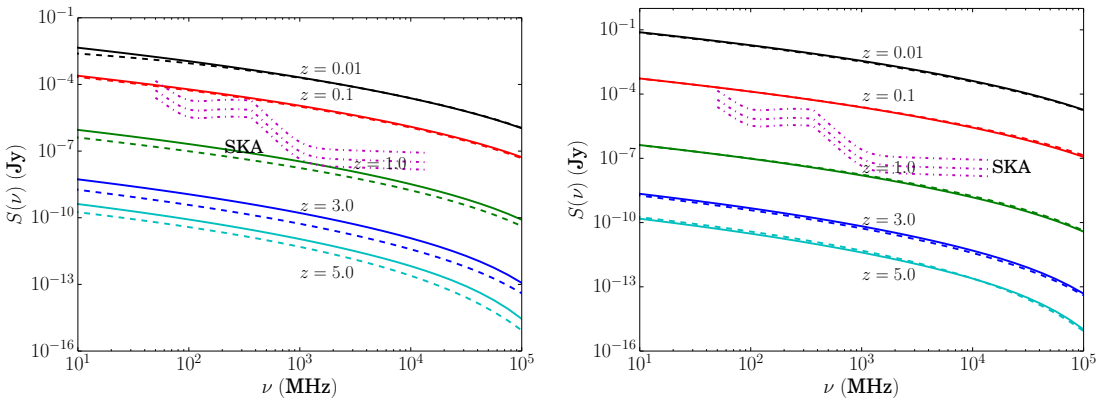

Figure 14. Flux densities for galaxies ($M = 10^{12}\mathrm{M}_{\odot}$), $\langle B \rangle = 5$ μG. WIMP mass is 60 GeV and the composition is $\tau^{+}\tau^{-}$. See the caption of Figure 3 for legend.

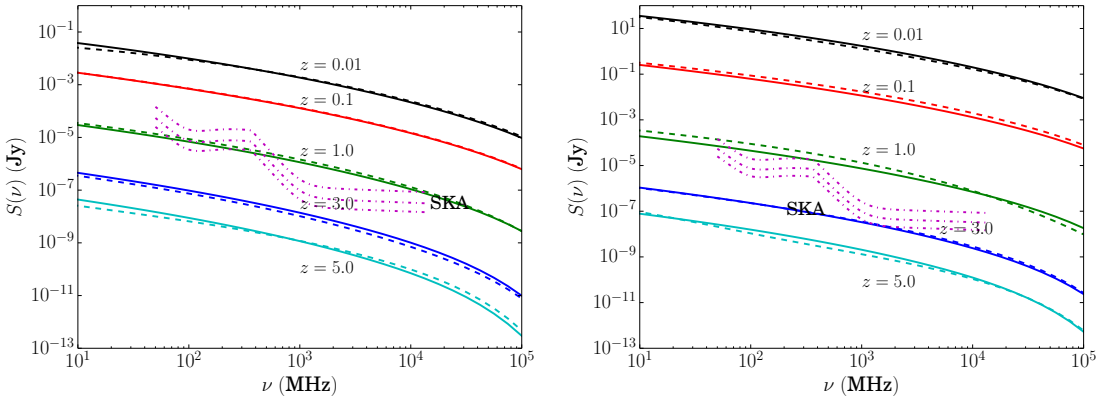

Figure 15. Flux densities for galaxy clusters ($M = 10^{15}\mathrm{M}_{\odot}$), the halo profile is NFW and $\langle B \rangle = 5$ μG. WIMP mass is 60 GeV and the composition is $\tau^{+}\tau^{-}$. See the caption of Figure 3 for legend.

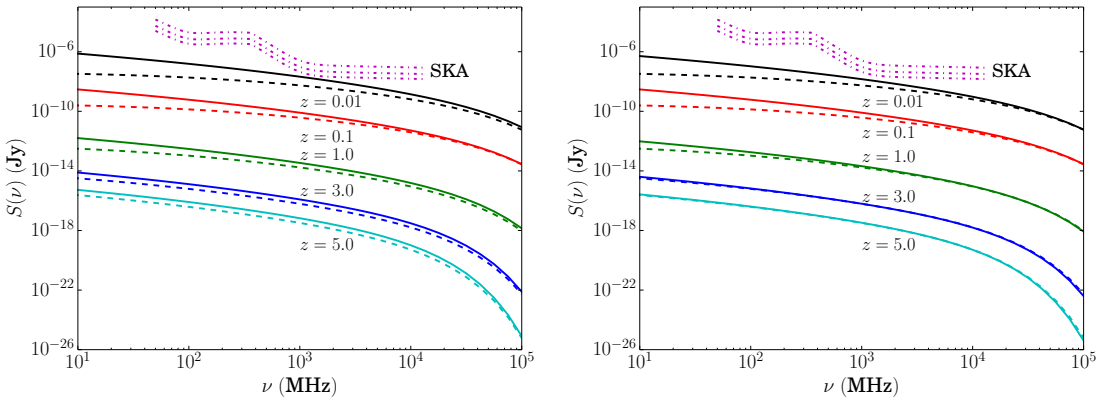

Figure 16. Flux densities for dwarf spheroidal galaxies ($M = 10^{7}\mathrm{M}_{\odot}$), the halo profile is NFW and $\langle B \rangle = 1$ μG. WIMP mass is 60 GeV and the composition is $\tau^{+}\tau^{-}$. See the caption of Figure 3 for legend.

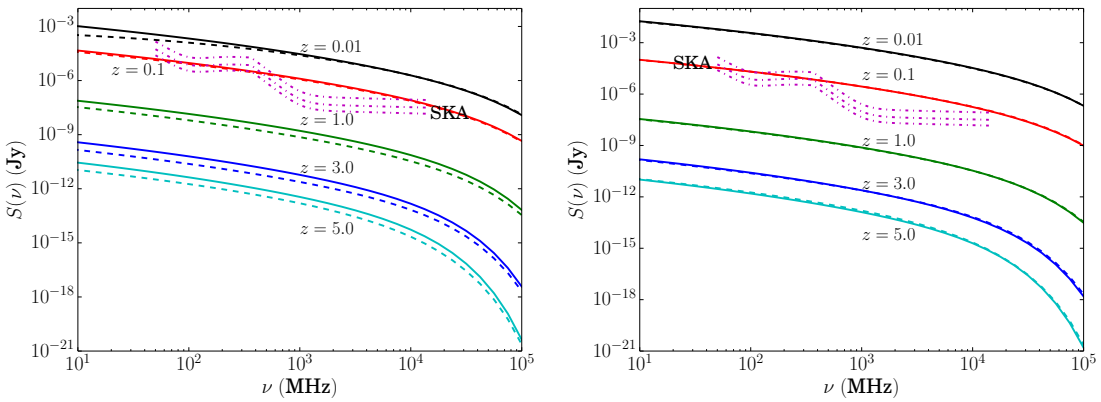

Figure 17. Flux densities for galaxies ($M = 10^{12}\mathrm{M}_{\odot}$), the halo profile is NFW and $\langle B \rangle = 1$ μG. WIMP mass is 60 GeV and the composition is $\tau^{+}\tau^{-}$. See the caption of Figure 3 for legend.

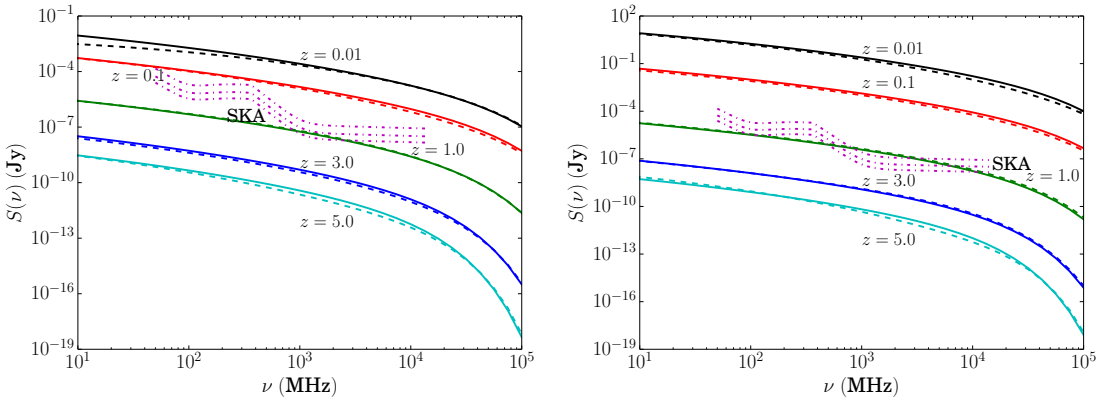

Figure 18. Flux densities for galaxy clusters ($M = 10^{15}\mathrm{M}_{\odot}$), the halo profile is NFW and $\langle B \rangle = 1$ μG. WIMP mass is 60 GeV and the composition is $\tau^{+}\tau^{-}$. See the caption of Figure 3 for legend.

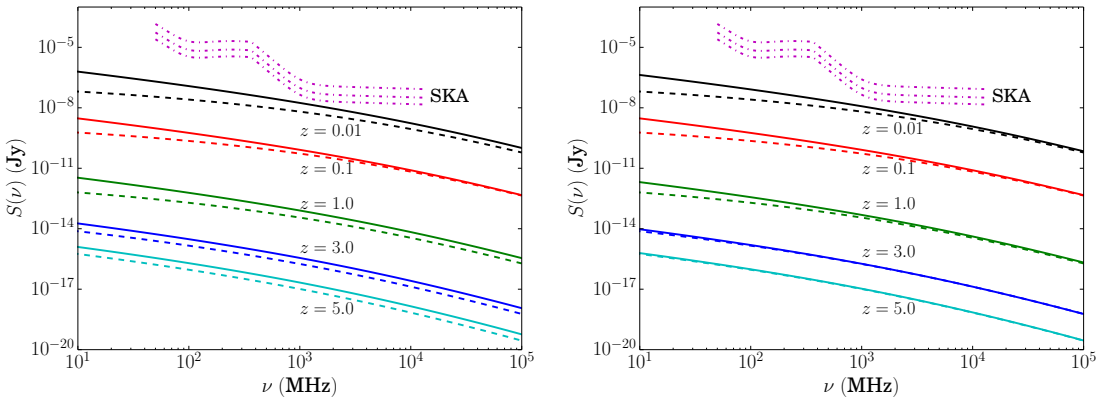

Figure 19. Flux densities for dwarf spheroidal galaxies ($M = 10^{7}\mathrm{M}_{\odot}$), $\langle B \rangle = 5$ μG. WIMP mass is 500 GeV and the composition is $b\bar{b}$. See the caption of Figure 3 for legend.

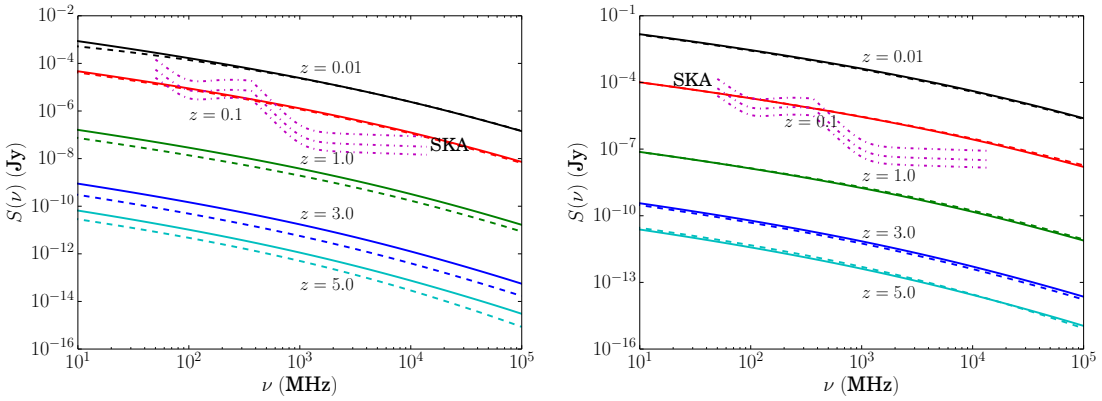

Figure 20. Flux densities for galaxies ($M = 10^{12}\mathrm{M}_{\odot}$), $\langle B \rangle = 5$ μG. WIMP mass is 500 GeV and the composition is $b\bar{b}$. See the caption of Figure 3 for legend.

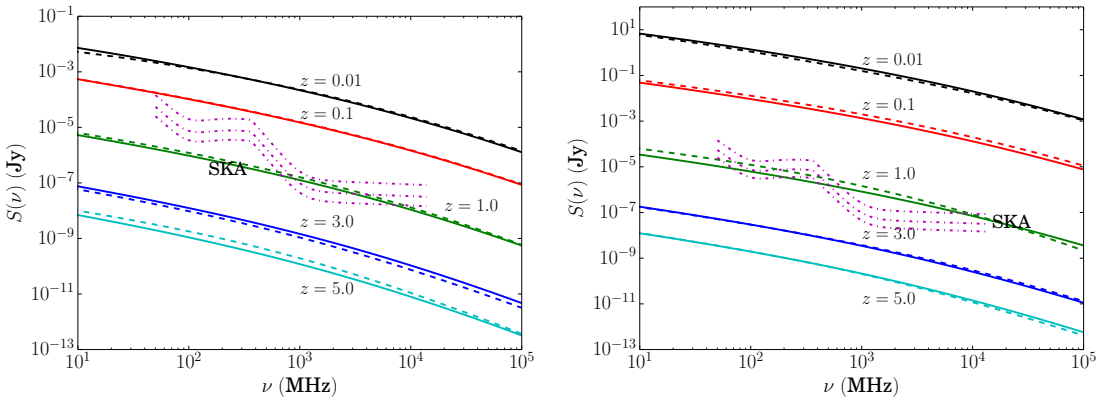

Figure 21. Flux densities for galaxy clusters ($M = 10^{15}\mathrm{M}_{\odot}$), the halo profile is NFW and $\langle B \rangle = 5$ μG. WIMP mass is 500 GeV and the composition is $b\bar{b}$. See the caption of Figure 3 for legend.

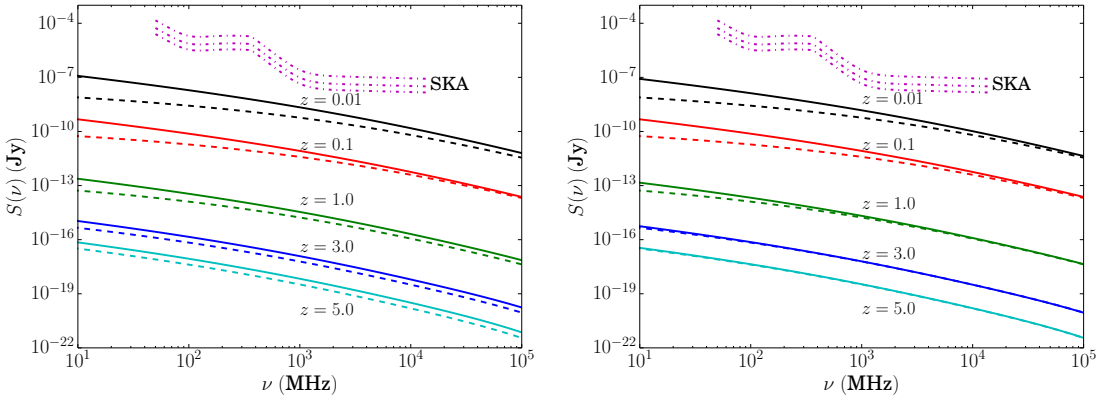

Figure 22. Flux densities for dwarf spheroidal galaxies ($M = 10^{7}\mathrm{M}_{\odot}$), the halo profile is NFW and $\langle B \rangle = 1$ μG. WIMP mass is 500 GeV and the composition is $b\bar{b}$. See the caption of Figure 3 for legend.

Figures 33, 34, and 35 display the WIMP mass-dependent sensitivity cross-section $\langle \sigma V \rangle$ derived from the projected 1σ sensitivity of the SKA, with 30 hour integration time, at redshifts 0.01, 1.0 for frequencies 300 MHz, 1 GHz and 5 GHz. It is clear that the dwarf galaxies with 10^7 $\mathrm{M}_{\odot}$ provide non-detection constraints at best on par with the relic density bound ($\langle \sigma V \rangle \sim \mathcal{O}(10^{-26})$ cm^3 s^{-1}) for any considered redshift, mass and frequency combination. However, both galactic and cluster halos provide strong restrictions in the event of non-detection by the SKA. This remains true for the cluster halos out to $z \approx 1$. In the case of larger redshifts, none of the halos provide good non-detection constraints. Therefore, we see that the optimal short integration time search region for the SKA is redshifts below 1, concentrating observation on larger halos or considering small halos at much smaller redshifts. A comparison of these figures also demonstrates that the optimal observation window varies with neutralino mass, with lighter neutralinos, below 50 GeV, favouring the lower frequency range while the heavier neutralino is more optimally detectable in frequencies between 1 and 5 GHz. Thus the SKA's frequency range is extremely well suited to studying neutralino-induced radio emissions across a broad range of neutralino masses.

Figure 36 displays the effect of magnetic field strength on synchrotron emissions and how this impacts on the value of the minimum cross-section required for SKA observation at various frequencies. It is evident that, for the displayed 60 GeV $b\bar{b}$ neutralino, stronger magnetic fields, especially those associated with galaxy clusters, such those found in [36], from $\mathcal{O}(1)$ to $\mathcal{O}(10)$ μG provide an excellent

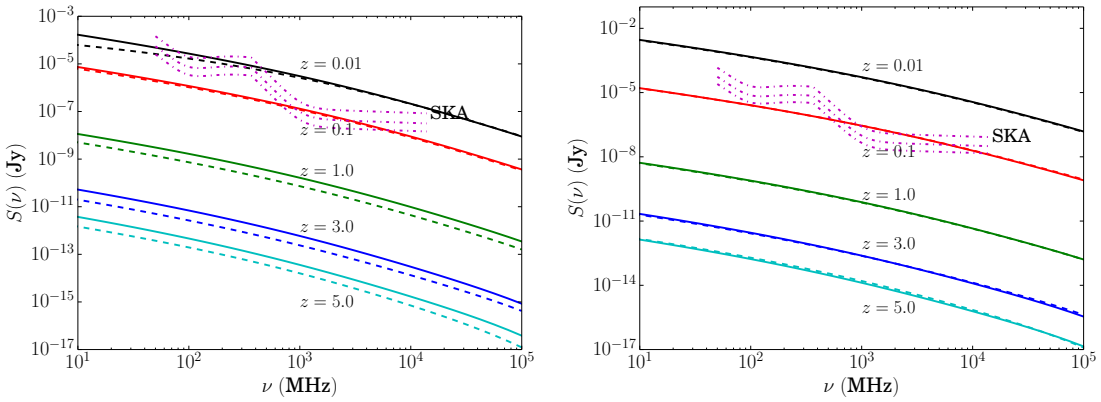

Figure 23. Flux densities for galaxies ($M = 10^{12}\mathrm{M}_{\odot}$), the halo profile is NFW and $\langle B \rangle = 1$ μG. WIMP mass is 500 GeV and the composition is $b\bar{b}$. See the caption of Figure 3 for legend.

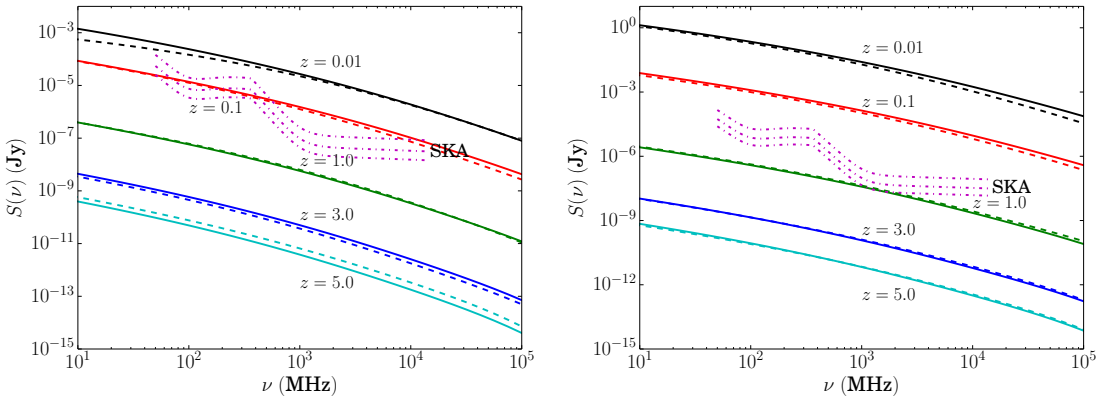

Figure 24. Flux densities for galaxy clusters ($M = 10^{15}\mathrm{M}_{\odot}$), the halo profile is NFW and $\langle B \rangle = 1$ μG. WIMP mass is 500 GeV and the composition is $b\bar{b}$. See the caption of Figure 3 for legend.

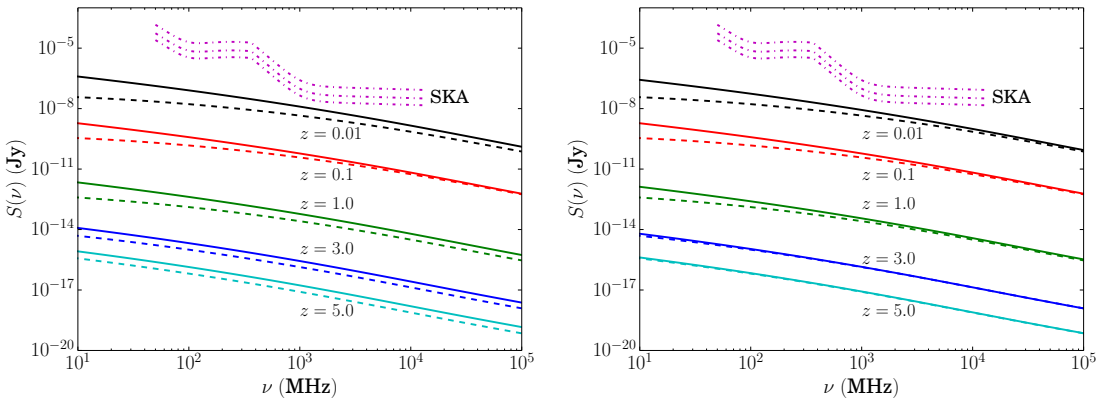

Figure 25. Flux densities for dwarf spheroidal galaxies ($M = 10^{7}\mathrm{M}_{\odot}$), $\langle B \rangle = 5$ μG. WIMP mass is 500 GeV and the composition is $W^{+}W^{-}$. See the caption of Figure 3 for legend.

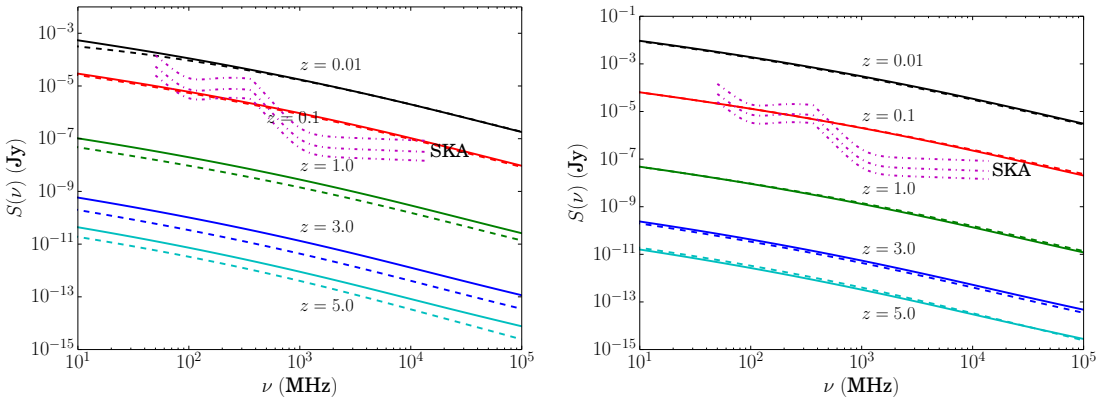

Figure 26. Flux densities for galaxies ($M = 10^{12}\mathrm{M}_{\odot}$), $\langle B \rangle = 5$ μG. WIMP mass is 500 GeV and the composition is W^+W^-. See the caption of Figure 3 for legend.

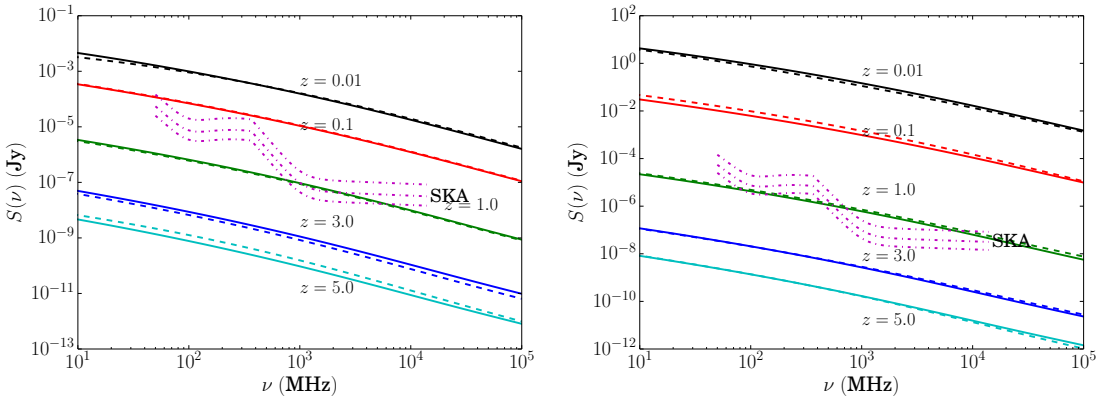

Figure 27. Flux densities for galaxy clusters ($M = 10^{15}\mathrm{M}_{\odot}$), the halo profile is NFW and $\langle B \rangle = 5$ μG. WIMP mass is 500 GeV and the composition is W^+W^-. See the caption of Figure 3 for legend.

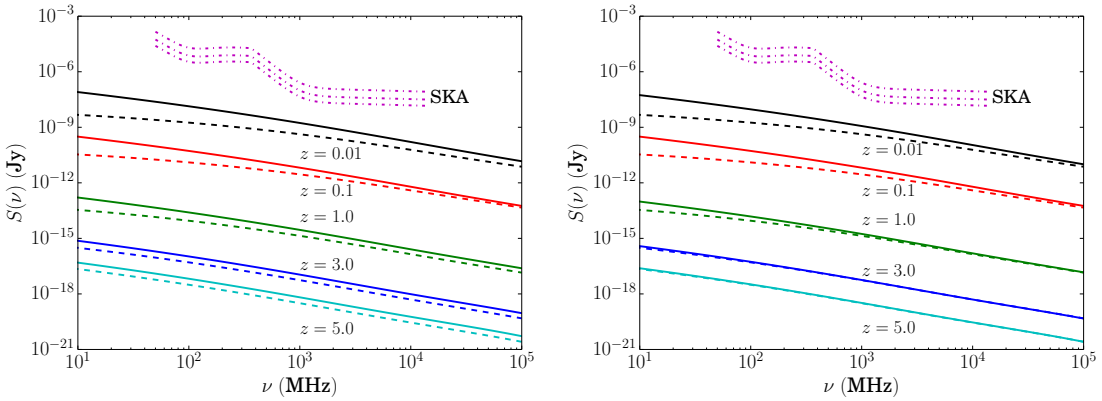

Figure 28. Flux densities for dwarf spheroidal galaxies ($M = 10^{7}\mathrm{M}_{\odot}$), the halo profile is NFW and $\langle B \rangle = 1$ μG. WIMP mass is 500 GeV and the composition is W^+W^-. See the caption of Figure 3 for legend.

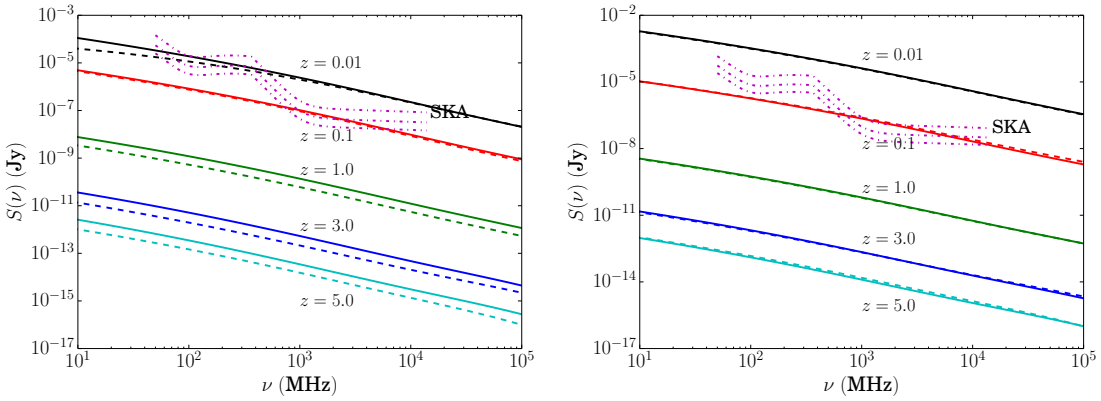

Figure 29. Flux densities for galaxies ($M = 10^{12}\mathrm{M}_{\odot}$), the halo profile is NFW and $\langle B \rangle = 1$ μG. WIMP mass is 500 GeV and the composition is W^+W^-. See the caption of Figure 3 for legend.

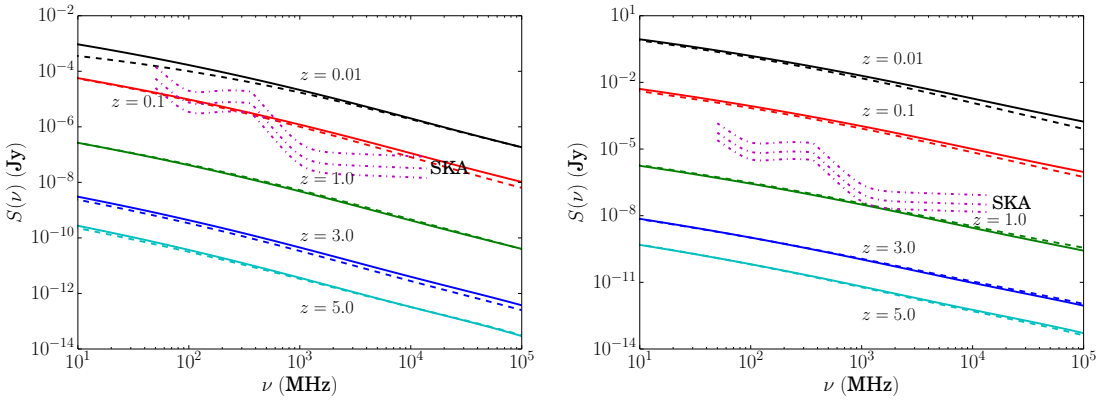

Figure 30. Flux densities for galaxy clusters ($M = 10^{15}\mathrm{M}_{\odot}$), the halo profile is NFW and $\langle B \rangle = 1$ μG. WIMP mass is 500 GeV and the composition is W^+W^-. See the caption of Figure 3 for legend.

test-bed for local observations ($z \leq 1$), with SKA non-detection producing restrictions well below the relic abundance value for both galaxies and clusters at all the displayed frequencies. However, increasingly strong fields offer no additional advantages as the synchrotron emission rapidly saturates. This demonstrates the importance of analysing the magnetic fields within target sources: here the SKA's capability of performing both Faraday Rotation and polarisation studies means that our single instrument can perform all the necessary observations to probe the nature of dark matter. Dwarf galaxies with mass 10^7 $\mathrm{M}_{\odot}$ can at best produce 1σ non-detection constraints that are of the same order of magnitude of the reference value for the thermal relic abundance limit ($\langle \sigma V \rangle = 3 \times 10^{-26}$ cm^3 s^{-1}). Thus even the faintest sources detectable to SKA are capable of producing results competitive with current observations.

4 Discussion and Conclusions

Figure 37 displays a source visibility bound as a function of a halo with mass M and redshift z. This assumes annihilation channel $b\bar{b}$ (with 60 GeV mass) and a cross-section given by $\langle \sigma V \rangle = 3 \times 10^{-26}$ cm^3 s^{-1} and shows the exclusion curves for 30 hour and 1000 hour integration times at 1 GHz with 3 different confidence intervals (being 1σ, 2σ, and 3σ c.l.). This figure also contains a selection of sources, those with known radio halos are depicted with circles while the squares are those for which

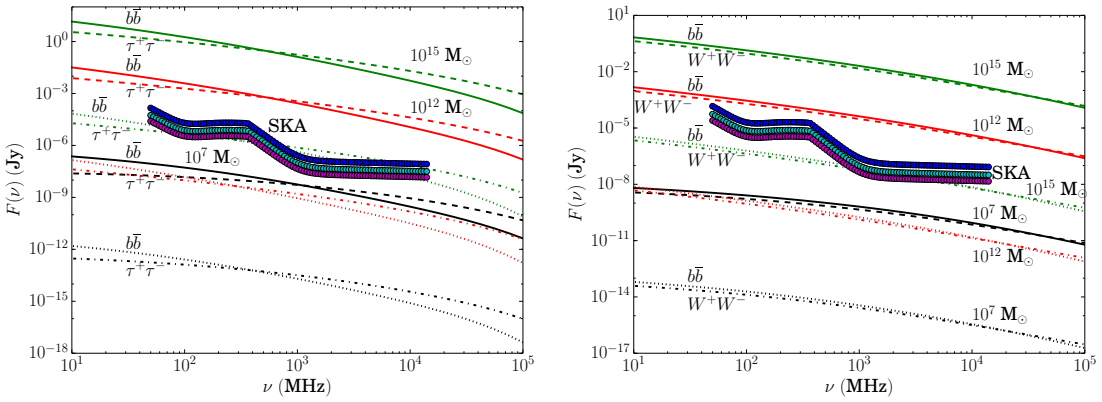

Figure 31. Comparison of fluxes from different annihilation channels. Green lines are for halos of mass 10^{15} $M_\odot$, red for 10^{12} $M_\odot$ and black for 10^7 $M_\odot$. Left: $m_\chi = 60$ GeV, solid lines correspond to the $b\bar{b}$ channel with $z = 0.01$, dotted lines to the same channel with $z = 1.0$, and dashed lines to $\tau^+\tau-$ with $z = 0.01$ while dash-dotted lines are for $z = 1.0$. Right: $m_\chi = 500$ GeV, solid lines correspond to the $b\bar{b}$ channel with $z = 0.01$, dotted lines to the same channel with $z = 1.0$, and dashed lines to W^+W- with $z = 0.01$ while dash-dotted lines are for $z = 1.0$. The circle points are SKA 1σ sensitivity limits for 30, 240, and 1000 hour integration times respectively.

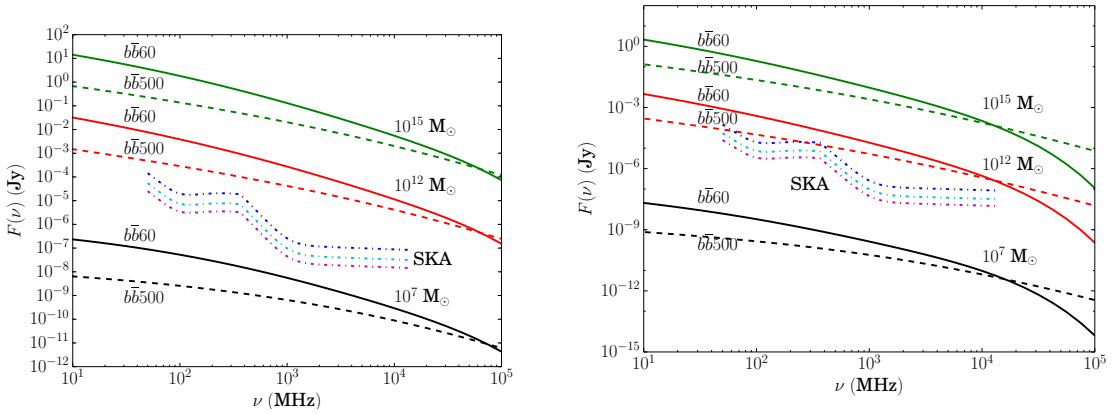

Figure 32. Comparison of fluxes from different WIMP masses in the $b\bar{b}$ channel. Solid lines correspond to $m_\chi = 60$ GeV and dashed lines to $m_\chi = 500$ GeV. Green lines are for halos of mass 10^{15} $M_\odot$, red for 10^{12} $M_\odot$ and black for 10^7 $M_\odot$. The pink dash-dotted lines are SKA 1σ sensitivity limits for 30, 240, and 1000 hour integration times respectively. Left: $B = 5$ μG. Right: $B = 1$ μG.

there is no strong evidence of a radio halo. This distinction is important as dark matter emissions should be visible from most structures, not just those with already discovered diffuse radio emissions and it is therefore necessary to probe both varieties of source. The region above the curve can only be observed by the SKA if the cross-section were larger than a given reference value (in this case the relic abundance cross-section $\langle \sigma V \rangle = 3 \times 10^{-26}$ cm^3 s^{-1}), while the region below the curve can be observed with cross-sections below the reference value. This demonstrates that with $\langle \sigma V \rangle = 3 \times 10^{-26}$ cm^3 s^{-1} and longer integration times (1000 hours) dwarf galaxies of $\sim 10^8$ M$_\odot$ are detectable at 1σ out to $z = 0.01$ ($\sim$ 40 Mpc). The dash-dotted curve shows off the fact that most of the displayed sources could provide non-detection constraints three or more orders of magnitude below the value $\langle \sigma V \rangle = 3 \times 10^{-26}$ cm^3 s^{-1}. The neutralino annihilation induced radio fluxes from nearby dwarf galaxies (at very small redshifts) can provide the strongest method of constraining the cross-section below the level of the reference cross-section value, as seen by the distance between the dSph group

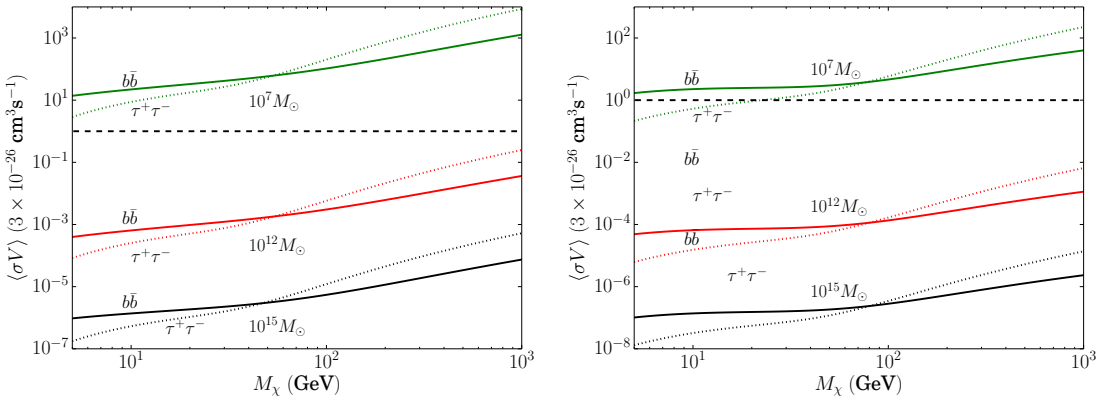

Figure 33. Minimum detectable cross-section ($\langle\sigma V\rangle$) from 30 hour SKA integration time for $z = 0.01$ at 300 MHz (left) and 1 GHz (right) as the neutralino mass M_χ is varied with annihilation channel $b\bar{b}$ in solid lines and $\tau^+\tau^-$ in dotted lines. Black lines correspond to halos with mass 10^{15} $M_\odot$, red lines to 10^{12} $M_\odot$ and green lines to 10^7 $M_\odot$. The black dashed line is $\langle\sigma V\rangle = 3\times10^{-26}$ cm^3 s^{-1}.

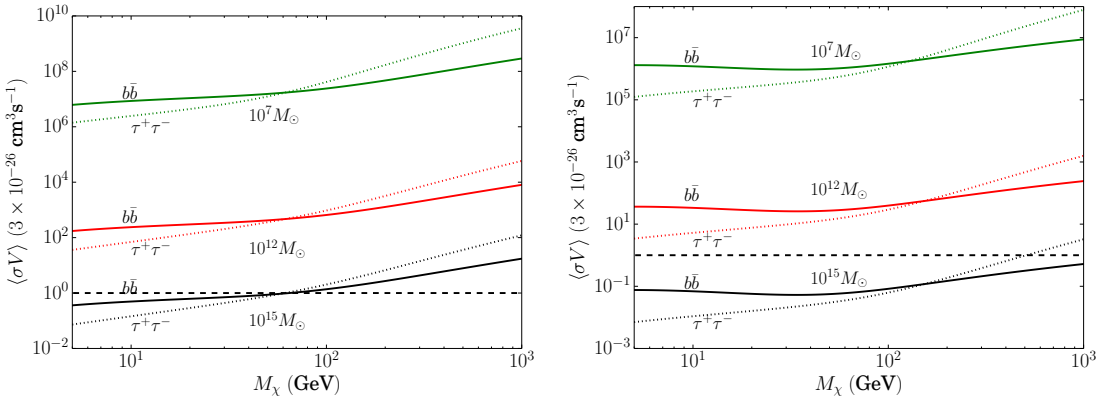

Figure 34. Minimum detectable cross-section ($\langle\sigma V\rangle$) from 30 hour SKA integration time for $z = 1$ at 300 MHz (left) and 1 GHz (right) as the neutralino mass M_χ is varied with annihilation channel $b\bar{b}$ in solid lines and $\tau^+\tau^-$ in dotted lines. Black lines correspond to halos with mass 10^{15} $M_\odot$, red lines to 10^{12} $M_\odot$ and green lines to 10^7 $M_\odot$. The black dashed line is $\langle\sigma V\rangle = 3\times10^{-26}$ cm^3 s^{-1}

and the reference cross-section value curves in Fig. 37. The extreme proximity of these dwarf galaxies makes their fluxes easily detectable and thus provides excellent detection prospects with the SKA as well as offering very strong constraints in the event of non-detection.

It is worth noting that constraints derived in this way may apply to a combination of the cross-section, sub-structure boost factor (as this is not a well known quantity), and the magnetic field amplitude in the halos. Further observational and simulation data are needed to remove this degeneracy by better constraining the magnitude of the sub-structure effect (we note that the substructure effect is also least apparent in dwarf galaxies) and by using the SKA to provide accurate Faraday rotation and polarisation measurements of the magnetic fields in cosmic structures. The polarized source counts at $\sim \mu$Jy levels expected to be detected with the SKA are not known and are extrapolated from current radio surveys at $\sim$ 1GHz. These estimates are currently made available for the SKA (see, e.g., [37]). This last study shows that extrapolating the counts from the deep survey in the GOODS-N field, at a sensitivity of ≈ 15 μJy and at a resolution of 1.6", one finds ≈ 315 polarized sources per square degree at a flux ≈ 1 μJy [64], a value in agreement with the extrapolation derived in [39], on the

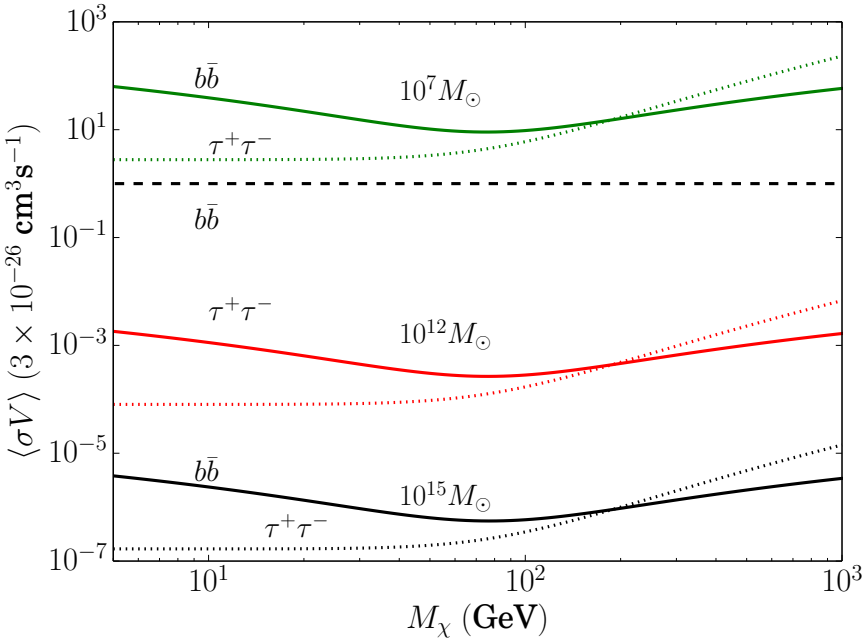

Figure 35. Minimum detectable cross-section ($\langle\sigma V\rangle$) from 30 hour SKA integration time for $z = 0.01$ at 5 GHz as the neutralino mass M_χ is varied with annihilation channel $b\bar{b}$ in solid lines and $\tau^+\tau^-$ in dotted lines. Black lines correspond to halos with mass 10^{15} $M_\odot$, red lines to 10^{12} $M_\odot$ and green lines to 10^7 $M_\odot$. The black dashed line is $\langle\sigma V\rangle = 3\times10^{-26}$ cm^3 s^{-1}

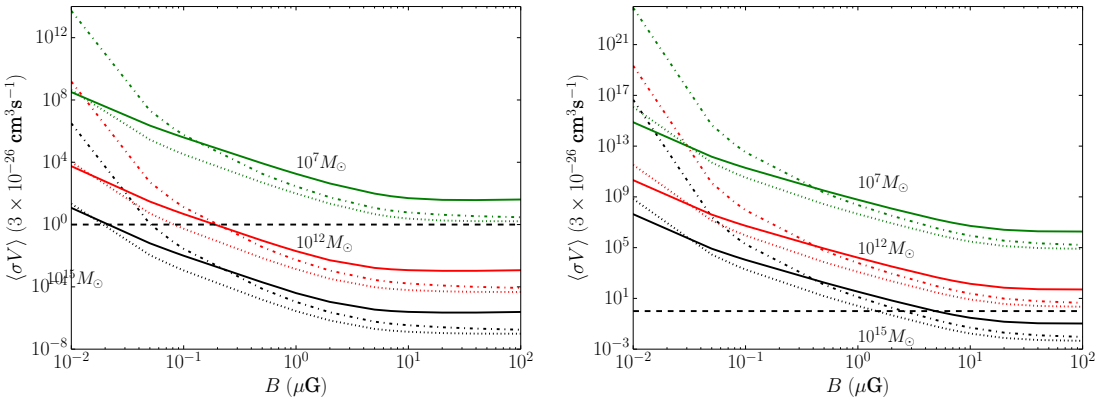

Figure 36. Sensitivity cross-section ($\langle\sigma V\rangle$) from 30 hour SKA integration time as the magnetic field B is varied for annihilation channel $b\bar{b}$ with $M_\chi = 60$ GeV. Solid lines reflect upper limits at 300 MHz, dotted lines are at 1 GHz while dash-dotted lines are at 5 GHz. Green lines represent dwarf galaxy halos, red lines are for galaxy halos and black lines for cluster halos. The black dashed line is $\langle\sigma V\rangle = 3\times10^{-26}$ cm^3 s^{-1}. Left: $z = 0.01$, right: $z = 1.0$.

basis of the second data release of the Australia Telescope Large Area Survey (ATLAS DR2), at a sensitivity of ≈ 25 μJy/beam and at a resolution of 10". Note that at a resolution of 1 arcmin, from NVSS polarization stacking, the expected number of polarized sources at a flux level of 1 μJy is of the order of ≈ 1300 sources per square degree as calculated in [71] with an overall uncertainty at the level of $\approx 50\%$ (see discussion in [37]). It is worth noting that the stacking result in [71] is derived

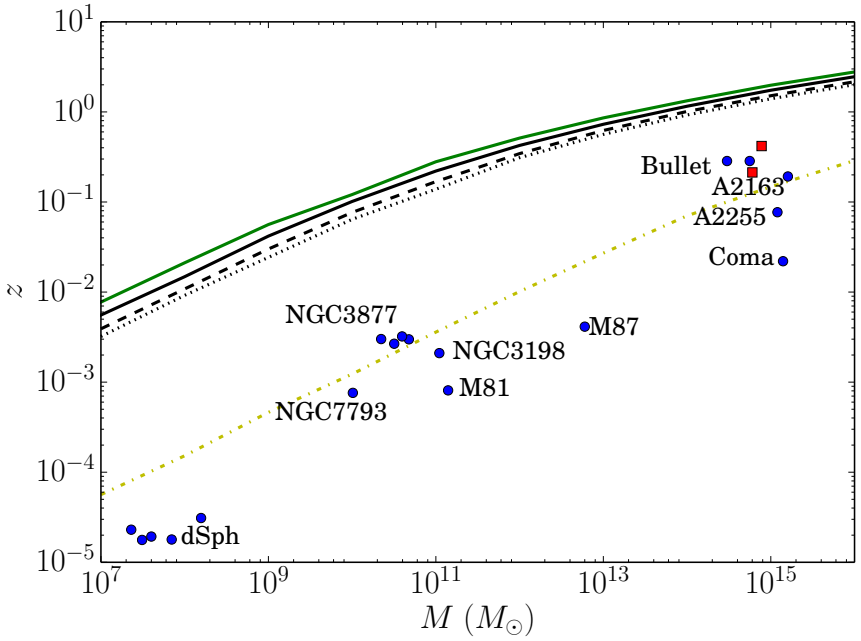

Figure 37. Source visibility as a function of redshift and halo mass. Based on projected SKA sensitivity data for the relic abundance cross-section value with 30 hour integration time (black lines) and 1000 hour integration time (green lines). Solid lines are the 1σ sensitivity exclusion, dashed lines that of 2σ and dotted lines correspond to 3σ. The yellow dash-dotted line corresponds to 30 hours of integration and 1σ confidence with $\langle\sigma V\rangle = 3 \times 10^{-30}$ cm^3 s^{-1}. Annihilation channel $b\bar{b}$ is assumed with a neutralino mass of 60 GeV. The dSph group contains the dwarf spheroidal galaxies: Draco, Sculptor, Fornax, Carina and Sextans. Unlabelled Galaxies are: NGC3917, NGC3949 and NGC4010 (also note that the Bullet cluster components are shown separately). The data for the selection of sources included in this figure was taken from [9, 13, 35, 40, 42, 45–47, 50, 56, 61, 73]. For extremely local objects redshifts were estimated from the average distance. The square points represent the clusters RXJ2228.6+2037 and A1423 [15].

from hundreds of thousands of NVSS sources over $\approx 80\%$ of the sky while the expected counts in [64] consider a very deep survey over a small field of view. These expectations ensure that the magnetic field structure in the cosmic structures we consider in our work (which have dimensions of order of half to a deg^2) can be proven with the SKA1 using a substantial (of order of at least $\sim 10^2$ FR measures per pointing) number of polarized sources that ensure a good analysis of the amplitude and spatial distribution of magnetic fields along the line of sight to our DM halos. We must finally note that the predictions of the number of faint polarized radio sources that can be detected with SKA1 depend on the polarization properties of radio sources with a flux density below ≈ 1 mJy. Total intensity source counts suggest a transition in the dominant population from AGN to star-forming galaxies around this flux density and the properties of brighter radio sources may not be representative for this fainter population. The evolution of the luminosity functions, in total intensity and in polarization, will be one of the headline science results of future SKA1 surveys (see, e.g., discussion in [37]).

Given that the SKA will be able to independently measure the magnetic fields in our DM halos, we note that the constraints based on heavier halos can be obtained, for our reference value of the magnetic field, out to a maximum redshift of $z \sim 2$, with 10^{15} M$_\odot$ halos remaining detectable at 1σ for the $\langle\sigma V\rangle = 3 \times 10^{-26}$ cm^3 s^{-1} out to this redshift with 1000 hour integration or $z \sim 1.7$ with 30 hour integration. In the case of higher σ detections the limiting redshift for the reference cross-section is around $z \sim 1.4$. This argument demonstrates the potential for SKA non-detection, in large halos, to constrain the annihilation cross-section both from deeper field observations (requiring more integration time), which allow constraint below the relic density bound, and local observations

which provide constraints at least 3 orders of magnitude below the relic abundance density bound even with short integration times as seen in Figs. 33 and 36.

The constraints derived here are highly competitive in the multi-frequency strategy for indirect detection of dark matter signals. However, a detailed discussion of the foreground emission from standard astrophysical processes has to be considered in the specific study of the telescope sensitivity to dark matter signals (see, e.g., [63] for a discussion). There are two main caveats in the forecasts for dark matter detection in the radio frequency band. The first stems from the fact that, for an extended radio emission, the confusion issue becomes stronger and stronger as one tries to probe fainter and fainter fluxes. Thus, source subtraction procedures become crucial and this can affect the estimated sensitivities. The impact of this effect on the actual sensitivity is hardly predictable at the present time, especially for the SKA, since it will depend on the properties of the detected sources, the efficiency of deconvolution algorithms, and the accuracy of the telescope beam shape. The second caveat is that by bringing down the observational threshold, one can possibly start to probe the very low levels of possible non-thermal emission associated to the tiny rate of star formation in dwarf galaxies, or in galaxies and galaxy clusters. The dark matter contribution should be then disentangled from such astrophysical background. The superior angular resolution of the SKA will allow for the precise mapping of emissions, putatively either dark matter or baryonically induced, and will enable their correlation with the stellar or dark matter profiles (obtained via optical and/or kinematic measurements). It is evident, however, that SKA non-detection holds the potential to be far more stringent than existing bounds on the thermally averaged annihilation cross-section, such as those in[1] from the Fermi collaboration, [38] using Fermi-LAT data, and [8] from the WMAP haze data. Specifically, the Fermi collaboration results place the most stringent restrictions, of $\mathcal{O}(10^{-27})$ cm^3 s^{-1}, on only neutralinos below 10 GeV, with neutralinos around 50 GeV being bounded by $\langle \sigma V \rangle < 10^{-25}$ cm^3 s^{-1}.

Additionally, the realistic analysis of the prospects of the CTA [67] show that it provides weak constraints, around $\langle \sigma V \rangle < 10^{-25}$ cm^3 s^{-1} for neutralinos below 100 GeV, but are maximally constraining for 1000 GeV at $\langle \sigma V \rangle < 10^{-26}$ cm^3 s^{-1}. The comparison of the Fermi results and the CTA prospects with the predictions presented here shows that the SKA is sufficiently sensitive to probe a far larger region of the cross-section parameter space than has been previously accessed astrophysically, making the SKA a strong contender as a "dark matter machine" in future indirect searches for unveiling the signatures of neutralino annihilation. This is particularly reinforced by the fact that the frequency range of the SKA encompasses the regions of greatest importance to the neutralino spectrum, i.e. lower frequencies around 1 GHz and below, which allow for the possibility to distinguish between annihilation channels and for the optimal detection constraints, and higher frequencies around 5 GHz and upwards, which are important in constraining the neutralino mass through the natural cut-off behaviour.

Following to the results displayed for magnetic field variation, the detection of neutralino-induced radio emission is maximised within halos that host stronger magnetic fields, of order $\mathcal{O}(10\ \mu\text{G})$, conditions which could hold for the central regions of galaxies and galaxy clusters and that can be easily verified with the SKA observations.

It must be noted, however, that the SKA phase-1 will have still limited ability to detect radio emission from the halos of small structures that are not at small redshifts, making concentration on nearby or very large structures necessary for optimal detection sensitivities with the technique here discussed.

However, it is evident that highly local dwarf spheroidal galaxies offer some of the best environments for either detection of neutralino annihilation or constraining the cross-section, as they are both rich in dark matter and close enough to provide highly detectable fluxes. Moreover, the ability of the SKA to probe structures at large redshifts allows for the observation of more primeval galaxies and galaxy clusters that may contain fewer foreground sources of baryon-induced radio emission. Additionally the radio emission spectra display qualitative features that distinguish the strength of the magnetic field and the mass of the neutralino, as these are both influential in determining the high-frequency cut-off of the spectrum. SKA-observable cut-off frequencies corresponding to either light neutralinos or weak magnetic fields, in either case the necessary frequencies for the scenarios displayed here will

be best observed with SKA phase-2. The characteristic annihilation channel is also evident in the low-frequency slope of the spectrum, with $b\bar{b}$ producing steeper spectra than $\tau^+\tau^-$ at 60 GeV with a cross-over around 1 GHz, while at 500 GeV $b\bar{b}$ is also marginally steeper than W^+W^- with a higher frequency cross-over. These properties are of great importance to the detection of non-thermal radio emission resulting from neutralino annihilation, as they provide tell-tale markers distinguishing the synchrotron emission of electrons produced in this manner from other sources of such radiation within the halo. It is of great significance that such radio spectra might fall within the observation window of the SKA, in particular this would aid in the unambiguous detection of neutralino annihilation products or place additional limits upon the annihilation cross-section, making the SKA a key player in piecing together the dark matter puzzle. This argument is enhanced by the fact that the SKA's frequency range covers the optimal detection regions for neutralinos with masses ranging from around 10 GeV to around 1000 GeV, while its sensitivity allows to probe far smaller values of the neutralino annihilation cross-section than has previously been achieved, thus allowing the SKA to survey a large range of the neutralino parameter space. We therefore conclude that radio observation, with future radio interferometers like the SKA, must be considered as a leading technique in the search for dark matter in the coming decades.

Acknowledgments

S.C. acknowledges support by the South African Research Chairs Initiative of the Department of Science and Technology and National Research Foundation and by the Square Kilometre Array (SKA). P.M. and G.B. acknowledge support from the DST/NRF SKA post-graduate bursary initiative.

References

[1] Ackerman, M. *et al.*, 2010, JCAP, 5, 25

[2] Adams, J. J. *et al.*, arXiv:1405.4854 [astro-ph.GA].

[3] Ade, P. A. R. *et al.* [Planck Collaboration], arXiv:1303.5076 [astro-ph.CO].

[4] Bauer, D. *et al.*., 2013, arXiv:1305.1605 [hep-ph]

[5] Bergström, L. & Kaplan, J., 1994, Astropart. Phys., 2(3), 261

[6] Bertone, G., Hooper, D. & Silk, J., 2005, J. Phys. Rep., 405(5), 279

[7] Bonafede, A., *et al.*., 2010, A&A, 513, A30

[8] Bottino, A., Donato, F., Fornengo, N. & Scopel, S., 2008, Phys. Rev. D, 77, 127301

[9] Bradac, M. *et al.*., 2006, ApJ, 652, 937

[10] Bryan, G. & Norman M., 1998, ApJ, 495, 80

[11] Bullock, J.S. *et al.*., 2001, MNRAS, 321, 559

[12] Burkert, A., 1995, ApJ, 447, L25

[13] Burns, J.O. *et al.*., 1995, ApJ, 446,583

[14] Carr, J. *et al.*, 2006, Rep. Prog. Phys., 69, 2475

[15] Cassano, R., Ettori, S., Brunetti, G., Giacintucci, S., Pratt, G. W., Venturi, T., Kale, R., Dolag, K. & Markevitch, M., 2013, ApJ, 777, 141

[16] Coe, D., 2010, arXiv:1005.0411

[17] Colafrancesco, S. & Blasi, S., 1998, Astropart. Phys., 9, 227

[18] Colafrancesco, S., Marchegiani, P., & Perola, G.C., 2005, A&A, 443, 1

[19] Colafrancesco, S., Profumo, S. & Ullio, P., 2006, A&A, 455, 21

[20] Colafrancesco, S., Profumo, S. & Ullio, P., 2007, Phys. Rev. D, 75, 023513

[21] Colafrancesco, S., 2010, arXiv:1004.3869 [astro-ph.CO]

[22] Conrad, J., 2012, arXiv:1210.4392

[23] Dewdney, P., Turner, W., Millenaar, R., McCool, R., Lazio, J. & Cornwell, T., 2012, SKA baseline design document, http://www.skatelescope.org/wp-content/uploads/2012/07/SKA-TEL-SKO-DD-001-1_BaselineDesign1.pdf

[24] Diemand J. *et al.*, 2008, Nature, 454,735

[25] Einasto, J., Publications of the Tartuskoj Astrofizica Observatory, 1968, 36, 414

[26] Eke, V. R., Navarro, J. F. & Steinmetz, M., 2001, ApJ, 554, 114

[27] Feng, J., 2010, ARA & A, 48, 495

[28] Fornengo, N., Lineros, R., Regis, M. & Taoso, M., 2012, JCAP, 03,033

[29] Frampton, P., Kawasaki, M., Takahashi, F. & Yanagida, T., 2010, arXiv:1001.2308 [hep-ph]

[30] Funk, S., 2013, arXiv:1310.2695 [astro-ph.HE]

[31] Gaitskell, R., 2004, Annu. Rev. Nucl. Part. Sci., 54, 315

[32] Gondolo, P., 1994, Nucl. Phys. B (Proc. Suppl.) 35, 148

[33] Gondolo, P. & Silk, J., 1999, Phys. Rev. D., 83, 1719

[34] Gondolo, P., Edsjo, J., Ullio, P., *et al.*. 2004, JCAP, 0407,008

[35] González, G. A. *et al.*, 2010, MNRAS, 404(1),468

[36] Govoni F. & Feretti L., 2004, Int. J. Mod. Phys. D, 13 , 1549

[37] Govoni, F., Johnston-Hollitt, M. et al. 2014, COSMIC MAGNETISM SCIENCE IN THE SKA1 ERA, SKA memo

[38] Hooper, D. & Linden, T., 2011, Phys. Rev. D, 84, 123005

[39] Hales, M. et al. 2014, ApJ submitted

[40] Jałocha, J. *et al.*, 2010, MNRAS, 406(4), 2805

[41] Jungman, G., Kamionkowski, M. & Griest, K.,1996, J. Phys. Rep., 267, 195

[42] Kostov, V., 2006, astro-ph/0604395

[43] Lamanna, G., Farnier, C., Jacholkowska, A., Kieffer, M., & Trichard, C. For The H.E.S.S. Collaboration, 2013, arXiv:1307.4918 [astro-ph.HE]

[44] Linden, T., Hooper, D. & Yusef-Zadeh, F., 2011, arXiv:1106.5493 [astro-ph.HE]

[45] Łokas, E. L. & Mamon, G.A., 2003, MNRAS, 343, 401

[46] Łokas, E. L. *et al.*., 2005, MNRAS, 363, 918

[47] Łokas, E. L., 2009, MNRAS, 394,L102

[48] Longair, M. S., 1994, High Energy Astrophysics (Cambridge University Press)

[49] Ludlow, A. D. *et al.*, 2013, MNRAS, 432, 1103L

[50] Merritt, D.0 & Tremblay, B., 1993, AJ, 106, 2229

[51] Moffat, J.W. et al., 2007, arXiv:0710.0364 [astro-ph]

[52] Morselli, A., Canadas, B. & Vitale, V. on behalf of the Fermi LAT collaboration, 2010, arXiv:1012.2292

[53] Muñoz-Cuartas, J. C., Macciò, A. V., Gottlöber, S. & Dutton, A. A., arXiv:1007.0438 [astro-ph.CO]

[54] Nagai, D. & Kravtsov, A. V., 2005, ApJ, 618, 557

[55] Navarro, J. F., Frenk, C. S. & White, S. D. M., ApJ, 1996, 462, 563

[56] Okabe, N. *et al.*., 2011, ApJ, 741, 116

[57] Peebles, P. J. E., 1980, Large-scale Structure of the Universe (Princeton University Press)

[58] Petraki, K. & Volkas, R., 2013, Int. J. Mod. Phys. A, 28, 1330028

[59] Pieri, L. & Branchini, E., 2004, Phys. Rev. D., 69, 043512

[60] Pieri L. *et al.*, 2011,Phys. Rev. D., 83,023518

[61] Pietrzynski, G. *et al.*, 2008, astro-ph/1008.3040

[62] Rave, G., Kushnir, D., & Waxman, E., 2013, arXiv:1304.4234

[63] Regis, M., Colafrancesco, S., Profumo, S., de Blok, W. J. G., Massardi, M. and Richter, L., 2014, JCAP, 10, 016R

[64] Rudnick, L. and Owen, F. 2014, ApJ submitted

[65] Shimizu M., Kitayama T., Sasaki S., & Suto, Y., 2003, Astro-phys. J., 590,197

[66] Siffert, B., Limone, A., Borriello, E., Longo, G. & Miele, G., 2011, Mon. Not. R. Astron. Soc., 410, 2463

[67] Silverwood, H., Weniger, C., Scott, P. & Bertone, G., 2014, arXiv:1408.4131 [astro-ph.HE]

[68] Sjöstrand, T., 1994, Comput. Phys. Commun., 82, 74

[69] Spekkens, K., Mason, B., Aguirre, J. & Nhan, B., 2013, arXiv:1301.5306 [astro-ph.CO]

[70] Sreenivasan, K. R. & Antonia, R. A., Ann. Rev. Fluid Mech. , 1997, 29, 435

[71] Stil, J.M. et al. 2014, ApJ submitted

[72] Storm, E., Jeltema, T., Profumo, S. & Rudnick, L., 2012, arXiv:1210.0872 [astro-ph.CO]

[73] Verheijen, M. A. W. & Sancisi R., 2001, A&A, 370, 765

[74] Verma, M.K., 1999, Physics of Plasmas, 6, 1455

[75] Walker, M. G., Mateo, M., Olszewski, E. W., Peñarrubia, J., Evans, N. W. & Gilmore, G., 2009, Astrophys. J., 704, 1274

Chapter 4

The SKA as an Instrument for Dark Matter Hunting

This chapter consists of a survey of the potential of the SKA as a dark matter instrument, dealing with technical specifications and uncertainties that were left largely un-addressed in the first chapter. Importantly, we make a highly detailed study of the prospect of detecting dark matter radio emission with the SKA based on the results of Chapter 3. This is supplemented by an argument for the ability of the SKA to resolve other baryonic sources of non-thermal radio emission from those of dark matter, as well as technical details of its capacity for polarimetry and Faraday rotation-measures, which obviate the magnetic field uncertainties inherent in synchrotron emissions.

This contributes to the multi-frequency argument by illustrating that future radio experiments can overcome the technical challenges that have long been seen as severely diminishing the ability of dark matter searches in radio. These practical considerations are essential to our argument for the use of radio measurements to compliment γ-ray searches for dark matter.

This chapter was published in the Proceedings of Science for *Advancing Astrophysics with the SKA*. The candidate produced the data used, as well as the figures themselves for Figures 2-5. The selection of these figures to reinforce the argument of the work was also made by the candidate. Additionally, the candidate composed the text for the sections Cosmological Evolution of Dark Matter Radio Emission, Optimal Dark Matter Laboratories, as well as contributing text to Section 3. The arguments and analysis expressed in the aforementioned sections were formulated by the candidate.

PROCEEDINGS OF SCIENCE

Probing the nature of Dark Matter with the SKA

Sergio Colafrancesco[*1], **Marco Regis**[2], **Paolo Marchegiani**[1], **Geoff Beck**[1], **Rainer Beck**[3], **Hannes Zechlin**[2], **Andrei Lobanov**[3], **Dieter Horns**[4]

[1]*School of Physics, University of the Witwatersrand, Johannesburg, South Africa*
[2]*Dipartimento di Fisica, Università degli Studi di Torino and INFN-Sezione di Torino, via P. Giuria, 1, 10125 Torino, Italy*
[3]*Max-Planck-Institut für Radioastronomie, Auf dem Hügel 69, 53121 Bonn, Germany*
[4]*Institut für Experimentalphysik, Universität Hamburg, Luruper Chaussee 149, 22761 Hamburg, Germany*

E-mail: sergio.colafrancesco@wits.ac.za

Dark Matter (DM) is a fundamental ingredient of our Universe and of structure formation, and yet its nature is elusive to astrophysical probes. Information on the nature and physical properties of the WIMP (neutralino) DM (the leading candidate for a cosmologically relevant DM) can be obtained by studying the astrophysical signals of their annihilation/decay. Among the various e.m. signals, secondary electrons produced by neutralino annihilation generate synchrotron emission in the magnetized atmosphere of galaxy clusters and galaxies which could be observed as a diffuse radio emission (halo or haze) centered on the DM halo. A deep search for DM radio emission with SKA in local dwarf galaxies, galaxy regions with low star formation and galaxy clusters (with offset DM-baryonic distribution, like e.g. the Bullet cluster) can be very effective in constraining the neutralino mass, composition and annihilation cross-section. For the case of a dwarf galaxy, like e.g. Draco, the constraints on the DM annihilation cross-section obtainable with SKA1-MID will be at least a factor $\sim 10^3$ more stringent than the limits obtained by Fermi-LAT in the γ-rays. These limits scale with the value of the B field, and the SKA will have the capability to determine simultaneously both the magnetic field in the DM-dominated structures and the DM particle properties. The optimal frequency band for detecting the DM-induced radio emission is around ~ 1 GHz, with the SKA1-MID Band 1 and 4 important to probe the synchrotron spectral curvature at low-ν (sensitive to DM composition) and at high-ν (sensitive to DM mass).

Advancing Astrophysics with the Square Kilometre Array,
June 8-13, 2014
Giardini Naxos, Sicily, Italy

[*]Speaker.

1. Unveiling the nature of Dark Matter

The Square Kilometre Array (SKA) is the most ambitious radio telescope ever planned, and it is a unique multi-disciplinary experiment. Even though the SKA, in its original conception, has been dedicated to constrain the fundamental physics aspects on dark energy, gravitation and magnetism, much more scientific investigation could be done with its configuration: the exploration of the nature of Dark Matter is one of the most important additional scientific themes.

Among the viable competitors for having a cosmologically relevant DM species, the leading candidate is the lightest particle of the minimal supersymmetric extension of the Standard Model (MSSM, Jungman et al. 1996), plausibly the neutralino χ, with a mass M_χ in the range between a few GeV to several TeV. Information on the nature and physical properties of the neutralino DM can be obtained by studying the astrophysical signals of their interaction/annihilation in the halos of cosmic structures. These signals (see Colafrancesco et al. 2006, 2007 for details) involve, in the case of a χ DM, emission along a wide range of frequencies, from radio to γ-rays (see Fig. 1 for a DM spectral energy distribution (SED) in a typical dwarf galaxy). Neutral pions produced in $\chi\chi$ annihilation decay promptly in $\pi^0 \to \gamma\gamma$ and generate most of the continuum photon spectrum at energies $E \gtrsim 1$ GeV. Secondary electrons are produced through various prompt generation mechanisms and by the decay of charged pions, $\pi^\pm \to \mu^\pm + \nu_\mu(\bar{\nu}_\mu)$, with $\mu^\pm \to e^\pm + \bar{\nu}_\mu(\nu_\mu) + \nu_e(\bar{\nu}_e)$. The different composition of the $\chi\chi$ annihilation final state will in general affect the form of the electron spectrum. The time evolution of the secondary electron spectrum is described by the transport equation:

$$\frac{\partial n_e}{\partial t} = \nabla\left[D\nabla n_e\right] + \frac{\partial}{\partial E}\left[b_e(E) n_e\right] + Q_e(E,r)\ , \tag{1.1}$$

where $Q_e(E,r)$ is the $e^\pm$ source spectrum, $n_e(E,r)$ is the $e^\pm$ equilibrium spectrum (at each fixed time) and $b_e \equiv -dE/dt$ is the $e^\pm$ energy loss per unit time, $b_e = b_{ICS} + b_{synch} + b_{brem} + b_{Coul}$ (see Colafrancesco et al. 2006 for details). The diffusion coefficient D in eq.(1.1) sets the amount of spatial diffusion for the secondary electrons: it turns out that diffusion can be neglected in galaxy clusters while it is relevant on galactic and sub-galactic scales (see discussion in Colafrancesco et al. 2006, 2007). Under the assumption that the population of high-energy $e^\pm$ can be described by a quasi-stationary ($\partial n_e/\partial t \approx 0$) transport equation, the secondary electron spectrum $n_e(E,r)$ reaches its equilibrium configuration mainly due to synchrotron and ICS losses at energies $E \gtrsim 150$ MeV and due to Coulomb losses at lower energies. Secondary electrons eventually produce radiation by synchrotron emission in the magnetized atmosphere of cosmic structures, bremsstrahlung with ambient protons and ions, and ICS of CMB (and other background) photons (and hence an SZ effect, Colafrancesco 2004). These secondary particles also heat the ambient gas by Coulomb collisions.

A large amount of efforts have been put in the search for DM indirect signals at γ-ray energies looking predominantly for two key spectral features: the $\pi^0 \to \gamma\gamma$ decay spectral bump , and the direct $\chi\chi \to \gamma\gamma$ annihilation line emission, with results that are not conclusive yet (e.g., Daylan et al. 2014, Weniger 2012, Doro et al. 2014). The non-detection of signals related to DM annihilation/decay from various astrophysical targets (including observations of dwarf spheroidal galaxies, the Galactic Center, galaxy clusters, the diffuse gamma-ray background emission) is interpreted in terms of constraints on the (self-)annihilation cross-section (or decay time) of the DM

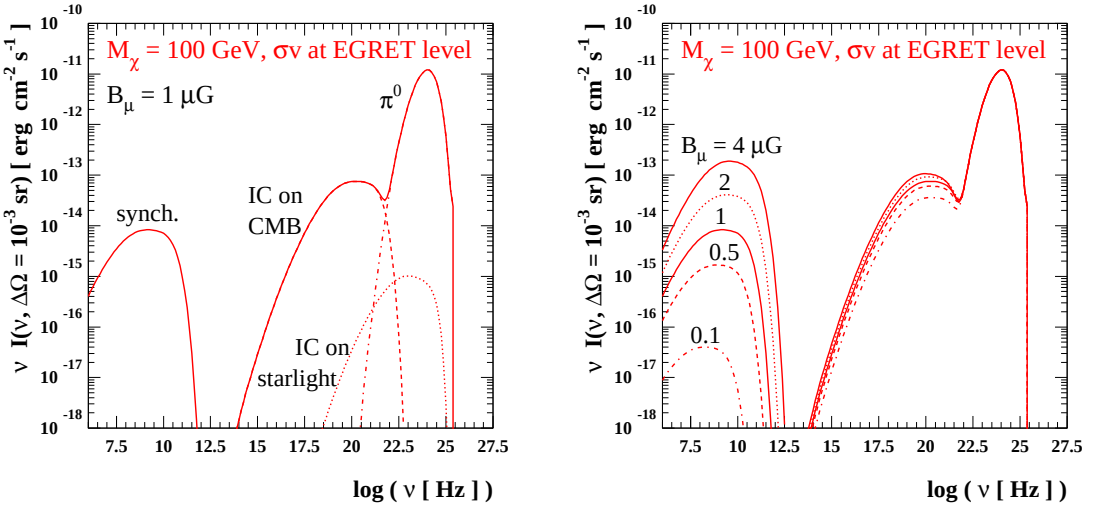

Figure 1: Left. The Draco dSph multi-wavelength spectrum for a 100 GeV WIMP annihilating into $b\bar{b}$. Right. The effect of varying the magnetic field strength on the Draco multi-wavelength spectrum for a 100 GeV WIMP annihilating into $b\bar{b}$. The WIMP pair annihilation rate has been tuned as to give a γ-ray signal at the level of the EGRET measured flux upper limit (from Colafrancesco et al. 2007).

particle candidate. Assuming, for instance, a canonical WIMP of $M_\chi = 100\,\mathrm{GeV}$ annihilating to *b*-quarks, stacked observations of dwarf spheroidal galaxies with Fermi-LAT put a constraint of $\langle\sigma V\rangle < 2\times10^{-25}\,\mathrm{cm^3\,s^{-1}}$ (95% c.l.) on the thermally-averaged self-annihilation cross-section of DM particles (Ackerman et al. 2014). Hopes of discovering annihilating WIMPs in γ-rays are relegated to Fermi-LAT successors and the forthcoming CTA experiment (Doro et al. 2013).
There are, however, also good hopes to obtain relevant information on the nature of DM from radio observations of DM halos on large scales, i.e. from dwarf galaxies to clusters of galaxies.

2. Radio emission signals from Dark Matter annihilation

Observations of radio halos produced by DM annihilations are, in principle, very effective in constraining the neutralino mass and composition (see, e.g., Colafrancesco and Mele 2001, Colafrancesco et al. 2006, 2007), under the hypothesis that DM annihilation provides an observable contribution to the radio-halo flux.

The wide range of frequencies probed by the SKA and the variety of achievable observational targets (and in turn of magnetic fields) will allow testing the non-thermal electron spectrum from about 1 GeV to few hundreds of GeV, that is the most relevant range in the WIMP search. Figure 2 displays the predicted spectral differences between various annihilation channels and WIMP masses: note that these differences manifest mainly in low-ν slope variation for differing annihilation channels and in the high-ν spectral flattening/steepening for larger/smaller masses. The SKA sensitivity curves for SKA1-LOW and SKA1-MID are taken from Dewdney et al. (2012).
The surface brigthness produced by DM-induced synchrotron emission is heavily affected by dif-

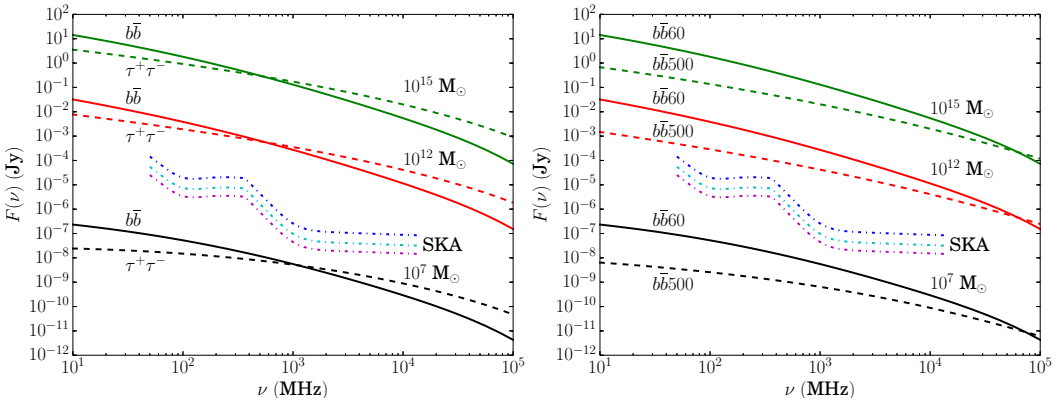

Figure 2: Flux densities for dwarf galaxies ($M = 10^7$ M$_\odot$), galaxies ($M = 10^{12}$ M$_\odot$), and galaxy clusters ($M = 10^{15}$ M$_\odot$). The halo profile is NFW, $\langle B \rangle = 5$ μG, and the annihilation cross section is fixed to the value $\langle \sigma V \rangle \approx 3 \times 10^{-27}$ cm ^{3} s^{-1}. Black lines are for dwarf galaxies, red lines for galaxies and green for clusters. Left: WIMP mass is 60 GeV, solid lines are for composition $b\bar{b}$ and dashed lines for $\tau^+\tau^-$. Right: Composition is $b\bar{b}$, solid lines are for WIMP mass 60 GeV and dashed lines for 500 GeV. Dash-dotted lines are SKA sensitivity limits for integration times of 30, 240 and 1000 hours (Dewdney et al. 2012). The flux is calculated within the virial radius (from Colafrancesco et al. 2014).

fusion in small scale structures, e.g., dwarf and standard galaxies, while it is less important in large structures, e.g., galaxy clusters (see Colafrancesco et al. 2006-2007 for a detailed discussion).

Polarization from DM-induced radio emission is expected at very low fractional levels due to the fact that DM spatial and velocity distribution is nearly homogeneous and that DM annihilation is mediated by secondary particle production. Therefore, a low polarization level of detectable radio signals in the directions of DM halos would be consistent with the DM origin of such radio emission. Residual high-polarization signals could be hence attributed to astrophysical sources in the direction or within the DM halos, and one could use these signals to infer properties of the magnetic field in these structures (see R. Beck et al. 2015, and F. Govoni et al. 2015).

2.1 Cosmological evolution of Dark Matter radio emission

Figure 3 displays the evolution of radio emission from DM halos of mass 10^7 M$_\odot$, 10^{12} M$_\odot$, and 10^{15} M$_\odot$ for a constant magnetic field of 5 μG, in accordance with arguments made in Colafrancesco et al. (2014). The annihilation channel is $b\bar{b}$, the mass of the neutralino is 60 GeV and a DM annihilation cross-section $\langle \sigma V \rangle = 3 \times 10^{-27}$ cm ^{3} s^{-1} was adopted. Emission from dwarf galaxy halos ($M \approx 10^7$ M$_\odot$) is just below the SKA detection threshold for this value of $\langle \sigma V \rangle$ but would be visible at redshift $z \leq 0.01$ for the assumed DM annihilation cross-section. This justify the search of DM-induced radio signals mainly in dwarf galaxies of the local environment, at distances $\lesssim 3$ Mpc ($z \lesssim 0.0007$). Emission from galactic DM halos ($M \approx 10^{12}$ M$_\odot$) are detectable by SKA out to $z \approx 0.8$ even with the reference value of $\langle \sigma V \rangle$, and can provide a non-detection upper-bound on $\langle \sigma V \rangle$ an order of magnitude below the assumed value even at such high redshifts. Emission form galaxy cluster halos can provide similar constraints but out to higher redshifts $z \lesssim 3$. These objects thus offer the option of deep-field observations that can scan a larger fraction of the DM parameter space than the best current data.

Figure 3 also shows that the effect of diffusion are far less significant when observing higher-z objects, again simplifying the modelling and analysis of the SKA observations.

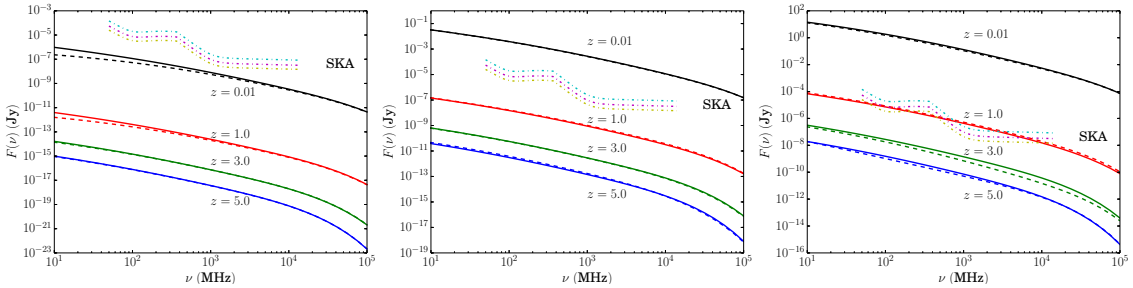

Figure 3: Flux densities for various DM halos within the virial radius. Left: dwarf spheroidal galaxies ($M = 10^7$ M$_\odot$); mid panel: galactic halos ($M = 10^{12}$ M$_\odot$); right panel: galaxy clusters ($M = 10^{15}$ M$_\odot$). We assume a NFW halo profile, $\langle \sigma V \rangle = 3 \times 10^{-27}$ cm ^{3} s^{-1} and $\langle B \rangle = 5$ μG. WIMP mass is 60 GeV and the composition is $b\overline{b}$. Solid lines are without diffusion, and dotted are with diffusion. The SKA sensitivity limits (dash-dotted lines, Dewdney et al. 2012) are shown for integration times of 30, 240 and 1000 hours, respectively (from Colafrancesco et al. 2014).

2.2 Optimal DM laboratories

In order to identify the optimal DM laboratories for radio observations we scan a parameter space extending from dwarf galaxies to galaxy clusters over a wide redshifts range $z \approx 0 - 5$. The choice to examine the halos of both large and small structures is crucial, as dwarf spheroidal galaxies are well known to be highly DM dominated but produce faint emissions, while larger structures, but not immaculate test-beds for DM emissions, provide substantially stronger fluxes. This indicates that a survey of DM halos with different mass is essential to identify the best detection prospects for future radio telescopes like the SKA.

Figure 4 shows the redshift-mass exclusion plot obtained by using the SKA sensitivity bound for SKA1 LOW and SKA1 MID (at 1 GHz in Band 1). For each DM halo we obtain the DM halo mass and redshift combination that produce the minimal SKA-detectable fluxes. DM-dominated objects lying above the black and green curves cannot be detected with the SKA1 at the given confidence threshold for $\langle \sigma V \rangle = 3 \times 10^{-27}$ cm^3 s^{-1}. Objects below a curve are visible to SKA1, and the further below the curve they lie the greater the region of the cross-section parameter space we can explore through the observation of the object. For reference, the yellow dash-dotted line displays the curve given for $\langle \sigma V \rangle = 3 \times 10^{-30}$ cm^3 s^{-1} and 1σ confidence level. A few representative know objects (irrespective of their location in the sky) with good estimates of the DM mass are plotted in the $M_{DM} - z$ plane for the sake of illustration of the DM search potential with the SKA.

Dwarf galaxies, given their extreme proximity, provide an excellent test-bed for DM radio probes, granting access to a parameter space that extends even below the value $\langle \sigma V \rangle = 3 \times 10^{-30}$ cm^3 s^{-1}. Additionally their large mass-to-light ratios and absence of strong star formation and diffuse non-thermal emission make them very clean sources for radio DM searches.

Galaxies can be probed to significantly larger redshifts than the dwarf galaxies due to their larger DM mass, and those located in the redshift range $0.5 \lesssim z \lesssim 1.0$ provide stronger constraints. However, an optimized DM search should be confined to galaxies with little background radio noise,

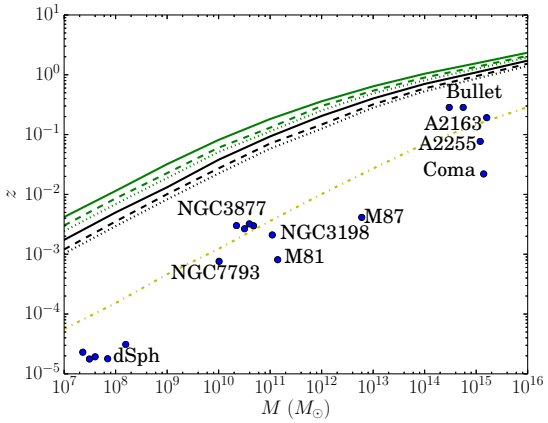

Figure 4: Exclusion plot in redshift versus halo mass based on projected SKA (at 1 GHz in Band 1) sensitivity data for the reference value of $\langle\sigma V\rangle = 3\times10^{-27}$ cm ^{3} s^{-1} with 30 hour integration time (black lines) and 1000 hour integration time (green lines). $\langle B\rangle = 5\ \mu$G was adopted. Solid lines are the 1σ sensitivity exclusion, dashed lines that of 2σ and dotted lines correspond to 3σ. The yellow dash-dotted line corresponds to 30 hours of integration and 1σ confidence with $\langle\sigma V\rangle = 3\times10^{-30}$ cm^3 s^{-1}. An annihilation channel $b\overline{b}$ is assumed with a neutralino mass of 60 GeV. Representative objects with known DM mass are shown for illustrative purposes of DM radio signal detection. The dSph group contains the galaxies: Draco, Sculptor, Fornax, Carina and Sextans. Unlabelled Galaxies are: NGC3917, NGC3949 and NGC4010. For very local objects the redshift is estimated from the average distance data. From Colafrancesco et al. 2014.

making low star-formation-rate galaxies good candidates. High-z galaxies come also with the advantage of observing more primitive structures with fewer sources of baryonic radio emission.
Clusters of galaxies provide extremely good candidates in cases, such as the Bullet cluster, where the dark and baryonic matter are spatially separated. Our recent analysis of the ATCA observation of the Bullet cluster (Colafrancesco and Marchegiani 2014) indicates that deeper radio observations (possible with the SKA) will be able indeed to separate the DM-induced signal from the CR-induced one and hence have the possibly to investigate the nature of DM particles using the technique here proposed. More in general, the large predicted radio fluxes due to DM annihilation in clusters indicate that DM-induced radio emission can be observed in radio out to large redshifts $z \approx 2$, again with the advantage of fewer sources of baryonic radio emission.

2.3 Disentangling magnetic fields and Dark Matter

Studying the magnetic properties of DM halos are crucial to disentangle the DM particle density from the magnetic field energy density contributing to the expected synchrotron radio emission from DM annihilation. The SKA is the most promising experiment to determine the magnetic field structure in extragalactic sources (see Johnston-Hollitt et al. 2015), and will have the potential of measuring RMs toward a large number of sources allowing a detailed description of the strength, structure, and spatial distribution of magnetic fields in dSph galaxies, galaxies (see Beck et al. 2015) and galaxy clusters (see Govoni et al. 2015). We stress that these measurements of the magnetic field can be obtained by the SKA simultaneously, for the first time, with the constraints on DM nature from the expected radio emission.

3. The impact of SKA on the search for the DM nature

Deep observations of radio emission in DM halos are not yet available, and this limits the capabilities of the current radio experiments to set relevant constraints on DM models. We have already explored a project (Regis et al. 2014a,b,c) dedicated to the WIMP search making use of radio interferometers, that could be considered as a pilot experiment for the next generation high-sensitivity and high-resolution radio telescope arrays like the SKA. For the particle DM search we are interested in, the use of multiple array detectors having synthesized beams of $\sim$ arcmin size has a number of advantages with respect to single-dish observations. First, the large collecting area allows for an increase in the sensitivity over that a single-dish telescope. The best beam choice for the detection of a diffuse emission requires a large synthesized beam (in order to maximize the integrated flux), but still smaller than the source itself to be able to resolve it. A good angular resolution is also crucial in order to distinguish between a possible non-thermal astrophysical emission and the DM-induced signal, which clearly becomes very hard if the DM halo is not well-resolved. The possibility of simultaneously detecting small scale sources with the long-baselines of the array allows one to overcome the confusion limit. In the case of arcmin beams, the confusion level can be easily reached with observations lasting for few tens of minutes, even by current telescopes. A source subtraction is thus a mandatory and crucial step of the analysis. Finally, single dish telescopes face the additional complication related to Galactic foreground contaminations, which are instead subdominant for the angular scales typically probed by telescope arrays at GHz frequency.

The limits derived from ATCA observations of 6 dSphs (Regis et al. 2014c) on the WIMP annihilation/decay rate as a function of the mass for different final states of annihilation/decay are already comparable to the best limits obtained with γ-ray observations and are much more constraining than what obtained in the X-ray band or with previous radio observations (Spekkens et al. 2013, Natarayan et al. 2013). In this context, the SKA will have the possibility to explore DM models with cross-section values well below the DM relic abundance one (see Fig.6 in Regis et al. 2014c). The SKA1-MID Band 1 (350 -1050 MHz) will probably be the most promising frequency range for the majority of WIMP models. The full SKA-2 phase will bring another factor $\sim 10\times$ increase in sensitivity and an extended frequency range up to at least 25 GHz. Typical values of the SKA sensitivity ($A_{eff}/T_{sys} = 2 \times 10^4$ m^2/K) and bandwidth (300 MHz at GHz frequency) provide rms flux values of ≈ 30 nJy for 10 hours of integration time. This is about a 10^3 factor of gain in sensitivity with respect to the most recent ATCA observations (Regis et al. 2014a). A further improvement by a factor of 2-3 can be confidently foreseen due to the larger number of accessible dSph satellites from the southern hemisphere. The SKA will also have the unique advantage to be able to determine the dSph magnetic field (via FR measurements and possibly also polarization), provided its strength is around the μG level (as expected from star formation rate arguments, Regis et al. 2014c). This will make the predictions for the expected DM signal much more robust and obtainable with a single experimental configuration. The prospects of detection/constraints of the WIMP particle properties with the SKA will therefore progressively close in on the full parameter space, even in a pessimistic sensitivity case, and up to $\sim$ TeV WIMP masses, irrespective of astrophysical assumptions.

The SKA will also allow to investigate the possibility that point-sources detected in the proximity of the dSph optical center might be associated to the emission from a DM cuspy profile.

This possibility is likely only in the "loss at injection" scenario, while spatial diffusion should in any case flatten the $e^{\pm}$ distribution, making the source extended rather than point-like. The investigation of these sources with the SKA will deserve particular attention, since we have already found that the WIMP scenario can fit the point-like emission with annihilation rates consistent with existing bounds (Regis et al. 2014c).

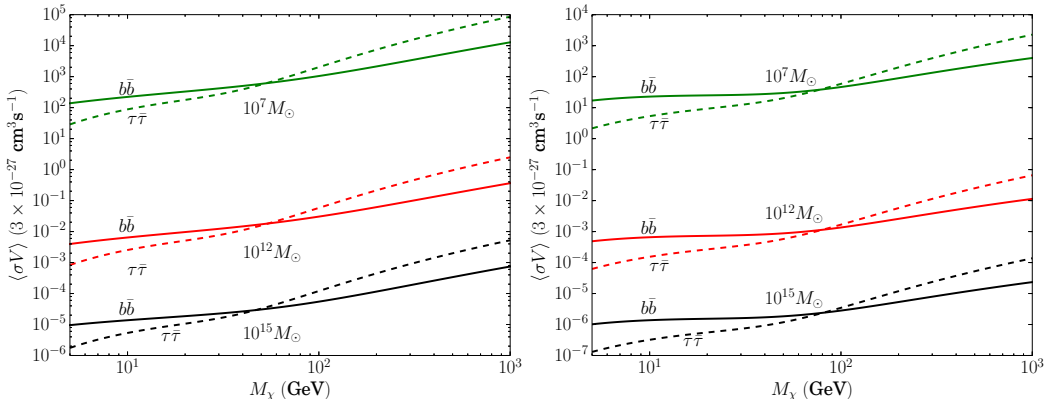

Figure 5: The $\langle\sigma V\rangle$ upper limits from 30 hour of SKA integration time for $z = 0.01$ at 300 MHz (top) and 1 GHz (bottom) as the neutralino mass M_χ is varied with annihilation channel $b\bar{b}$ in solid lines and $\tau\bar{\tau}$ in dashed lines. A value $\langle B\rangle = 5\ \mu$G was adopted. Black lines correspond to halos with mass 10^{15} $M_\odot$, red lines to 10^{12} $M_\odot$ and green lines to 10^7 $M_\odot$ (from Colafrancesco et al. 2014).

The SKA1-MID Band 1 (350-1050 MHz) to Band 4 (2.8-5.18 GHz) are important to probe the DM-induced synchrotron spectral curvature at low-ν (sensitive to DM composition) and at high-ν (sensitive to DM particle mass), and the implementation of Band 5 (4.6-13.8 GHz) will bring further potential to assess the DM-induced radio spectrum. As we can see from Fig.3, the best frequency range to detect these radio emissions is around 1 GHz. So, the upper frequency regions of SKA1-MID Band 1 provides the strongest spectral candidate for probing the cross-section parameter space due to an optimal combination of the SKA sensitivity within this band and the relatively strong fluxes at these frequencies. This frequency band will also allow for an optimal description of the magnetic field (see Johnston-Hollitt et al. 2014).

There are two main caveats in the forecasts for DM detection in the radio frequency band. The first stems from the fact that, for an extended radio emission,the confusion issue becomes stronger and stronger as one tries to probe fainter and fainter fluxes. Thus, the source subtraction procedure becomes crucial and this can affect the estimated sensitivities. The impact of this effect on the actual sensitivity is hardly predictable at the present time, especially for the SKA, since it will depend on the properties of the detected sources, the efficiency of deconvolution algorithms, and the accuracy of the telescope beam shape.

The second caveat is that by bringing down the observational threshold, one can possibly start to probe the very low levels of possible non-thermal emission associated to the tiny rate of star formation in dSph, or in galaxies and galaxy clusters. The DM contribution should be then disentangled from such astrophysical background. The superior angular resolution of the SKA will allow for the precise mapping of emissions, putatively either DM or baryonically induced, and will enable their correlation with the stellar or DM profiles (obtained via optical and/or kinematic measurements).

Early DM science can be done with a small sample of local dSphs, a small sample of nearby galaxies with good DM density profile reconstruction, and the Bullet cluster, observing with a somewhat larger beam ($\approx 7'' - 10''$). These objects have been already studied in radio with similar objectives (e.g., DM limits) and therefore provide the best science cases to prove the capabilities of the SKA1 for the study of the nature of DM with radio observations. The implementation of the SKA1-MID Band 5 (4.6-13.8 GHz) will increase the ability to detect the expected high-frequency spectral curvature of DM-induced radio emissions, and the ability to place constraints on the DM cross-section and to differentiate between different annihilation channel spectra. The $10\times$ increased sensitivity of SKA2-MID compared to SKA1-MID will allow us to increase the angular resolution by a factor ≈ 20 or to increase the sensitivity of SKA2-MID to DM-induced radio signals by a factor ≈ 10. The possibility to extend the frequency coverage of the SKA in its Phase-2 realization up to ~ 25 GHz, will allow to detect the expected high-ν spectral cut-off of DM-induced radio emissions, and then set accurate constraints to the DM particle mass.

4. Conclusion

The SKA has the potential to unveil the elusive nature of Dark Matter. Its ability to resolve the intrinsic degeneracy (between magnetic field properties and particle distribution) of the synchrotron emission expected from secondary particles produced in DM annihilation (decay) will allow such a discovery to be unbiased and limited only by the sensitivity to the DM particle mass and annihilation cross-section (decay rate). The unprecedented sensitivity of the SKA to the DM fundamental properties will bring this instrument in a leading position for unveiling the nature of the dark sector of the universe.

The information provided by the SKA can be complemented with analogous studies in other spectral bands, which will be able to prove the ICS signal of DM-produced secondary electrons (spanning from μwaves to hard X-rays and γ-rays) and the distinctive presence of the $\pi^0 \to \gamma\gamma$ emission bump in the γ-rays (see Fig. 1). The next decade will offer excellent multi-frequency opportunities in this respect with the advent of Millimetron, the largest space-borne single-dish mm. astronomy satellite operating in the $10^2 - 10^3$ GHz range (optimal to prove the DM-induced SZ effect), the Astro-H mission operating in the hard X-rays frequency range (with the highest expected sensitivity to probe the high-energy tail of the DM-induced ICS emission), and the CTA with unprecedent sensitivity in the energy range between a few tens GeV to hundreds TeV.

References

[1] Ackermann, M., et al., 2014, Phys. Rev. D, 89, 042001

[2] Beck, R., Bomans, D., Colafrancesco, S., et al. 2015, in Advancing Astrophysics with the Square Kilometre Array, PoS(AASKA14)94

[3] Borriello, E. et al. 2010, ApJ, 709, L32

[4] Burns, J.O. *et al..*, 1995, ApJ, 446,583

[5] Colafrancesco, S., 2004, A&A, 422, L23

[6] Colafrancesco, S. 2010, invited lecture at the 4th Gamow International Conference on Astrophysics & Cosmology After Gamow (9th Gamow Summer School), AIPC, 1206, 5C

[7] Colafrancesco, S. & Mele, B. 2001, ApJ, 562, 24

[8] Colafrancesco, S., Profumo, S. and Ullio, P. 2006, A&A, 455, 21

[9] Colafrancesco, S., Profumo, S. and Ullio, P. 2007, PhRvD, 75, 3513

[10] Colafrancesco, S. et al. 2011, A&A, 527, 80

[11] Colafrancesco, S., and Marchegiani, P, 2014, A&A in press

[12] Colafrancesco, S., Marchegiani, P. and Beck, G., 2014, [2014arXiv1409.4691C]

[13] Daylan, T. et al., 2014, [arXiv:1402.6703]

[14] Deiss, B.M., Reich, W., Lesch, H. & Wielebinski, R. 1997, A&A, 321, 55

[15] Dewdney, P., Turner, W., Millenaar, R., McCool, R., Lazio, J. & Cornwell, T., 2012, SKA baseline design document, *http://www.skatelescope.org/wp-content/uploads/2012/07/SKA-TEL-SKO-DD-001-1_BaselineDesign1.pdf*

[16] Doro, M., 2014, Nuclear Instruments and Methods in Physics Research A,742, 99

[17] Doro, M., et al., 2013, Astroparticle Physics, 43, 189

[18] Govoni, F., Murgia, M., Feretti, L., et al., 2006, A&A, 460, 425

[19] Govoni, F. et al. 2015, in Advancing Astrophysics with the Square Kilometre Array, PoS(AASKA14)105

[20] Johnston-Hollitt, M. et al. 2015, in Advancing Astrophysics with the Square Kilometre Array, PoS(AASKA14)092

[21] Jungman, G., Kamionkowki, M. & Griest, K. 1996, Phys.rep, 267, 195

[22] Moran, E.C. et al. 2014, [arXiv:1408.4451]

[23] Natarajan, A. et al., 2013, Phys. Rev. D 88 083535 [arXiv:1308.4979 [astro-ph.CO]].

[24] Planck Collaboration, 2011, A&A, 536, A7

[25] Regis, M., Richter, L., Colafrancesco, S., Massardi, M., de Blok, W. J. G., Profumo, S., Orford, N. 2014a, [arXiv:1407.5479]

[26] Regis, M., Richter, L., Colafrancesco, S., Profumo, S., de Blok, W. J. G., Massardi, M. 2014b, [arXiv:1407.5482]

[27] Regis, M., Colafrancesco, S., Profumo, S., de Blok, W. J. G., Massardi, M., Richter, L. 2014c, JCAP, 10, 016R [arXiv:1407.4948]

[28] Spekkens, K., Mason, B.S., Aguirre, J.E. and Nhan, B., 2013, ApJ, 773, 61 [arXiv:1301.5306 [astro-ph.CO]].

[29] Weniger, C., 2012, JCAP, 1208, 007

Chapter 5

X-rays, Dark Matter, and Multi-Frequency Analysis

This chapter contains a demonstration of multi-frequency methods in the context of dark matter. We examine several dark matter models proposed to account for observed excesses and show them to incompatible with observations of a selection of sources in the radio and γ-ray spectra. This analysis is hinged on the universality of dark matter effects, thus any hosting structure should be compatible, across the spectrum, with a given model if it is not to be eliminated. Additionally, we show that up-coming X-ray projects like ASTRO-H have the potential to compliment radio measurements in the search for dark matter. We do this by analysing the potential constraints that ASTRO-H might derive in the soft X-ray spectrum and showing that it is sensitive to a spectral region that contains information on the neutralino mass and annihilation channel.

It must be noted that this chapter uses a bound on the radio-flux produced by the Draco dwarf galaxy, sourced from the Very Large Array (VLA, see references within the chapter). This bound is on fluxes within a four arcminute radius of the galaxy centre but may not be applicable to diffuse emissions, such as those produced by DM-induced synchrotron radiation. However, this caveat does not affect the conclusions made in the following chapter.

The argument for multi-frequency dark matter hunting is clearly illustrated here, in the power of the method to demand that a proposed model is consistent with observations in all dark matter hosting structures, across the frequency spectrum. This is especially important since models that fit observations are usually derived within a single spectral region and for a given source or class of sources.

This chapter was published in the Journal of Cosmology and Astroparticle Physics. The candidate wrote the software, an extension of that used to produce the results in Chapter 3. The candidate also produced all of the data and figures, as well as composing the text, including the analysis and argument structure expressed therein (with editing and consultation with Professor Colafrancesco).

Prepared for submission to JCAP

A Multi-frequency analysis of dark matter annihilation interpretations of recent anti-particle and γ-ray excesses in cosmic structures.

G. Beck[a] **S. Colafrancesco**[a,1]

[a]School of Physics, University of the Witwatersrand, Private Bag 3, WITS-2050, Johannesburg, South Africa

E-mail: geoff.m.beck@gmail.com, sergio.colafrancesco@wits.ac.za

Abstract. The Fermi-LAT observation of a γ-ray excess from the galactic-centre, as well as the PAMELA, AMS, and AMS-2 anti-particle excesses, and the recent indications of a Fermi-LAT γ-ray excess in the Reticulum II dwarf galaxy have all been variously put forward as possible indirect signatures of supersymmetric neutralino dark matter. These are of particular interest as the neutralino annihilation models which fit these observations must have observable consequences across the frequency spectrum, from radio to γ-ray emission. Moreover, since dark matter is expected to be a major constituent of cosmic structure, these multi-frequency consequences should be common to such structures across the mass spectrum, from dwarf galaxies to galaxy clusters. Thus, in this work we make predictions for the multi-frequency spectra of three well-known sources dominated by dark matter on cluster, galaxy and dwarf galaxy scales, e.g. the Coma cluster, the galaxy M81, and the Draco dwarf galaxy, using models favoured by dark matter interpretations of the aforementioned observations. We pay special attention to the consequences for these models when their cross-sections are renormalised to reproduce the recent γ-ray excess observed in the Reticulum II dwarf galaxy, as well as using cross-sections from the Fermi-LAT dwarf galaxy limits, which throw a dark matter interpretation of this excess into doubt. We find that the multi-frequency data of Coma and Draco are in conflict with the dark matter interpretation of the AMS, PAMELA and Fermi positron excess. Additionally, models derived from Fermi-LAT galactic centre observations, and AMS-2 re-analysis, present similar but less extensive conflicts. Using the sensitivity projections for the Square Kilometre Array, the Cherenkov Telescope Array, as well as the ASTROGAM and ASTRO-H satellites, we determine the detection prospects for a subset of neutralino models that remain consistent with Planck cosmological constraints. Although the SKA has the greatest sensitivity to dark matter models, we demonstrate that ASTRO-H is well positioned to probe the inverse-Compton scattering emissions from neutralino annihilation and identify characteristics of the spectra which contain information about the neutralino mass and annihilation channel. This means that, given environments with favourable X-ray backgrounds, multi-frequency observation with the next generation of experiments will allow for unprecedented sensitivity to the neutralino parameter space as well as offsetting the individual weaknesses of each observation mode. Finally we show that all of the studied models can be better tested with the SKA phase 1.

[1]Corresponding author.

Contents

1 Introduction

The recent observed excesses of γ-ray emission from the galactic centre (GC) and anti-particle fluxes have been reported as possible signatures of dark matter (DM) annihilation [1–3].
In particular, the limits derived from both the Fermi-LAT [4] data on the galactic centre γ-ray excess emission and the PAMELA [5] anti-proton excess have been indicated to favour supersymmetric neutralino DM models with a particle mass of around 35 GeV and a thermal annihilation cross-section of $\langle\sigma V\rangle \sim 3 \times 10^{-26}$ cm^3 s^{-1} [3, 6]. However, this must be considered alongside the arguments in [1], where it is indicated that background uncertainties for the GC imply that a far larger range of models, with masses between 10 and 100 GeV and annihilation cross-sections between 10^{-27} cm^3 s^{-1} and 10^{-26} cm^3 s^{-1}, may be consistent with the observed GC γ-ray excess. A DM interpretation of these GC measurements has been, however, further disputed [7–11], where these authors argue that unresolved populations of millisecond or young pulsars are sufficient to explain the observations.
In addition, the results from the Alpha Magnetic Spectrometer (AMS) [12] cosmic-ray detector have been used to claim that a dark matter mass of $\mathcal{O}$(TeV) with annihilation cross-section $\langle\sigma V\rangle \sim 3 \times 10^{-24}$ cm^3 s^{-1} will consistently reproduce observed excesses via secondary positron production [2], although the authors note that an unresolved population of young pulsars could equally account for the observations. It has been, nonetheless, demonstrated [13] that the results of the Fermi-LAT dwarf galaxy observations [14] are largely incompatible with a DM explanation of the positron excess seen by AMS-2 for most annihilation channels, and masses below TeV scales. The aforementioned study [14], produced constraints ranging from $\langle\sigma V\rangle < 3 \times 10^{-26}$ cm^3 s^{-1} for $m_\chi < 10$ GeV to $\langle\sigma V\rangle < 2 \times 10^{-23}$ cm^3 s^{-1} for $m_\chi < 10^4$ GeV. These were further improved upon in the sub-TeV range [15] with constraints $\langle\sigma V\rangle < 2.2 \times 10^{-26}$ cm^3 s^{-1} for $m_\chi \leq 114$ GeV. A recent re-analysis of the AMS-2 electron/positron data [16] also indicates that it is compatible with DM models with cross-sections $\sim (2-8) \times 10^{-26}$ cm^3 s^{-1} and masses in the range $51 - 140$ GeV, depending on the annihilation channels studied. A very similar set of models are proposed to account for excess γ-ray emission observed by Fermi-LAT at the 2.3σ confidence level, reported in the dwarf galaxy Reticulum II [17]. In particular, these authors argued for a DM interpretation with mass $\sim$ 40 GeV and a cross-section $\langle\sigma V\rangle \sim 3 \times 10^{-26}$ cm^3 s^{-1}. We note that similar cross-sections are favoured based upon estimates of the astrophysical J-factor

for Reticulum II [18]. However, a dark matter interpretation of this excess appears to be at odds with the recent Fermi-LAT dwarf galaxy analysis, which includes Ret. II [19].

The release of the latest wave of Planck [20] cosmological results [21] also marks the current status on the hunt for neutralino DM from the cosmological side, i.e. using the CMB anisotropy power spectrum analysis. Planck substantially curtailed the allowed regions of the mass vs. cross-section parameter space all but eliminating the models compatible with the reported AMS-2/Fermi/PAMELA (hereafter AFP) positron excess [2], for cases where DM annihilation is efficient at depositing energy into the inter-galactic medium. Additionally, sub-TeV neutralinos with cross-section values above the relic density bound [22] were largely ruled out. The models favoured by the Fermi-LAT observations of the galactic centre (GC) [1, 3], however, still remain largely unaffected by the Planck result. In cases where DM annihilation has a low energy deposition efficiency below 0.3 the AFP region is also unaffected (as is true for the neutralino annihilation channels studied here).

In this observational framework, it is worthwhile to examine the future prospects of the remaining models allowed by PAMELA/Fermi/AMS-2 data as well as those allowed by the Fermi-LAT GC data in terms of a possible explanation due to DM annihilation.
The purpose of this paper is, in fact, to explore the consequences of the possibly DM-consistent signals from AMS-2, PAMELA and those of the Ret. II dwarf galaxy observed with Fermi-LAT on the multi-frequency expectations for well known DM-dominated halos like galaxy clusters, galaxies and dwarf galaxies. Along this line of exploration, we define a multi-frequency observational strategy for neutralino hunting with coming experiments in the hard X-ray/soft γ-ray band (like ASTRO-H and ASTROGAM), in the very high-E γ-ray band (like the Cherenkov Telescope Array, CTA), and in the very low-frequency radio range of the electromagnetic spectrum (like the Square Kilometre Array, SKA). This examination will take the form of specific predictions of multi-frequency observation for a key reason, i.e. to confirm the possibility that these potential DM signatures are consistent with a larger set of observations or constraints and then to produce a consistent search for DM signals over the whole accessible frequency range of the electromagnetic spectrum.

For the aims of this paper we will consider representative models from each of the aforementioned regions of the parameter space and we will study their multi-frequency predictions in the light of the achievable sensitivities of the upcoming instruments at radio (e.g., SKA), hard X-ray (e.g., ASTRO-H), soft γ-rays (e.g., ASTROMEV and ASTROGAM) and high-E γ-rays (e.g., CTA). We will confine our analysis to a few well known target environments for which data and theoretical modelling are rich and available. These are the Coma cluster, the M81 galaxy, and the Draco dwarf spheroidal galaxy. This will allow us to make concrete predictions of the prospective ability of multi-frequency observations to explore the neutralino parameter space in these environments, as well as to compare the studied models to current observational data. We will use the spectral energy distributions (SED) of these sources to demonstrate the synergy between radio-frequency and high-energy observations, which will serve to increase the robustness of any purported indirect neutralino signatures as well as allow for the characterization of the neutralino through these observations.
In particular, we will show that the ASTRO-H space mission has an observational window on a portion of the DM-induced inverse-Compton scattering (ICS) spectrum which is sensitive to the neutralino mass and to the annihilation channel. In the environments we have considered here, ASTRO-H cannot provide better constraints than Fermi-LAT, due to the existence of strong X-ray backgrounds in these sources. Therefore, it remains a subject of future work to locate more favourable environments for the hard X-ray study of DM models.
In the case of γ-rays we find that both CTA and ASTROGAM will be able to make little impact in the study of the GC and AFP models. In the case of ASTROGAM this is because the instrument is insufficiently sensitive to detect the soft γ-ray spectrum produced by neutralino annihilation within these models. For CTA we find that it is sensitive to energies largely above the typical mass-dependent cut-off for the studied models, even in the case of the AFP with TeV scale masses. In galaxy cluster environments, like Coma, the CTA may be capable of marginal detection for the $\tau^+\tau^-$ decay channel, which produces harder spectra, but this is complicated by the comparatively

low sensitivity of CTA in this spectral range. Despite these issues, CTA may still have a role in determining whether observed hard γ-ray emission is not inconsistent with the aforementioned dark matter models, as the discovery of anomalous hard γ-ray excesses would pose difficulties for these models if DM were found to be the most likely explanation.
For the radio frequency search we find that SKA is well situated to study a large swathe of the dark matter parameter space, providing optimistic constraints up to 2 orders of magnitude below the current Planck limits in the studied environments. This despite accounting for the need to differentiate between sub-dominant DM emissions and astrophysical backgrounds. In addition the SKA will have access to a frequency range highly sensitive to neutralino annihilation channel and mass.

In our study, we also draw on the recently reported Reticulum II dwarf galaxy γ-ray excess [17], and argue that its consequent radio and γ-ray emissions are incompatible with data available on the studied environments. Thus doubt is cast on the DM interpretation of the excess put forward in [17].

This paper is structured as follows: in Section 2 we detail models of multi-frequency emission from DM annihilation and in Section 3 we discuss the neutralino parameters corresponding to our representative models. In Section 4 we detail the relevant instrument parameters as well as the multi-frequency data used in this study. We provide multi-frequency predictions for the chosen environments in Section 5, as well as examining further detection prospects with SKA and ASTRO-H in Section 6, and discuss the results of our analysis in Section 7 before drawing conclusions in Section 8.

2 Models of Dark Matter Halos and Multi-frequency Emission

In modelling the halos of our structures of interest we refer to both a cuspy DM Navarro-Frenk-White (NFW) density profile [23] and a cored Burkert profile [24], that can bracket a larger range of possible phenomenological models.
The NFW profile is described by

$$\rho(r) = \frac{\rho_s}{\frac{r}{r_s}\left(1+\frac{r}{r_s}\right)^2} , \tag{2.1}$$

with r_s being the scale radius of the profile, and ρ_s is the halo characteristic density.
The Burkert profile is described by

$$\rho(r) = \frac{\rho_s}{\left(1+\frac{r}{r_s}\right)\left(1+\left(\frac{r}{r_s}\right)^2\right)} \tag{2.2}$$

We define the virial radius R_{vir}, of a halo with mass M_{vir}, as the radius within which the mean density of the halo is equal to the product of the collapse over-density Δ_c and the critical density ρ_c, where

$$\rho_c(z) = \frac{3H(z)^2}{8\pi G} , \tag{2.3}$$

$$M_{vir} = \frac{4}{3}\pi\Delta_c\rho_c R_{vir}^3 , \tag{2.4}$$

with $H(z)$ being the Hubble parameter. The density contrast parameter at collapse is given in a flat cosmology by the approximate expression [25]

$$\Delta_c \approx 18\pi^2 - 82x - 39x^2 , \tag{2.5}$$

with $x = 1.0 - \Omega_m(z)$, where $\Omega_m(z)$ is the matter density parameter at redshift z

$$\Omega_m(z) = \frac{1}{1+\frac{\Omega_\Lambda(0)}{\Omega_m(0)}(1+z)^{-3}} . \tag{2.6}$$

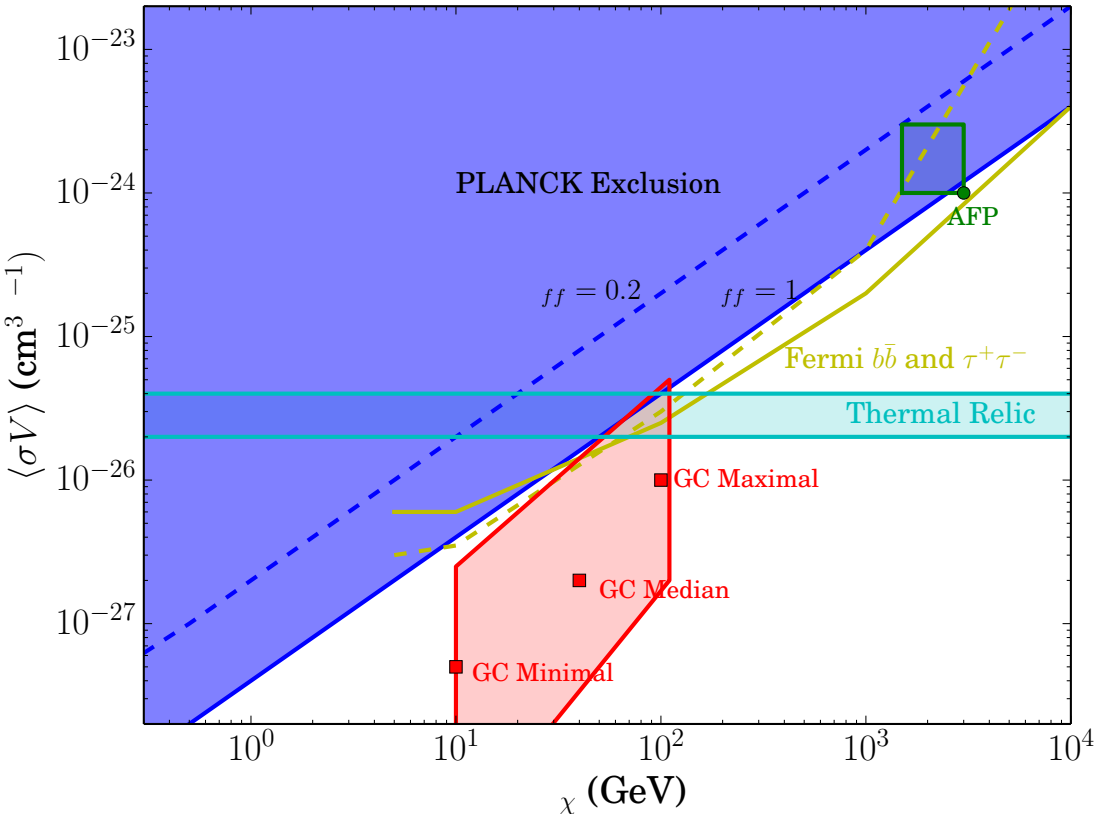

Figure 1. Currently Excluded regions and DM signal scenarios in the $\langle \sigma V \rangle$ vs. mass parameter space [21]. f_{eff} refers to the DM annihilation energy deposition efficiency factor (note that $b\bar{b}$ and $\tau^+\tau^-$ annihilation channels have $f_{eff} \sim 0.2 - 0.3$). The representative AMS-2/PAMELA/Fermi positron excess model is given by the AFP point, whereas the GC Maximal, Median, and Minimal are three representative models from the DM interpretation of the Fermi-LAT galactic centre observations. The Fermi-LAT dwarf-galaxy exclusion for $b\bar{b}$ and $\tau^+\tau^-$ (yellow, solid and dashed curves), as well as DM thermal relic abundance band on $\langle \sigma V \rangle$ are also shown for comparison.

The concentration parameter for the halo defines the scale radius as follows

$$r_s = \frac{R_{vir}}{c_{vir}} \, . \tag{2.7}$$

where c_{vir} is determined either for a particular environment or from the model for $c_{vir}(M_{vir})$ given in [26]. We note that this relation is true only for NFW and Einasto profiles, as it assumes that $r_s \equiv r_{-2}$, where r_{-2} is the radius at which the effective logarithmic slope of ρ is -2. In the case of a Burkert profile $r_s \approx \frac{R_{vir}}{1.52 c_{vir}}$. The dimensionless characteristic density contrast $\frac{\rho_s}{\rho_c}$ is defined to ensure the normalisation

$$\int_0^{R_{vir}} dr \, 4\pi r^2 \rho(r) = M_{vir} \, . \tag{2.8}$$

In the case of the NFW halo this can written [27] in terms of c_{vir} as

$$\frac{\rho_s(c_{vir})}{\rho_c} = \frac{\Delta_c}{3} \frac{c_{vir}^3}{\ln(1 + c_{vir}) - \frac{c_{vir}}{1+c_{vir}}} \, . \tag{2.9}$$

In addition to their global structure (NFW and/or Burkert density profile), DM halos are generally thought to have sub-structure in the form of sub-halos that are denser than their parent halo [28, 29] and can then boost the annihilation signals by a factor b, which has a radial dependence based on the assumption that sub-halo distribution follows a similar pattern to the DM density of the parent halo, with a longer scale radius [28, 29]. In order to derive the boost factor b we follow the prescription presented in [30], as this conforms to recent analysis performed on Fermi-LAT data. This sub-structure boost factor is defined as a luminosity increase caused by integrating over sub-halo luminosities determined by the virial mass and by halo concentration parameters found numerically according to the method discussed in [31]; we note that a similar method is provided in [32]. These methods place the boosting factor of cluster sized halos around $b \sim 30$, with the large dwarf-like galaxy Draco having $b \sim 3$. As noted in [30], these values of b are substantially smaller than those of many popular models quoted in the literature, and are based upon the c_{vir} - M_{vir} relations that agree well with N-body simulations [31]. We note, however, that this form of the boost factor has no explicit radial dependence $b(r) \equiv b$ as it represents a total contribution from all sub-halos. In addition to these considerations, a recent study [33] indicates that tidal-stripping of sub-halos has the potential to enhance the sub-halo luminosity boost by a factor of $2 - 3$. This indicates that there may be additional dynamical considerations that increase boost factors, strengthening the certainty of the conclusions reached here with more conservative boosts that do not account for dynamical effects.

An additional consideration in studying DM emissions is diffusion of the electrons/positrons which are responsible for synchrotron and inverse-Compton scattering emissions. In [34, 35], it was argued that energy-loss dominates particle diffusion in large-scale structures like large galaxies and galaxy clusters, while diffusion is significant in small-size galaxies like dwarf galaxies [35] particularly when observation is confined to a small angular segment of the target. For this reason we will consider the impact of spatial diffusion in dwarf galaxy environments according to the following method.

The equation for the equilibrium electron spectrum is found as follows:

$$\frac{\partial}{\partial t}\frac{dn_e}{dE} = \boldsymbol{\nabla}\left(D(E,\mathbf{r})\boldsymbol{\nabla}\frac{dn_e}{dE}\right) + \frac{\partial}{\partial E}\left(b(E,\mathbf{r})\frac{dn_e}{dE}\right) + Q_e(E,\mathbf{r}) \,, \tag{2.10}$$

where $\frac{dn_e}{dE}$ is the electron equilibrium spectrum, $D(E,\mathbf{r})$ and $b(E,\mathbf{r})$ are the spatial diffusion and energy-loss functions respectively (see [29, 34] and below), and $Q_e(E,\mathbf{r})$ is the electron source function. A detailed analysis of the solution to this equation in the case of electron production via neutralino annihilation can be found in [29].

In order to take into account the effects of the magnetic field and thermal plasma on electron diffusion we take average values for the field strength and thermal plasma density, being $\overline{B} \equiv \sqrt{\langle B(r)^2 \rangle}$ and $\overline{n} \equiv \langle n(r) \rangle$, respectively. We use $\langle\ \rangle$ to denote a spatial average over the target structure out to the virial radius. We then define the spatial diffusion coefficient as [36]

$$D(E) = \frac{1}{3} c r_L(E) \frac{\overline{B}^2}{\int_{k_L}^{\infty} dk P(k)} \,, \tag{2.11}$$

where r_L is the Larmour radius of a relativistic particle with energy E and charge e and $k_L = \frac{1}{r_L}$, and require that

$$\int_{k_0}^{\infty} dk P(k) = \overline{B}^2 \,. \tag{2.12}$$

This leads us to the result that

$$D(E) = D_0 d_0^{\frac{2}{3}} \left(\frac{\overline{B}}{1\mu\mathrm{G}}\right)^{-\frac{1}{3}} \left(\frac{E}{1\mathrm{GeV}}\right)^{\frac{1}{3}} \,, \tag{2.13}$$

where $D_0 = 3.1 \times 10^{28}$ cm^2 s^{-1}. It is worth noting that the diffusion coefficient is assumed to be lacking radial dependence. While it is possible to implement diffusion without this simplification,

we present results here under the assumption we can substitute the averaged value of the magnetic field in the diffusion coefficient as it is evident that the weak radial dependence of the magnetic fields and the weak dependence of the diffusion coefficient on the field strength imply that our approximation is not unwarranted. For this analysis we will assume the minimum scale on which a dwarf galaxy magnetic field is homogeneous is given by $d_0 \sim 100$ pc.

Finally, the energy-loss function takes the form,

$$\begin{aligned} b(E) =& b_{IC} E^2 (1+z)^4 + b_{sync} E^2 \overline{B}^2 \\ &+ b_{Coul} \overline{n} (1+z)^3 \left(1 + \frac{1}{75} \log\left(\frac{\gamma}{\overline{n}(1+z)^3}\right)\right) \\ &+ b_{brem} \overline{n} (1+z)^3 \left(\log\left(\frac{\gamma}{\overline{n}(1+z)^3}\right) + 0.36\right) \end{aligned} \tag{2.14}$$

where $\overline{n}$ is given in cm^{-3} and b_{IC}, b_{synch}, b_{col}, and b_{brem} are the Inverse Compton, synchrotron, Coulomb and Bremsstrahlung energy loss factors, taken to be 0.25, 0.0254, 6.13, and 1.51 respectively in units of 10^{-16} GeV s^{-1}. Here E is the energy in GeV and the B-field is in μG.

Three particular dark matter halos with very different mass will be of interest in our study: that of the Coma cluster, the M81 galaxy, and the Draco dwarf galaxy. We also considered the case of the Reticulum II dwarf galaxy for its recent interest as a possible source of γ-ray emission. For the Coma cluster DM halo we consider the model described in [29]. The virial mass of this cluster is taken to be $M_{vir} = 1.33 \times 10^{15}$ M$_\odot$, with virial concentration $c_{vir} = 10$, at the redshift $z = 0.0231$. The thermal electron density of the ICM in Coma $n(r)$ is given by

$$n_e(r) = n_0 \left(1 + \left[\frac{r}{r_s}\right]^2\right)^{-q_e} , \tag{2.15}$$

with r_s being a characteristic radius (taken equal to the halo scale radius), $n_0 = 3.44 \times 10^{-3}$ cm^{-3} and $q_e = 1.125$ [37]. The magnetic field in Coma is assumed to follow the one derived by [38] having a radial profile given by

$$B(r) = B_0 \left(\frac{n_e(r)}{n_0}\right)^{q_b} , \tag{2.16}$$

where r is the distance from the cluster centre, $B_0 = 4.7$ μG, and $q_b = 0.5$. Additionally, this magnetic field has a Kolmogorov turbulence power spectrum with a minimal coherence length of ≈ 2 kpc.

In M81 we use of the following magnetic field model:.

$$B(r) = B_0 \left(1 + \left(\frac{r}{r_b}\right)^2\right)^{-q_b q_e} , \tag{2.17}$$

here, $r_b = 13$ kpc, $q_b = 0.5$, $q_e = 1.125$, and $B_0 = 7.5$ μG [39]. In the case of the thermal electron density we use a central value of $n_0 = 0.03$ cm^{-3} [39] with a similar radial profile to the one used for Coma but with scale radius of 3 kpc [39], and the DM halo of this galaxy is taken to have a virial mass $M_{vir} = 1.4 \times 10^{11}$ M$_\odot$ at a distance of 3.6 Mpc [40].

For the case of the Draco dwarf galaxy we take the virial mass to be $M_{vir} = 7 \times 10^7$ M$_\odot$ at a distance of ~ 80 kpc [41], with a constant magnetic field model with magnitude $B(r) = B_0 = 1$ μG, and a thermal electron density $n_e(r) = n_0 = 10^{-6}$ cm^{-3}, both in accordance with [35].

Finally, we make use of a conservative model for the Reticulum II dwarf galaxy, using a distance of ~ 30 kpc [17], and assuming a J-factor from [18] with a constant magnetic field model with magnitude $B(r) = B_0 = 1$ μG, and a thermal electron density $n_e(r) = n_0 = 10^{-6}$ cm^{-3}.

The structure parameters on the three target environments are reported in Table 2.

As a supplementary summary of pertinent halo parameters, we calculate the astrophysical "J-factor" for each halo:

$$J = \int_{\Delta\Omega} \int_l \rho^2_{DM}(\mathbf{r}) dl' d\Omega' , \tag{2.18}$$

Quantity	Draco	M81	Coma
M_{vir} ($M_\odot$)	7×10^7	1.4×10^{11}	1.33×10^{15}
boost-factor	3.43	10.1	35.2
B_0 (μG)	1.0	7.5	4.7
$\langle B \rangle$ (μG)	1.0	1.9	1.2
n_0 (cm^{-3})	10^{-6}	0.03	3.44×10^{-3}
$\langle n_0 \rangle$ (cm^{-3})	10^{-6}	8.8×10^{-4}	4.8×10^{-4}

Table 1. Summary of the relevant halo parameters.

where the integral is performed over the line of sight l and the solid angle $\Delta\Omega$. For reference we present the J-factor calculated when integrating over the solid angle of the entire halo virial radius given in Table 2, along with the Ret. II J from [18].

Halo	NFW	Burkert
Draco	1.1×10^{17}	3.1×10^{16}
Coma	1.0×10^{18}	2.8×10^{17}
M81	3.0×10^{16}	1.0×10^{16}
Ret. II	2.0×10^{19}	2.0×10^{19}

Table 2. J-factors for each studied environment and for Reticulum II. These include sub-structure boosting factors (where appropriate), and are given in units of GeV^2 cm^{-5}.

For the general description of DM halos and synchrotron emissions we follow the approach described in [34] and in the references contained therein, while for the high-energy emission properties of DM annihilation we follow the approach of [29]. Here in the following we report the basic formulae we will use for the multi-frequency spectral energy distribution produced by DM annihilation.

The average power of the synchrotron radiation at observed frequency ν emitted by an electron with energy E in a magnetic field with amplitude B is given by [42]

$$P_{synch}(\nu, E, r, z) = \int_0^\pi d\theta \, \frac{\sin\theta^2}{2} 2\pi\sqrt{3} r_e m_e c \nu_g F_{synch}\left(\frac{\kappa}{\sin\theta}\right) \, , \tag{2.19}$$

where m_e is the electron mass, $\nu_g = \frac{eB}{2\pi m_e c}$ is the non-relativistic gyro-frequency, $r_e = \frac{e^2}{m_e c^2}$ is the classical electron radius, and the quantities κ and F_{synch} are defined

$$\kappa = \frac{2\nu(1+z)}{3\nu_g \gamma^2}\left[1 + \left(\frac{\gamma\nu_p}{\nu(1+z)}\right)^2\right]^{\frac{3}{2}} \, , \tag{2.20}$$

with $\nu_p \propto \sqrt{n_e}$, and

$$F_{synch}(x) = x\int_x^\infty dy \, K_{5/3}(y) \simeq 1.25 x^{\frac{1}{3}} \mathrm{e}^{-x}\left(648 + x^2\right)^{\frac{1}{12}} \, . \tag{2.21}$$

and the average power of inverse-Compton Scattering (ICS) is given by

$$P_{IC}(\nu, E, z) = cE_\gamma(z)\int d\epsilon \, n(\epsilon)\sigma(E, \epsilon, E_\gamma(z)) \, , \tag{2.22}$$

where $E_\gamma(z) = h\nu(1+z)$ is the emitted photon energy, $n(\epsilon)$ is the black-body spectrum of the CMB photons, and E is the electron energy. Here we consider mainly the ICS on CMB photons because this is the largest radiation background available in the universe.
Additionally,

$$\sigma(E, \epsilon, E_\gamma) = \frac{3\sigma_T}{4\epsilon\gamma^2} G(q, \Gamma_e) \, , \tag{2.23}$$

where σ_T is the Thompson cross-section, γ is the electron Lorentz factor, and

$$G(q,\Gamma_e) = 2q\ln q + (1+2q)(1-q) + \frac{(\Gamma_e q)^2(1-q)}{2(1+\Gamma_e q)} \ , \tag{2.24}$$

with

$$\begin{aligned} q &= \frac{E_\gamma}{\Gamma_e(\gamma m_e c^2 + E_\gamma)} \ , \\ \Gamma_e &= \frac{4\epsilon\gamma}{m_e c^2} \end{aligned} \tag{2.25}$$

Bremstrahlung emission of DM-produced secondary electrons from the intra-cluster medium (ICM) and from the inter-stellar medium (ISM) has an average power

$$P_B(E_\gamma, E, r) = cE_\gamma(z)\sum_j n_j(r)\sigma_B(E_\gamma, E) \ , \tag{2.26}$$

where $n_j(r)$ is the density of intra-cluster species j, and

$$\sigma_B(E_\gamma, E) = \frac{3\alpha\sigma_T}{8\pi E_\gamma}\left[\left(1+\left(1-\frac{E_\gamma}{E}\right)^2\right)\phi_1 - \frac{2}{3}\left(1-\frac{E_\gamma}{E}\right)\phi_2\right] \ , \tag{2.27}$$

with ϕ_1 and ϕ_2 being energy dependent factors determined by the species j(see [42]).

For the DM-induced γ-ray production through $\pi^0 \to \gamma\gamma$ decay the flux calculation is somewhat simplified

$$S_\gamma(\nu, z) = \int_0^r d^3r' \, \frac{Q_\gamma(\nu, z, r)}{4\pi D_L^2} \ , \tag{2.28}$$

with $Q_\gamma(\nu, z, r)$ being the source function for neutral pion decay within the given DM halo.

The local emissivity for the $i-th$ emission mechanism (Synchrotron, ICS, Bremstrahlung) can then be found as a function of the electron and positron equilibrium distributions as well as the associated power

$$j_i(\nu, r, z) = \int_{m_e}^{M_\chi} dE \left(\frac{dn_{e^-}}{dE} + \frac{dn_{e^+}}{dE}\right) P_i(\nu, E, r, z) \ . \tag{2.29}$$

The flux density spectrum within a radius r is then written as

$$S_i(\nu, z) = \int_0^r d^3r' \, \frac{j_i(\nu, r', z)}{4\pi D_L^2} \ , \tag{2.30}$$

where D_L is the luminosity distance to the halo.

3 Neutralino Models

In this paper our neutralino DM particle is drawn from the minimal supersymmetric extension to the standard model, following the DarkSUSY package [43]. The source function for the production of a stable particle i, produced promptly by neutralino annihilation or ancillary processes is given by

$$Q_i(r, E) = \langle\sigma V\rangle \sum_f \frac{dN_i^f}{dE} B_f \mathcal{N}_\chi(r) \ , \tag{3.1}$$

where $\langle\sigma V\rangle$ is the non-relativistic velocity-averaged neutralino annihilation cross-section at 0 K, the index f labels kinematically allowed annihilation final states with branching ratios B_f and spectra $\frac{dN_i^f}{dE}$, and $\mathcal{N}_\chi(r)$ is the neutralino pair density at a given halo radius r. In keeping with standard procedure in indirect detection studies we will focus on one annihilation channel at a

time and assume a branching ratio of 1 for the channel of interest. We will examine the $b\bar{b}$ and $\tau^+\tau^-$ channels. The factor $\frac{dN_i^f}{dE}$ is determined using the PYTHIA Monte-Carlo routines in DarkSUSY [44].

Our study examines four neutralino mass models, each of which is then further differentiated by three cross-section values: a best-fit cross-section, the one derived from Reticulum II γ-ray excess (as detailed below), and the one derived from Fermi-LAT dwarf studies [19]. The first model is taken to represent the neutralino model interpretation of the PAMELA/AMS-2/Fermi (AFP) positron excess, which is still accommodated by the Planck results regardless of DM annihilation energy deposition efficiency factor, and has $M_\chi \sim 3$ TeV and best-fit cross-section $\langle\sigma V\rangle \sim 10^{-24}$ cm^3 s^{-1} (see Fig.1). The other three models are representative of the minimal, median, and maximal cases of the neutralino model interpretation of the Fermi-LAT galactic centre (GC) observations: these have values $M_\chi \sim 10$ GeV, best-fit $\langle\sigma V\rangle \sim 10^{-28}$ cm^3 s^{-1}, $M_\chi \sim 40$ GeV, best-fit $\langle\sigma V\rangle \sim 10^{-27}$ cm^3 s^{-1}, and $M_\chi \sim 100$ GeV, best-fit $\langle\sigma V\rangle \sim 10^{-26}$ cm^3 s^{-1}, respectively (see Fig.1). The choice of the GC models is predicated on covering the range of the parameter space favoured by the analysis of the Fermi-LAT data [1, 3].

Each of these GC models will be tested for both $b\bar{b}$ and $\tau^+\tau^-$ channels with the same cross-section used in both cases. However, we note that the best-fit cross-sections for these two channels will typically differ for any given neutralino mass. In the case of GC excess models [1] the $b\bar{b}$ best-fit model is $\langle\sigma V\rangle \sim 10^{-26}$ cm^3 s-1 for $m_\chi \sim 50$ GeV. Whereas for $\tau^+\tau^-$ it is $\langle\sigma V\rangle \sim 3 \times 10^{-27}$ cm^3 s-1 for $m_\chi \sim 10$ GeV. Thus GC region, and its representative points, displayed in Fig. 1 attempts to encompass the whole range of models favoured by the GC excess for $b\bar{b}$ and $\tau^+\tau^-$ channels.

In order to determine the annihilation cross-section required to match DM emissions to the Reticulum II γ-ray signal we use the reported 2.3σ Fermi-LAT excess and calculate the relative value of the annihilation cross-section $\langle\sigma V\rangle$ by normalising the maximum γ-ray flux, for a given neutralino mass and from the Reticulum II halo model, to match the 2.3σ Fermi-LAT excess at the appropriate observed energy (these values are determined separately for $b\bar{b}$ and $\tau^+\tau^-$ channels).

4 Multi-frequency Data and Instruments

Our choice of particular DM dominated cosmic structures is justified by two considerations, the first being the availability of data/limits for optimal comparison to predictions. The second is that emissions of any structure expected to host DM should be compatible with models derived from DM interpretations of observed excesses in other environments. Moreover, we choose environments that are not ideal detection test-beds in order to strengthen our conclusions, as if a neutralino model fails to accommodate existing data from non-ideal detection environments then this serves as stronger evidence against it.

For the Coma cluster we use the diffuse radio data set from [45], total X-ray flux data [46] from the ASCA experiment [47] in the 2-10 keV band, as well as from INTEGRAL [48] in the 20-50 keV band [49]. These X-ray sources were selected from the NED SED builder [50], under the requirement they were broad-band measurements yielding a total flux integrated over a map of the target. In addition to this, we use direct Fermi-LAT limits on Coma γ-ray emission [51], and those derived from stacked cluster analysis of Fermi-LAT data [52]. These are compared to the neutralino-induced emission over the entire virial radius, due to the extended nature of these limits. The neutralino predictions can be tested against this data, as if they exceed either the measured points or limits then the model is unviable within the Coma environment.

As the radio data for Coma prove highly important in this work, we must note that there are difficulties in the precise measurement of a diffuse radio flux from an extended target like Coma. This is because such diffuse emission can only be found by subtracting out identified point sources and known extended radio sources (like e.g. radio-galaxies). Thus the accuracy of such a flux determination is dependent on the ability of the instrument to resolve point and extended astrophysical sources within the cluster environment.

For the M81 galaxy we make use of an SED composed of data points, from broad-band measurements only, where the flux is integrated over a map of M81 [53–68]. These points were selected by hand using the ASDC and NED SED builders [50, 69], on the criterion that they are integrated over a map and not limited to an aperture area. The chosen points span the radio and far infra-red spectrum, with a slight incursion into soft X-rays [70, 71] from Chandra [72, 73] and EXOSAT [74], respectively.

For the Draco dwarf we make use of the VLA radio limit [75], integrated over a $4' \times 4'$ area around the centre of the galaxy (comparing it to DM synchrotron emission within the same region). In addition we use Fermi-LAT upper limits from dwarf observations on Draco [14] compared to the flux integrated over the virial radius of Draco. Given the appropriate area of flux integration, it is clear that neutralino emission predictions cannot exceed these upper limits in Draco.

We note that the ASTRO-H telescope has a $34' \times 34'$ field of view in the soft X-ray band while in harder X-rays it is limited to $9' \times 9'$ [76]. We will take this into account by limiting the area of flux integration appropriately when comparing the ASTRO-H sensitivities to the model predictions. The size of the soft X-ray FOV, when compared to DM-induced surface brightness profiles, means we will use the virial radius in this spectral region (as the FOV captures upwards of 95% of the flux). This consideration is unnecessary for SKA which has a field of view of at least one square degree.

In all of the following comparisons we will show point-source sensitivities for the considered instruments (we note that extended source sensitivities are not officially available for the SKA or ASTRO-H, so we use the point-source information as a benchmark), typically at 1000 hours of observation, but for Fermi-LAT we use the 10 year sensitivity for P8R2_SOURCE_V6 [77]. For comparisons with SKA and ASTRO-H in M81 and Coma we will be accounting for observed backgrounds, thus we are comparing SKA sensitivity to DM-induced fluxes against these backgrounds. This approach is in accordance with the fact that NFW halos are point sources within $1'$ (resolution of ASTRO-H is around $1.5'$ [76]), for Burkert halos there will be some extension of the source but ASTRO-H/SKA extended sensitivities are unavailable as yet and CTA is largely affected only in the upper regions of its observation window [78] (which are not reached with the studied models).

5 Multi-frequency analysis

In this section we present the results of our multi-frequency analysis, discussing separately each one of the cosmic environments we consider.

5.1 Coma Cluster

For the Coma cluster we begin by presenting the upper panel of Figure 2, which shows the multi-frequency spectra for the considered neutralino models. It is clear that the shape of the observed synchrotron spectrum in Coma is incompatible with the predictions of the AFP model because these exceed the Coma radio halo flux and also show a spectral flattening for $\nu > 1$ GHz which is not observed.

The maximal and median GC models ($\tau^+\tau^-$ only for median GC) also predict unobserved flux excesses as well as spectral flattening for $\nu > 1$ GHz. The aforementioned models also have issues with their amplitude exceeding the observed spectrum. However, we find that the synchrotron flux amplitude and slope are not an issue for the minimal GC model. Only the GC minimal model with $b\bar{b}$ is in tension with the Fermi-LAT stacked cluster limit.

In the lower panel of Fig. 2 we see that only the AFP $b\bar{b}$ model conflicts with the radio data when a Burkert profile is used. However, this halo profile does lead to sub-dominant DM emissions. In general the Burkert profile will be seen to reduce the flux by more than an order of magnitude at all frequencies.

In terms of differentiating between neutralino spectra, substantial differences are apparent between the spectral slopes of different annihilation channels in both the radio (SKA) and X-ray (ASTRO-H) observation windows for all of the models. Notably the $\tau^+\tau^-$ spectra are of lower

Halo	10 GeV	40 GeV	100 GeV	3 TeV
Coma	-	$\sim 3.5\sigma$	$\sim 3.5\sigma$	$\sim 4\sigma$
M81	-	-	-	-

Table 3. Magnetic field deviations needed to keep neutralino $b\bar{b}$ models with given masses, and Fermi-LAT dwarf cross-sections, consistent with available synchrotron data.

amplitude at low frequencies (with respect to form of emission) and cross over the $b\bar{b}$ spectrum at higher frequencies, resulting in a harder spectrum. This is true for all the models and all forms of emission, and this kind of spectral crossing also extends to the effect of variations in the mass of the neutralino. At low frequencies the spectra of heavy neutralino models fall below their lighter counterparts, which is in complement to the hardening of the spectrum for heavy neutralinos. It is notable that such regions of spectral difference between the GC models fall within the observational window of ASTRO-H (middle figure panels), whether this is observable will be discussed in Section 6. It seems, therefore, that ASTRO-H will be well positioned to discriminate between the various neutralino compositions.

We note that the ASTRO-H observation window also encompasses the region of the ICS spectrum that shows significant differences between various choices of neutralino mass and annihilation channel within the Coma cluster. Importantly, CTA seems only to be able to observe heavier DM models (like AFP) in this environment, with the GC masses falling below the region of CTA sensitivity. In the case of ASTROGAM it is evident that it is insufficiently sensitive to observe emissions from the studied DM models, even in the case of a large DM halo like the Coma cluster.

In Figure 3 we display the predictions of assuming the annihilation cross-section necessary to reproduce the Reticulum II γ-ray excess [17]. This prediction was derived by assuming a J-factor for Ret. II from [18] (see Table 2). and using this to determine a γ-ray SED. Then we took a 2.3σ Fermi-LAT excess reported by [17] and normalised our model of Reticulum II so that it is the maximal γ-ray flux matching the Fermi-LAT excess. The cross-sections thus derived are listed in order of model mass as: 1.9×10^{-26} cm^3 s^{-1}, 4.8×10^{-26} cm^3 s^{-1}, 1.4×10^{-25} cm^3 s^{-1}, and 1.0×10^{-22} cm^3 s^{-1}. When the model is applied to other DM halos, we see that in the radio and γ-ray frequency ranges the predicted fluxes for this models greatly exceed the known measurements/limits for the Coma cluster. It is evident then that the consequences of a DM interpretation of the excess γ-rays in the Reticulum II dwarf galaxy are unacceptable for the considered neutralino mass range (10-3000 GeV) in the case of Coma. We note that the use of the Burkert profile in the lower panel only removes conflicts between the 10 GeV mass and radio data, while γ-ray incompatibility remains for all models. In conclusion, the available SED of Coma discards the DM interpretation of the Reticulum II γ-ray excess in the case that the same DM model is responsible for the formation of the halo of dwarf galaxies and galaxy clusters.

Since the previous results have been obtained with a NFW profile and with the relative boost factor (as described in Sect. 2), we show in Figure 4 a conservative version of Fig. 3, which considers the same set of neutralino masses but with the cross-sections derived by the Fermi-LAT collaboration from dwarf galaxy observations, including Reticulum II [19]. We can see that many of the features we highlight for Fig. 3 remain in evidence, and particularly the predictions being in excess in the synchrotron spectrum and in violating both Fermi-LAT Coma and stacked cluster limits in γ-rays. The lower panel shows that the Burkert profile has only the 100 GeV $\tau^+\tau^-$ and 3 TeV $b\bar{b}$ in conflict with the radio data. However, 10 GeV $b\bar{b}$ is in tension with the Fermi-LAT stacked cluster limit in this case.

We also attempted this exercise by assuming a virial mass of 10^6 M$_\odot$ and a distance of 30 kpc for Ret. II, in this case the required cross-sections are far larger and the resulting excesses in Coma are thus greater.

Given the sensitivity of synchrotron radiation to magnetic field strength we show in Fig. 5 the factor by which the magnetic field strength must be multiplied in order to return the predictions in Fig. 4 (for the $b\bar{b}$ cases) to consistency with available radio data; this is also summarised in

Table 5.1. We find that the 4σ deviation that would be required for the synchrotron spectrum to be accommodated by the data, for all but the 10 GeV neutralino mass model, demonstrate that the inconsistencies we previously highlight cannot be solely blamed upon magnetic field values. In fact, a value as low as ≈ 1 μG for Coma is in sharp contrast with the results of Bonafede et al. [38] indicating $B \approx 5$ μG. Therefore, we conclude that even the cross-sections derived by the Fermi-LAT Collaboration for dwarf galaxies cannot support an interpretation of a γ-ray excess being the result of neutralino DM annihilation.
We note that the Fermi-LAT cross-sections are similar to the value reported in [17] for neutralinos around ≈ 40 GeV, this increases the robustness of our results as the highlighted conflicts with available data will not be exorcised by such a sub-order-of-magnitude cross-section reduction.
Finally, we note that recent Fermi-LAT analysis for Coma [83] produces more stringent limits upon the γ-ray flux and thus will strengthen the results here, as well as exclude any currently marginal cases.

5.2 M81 Galaxy

Figure 6 shows the spectrum expected in the given DM models for the M81 galaxy environment. CTA observation of the predicted DM models are less likely from this source, even with the super-TeV masses, and its study is complicated by the extreme dominance of its active nucleus over a broad range of frequencies. As in the Coma environment, the ASTRO-H window covers several ICS spectral crossings between differing neutralino masses and annihilation channels. In the radio frequency range it is notable that, regardless of halo profile, there are no conflicts between any of the models and the data.

Figure 7 shows the consequences of assuming the Reticulum II DM annihilation cross-section. All of the neutralino masses are incompatible with the available radio measurements. The DM models would be observable by Fermi-LAT for ~ 10 year observations at $E > 0.04$ GeV and the 3 TeV mass neutralino should produce a sufficiently high flux for CTA observation with ~ 1000 hours exposure. Despite the large flux produced by the active nucleus of M81, the Reticulum II excess annihilation cross-section proves to be incompatible with existing measurements of M81. When the Burkert profile is used in Figure 7 we see that 3 TeV models as well as $\tau^+\tau^-$ with 100 and 40 GeV masses remain in tension with the data. The case of particular relevance is the best-fit Reticulum II model of $m_\chi \sim 40$ GeV and $\langle \sigma V \rangle \sim 3 \times 10^{-26}$ cm^3 s^{-1}, which is excluded by the data for an NFW profile and is marginal with $\tau^+\tau^-$ annihilation and a Burkert halo.

In Figure 8 we show the consequences of the cross-sections derived from Fermi-LAT dwarf studies including Reticulum II. In the case there are once again no conflicts between the data and the models.

5.3 Draco dwarf galaxy

Figure 9 shows the spectrum of the considered DM models in the Draco dwarf galaxy environment. In the radio range we find that there is no tension with the VLA limit on Draco [75] (while integrating the flux over an appropriate $4' \times 4'$ area at the centre of Draco) but stronger magnetic field/diffusion characterisation would be needed to robustly support this conclusion. Additionally there are no conflicts with the Fermi-LAT upper limits. These results holds with both NFW and Burkert halo profiles. We note that this work does not account for possible diffuse foreground emissions [84], which may substantially impact upon Draco observations.

Once again, for each form of emission, at low frequencies the $\tau^+\tau^-$ spectrum lies below the $b\bar{b}$ one but then it crosses over at high frequencies. The exact frequency at which the cross-over occurs is dependent on the neutralino mass and is trivially red-shifted as discussed in [34] and shows a mild sensitivity to the conditions of the halo in the form of being shifted to higher frequencies for larger magnetic fields (synchrotron only) and ICM densities (as can be seen from comparison of Figs. 2,6, and 9). The fact that this cross-over behaviour appears in each region of the spectrum, although the ICS cross-over can be hidden by the γ-ray spectrum, suggests that such features should be attributed to the underlying differences in the particle distributions produced by these neutralino annihilation channels, and thus the shape of the emission spectrum constitutes

a signature of the dominant channel. All of the models are compatible with the Fermi-LAT dwarf upper bounds, which conforms to the slope and shape of the high-energy spectrum. Although more sensitive measurements will be necessary to constrain the γ-ray spectrum more effectively.

The ICS spectra are significantly different within the energy window of ASTRO-H, similar to the environment of Coma, with the crossing of spectra due to differing annihilation channels being present for the GC models. Where the spectra for different models/channels have similar amplitudes, they differ substantially in slope over the observational region of ASTRO-H, greatly increasing the possibility of identifying the neutralino mass and annihilation channel from the nature of an observed signal.

Figure 10 shows the consequences of assuming the Reticulum II annihilation cross-section. All of the models explored here are incompatible with the Fermi-LAT γ-ray limits on Draco, while all but the 10 GeV cases and the 40 GeV $b\bar{b}$ models are incompatible with the VLA limit on Draco. This is slightly affected by the use of the Burkert profile in the lower panels, with only no models in tension with the VLA limit, but γ-ray limits still exclude all models. Thus, the Reticulum II DM interpretation seems untenable for all the studied masses and this is not subject to the halo profile uncertainty between NFW and Burkert.

Figure 11 displays the effects of assuming the Fermi-LAT annihilation cross-section for dwarf spheroidal galaxies. Once again the effects of diffusion ensure that no models are in conflict with the VLA limit. In the case without spatial diffusion, the 3 TeV and $\tau^+\tau^-$ 100 GeV models are in tension with the VLA radio limit with an NFW profile (the conflict is removed by the Burkert profile in this case). Additionally, there is no tension with the Fermi-LAT limits as one should expect. The use of the Burkert profile (see lower panel of this figure) does not affect this. For neutralino masses above 100 GeV without spatial diffusion, a magnetic field reduction of at most $\sim 40\%$ would be necessary for consistency of the featured models with the VLA data, as can be seen in Fig. 5 for an NFW profile. Thus uncertainty is provided by both the diffusion/magnetic-field and the DM halo profile, the latter is particularly important in Draco given the compatibility of many dwarf halos with cored distributions [85, 86]. Therefore we take the Draco results to provide some support for the conclusion that only cross-sections below the Fermi-LAT limit for dwarf galaxies could justify a DM interpretation of the Reticulum II γ-ray excess. The radio frequency uncertainty emanates mainly from the magnetic field and diffusion characteristics.

5.4 Dark matter constraints

It is worth noting that the synchrotron portions of the spectra displayed in Figs. 2,6, and 9 are sensitive to the assumed magnetic field strength, as seen in Eq. (2.19). This is significant because it will be necessary to obtain accurate estimates of the magnetic fields within cosmic structures in order to properly constrain the synchrotron spectra resulting from DM annihilation. In this regard, the SKA is expected to play a prominent role, as discussed in [87]. This is because, for arcminute resolution at flux levels of ~ 1 μJy, it has been shown [88] that polarisation stacking calculations indicate an expected polarised source density of the order of ≈ 1300 sources per square degree, with the analysis of [89] indicating that this involves an overall uncertainty of $\approx 50\%$. This means that already the SKA-1 will be able to derive stringent constraints for cosmic magnetic fields on the required scale with a sufficiently large source count for spatial profiling.

In Figures 12 and 15, we derive the cross-section limits that can be placed on the parameter space using the Coma radio data, as well as the M81 spectrum. In the Coma cluster case (Fig. 12), the data provides 3σ constraints that are about an order of magnitude stronger than the Fermi-LAT dwarf limits at all masses above 10 GeV, where Fermi-LAT is similar. We note that the strength of these limits is significantly affected by the use of the Burkert profile in the lower panel, weakening constraints by roughly an order of magnitude at all masses.

It is instructive to compare these derived limits to previous works such as [90, 91], which derive limits from radio observation of the galactic centre. We see that our Coma limits produce similar constraints to [90] around 100 GeV ($\langle\sigma V\rangle \lesssim 10^{-26}$ cm^3 s^{-1} for $b\bar{b}$ with NFW profile) but improve over [90] substantially towards 1 TeV ($\langle\sigma V\rangle \lesssim 10^{-25}$ cm^3 s^{-1} for $b\bar{b}$ with NFW profile). In the case of [91] we find that their best-case magnetic field results for 10 GeV, $\langle\sigma V\rangle \lesssim 10^{-26}$

cm^3 s^{-1} for $b\bar{b}$ with NFW profile, are somewhat weaker than those derived here, in addition to this they scale more severely with m_χ, reaching $\langle\sigma V\rangle \lesssim 10^{-23}$ cm^3 s^{-1} for $b\bar{b}$ with NFW profile by masses of 1 TeV.

We note that the Coma radio flux we obtained here differs from previous derivations of DM-induced radio emission in this cluster, such as in [29]. In order to understand this difference, we show in Figure 13 the two calculations, and we see a two order-of-magnitude difference in flux between our model and that performed using the model from the aforementioned work [29]. In this figure we use the best-fit cross-section derived in [29] to illustrate that using our approach we can reproduce the results of [29] when we employ the same halo model. Due to the magnitude of the difference between the fluxes obtained in these two cases, the differences in the underlying models of Coma deserve to be remarked upon.

In the upper-panel of Figure 14 we show a comparison of c_{vir} and sub-structure boost factor values between our work and the aforementioned earlier study of Coma. As previously stated, we take our c_{vir} value for Coma from the fits done in [29]. Therefore, in this regard the two calculations do not differ; however, this c_{vir} calculational method is of interest for its contribution to the sub-structure boosting factor (as it will be used to find c_{vir} for sub-halos). It is important to note that when we determine the boosting factor for a halo with Coma-like mass using the model from [30] we obtain a boost factor that is twice as large as that derived from the sub-structure calculations used in [29] (see Table 4). However, the differences in these parameters are clearly insufficient to explain the difference between the radio fluxes shown in Fig. 13. In the lower panel of Fig. 14 we also note that the DM halo density profiles are similar: we use an NFW profile while [29] use an NFW-like Einasto profile with $\alpha = 0.17$. However, we point out that the magnetic field model from [29] peaks well outside the scale-radius of Coma (~ 0.29 Mpc), while the one we employ in this paper following a later analysis from [38] peaks at the cluster centre. It is clear from Figure 14 that DM density has dropped by two orders of magnitude before we reach the peak of the magnetic field model used in [29]. This effect is able to reduce substantially the synchrotron flux generated by annihilations (which is proportional to ρ^2) in the dense central region of the cluster, in comparison to our model, and accounts for the remaining difference between the radio flux density curves displayed in Fig. 13.

Therefore, we conclude that the main difference between our radio flux calculations in Coma and those of [29] is due to the spatial profile of the magnetic field within the inner parts of the halo, with the boosting factor only accounting for a factor of 2 of the difference.

We also note that the boosting factor we employ, following [30], depends only the DM sub-halo mass distribution within the parent halo and it is therefore a DM pair-annihilation boost; as such it does not account for the spatial variation of the magnetic field which would affect how much synchrotron radio flux is produced by sub-halos. In other words, by applying this method one assumes that all types of DM-induced e.m. emission will benefit similarly from sub-structure boosting. In the specific case of DM-induced radio synchrotron emission, since sub-halos are distributed radially within their parent halo, they will not all encounter the same value of the magnetic field strength and thus the secondary electrons produced in DM annihilations within sub-halos at different radii will provide differing boosts to the total synchrotron flux. Taking this into account would then have the effect of reducing the total synchrotron flux produced by sub-halos [92]. However, it was also shown in [29] that, if the sub-halos distributions follow a similar profile to the DM density profile of their parent halo, most of the substructure boosting occurs near the cusp/core region, which will mitigate the aforementioned synchrotron reduction effect given a magnetic field model that peaks centrally within the halo, as in our case.

For the case of M81 (Fig. 15), we note that the use of the Burkert profile has a significant effect, reducing the limits from slightly weaker than Fermi-LAT to significantly weaker than this benchmark.

6 SKA and ASTRO-H Constraints

In order to determine how far into the $m_\chi - \langle\sigma V\rangle$ parameter future experiments could probe in the studied environments, we will determine the smallest cross-section to which they are sensitive. We

Halo	Boost A	Boost B
Coma	35.2	17.7
M81	10.1	1.00
Draco	3.43	1.00

Table 4. Substructure boosting factors for two cases. A: from [31] as used in this work. B: from [29] used to study Coma.

do this first by locating the smallest cross-section observable by the instrument (assuming 100% of emissions results from DM annihilation) and then by determining the minimal cross-section for which the DM-induced emissions can be disentangled from the dominant foreground emission with a power-law spectrum. This is important as DM-induced radio emissions will likely be sub-dominant in all the environments for cross-sections below those shown in Fig. 12; for X-rays the sub-dominance in the studied sources will evidently begin at much larger cross-sections (see Figs. 2 and 6).

This disentangling process is performed by assuming a power-law spectrum $S_n\nu^{-\eta}$ with either $\eta = 0.85$ or $\eta = 0.7$ as appropriate (resulting from an electron distribution with power-law index 2.7 or 2.4 respectively) with S_n chosen to closely match the flux level of available data (same points as displayed in previous plots). We then assume that the total flux from the source will be the sum of the DM and power-law fluxes characterized to within a 1% error. The DM flux will then be found subtracting off the power-law, characterized to within a 2% error, and averaged over many random realizations of this "simulated measurement". The error assigned to the resulting "measurement" of the DM-induced flux at each frequency is taken to be the variance of the set of simulated measurements. The given error limits are chosen to reasonably match the capabilities of the SKA and ASTRO-H experiments. This analysis is performed separately for both the ICS and synchrotron spectra.

In the case of Draco and ASTRO-H, we chose to normalize S_n using the WISE [93] 3-Band limit for Draco, lacking for any hard X-ray data.

The minimal cross-section to which the instrument is sensitive is then taken to be the smallest that can be resolved from the power-law spectrum (such that it is not dominated by the 1σ uncertainties), provided this is larger than the 100% DM analysis result. We also require that the case of power-law plus DM has a χ^2 value 10^3 times smaller than power-law alone (when comparing these cases to the total flux) in order to ensure that it is the strongly preferred hypothesis.

Figure 16 displays the constraints that can be derived from the minimal cross-section with which ASTRO-H could observe DM-induced Inverse-Compton Scattering (ICS) emission for each neutralino mass. The large background X-ray fluxes in the chosen environments mean that ASTRO-H cannot resolve DM emissions of models below the Fermi-LAT limit. However, in earlier figures it was argued that ASTRO-H is well positioned to observe features of the DM ICS, so environments with less X-ray background might be more suitable. A study of this nature will be confined to further work to determine the possible usefulness of ASTRO-H data in DM searches. The lack of higher frequency X-ray limits in the Draco dwarf will also play a role in reducing the displayed constraints.

Given that ASTRO-H has a larger collecting area in the lower frequency part of the ICS spectrum, the $b\bar{b}$ channel has stronger fluxes and thus can provide better constraints. The use of the Burkert profile in the lower panel of Fig. 16 weakens the constraints that can be derived by roughly an order of magnitude.

Figure 16 should also be compared to Fig. 17 sourced from [34] but applying the above "disentanglement test". This shows the potential cross-section constraints for the case of the SKA. We stress that the SKA constraints are several orders of magnitude better in all environments. In the case of Draco the Burkert profile constraints are substantially weakened by the fact that its flux is only integrated over a 4 arcminute squared area, as the dominant spectrum is chosen to respect the VLA limit. The limited area also greatly exaggerates the effects of spatial diffusion in reducing the severity of these constraints. The use of the Burkert halo profile in the lower

panel of Fig. 17 weakens all the constraints by more than an order of magnitude. For an NFW halo profile, the SKA can probe models well below the GC favoured region in Coma and reaching $\langle\sigma V\rangle \sim 6\times10^{-28}$ cm^3 s^{-1} in M81, while in Draco it can cover the region given by $\langle\sigma V\rangle \gtrsim 5\times10^{-27}$ cm^3 s^{-1} and $m_\chi \gtrsim 20$ GeV. When the Burkert profile is used, however, Draco can no longer be used to probe the GC model region at all (for this 4 square arcminute integration area) and M81 can be used to study models with $\langle\sigma V\rangle \gtrsim 3\times10^{-27}$ cm^3 s^{-1} and $m_\chi \gtrsim 12$ GeV. With the Burkert profile Coma can still be used to probe down to $\langle\sigma V\rangle \sim 1\times10^{-27}$ cm^3 s^{-1} for all the GC masses.

7 Discussion

We will proceed to discuss our results examining the consequences for each studied neutralino mass model with its best-fit cross-section. We will then examine the consequences of our results for the purported Reticulum II γ-ray excess. Finally, we will discuss general spectral features and the potential of multi-frequency searches for DM-induced signals with next coming experiments.

Before proceeding to this discussion we note that the synchrotron results in Coma are much more constraining for certain neutralino masses than others. This depends on two aspects. The first being that larger mass neutralinos produce electrons with a greater average energy, shifting the peak of the resulting synchrotron spectrum to higher frequencies (for the same choice of the magnetic field). The second aspect is the slope of the Coma diffuse radio emission spectrum, which tails off rapidly above 1 GHz. When we combine these two aspects we see that larger mass neutralino models will be more constrained by the available Coma diffuse radio emission data, as the synchrotron peak is rapidly shifted towards frequencies where the amplitude of the data is tailing off. Of course, a sufficiently large cross-section will make the spectral amplitude of any model incompatible with the Coma data at most frequencies.

For the AFP models we find that Coma predictions are incompatible with the slope (and often also with the amplitude) of its synchrotron radio spectrum, predicting unobserved flux excess and spectral flattening above 1 GHz. This conclusion is largely unmitigated by the use of the Burkert profile and, as shown in Fig. 5, magnetic field uncertainties cannot account for the conflict with the data.
The M81 spectra show no conflicts with the available SED.
However, the Draco spectra conflict with the VLA limit for an NFW profile and $b\bar{b}$ annihilation channel. Therefore, even though Draco does not provide a definitive dismissal of the AFP with best-fit annihilation cross-section, it does serve to suggest that there is cause for concern, and thus reinforces the Coma results. Further observations will increase the constraining power of Draco. We note that the flatness of the AFP spectra might well conflict with future radio studies of Draco, as also occurs in Coma.

Taking all these results into consideration, and as the studied representative model was the most compatible with the Planck data, we must conclude that the remaining AFP model not yet excluded by Planck must be now considered eliminated through this analysis. This is reinforced by the fact that Fig. 1 shows that the Fermi-LAT data excludes these models in the $b\bar{b}$ channel.

A recent re-analysis of the AMS-2 results [16] indicates that a more sophisticated astrophysical model would allow a neutralino with mass ~ 50 GeV and a cross section $\sim 3\times10^{-26}$ cm^3 s^{-1} to account for observed positron excesses. We note that this model will be covered by the conclusions which apply to the GC median mass model (40 GeV) with the Fermi-LAT dwarf cross-section ($\sim 1\times10^{-26}$ cm^3 s^{-1}) as their results do not differ sufficiently to alter any conclusions. Therefore, we find that this revised AFP model will be ruled out by a violation of Fermi-LAT stacked-cluster limits on Coma and by the conflict with the flux and the slope of Coma radio data (see the Fermi GC discussion below). This is subject, however, to uncertainty over the halo density profile of Coma, as the use of the Burkert profile removes all aforementioned conflicts.

For the Fermi GC models with best-fit annihilation cross-sections we find that there are conflicts between Coma radio data and the predicted synchrotron slope of all but the minimal (10 GeV) GC model and the 40 GeV $b\bar{b}$ cases. There are, however, no significant conflicts with the γ-ray limits on Coma. Neither M81 nor Draco serve to further constrain these DM models.

However, in these cases neutralino-induced emissions must be sub-dominant complicating hence attempts at robust detection in cosmic structures like dwarf galaxies.

In the case of the 3 TeV neutralino model (with AFP-consistent mass) with Reticulum II and Fermi-LAT dwarf cross-sections [19] we show that there is a conflict with Coma radio data regardless of the assumed DM halo profile. Moreover, this model also conflicts with the Fermi-LAT stacked-cluster limit as well as the direct Fermi-LAT observational limits on Coma (though for the Fermi-LAT cross-section $b\bar{b}$ 3 TeV does not conflict with γ-ray limits and the Burkert profile removes all such conflicts). This means that the Coma data is not compatible with a TeV neutralino causing Reticulum II γ-ray emission with our derived Reticulum II annihilation cross-section or that sourced from Fermi-LAT dwarf studies, which included Ret. II in their analysis [19]. Similarly, the radio spectra for M81 conflicts with the AFP mass neutralino model as a source of Reticulum II γ-ray emission for the Ret. II cross-section but no the Fermi-LAT case. Lastly, TeV neutralino models with both the Reticulum II and Fermi-LAT dwarf annihilation cross-sections are in conflict with the VLA Draco limit for both halo profiles (Ret. II) and NFW only in the of Fermi-LAT cross-sections. As argued previously, this conclusion cannot be easily mitigated by appealing to magnetic field uncertainties, as these would have to be large to account for the excesses over the data.

In the case of the neutralino models with Fermi GC masses and the Reticulum II annihilation cross-section, the Ret. II cases conflict with the Coma radio data for both NFW and Burkert halo density profiles. The Fermi-LAT dwarf cross-section cases only conflict with Coma data when the NFW profile is used, apart from the 10 GeV $b\bar{b}$ case. We note that although we do not display W^+W^- spectra, their relative hardness compared to $b\bar{b}$ makes them difficult to accommodate with the slope of the Coma data [29], which remains true in our analysis with models with similar mass to GC maximal, even with cross-sections which correspond to those used in [94] (including comparison with appropriate W^+W^- spectra). However, all of the GC masses are incompatible with the Fermi-LAT stacked cluster limit and direct γ-ray limits on Coma with both NFW and Burkert density profiles for the Ret. II cross-section. In the case of the Fermi-LAT dwarf cross-section, all neutralino masses conflict with the γ-ray limits for an NFW density profile and $b\bar{b}$ emissions, for the Burkert case there are no conflicts. For M81, all of the masses between 10 and 100 GeV conflict with the data when the Ret. II cross-section is used with an NFW profile. For the Burkert profile only 40 and 100 GeV $\tau^+\tau^-$ remain in tension. In the case of the Fermi-LAT cross-sections there are no conflicts with M81 data. For Draco, with an NFW profile and the Ret. II annihilation cross-section, only the GC minimal mass (i.e., 10 GeV) and median mass with $b\bar{b}$ are compatible with the VLA limit but all the masses/channels violate the Fermi-LAT dwarf limits from [14]. In the Burkert density profile case only the 100 GeV mass with $\tau^+\tau^-$ violates the VLA limit, and all the Fermi-LAT limit violation constraints are removed. For the Fermi-LAT dwarf annihilation cross-section, only the 100 GeV $\tau^+\tau^-$ conflicts with the VLA limit, but a Burkert profile allows all masses with no conflicts with Fermi-LAT or VLA data. This makes Draco conclusions uncertain, as there are good reasons to believe that dwarf galaxies may have cored profiles [85, 86]. From the strength of the Coma data we can conclude that the violation of the Fermi-LAT stacked cluster and direct limits on Coma, as well as radio conflict, means that none of the GC masses (between 10 and 100 GeV) are compatible with being responsible for any excess Reticulum II γ-ray emission, given the current Fermi-LAT limits on dwarf galaxies. This is especially important as the best-fit model for the Ret. II γ-ray excess is one with mass 40 GeV and $\langle\sigma V\rangle \sim 3 \times 10^{-26}$ cm^3 s^{-1}. We also note that the Ret. II DM explanation of its γ-ray excess is already disfavoured by dwarf galaxy observations with Fermi-LAT [19].

As a matter of the validation of our numerical results, in Section 5.4 it is shown that the most significant differences between our results for the Coma cluster radio flux and the one derived in previous work, like [29], are due to the modelling of the magnetic field spatial profile within the inner parts of the halo. It is important to highlight the fact that we use here an updated model of the Coma cluster magnetic field derived by [38] several years after the publication of the [29] results.

It must be noted that, as we do not take into account the fact that sub-halos at differing radii within the parent halo would experience differing magnetic field values, our predictions of the

synchrotron flux for Coma may be slightly optimistic [92]. However, if sub-halos follow a similar distribution to the DM density of their parent halo, then this effect is mostly significant within cored halo profiles.

It is clear from our discussion in Section 5 that the mass of the neutralino has a very prominent effect on the DM-induced SED, regardless of environment. This being that it controls the position of the γ-ray, X-ray and synchrotron peaks through the maximal energy of electrons produced in DM annihilations, and also the distinctness of the ICS and γ-ray peaks. This latter property is a result of the effect of the neutralino mass on both shifting the ICS peak towards higher energies as well as its effect on the bremsstrahlung emission, which lies between the ICS and gamma peaks. Low mass neutralinos produce electron distributions capped at lower energies and thus result in a lower energy bremsstrahlung emission, resulting in the fact that the bremsstrahlung emissions occupy a spectral region over-shadowed by ICS emissions. It is notable that the mass of the neutralino also has a suppressive effect on the intensity of the emitted radiation, as a result of suppressing collisions, which competes with the effects of the higher mass on the electron and γ-ray product distributions from annihilation. In this setting, the larger cross-section of the high mass models compensates for this.

The effect of the dominant annihilation channel on the SED is also apparent in the results shown in Figs. 2,6, and 9. The difference between the $b\bar{b}$ and $\tau^+\tau^-$ channels is the hardening of the spectrum induced by the latter, which produces a spectral cross-over between the two channels. The position of the cross-over is shifted by the neutralino mass as discussed above. For the GC models, these cross-over points lie within the observation ranges of the SKA (synchrotron emission) and ASTRO-H (ICS emission), opening up avenues for identifying the dominant annihilation channel of any putative neutralino DM particle observation. The DM-induced γ-ray emission exhibits the same patterns of variation due to neutralino mass and annihilation channel as the ICS and synchrotron emission processes. This means that the identified spectral characteristics are also independent of the mode of emission, making it possible to make far more robust neutralino characterizations using a multi-frequency approach than with isolated spectral region studies.

In the case of all of the models we studied in this paper, the SKA is excellently placed to measure the slope and magnitude of the synchrotron spectrum as discussed already in [34], as well as being able to scan the majority of the GC model parameter space in the studied environments. In contrast to this, ASTRO-H is unsuitable to extend constraints in the studied environments, due to their significant X-ray backgrounds or weak available limits. However, the ASTRO-H observation window is positioned to be sensitive to the peak of the ICS spectrum, which is determined by the mass of the neutralino. Furthermore, ASTRO-H is sensitive to a region of the spectrum that displays a large variation between neutralino annihilation channels: in fact for $10\ \mathrm{GeV} < M_\chi \leq 100\ \mathrm{GeV}$, this encompasses the point of crossing between $b\bar{b}$ and $\tau^+\tau^-$ ICS spectra. This means that both mass and composition can be informed by ASTRO-H observation for the whole range of masses favoured by GC observations. Therefore, bearing all of this mind, further work will be required to determine the usefulness of the ASTRO-H observations in dark matter searches. In this vein we will perform a similar study for more favourable environments in future work. This is particularly important as, combined with the analysis in [34], X-ray results would give multi-frequency indirect observations two complimentary means of identifying the nature of the neutralino from the associated emissions. Moreover, the differing emission mechanisms mean that these two methods are not subject to the same confusion or error limits and thus can be used as independent consistency checks and to provide robustness to any putative DM detection by indirect methods.

A multi-frequency observational strategy could then combine SKA constraints and those from experiments like ASTRO-H, should favourable detection environments be determined. The importance of this is that synchrotron radiation is sensitive to the magnetic field strength, and detailed structure [36], as well as the thermal electron density in the target environment. Thus constraints based on synchrotron radiation can be said to be degenerate with respect to the neutralino model as well as some function of the magnetic field and thermal electron density. However, inverse-Compton emissions are not sensitive to the magnetic field but still depend upon the thermal electron density. The combined constraints are then sensitive only to the neutralino as well as the

magnetic field, as the thermal electron density is eliminated through recognizing that the ratio of energy densities becomes $\frac{U_B}{U_{IC}} \propto B^2$. This means that the consistency between radio and higher-energy observations purporting to identify neutralino DM is a vital piece of evidence strengthening such an identification, as these different emissions mechanisms are sensitive to differing errors and confusions and serve to eliminate common dependencies. This also emphasyses the importance of Faraday rotation and polarimetry measurements made by the SKA in order to characterize magnetic fields in the target DM environments, as this is crucial to demonstrate the robustness of any potential neutralino identification.

8 Conclusions

The Coma, M81, and Draco environments were shown to be promising targets for multi-frequency analysis as well as demonstrate its power to restrict the parameter space. This is of particular significance to the further constraint of models currently favoured by the galactic centre observations. In the case of the AMS-2/Fermi/PAMELA positron excess models, with best-fit cross-sections, these environments provide evidence that the remaining models in this family are excluded by existing multi-frequency observations, although this is somewhat weakly subject to magnetic field and halo substructure uncertainties. In the case of the best-fit Fermi GC models we demonstrate similar conflicts with existing data over the whole 10-100 GeV mass range. This is already suggestive of the need of a multi-frequency approach to study these DM models. Finally, the SKA is shown to be very well placed for future study of these models, with ASTRO-H being attractive but requiring further study in more favourable detection environments. We also showed that the Coma radio data can be used to derive limits on the neutralino cross-section that are stronger than the Fermi-LAT limits, regardless of halo profile. The magnetic field uncertainties were also too small to account for this improvement.

The three environments here analyzed also demonstrate that the annihilation cross-sections which matches the reported Reticulum II γ-ray excess, under modest assumptions, are in conflict with current multi-frequency data, indicating that the DM interpretation of this excess is untenable for all the considered neutralino masses which cover a range from 10 GeV to 3 TeV. This conclusion remains relatively robust even with a far more conservative annihilation cross-section limits derived from Fermi-LAT dwarf observations. This is of particular significance as the Draco γ-ray predictions remains largely in agreement with the Fermi-LAT analysis. Moreover, this reinforces the existing conflicts between the proposed Ret. II dark matter excess and the Fermi-LAT results [19] from dwarf galaxies including Ret. II.

Given the strength of the Coma radio results reported here it is worth mentioning that the constraining power of Coma is much greater in this study than in earlier ones, like [29], as we use an updated magnetic field model for Coma that provides larger synchrotron fluxes, due to its spatial profile peaking at the centre of the cluster. However, due to the nature of the model we employ for sub-structure flux-boosting, our synchrotron flux results for Coma may be slightly optimistic, as they do not account for sub-halos experiencing weaker magnetic fields at large distances from the cluster center. In this sense the spatial dependence of the magnetic field model used for Coma introduces some uncertainty into our results (although its magnitude was shown to provide only small uncertainties), as we have clearly discussed in this work.

Despite the fact that the chosen sources are not ideal DM detection environments, we have shown that SKA has great potential in the study of the DM parameter space. We will consider a similar analysis of more favourable detection environments in further work in order to discern the potential constraints that might be yielded by ASTRO-H.

Multi-frequency searches for DM involving the upcoming SKA and ASTRO-H show great promise in their ability to probe the DM parameter space. Should it be possible to locate environments with weaker X-ray backgrounds, ASTRO-H will be able to provide a new window on neutralino DM while the SKA is constructed. We have shown, in fact, that the ASTRO-H observation window contains a spectral region that can be used to differentiate both the mass and dominant annihilation channel which characterize the neutralino. The importance of having multiple future experiments capable of furthering the neutralino search is that it opens up the

potential for multi-frequency examinations of the DM parameter space. This is highly attractive given the uncertainties and errors inherent in indirect DM search methods due to the complexity of DM halo environments. Moreover, indirect multi-frequency searches benefit from the fact that the signatures of the neutralino spectrum occur for each emission mechanism, despite the fact that each has different dependencies and sources of error. This means that multi-frequency observations provide a series of consistency checks, allowing for far more robust identifications and for the elimination of common error dependencies, like the density of thermal electrons within the halo (a common dependency between synchrotron and ICS emissions). We must note, however, that the uncertainties found in substructure boosting effects, nature of the halo profile, and disentangling dark matter emissions from purely baryonic processes remain significant. Although the precision of the SKA mitigates the last point as we have shown for these unfavourable detection environments, and the angular resolution of the SKA will be able to supplement this through source-subtractions [87, 95]. Despite this, in the case of the SKA and ASTRO-H, a major source of error in a multi-frequency DM search, in the form of the magnetic field, can be eliminated, as this can be fully characterized by the SKA during the observations required for DM searches, as discussed in [87]. It remains to be seen whether the dominant error, in the form of resolving DM emissions from astrophysical backgrounds, can be mitigated for ASTRO-H through a choice of more favourable DM search environments.

Therefore, based upon all the preceding arguments, we conclude that multi-frequency strategies revolving around the SKA, with the possible inclusion of the ASTRO-H experiment, have considerable advantages to be leveraged in the continuing hunt for neutralino dark matter.

Acknowledgments

S.C. acknowledges support by the South African Research Chairs Initiative of the Department of Science and Technology and National Research Foundation and by the Square Kilometre Array (SKA). G.B. acknowledges support from the DST/NRF SKA post-graduate bursary initiative.

This publication makes use of data products from the Wide-field Infrared Survey Explorer (WISE), which is a joint project of the University of California, Los Angeles, and the Jet Propulsion Laboratory/California Institute of Technology, funded by the National Aeronautics and Space Administration and from the NASA/IPAC Extragalactic Database (NED). Part of this work is also based on archival data and online services provided by the ASI SCIENCE DATA CENTER (ASDC).

We finally thank the Referee for his/her careful review of the results, as well as for several comments and valuable suggestions that allowed us to improve the presentation of this work.

References

[1] Calore, F., Cholis, I., McCabe, C. & Weniger, C., 2015, Phys. Rev. D, **91**, 063003, arXiv:1411.4647 [astro-ph].

[2] Cholis, I. & Hooper, D., 2013, Phys. Rev. D, **88**, 023013, arXiv:1304.1840 [astro-ph].

[3] Hooper, D. & Linden, T., 2011, Phys. Rev. D, **84**, 123005.

[4] Atwood, W. B. *et al.* for the Fermi/LAT collaboration, 2009, Astrophys. J., **697**,1071, arXiv:0902.1089 [astro-ph].

[5] Picozza, P. *et al.*, 2007, Astropart. Phys., **27**(4), 296.

[6] Hooper, D., Linden, T. & Mertsch, P., 2015, JCAP, **03**, 021, arXiv:1410.1527 [astro-ph].

[7] O'Leary, R., Kistler, M., Kerr, M. & Dexter, J., 2015, arXiv:1504.02477 [astro-ph].

[8] Bartels, R., Krishnamurthy, S. & Weniger, C. , 2015, arXiv:1506.05104 [astro-ph].

[9] Lee, S. K. *et al.*, 2015, arXiv:1506.05124 [astro-ph].

[10] Brandt, T. & Kocsis, B., 2015, arXiv:1507.05616 [astro-ph].

[11] Calore, F., Di Mauro, M., Donato, F., Hessels, J. W. T. & Weniger, C., 2015, arXiv: 1512.06825 [astro-ph].

[12] Kounine, A. on behalf of the AMS collaboration, 2012, Int. J. Mod. Phys. E, **21**, 1230005.

[13] López, A., Savage, C., Spolyar, D. & Adams, D., 2015, arXiv:1501.01618 [astro-ph].

[14] Ackermann, M. et al. for the Fermi-LAT collaboration, 2014, Phys. Rev. D, **89**, 042001, arXiv:1310.0828 [astro-ph.HE].

[15] Geringer-Sameth, A., Koushiappas, M. & Walker, M., 2014, arXiv:1410.2242 [astro-ph].

[16] Di Mauro, M., Donato, F., Fornengo, N. & Vittino, A., 2015, arXiv:1507.07001 [astro-ph].

[17] Geringer-Sameth, A. *et al.*, 2015, arXiv:1503.02320 [astro-ph].

[18] Bonnivard, V. *et al.*, 2015, ApJ, **808**, L36.

[19] Drlica-Wagner, A. *et al.* for the Fermi-LAT collaboration & Abbott, T. *et al.* for the DES collaboration, 2015, arXiv: 1503.02632 [astro-ph].

[20] Bersanelli, M. *et al.*, A& A, 2010, **520**, A4.

[21] Ade, P. et al. for the Planck Collaboration, 2015, arXiv:1502.01589 [astro-ph].

[22] Jungman, G., Kamionkowski, M. & Griest, K.,1996, J. Phys. Rep., **267**, 195.

[23] Navarro, J. F., Frenk, C. S. & White, S. D. M., ApJ, 1996, **462**, 563.

[24] Burkert, A., 1995, ApJ, **447**, L25.

[25] Bryan, G. & Norman M., 1998, ApJ, **495**, 80.

[26] Muñoz-Cuartas, J. C., Macciò, A. V., Gottlöber, S. & Dutton, A. A., 2011, MNRAS, **411** (1), 584, arXiv:1007.0438 [astro-ph.CO].

[27] Ludlow, A. D. *et al.*, 2013, MNRAS, **432**, 1103L.

[28] Pieri L. *et al.*, 2011, Phys. Rev. D., **83**, 023518.

[29] Colafrancesco, S., Profumo, S. & Ullio, P., 2006, A&A, **455**, 21.

[30] Sanchez-Conde, M. & Prada, F., 2014, MNRAS, **442** (3), 2271, arXiv:1312.1729 [astro-ph].

[31] Prada, F. *et al.*, 2012, MNRAS, **423** (4), 3018, arXiv:1104.5130 [astro-ph].

[32] Ng, K. *et al.*, 2014, Phys. Rev. D, **89**, 083001, arXiv: 1310.1915 [astro-ph.CO].

[33] Bartels, R. & Shin'ichiro, A., 2015, arXiv:1507.08656 [astro-ph.CO].

[34] Colafrancesco, S., Marchegiani, P. & Beck, G., 2015, JCAP, **02**, 032C.

[35] Colafrancesco, S., Profumo, S. & Ullio, P., 2007, Phys. Rev. D, **75**, 023513

[36] Colafrancesco, S. & Blasi, S., 1998, Astropart. Phys., **9**, 227.

[37] Briel, U. *et al.*, 1992, A&A, **259**, L31.

[38] Bonafede, A., *et al.*, 2010, A&A, **513**, A30.

[39] Beck, R., Klein, U. & Krause, M., 1985, A&A, **152**, 237.

[40] Kostov, V., 2006, arXiv:astro-ph/0604395.

[41] Łokas, E. L. *et al.*., 2005, MNRAS, **363**, 918.

[42] Longair, M. S., 1994, *High Energy Astrophysics* (Cambridge University Press).

[43] Gondolo, P., Edsjo, J., Ullio, P., *et al.*. 2004, JCAP, **0407**, 008.

[44] Sjöstrand, T., 1994, Comput. Phys. Commun., 82, 74.

[45] Thierbach, M., Klein, U. & Wielebinski, R., 2003, A&A, **397**, 53.

[46] Henry, J. P., 2004, ApJ, **609**, 603H

[47] https://heasarc.gsfc.nasa.gov/docs/asca/asca2.html

[48] http://sci.esa.int/integral/ & https://heasarc.gsfc.nasa.gov/docs/integral/integral.html

[49] Krivonos, R., Vikhlinin, A., Churazov, E., Lutovinov, A., Molkov, S. & Sunyaev, R., 2005, ApJ, **625**, 89K.

[50] https://ned.ipac.caltech.edu/

[51] Rephaeli, Y. for the Fermi-LAT collaboration, 2015, submitted to ApJ, arXiv: 1507.08995 [astro-ph].

[52] Griffin, R. D., Dai, X. & Kochanek, C. S., 2014, ApJ, **795**, L21.

[53] Israel, F. P. & Mahoney, M. J., 1990, ApJ, **352**, 30I.

[54] Murphy, E. J., Kenney, J. D. P., Helou, G., Chung, A. & Howell, J. H., 2009, ApJ, **694**, 1435M.

[55] White, R. L. & Becker, R. H., 1992, ApJ, **79**, 331W.

[56] Condon, J. J. *et al.*, 1998, ApJ, **155**, 1693C.

[57] Condon, J. J., Cotton W. D., Broderick, J. J., 2002, ApJ, **124**, 675C.

[58] Stil, J. M., Krause, M., Beck, R., Taylor, A. R., 2009, ApJ, **693**, 13925.

[59] Becker, R. H., White, R. L., Edwards, A. L., 1991, ApJS, **75**, 1B.

[60] Nagar, N. M., Falcke, H., Wilson, A. S., 2005, A&A, **435**, 521N.

[61] Sramek, R., 1975, **80**, 771.

[62] Healer, S. E. *et al.*, 2007, ApJS, **171**, 61H.

[63] Doi, A., Nakanishi, K., Nagai, H., Kohno, K., Kameno, S., 2011, **142**, 167D.

[64] Doi, A., Kameno, S., Kohno, K., Nakanishi, K., Inoue, M., 2005, MNRAS, **363**, 692D.

[65] Dale, D. A. *et al.*, 2007, ApJ, **655**, 863D.

[66] Suzuki, T., Kaneda, H., Onaka, T., Nakagawa, T., Shibai, H., 2010, A&A, **521A**, 48S.

[67] Sun, A., Hirashita, H., 2011, MNRAS, **411**, 1707S.

[68] Rice, W., 1988, ApJS, **68**, 91R

[69] www.asdc.asi.it

[70] Young, A. J., Nowak, M. A., Markoff, S., Marshall, H. L. & Canizares, C. R., 2007, ApJ, **669**,830Y

[71] Smith, A. & Stewart, G., 1985, Space Science Reviews, **40** (3), 661

[72] Weisskopf, M. C., 1988, Space Science Reviews, **40**, 47

[73] Weisskopf, M.C. *et al.*, 1987, Ap. Lett. Comm., **26**, 1

[74] Taylor, B. G., Andresen, R. D., Peacock, A. & Zobl, R., 1981, Space Science Reviews, **30** (1), 479

[75] Fomalont, E. & Geldzhaler, B., 1979, AJ, **84**, 12.

[76] http://astro-h.isas.jaxa.jp/researchers/sim/sensitivity.html

[77] http://www.slac.stanford.edu/exp/glast/groups/canda/lat_Performance.htm

[78] Silverwood, H., Weniger, C., Scott, P. & Bertone, G., 2014, arXiv:1408.4131 [astro-ph.HE]

[79] Funk, S. & Hinton, J., 2013, APh, **43**, 348.

[80] Aharonian, F. *et al.*, 2009, A & A, **502**, 437.

[81] Dewdney, P., Turner, W., Millenaar, R., McCool, R., Lazio, J. & Cornwell, T., 2012, SKA baseline design document, http://www.skatelescope.org/wp-content/uploads/2012/07/SKA-TEL-SKO-DD-001-1_BaselineDesign1.pdf

[82] http://astrogam.iaps.inaf.it/scientific_instrument.html

[83] Ackermann, M. *et al.* for the Fermi collaboration, 2015, arXiv:1507.08995 [astro-ph].

[84] Regis, M. *et al.*, 2015, MNRAS, **448**, 3747R.

[85] Walker, M. G., Mateo, M., Olszewski, E. W., Peñarrubia, J., Evans, N. W. & Gilmore, G., 2009, ApJ, **704**, 1274.

[86] Adams, J. J. *et al.*, arXiv:1405.4854 [astro-ph.GA].

[87] Colafrancesco , S. et al, arXiv:1502.03738 [astro-ph], to appear in Proceedings of Science.

[88] Stil, J.M. et al. 2014, ApJ submitted.

[89] Govoni, F., Johnston-Hollitt, M. et al. 2014, COSMIC MAGNETISM SCIENCE IN THE SKA1 ERA, SKA memo.

[90] Bertone, G., Cirelli, M., Strumia, A. & Taoso, M., 2009, JCAP, **2009** (03), 009.

[91] Crocker, R. M., Bell, N. F., Balázs, C. & Jones, D. I., 2010, Phys.Rev.D, **81**,063516.

[92] Storm, E., Jeltema, T. E., Profumo, S. & Rudnick, L., 2012, arXiv: 1210.0872 [astro-ph].

[93] https://irsa.ipac.caltech.edu/Missions/wise.html

[94] Achterberg, A. *et al.*, 2015, JCAP, **08**, 006.

[95] Regis, M., Colafrancesco, S., Profumo, S., de Blok, W. J. G., Massardi, M. and Richter, L., 2014, JCAP, **10**, 016R.

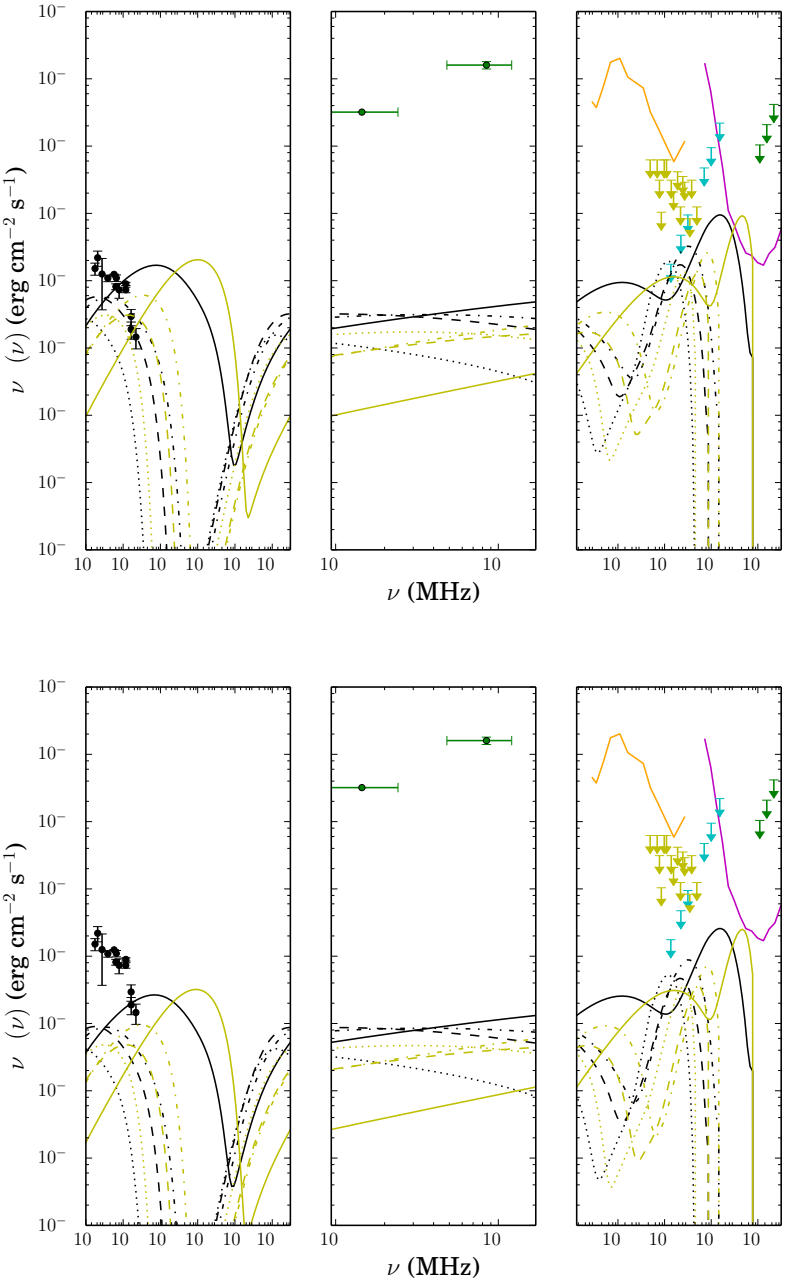

Figure 2. Dark matter annihilation spectra for the Coma cluster with best-fit cross-sections from Section 3. Black lines indicate predicted spectra for $b\bar{b}$, while yellow correspond to $\tau^+\tau^-$, with the solid curve corresponding to the AFP model, the dash-dotted, dashed, and dotted curves correspond to maximal, median, and minimal GC models respectively. The solid pink curve corresponds to the 1000 hours sensitivity of the CTA [79]. The black points correspond to the coma radio data [45], green points are X-ray data from [46, 49], the the cyan arrows to the Fermi-LAT stacked cluster limit [52], yellow are Fermi-LAT Coma limits [51], while green arrows are the HESS Coma limit [80]. The solid orange curve is the ASTROGAM 1-year sensitivity [82]. Upper panel: halos use NFW profile. Lower panel: halos use Burkert profile. All fluxes are integrated over the virial radius. The central frequency windows cover the ASTRO-H frequency range.

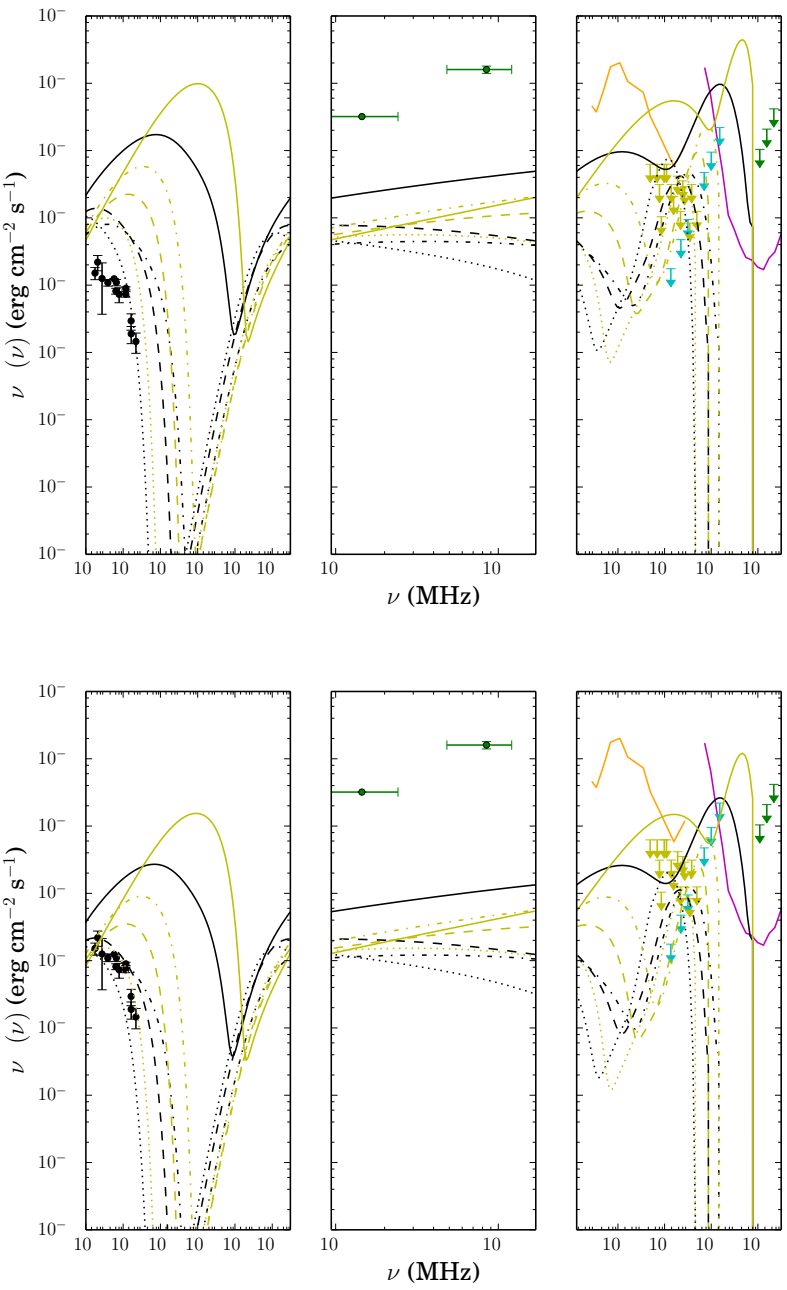

Figure 3. Dark matter $b\bar{b}$ annihilation spectra for the Coma cluster with cross-sections determined from Reticulum II excess as detailed in text. Solid curves correspond to the 3 TeV model, the dash-dotted, dashed, and dotted curves correspond to 10, 40, and 100 GeV models respectively. The solid pink curve corresponds to the 1000 hours sensitivity of the CTA [79]. The black points correspond to the coma radio data [45], green points are X-ray data from [46, 49], the cyan arrows to the Fermi-LAT stacked cluster limit [52], while yellow are Fermi-LAT Coma limits [51]. Green arrows are the HESS Coma limit [80]. Upper panel: halos use NFW profile. Lower panel: halos use Burkert profile. All fluxes are integrated over the virial radius. The central frequency windows cover the ASTRO-H frequency range.

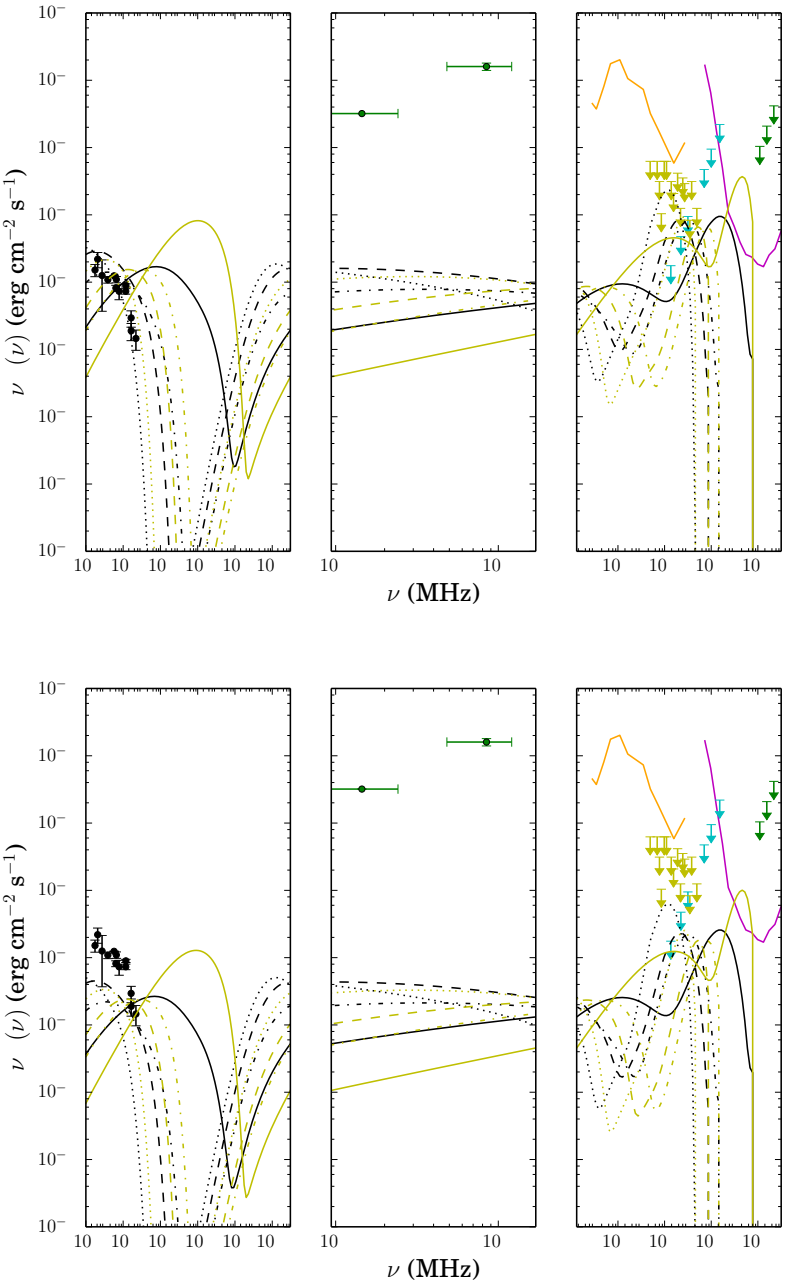

Figure 4. Dark matter $b\bar{b}$ annihilation spectra for the Coma cluster with cross-sections from Fermi-LAT dwarf limits. Solid curves correspond to the 3 TeV model, the dash-dotted, dashed, and dotted curves correspond to 10, 40, and 100 GeV models respectively. The solid pink curve corresponds to the 1000 hours sensitivity of the CTA [79]. The black points correspond to the coma radio data [45], green points are X-ray data from [46, 49], the cyan arrows to the Fermi-LAT stacked cluster limit [52], while yellow are Fermi-LAT Coma limits [51]. Green arrows are the HESS Coma limit [80]. Upper panel: halos use NFW profile. Lower panel: halos use Burkert profile. All fluxes are integrated over the virial radius. The central frequency windows cover the ASTRO-H frequency range.

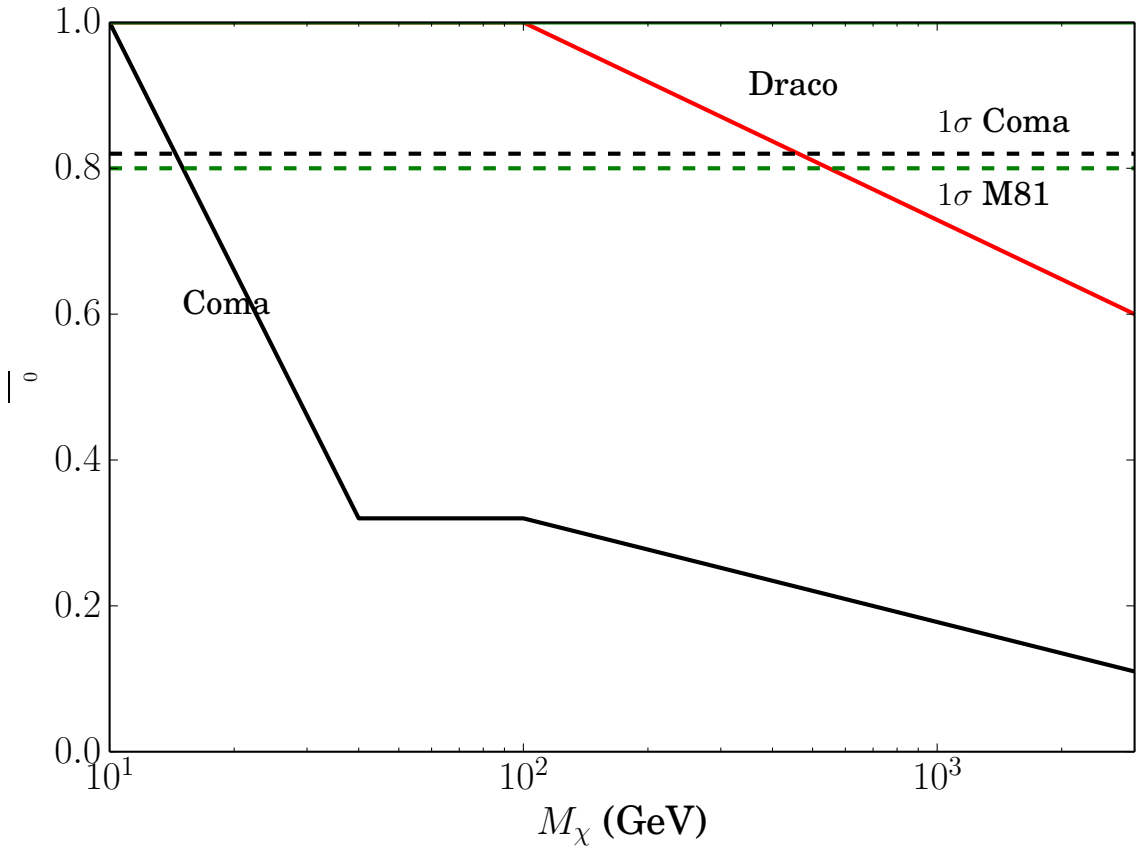

Figure 5. Magnetic field strength reduction factor required to bring spectra in Figs. 3, 7, and 10 into consistency with available radio data. Coma is plotted in black, M81 in green, and Draco in red. The dashed lines represent the 1σ error range for the magnetic field values quoted in Section 2. The data is plotted only for points corresponding to the neutralino masses studied here.

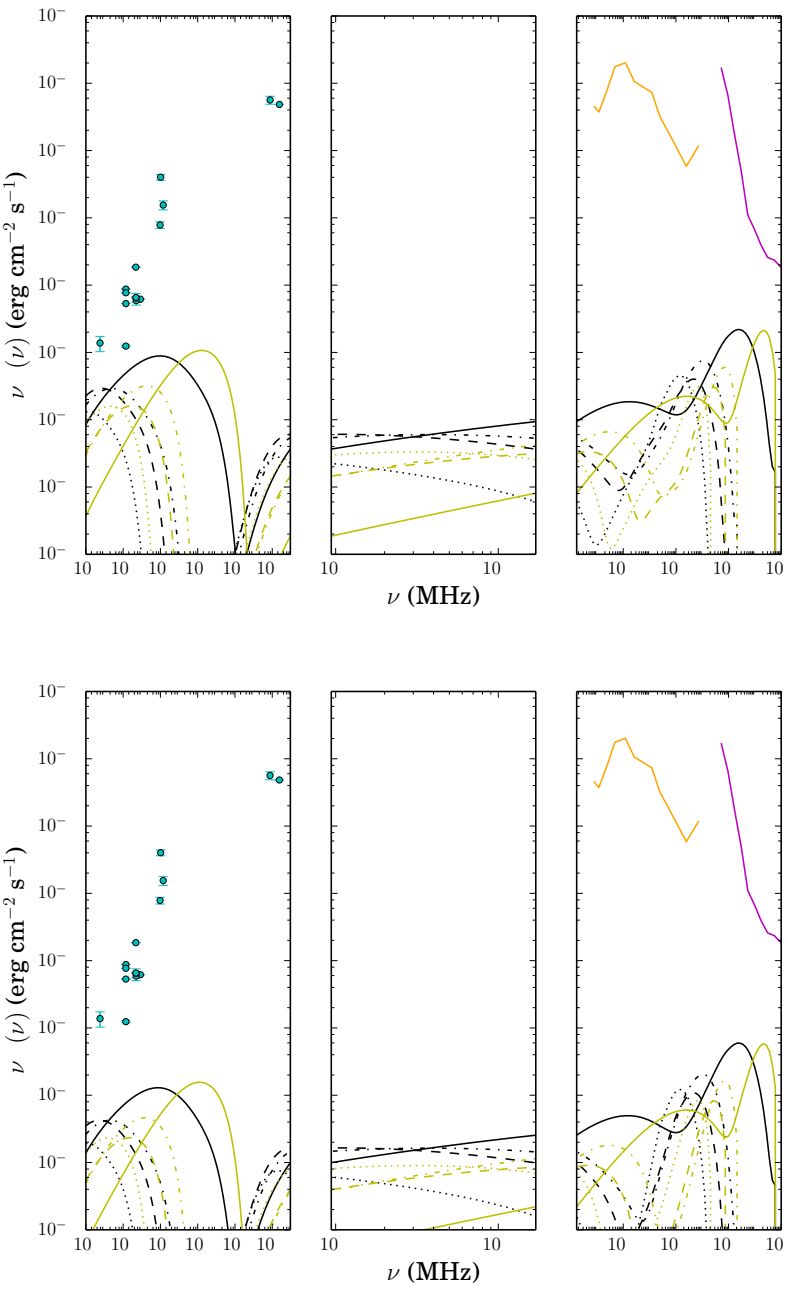

Figure 6. Dark matter annihilation spectra for the M81 galaxy with best-fit cross-sections from Section 3. Black lines indicate predicted spectra for $b\bar{b}$, while yellow correspond to $\tau^+\tau^-$, with the solid curve corresponding to the AFP model, the dash-dotted, dashed, and dotted curves correspond to maximal, median, and minimal GC models respectively. The solid pink curve corresponds to the 1000 hours sensitivity of the CTA [79]. Green points correspond to the M81 SED [53–68]. The solid red and blue curves are the 1000 hours SKA-1 and ASTRO-H sensitivities [76, 81]. The solid orange curve is the ASTROGAM 1 year sensitivity [82]. Upper panel: halos use NFW profile. Lower panel: halos use Burkert profile. All fluxes are integrated over the virial radius. The central frequency windows cover the ASTRO-H frequency range.

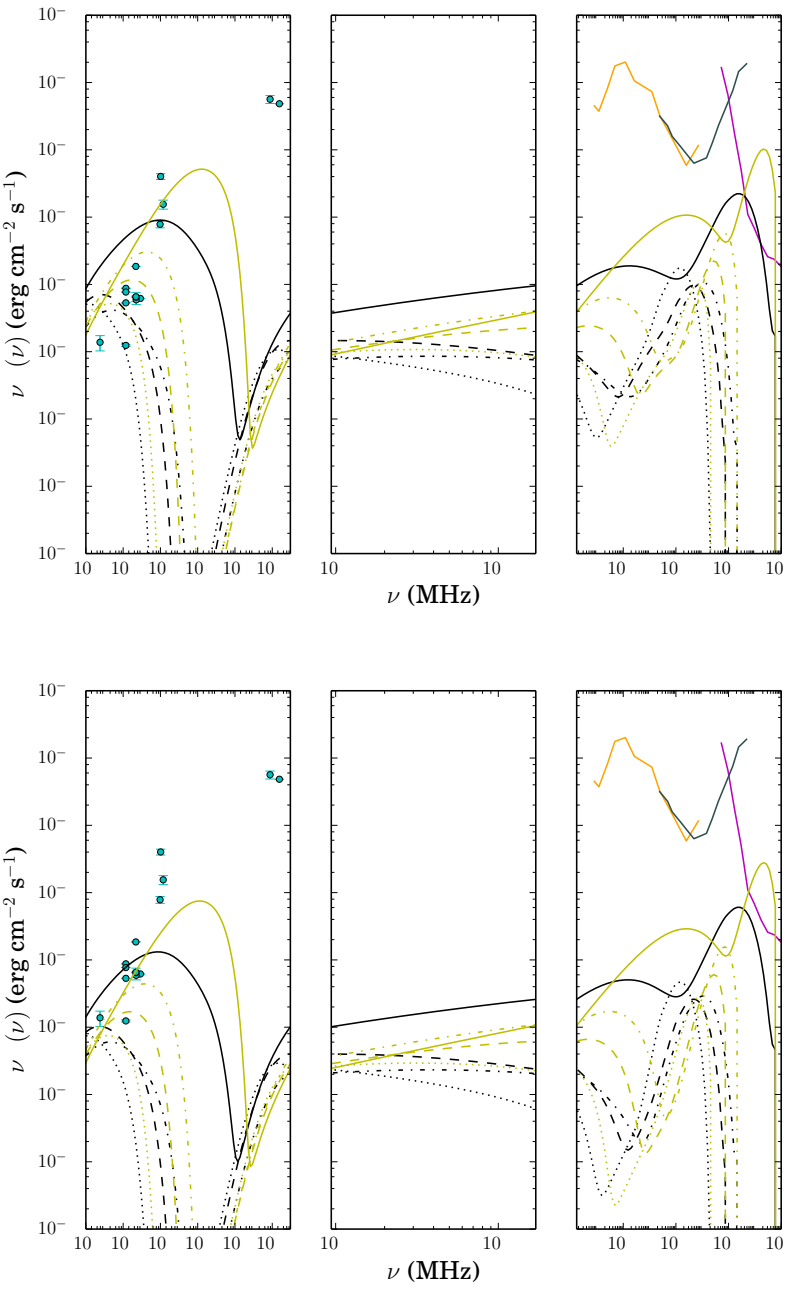

Figure 7. Dark matter annihilation spectra for the M81 galaxy with cross-sections determined from Reticulum II excess as detailed in text. Black lines indicate predicted spectra for $b\bar{b}$, while yellow correspond to $\tau^+\tau^-$, with the solid curves corresponding to the 3 TeV model, the dash-dotted, dashed, and dotted curves correspond to 10, 40, and 100 GeV models respectively. The solid pink curve corresponds to the 1000 hours sensitivity of the CTA [79], the solid grey curve shows the Fermi-LAT 10 year point sensitivity [77]. Green points correspond to the M81 SED [53–68]. Upper panel: halos use NFW profile. Lower panel: halos use Burkert profile. The left and right panels integrate flux over R_{vir}, while the centre does so over a 4.5′ radius.

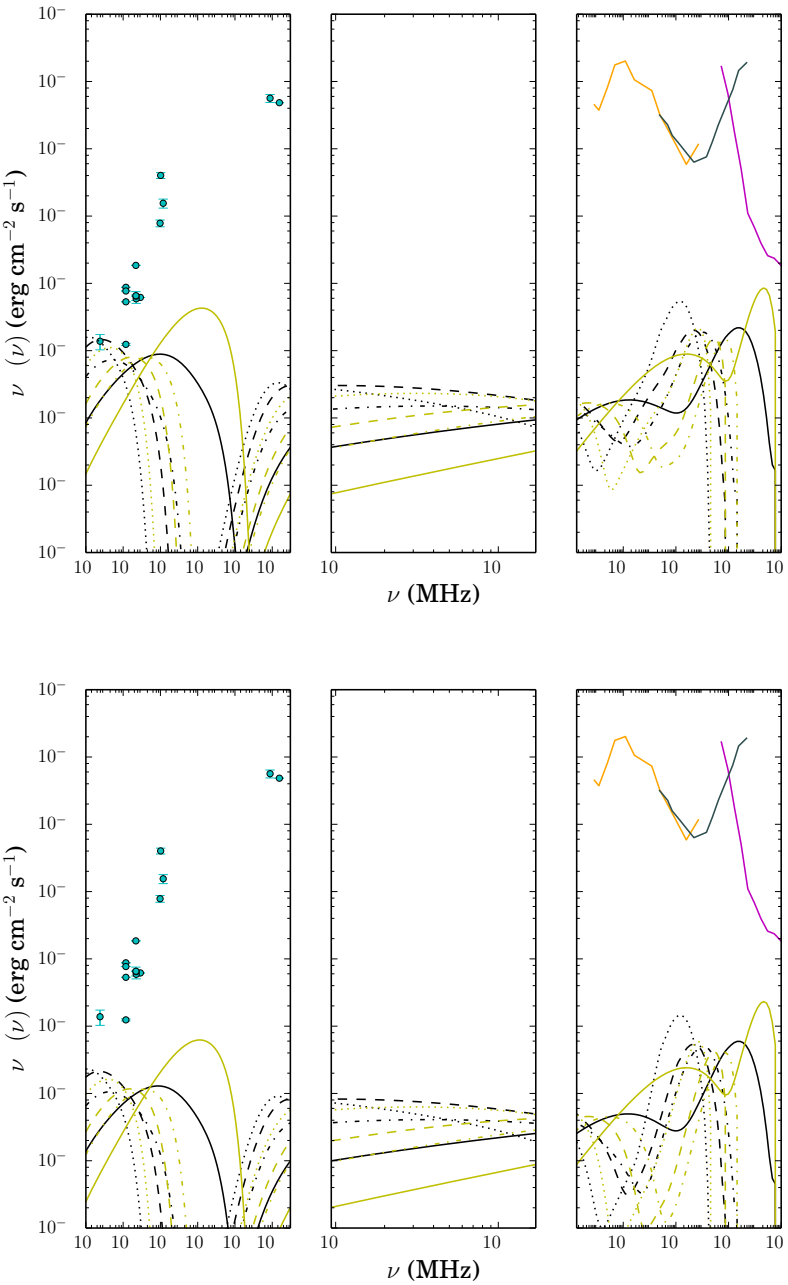

Figure 8. Dark matter $b\bar{b}$ annihilation spectra for the M81 galaxy with cross-sections from Fermi-LAT dwarf limits. Solid curves correspond to the 3 TeV model, the dash-dotted, dashed, and dotted curves correspond to 10, 40, and 100 GeV models respectively. The solid pink curve corresponds to the 1000 hours sensitivity of the CTA [79], the solid grey curve shows the Fermi-LAT 10 year point sensitivity [77]. Green points correspond to the M81 SED [53–68]. Upper panel: halos use NFW profile. Lower panel: halos use Burkert profile. All fluxes are integrated over the virial radius. The central panel covers the ASTRO-H frequency range.

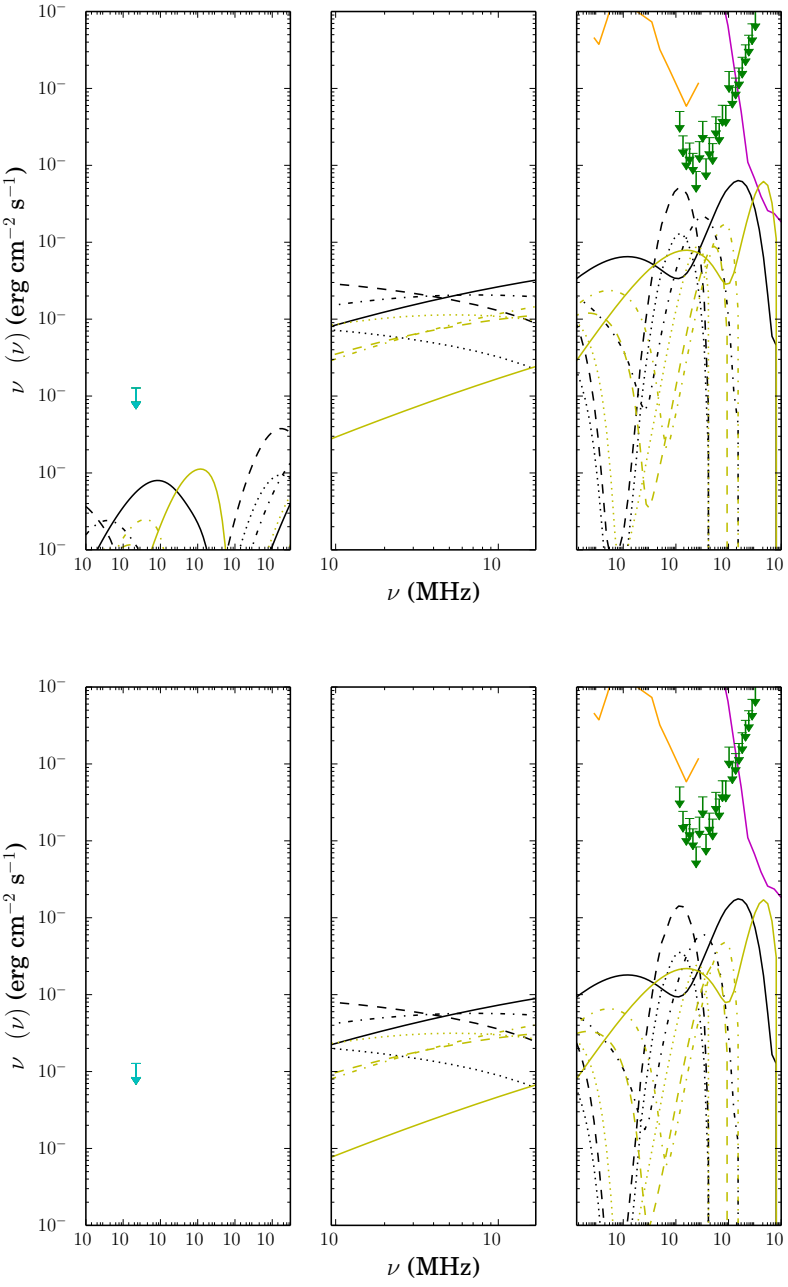

Figure 9. Dark matter annihilation spectra for the draco dwarf galaxy with best-fit cross-sections from Section 3. Black lines indicate predicted spectra for $b\bar{b}$, while yellow correspond to $\tau^+\tau^-$, with the solid curve corresponding to the AFP model, the dash-dotted, dashed, and dotted curves correspond to maximal, median, and minimal GC models respectively. The solid pink curve corresponds to the 1000 hours sensitivity of the CTA [79]. Green arrows indicate the upper limits set by the Fermi-LAT observations [14], while the cyan arrow corresponds to the VLA limit [75]. The solid red and blue curves are the 1000 hours SKA-1 and ASTRO-H sensitivities [76, 81]. The solid orange curve is the ASTROGAM 1 year sensitivity [82]. Upper panel: halos use NFW profile. Lower panel: halos use Burkert profile. The left panel integrates flux over a $2'$ radius, other panels have fluxes integrated over the virial radius. The central panel covers the ASTRO-H frequency range.

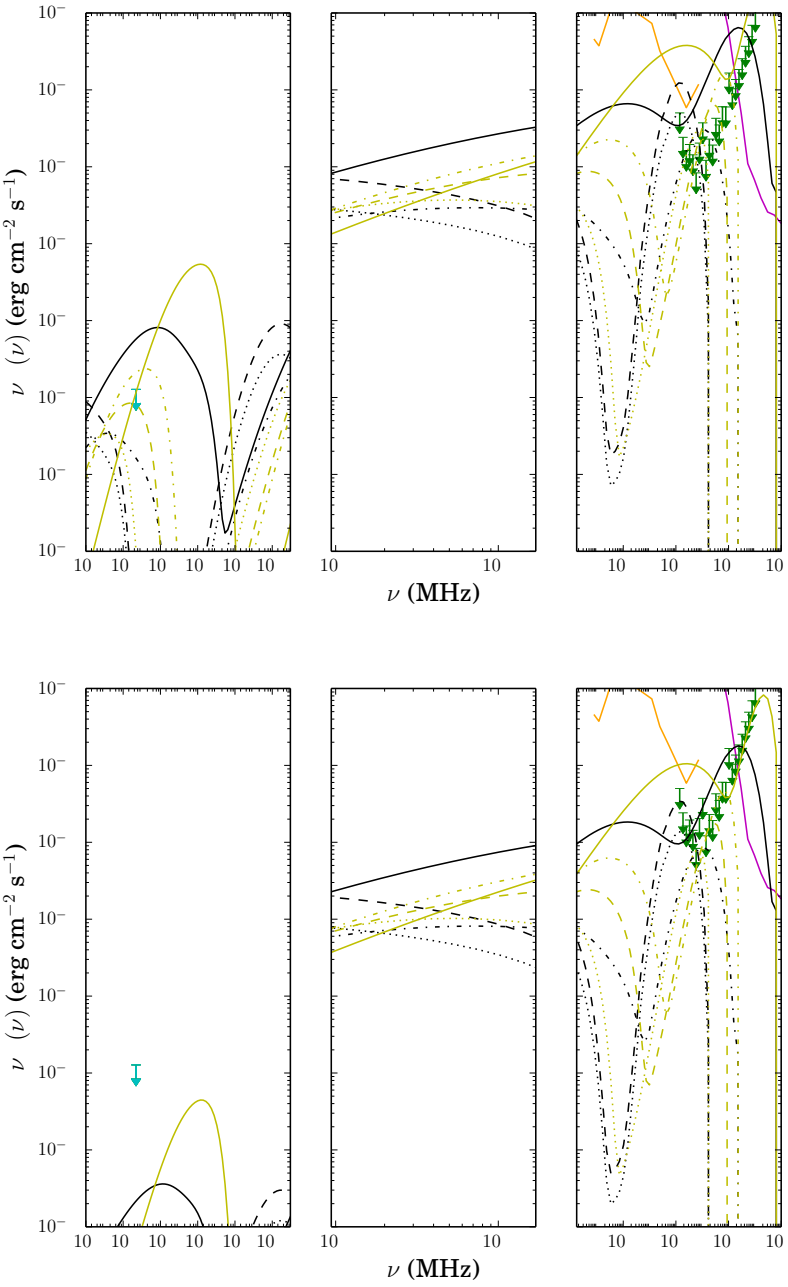

Figure 10. Dark matter annihilation spectra for the draco dwarf galaxy with cross-sections determined from Reticulum II excess as detailed in text. Black lines indicate predicted spectra for $b\bar{b}$, while yellow correspond to $\tau^+\tau^-$, with the solid curve corresponding to the 3 TeV model, the dash-dotted, dashed, and dotted curves correspond to 10, 40, and 100 GeV models respectively. The solid pink curve corresponds to the 1000 hours sensitivity of the CTA [79]. Green arrows indicate the upper limits set by the Fermi-LAT observations [14], while the cyan arrow corresponds to the VLA limit [75]. Upper panel: halos use NFW profile. Lower panel: halos use Burkert profile. The left panel integrates flux over a $2'$ radius, other panels have fluxes integrated over the virial radius. The central panel covers the ASTRO-H frequency range.

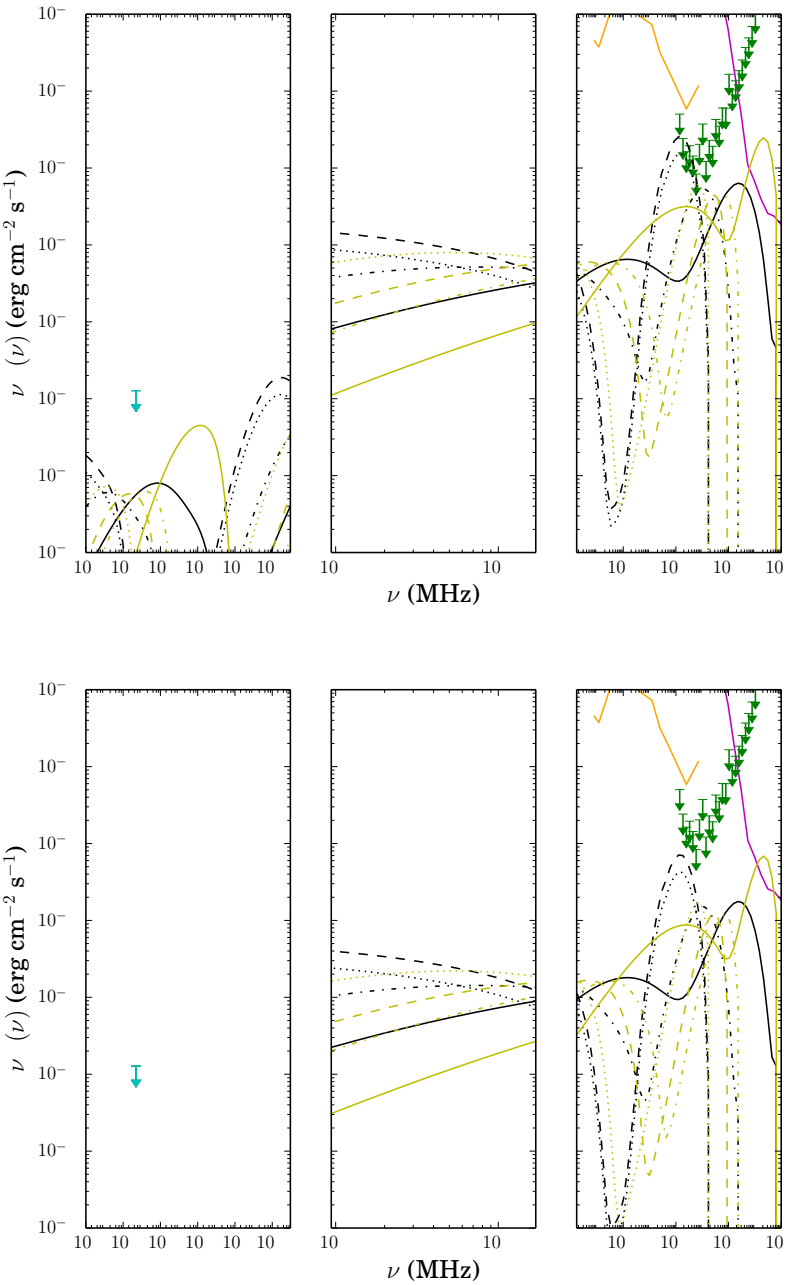

Figure 11. Dark matter $b\bar{b}$ annihilation spectra for the draco dwarf galaxy with Fermi-LAT dwarf limits. Solid curves correspond to the 3 TeV model, the dash-dotted, dashed, and dotted curves correspond to 10, 40, and 100 GeV models respectively. The solid pink curve corresponds to the 1000 hours sensitivity of the CTA [79]. Green arrows indicate the upper limits set by the Fermi-LAT observations [14], while the cyan arrow corresponds to the VLA limit [75]. Upper panel: halos use NFW profile. Lower panel: halos use Burkert profile. The left panel integrates flux over a $2'$ radius, other panels have fluxes integrated over the virial radius. The central panel covers the ASTRO-H frequency range.

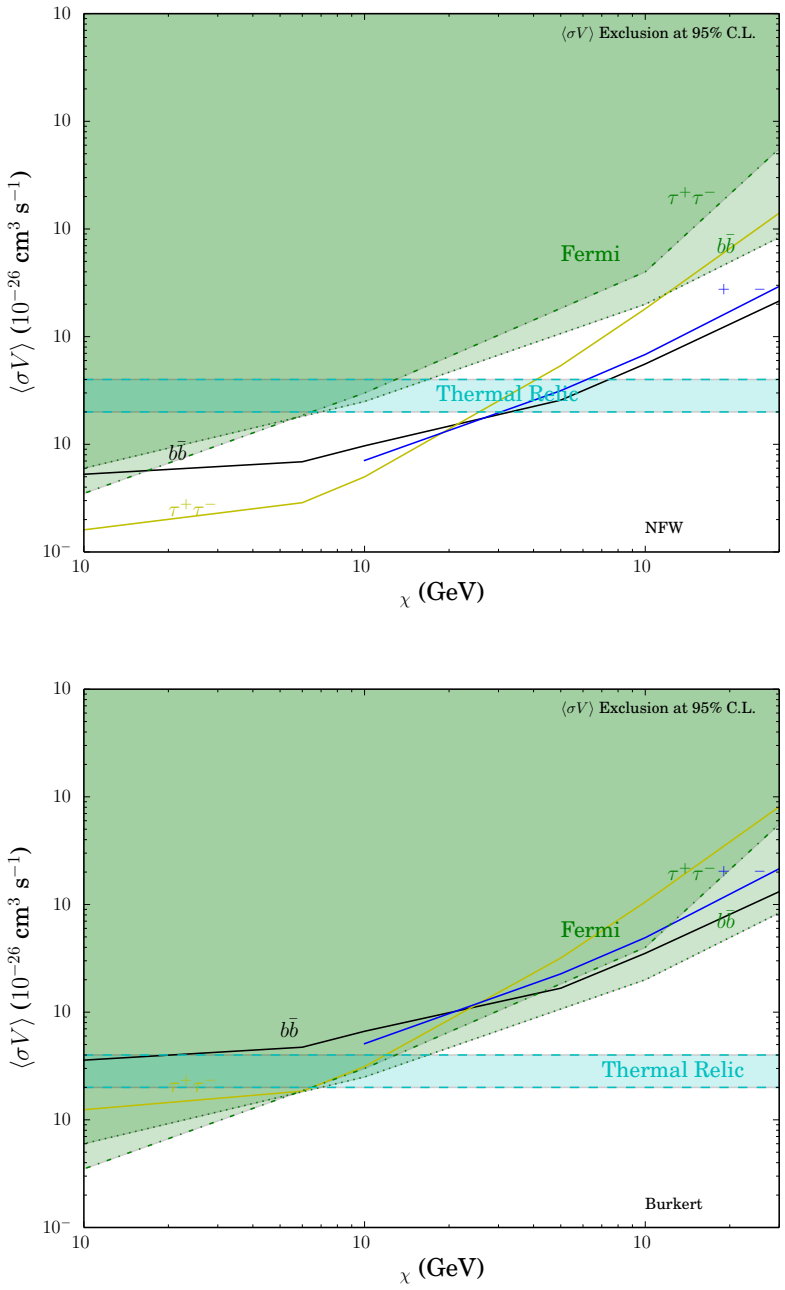

Figure 12. The 3σ cross-section limit derived from Coma is shown as a function of neutralino mass. The black curve corresponds to $b\bar{b}$, yellow to $\tau^+\tau^-$, and blue to W^+W^-. The green region is for the Fermi-LAT exclusion derived via J-factor estimation in dwarf galaxies which were assumed to be point-sources. The cyan region shows the thermal relic region. Upper panel: NFW halo profile. Lower panel: Burkert halo profile.

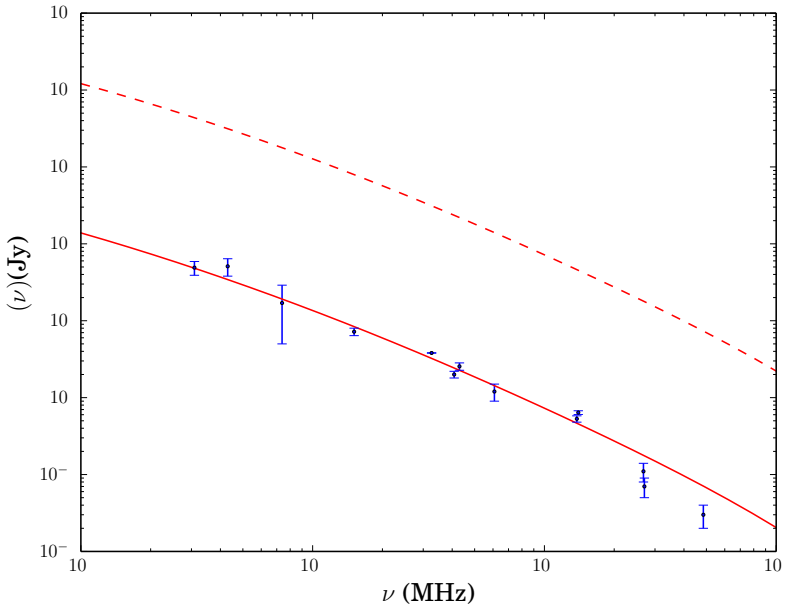

Figure 13. Comparison of spectra for $m_\chi = 40$ GeV in the $b\bar{b}$ channel with the best-fit cross-section from [29]: $\langle \sigma V \rangle = 4.7 \times 10^{-25}$ cm^3 s^{-1}. The solid curve is that using the parameters for [29] (see text) and the dashed curve uses those of this work.

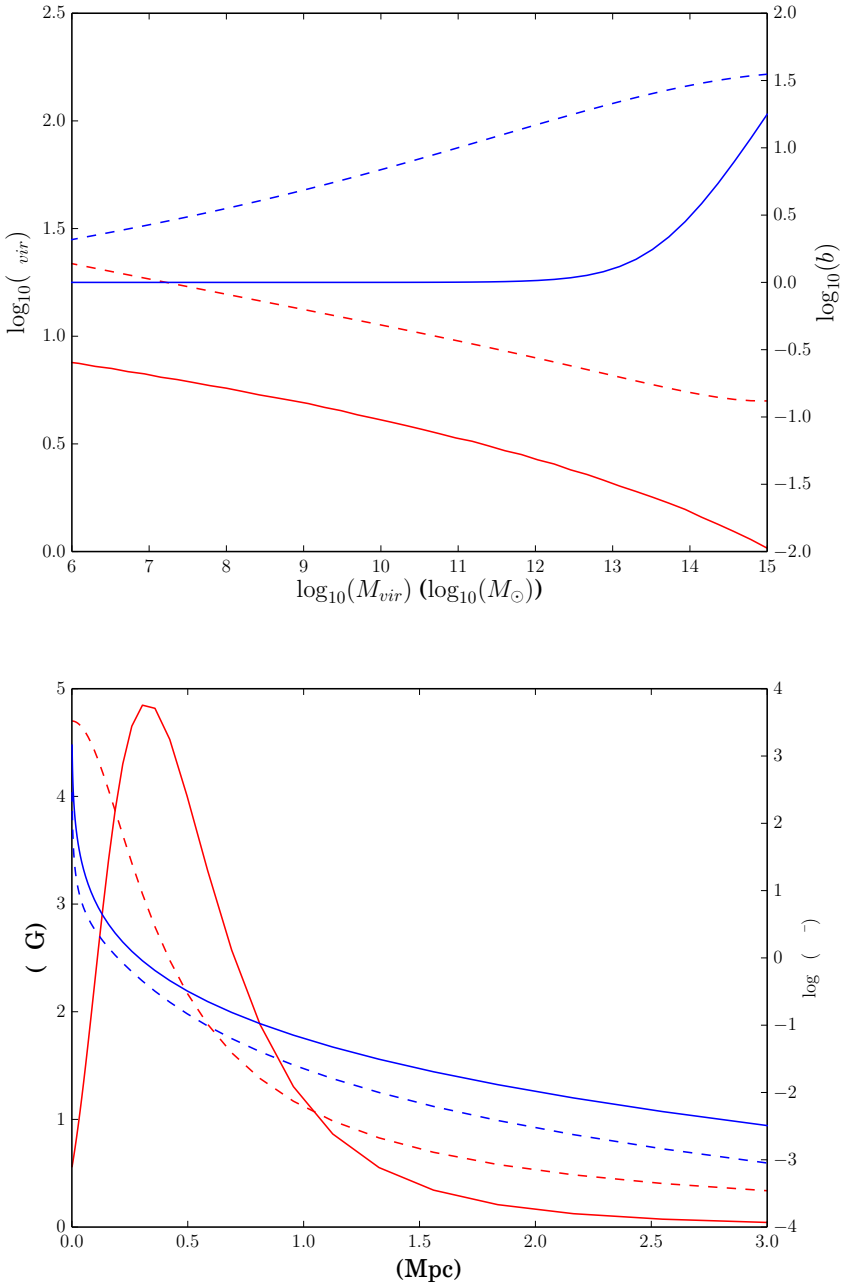

Figure 14. Comparison plots between this work and [29] for parameters relevant to Coma. Solid lines are for the [29] case while dashed lines display the parameters used in this work. Upper panel: c_{vir} and b as functions of the halo virial mass. Blue curves show the sub-structure boost factor b, while red show the parameter c_{vir}. Lower panel: ρ_{DM} (blue) and B (red) as functions of radius r.

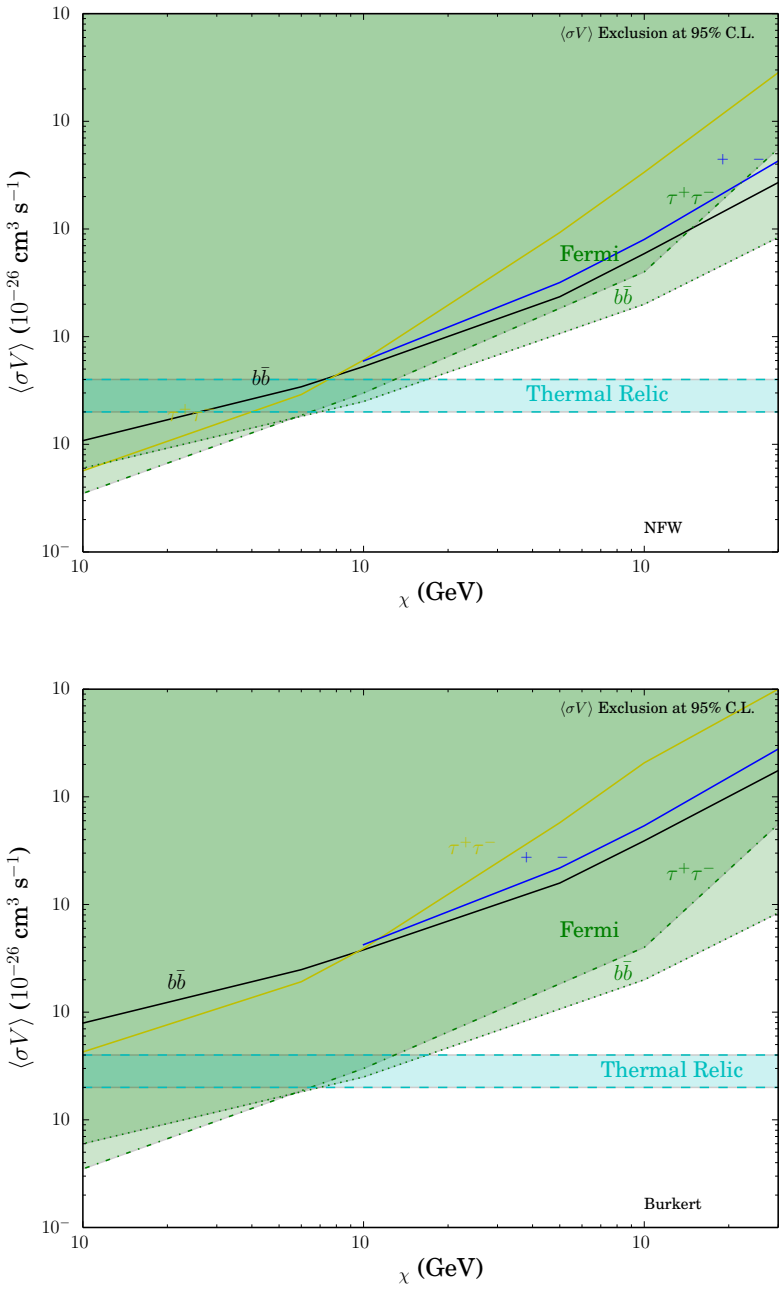

Figure 15. The 3σ cross-section limit derived from M81 data is shown as a function of neutralino mass. The black curve corresponds to $b\bar{b}$, yellow to $\tau^+\tau^-$, and blue to W^+W^-. The green region is for the Fermi-LAT exclusion derived via J-factor estimation in dwarf galaxies which were assumed to be point-sources. The cyan region shows the thermal relic region. Upper: NFW halo profile. Lower: Burkert halo profile.

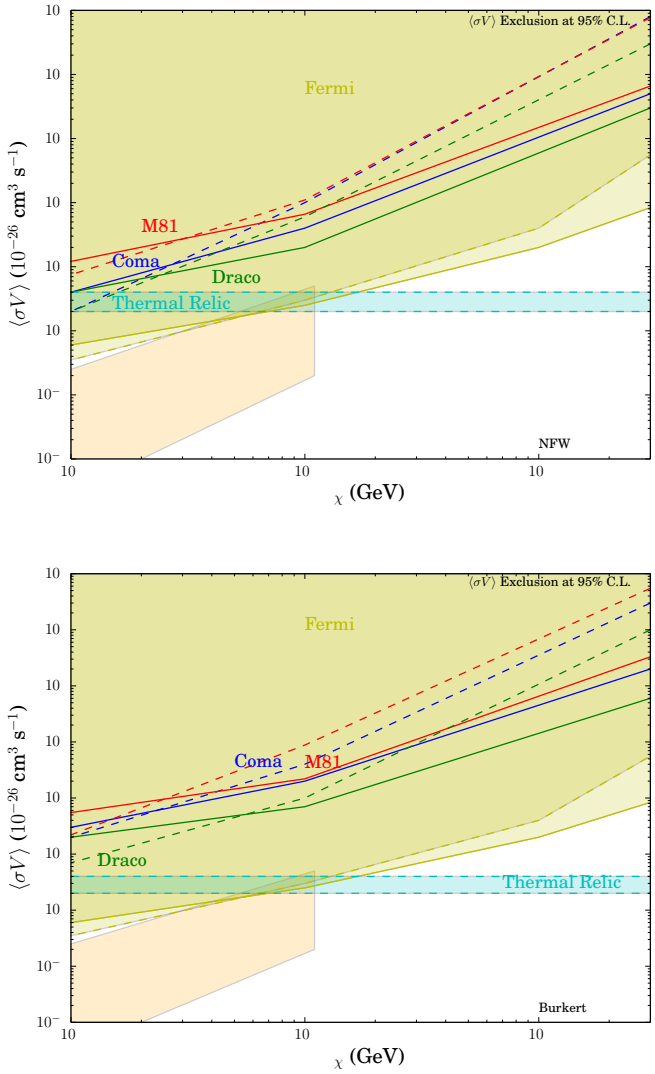

Figure 16. ASTRO-H 1000 hrs sensitivity cross-section as a function of neutralino mass. The red curve corresponds to the M81 galaxy, the green curve to the Draco dwarf and the blue to the Coma cluster. The yellow region is for the Fermi-LAT exclusion derived via J-factor estimation in dwarf galaxies which were assumed to be point-sources [19], while the cyan shaded area is the thermal wimp region, and the orange region covers the Fermi-LAT GC models. Solid curves are $b\bar{b}$ and dashed are $\tau^+\tau^-$. Upper panel: NFW halo profile. Lower panel: Burkert halo profile.

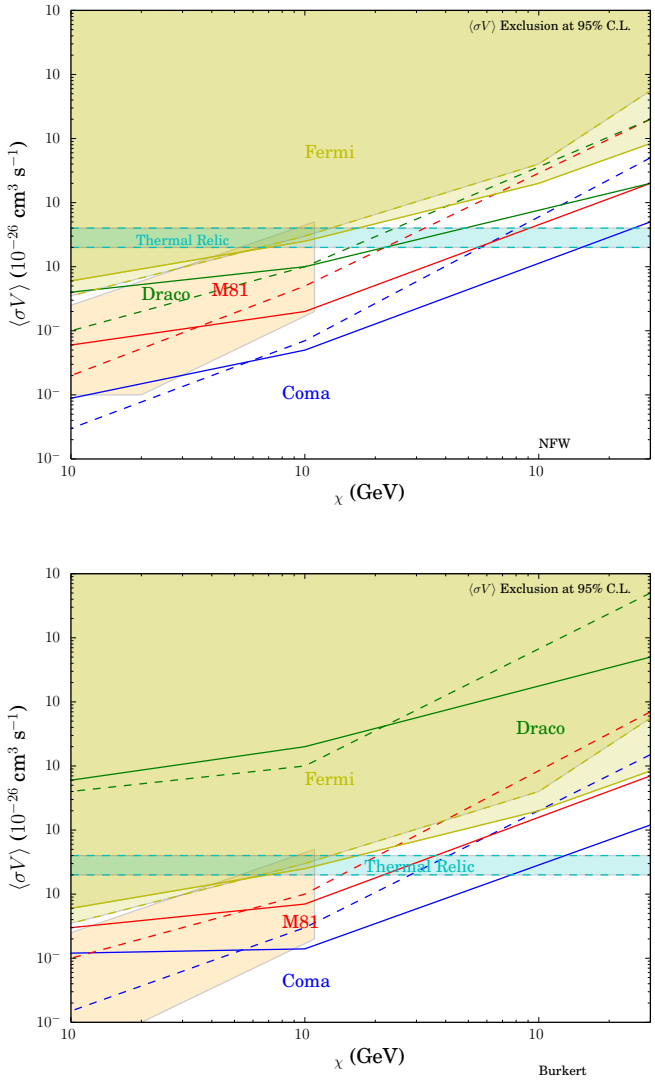

Figure 17. SKA 1000 hrs sensitivity cross-section as a function of neutralino mass. The red curve corresponds to the M81 galaxy, the green curve to the draco dwarf and the blue to the Coma cluster. The yellow region is for the Fermi-LAT exclusion derived via J-factor estimation in dwarf galaxies which were assumed to be point-sources [19], while the cyan shaded area is the thermal wimp region, and the orange region covers the Fermi-LAT GC models. Solid curves are $b\bar{b}$ and dashed are $\tau^+\tau^-$. Upper panel: NFW halo profile. Lower panel: Burkert halo profile.

Chapter 6

Going Forward with Reionisation and 21cm Emissions

The analysis presented here can obviously be extended to encompass more targets and a larger range of the parameter space. In particular, more emphasis might be placed on future prospects from various high J-factor dwarf galaxies with both radio and γ-ray observation. However, other pathways are available. The machinery built up to model dark matter annihilation in cosmic structures can be utilised to study the effect of dark matter annihilation during the Cosmic Dark Ages (CDA) and Epoch of Reionisation (EOR). In addition to this, the generic features of DM annihilation/decay on reionisation and heating of neutral gas would allow us to expand our examination to other forms of DM. Particularly, annihilation/decay products have the potential to modify levels of ionisation, heat up neutral gas, increase the production of Lyman-α photons, and to distort the Cosmic Microwave Background (CMB) energy spectrum through low-energy photon production. This is particularly significant given that neutral hydrogen will trace the dark matter distribution in large-scale structures during the cosmic dark ages. Generically dark matter models do not change the redshift of recombination but alter the residual ionisation levels. Figure 6.1 displays results from [184] showing the effects of various WIMP models on the fraction of ionised hydrogen x_e. The influence of the parameter β, which represents energy injection boosting factor due to the contribution of halos, is clearly evident. Additionally, the effect of the halo formation redshift z_h is also evident in the differences around $z \sim 10^2$, with larger values of z_h beginning to reionise hydrogen significantly earlier. The fact that the DM-induced ionised fraction is so sensitive to β and z_h is highly suggestive of the ability of any quantity sensitive to the ionisation fraction to probe the formation of cosmic structure. In order to illustrate the power of using reionisation data to constrain DM models we display Figure 6.2, taken from [188]. This shows the potential WIMP annihilation cross-section constraints that result from CMB limits on the ionised fraction of hydrogen x_e at $z \sim 6$. These constraints are highly competitive, being somewhat stronger than those from Planck experiment [26]. However, these are formulated for the most optimistic cases of the structure parameter β. In scenarios of smaller β values it will be necessary to extend the examined redshift to larger values (which CMB constraints are unsuited for), in order to avoid DM effects being eclipsed by those induced by stars (as will be seen below in Fig. 6.4).

The effects of the heating and reionisation of neutral gas will in turn produce effects on the 21-cm Hydrogen background [189, 190, 191]. This is illustrated by the Figure. 6.3, which shows results from [189] displaying the effects of sterile neutrinos and decaying dark matter on the spin temperature of the 21-cm line. The figure demonstrates that decaying dark matter is very effective at influencing the temperature of the neutral gas, this effect is strongly influenced by the mass, with light 25 keV sterile neutrinos being fair less effective than the 10 MeV dark matter. In the case of the sterile neutrino, there is little effect on the 21-cm spin temperature, however, the efficient heating of 10 MeV model results in the the CMB temperature and spin temperature remaining decoupled until $z \sim 10$. This means that future measurements of the 21-cm background will be able to effectively constrain many

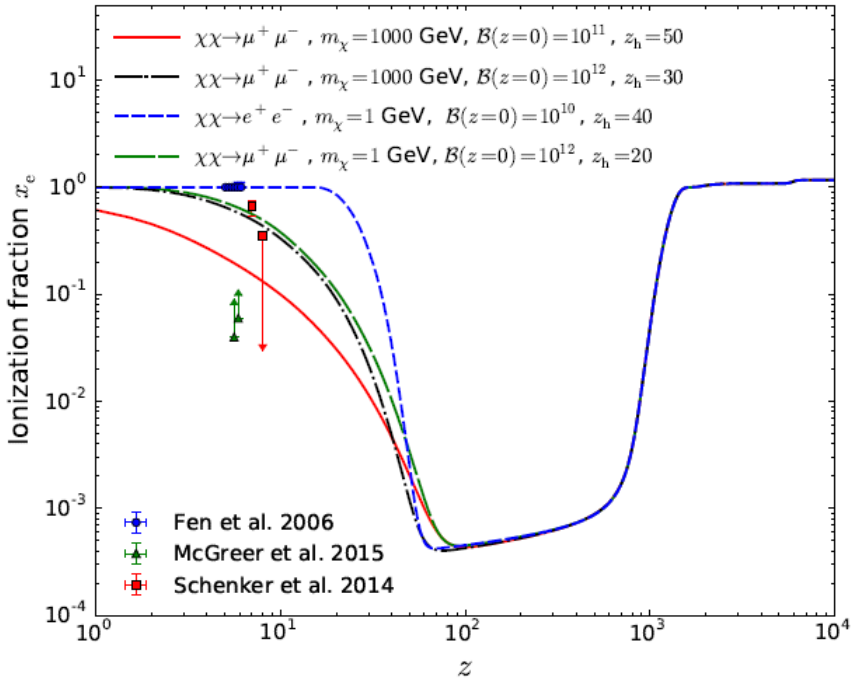

Figure 6.1: Figure from [184] showing the evolution of the ionised hydrogen fraction in a universe with reionization from DM annihilations in halos only, for the most optimistic cases, and for a few halo formation parameters all resulting in the same reionisation optical depth. The points display a few direct astrophysical bounds from [185, 186, 187]. z_h is the redshift of halo formation and β is the boosting factor from halos.

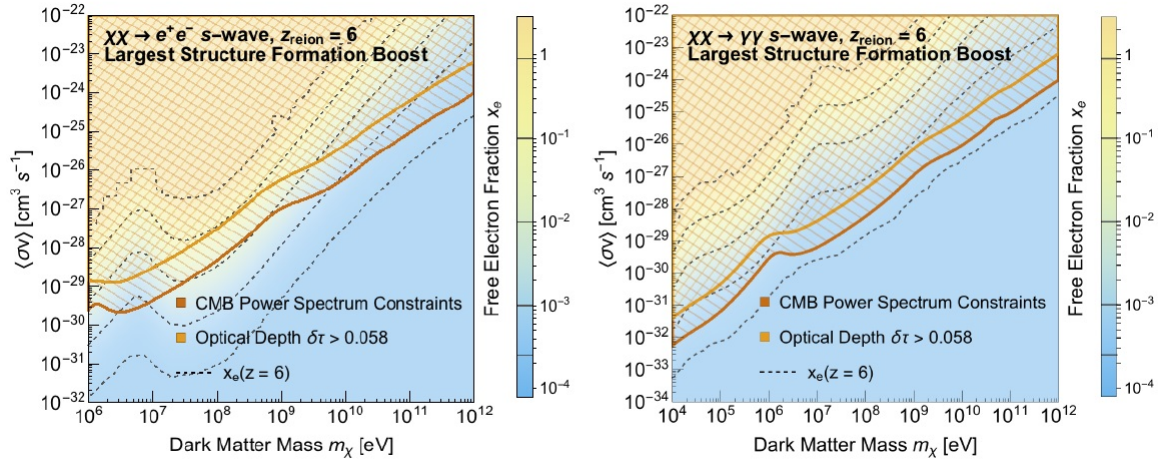

Figure 6.2: Figure from [188] showing constraints derived on the WIMP annihilation cross-section via CMB measurements of the ionisation fraction at $z = 6$ and reionisation optical depth. The colour gradient reflects the ionisation fraction x_e.

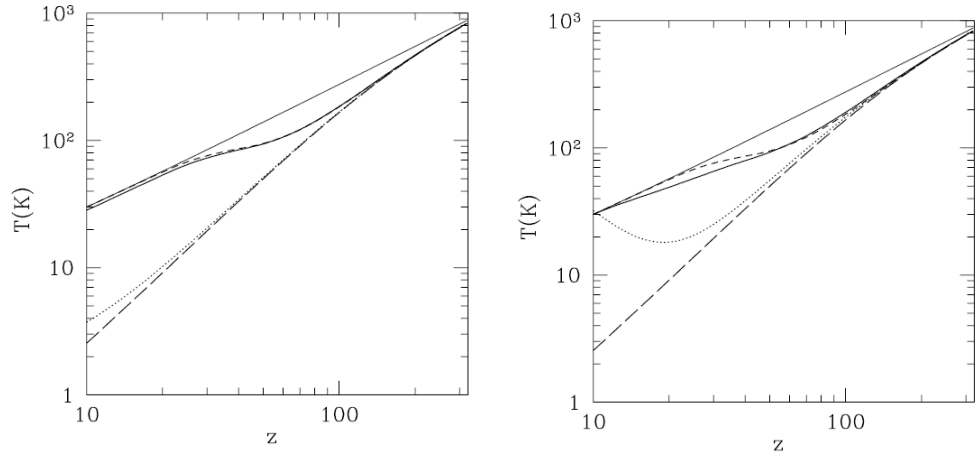

Figure 6.3: Figures from [189] showing the spin and matter temperatures as a function of redshift. *Left*: for 25 keV sterile neutrino decays. Thin solid line: CMB temperature; thick solid (short-dashed) line: spin temperature with (without) 25 keV neutrino decays; dotted (long-dashed) line: matter temperature with (without) 25 keV neutrino decays. *Right*: for 10 MeV DM decays. Thin solid line: CMB temperature; thick solid (short-dashed) line: spin temperature with (without) 10 MeV DM decays; dotted (long-dashed) line: matter temperature with (without) 10 MeV DM decays.

models of decaying dark matter.

The significance of this dark matter detection channel is greatly increased because it can be used to constrain a vast array of dark matter models, as the injection of energy into the reionisation history is a generic feature of annihilating/decaying dark matter [192]. This can also be combined with the possibility to discriminate between dark matter models based on the manner of their energy injection, as 21-cm emissions will be modified by differing reionisation histories generated within specific dark matter scenarios. In some dark matter models the 21-cm power spectrum reaches a minimum amplitude at a redshift when the matter temperature approaches that of the CMB, allowing for precision testing of these models. Additionally, the 21-cm background is highly sensitive to the effects of DM structures, rather than simply being sensitive only to a uniform DM distribution, as with the CMB power spectrum [189, 184]. As the 21-cm line is sensitive to structure formation in the CDA, it can be used to probe fundamental cosmological questions around early structure. This is illustrated in Fig. 6.4 from [184] displaying the effects of dark matter models on the matter temperature (which has a direct effect on the spin temperature as seen in Fig. 6.3). In this case we can see that the effects of DM halos might allow for a redshift window in which the DM heating effects are visible before being obscured by the effects of stellar heating. Additionally, the matter temperature is sensitive to both the redshift of halo formation z_h and the magnitude of the halo contribution β.

Furthermore, we display the Figure 6.5 from [191], which shows the evolution of differential brightness temperature of the 21-cm line (relative to the CMB) for an assumed annihilation cross-section $\langle \sigma V \rangle = 3 \times 10^{-26}$ cm^3 s^{-1}. The structure parameter c_{200} (similar to c_{vir} used in Chapter 2) has a strong effect on the visibility of the 21-cm background against the CMB. The figure also demonstrates this differential brightness temperature could be used to produce mass dependent constraints on the DM annihilation cross-section provided it can be accurately characterised by upcoming experiments, and that the temperature is also highly sensitive to the properties of DM halos.

The insensitivity of CMB power spectrum is illustrated in Figure 6.6, where it is evident that the effect of a halo-boosted model on the CMB power spectrum is almost identical to that of a smooth dark matter background (the difference is significantly below cosmic variance). In order to make the comparison valid, both the halo-boosted and smooth DM models are chosen to agree with Planck data on reionisation optical depth and angular

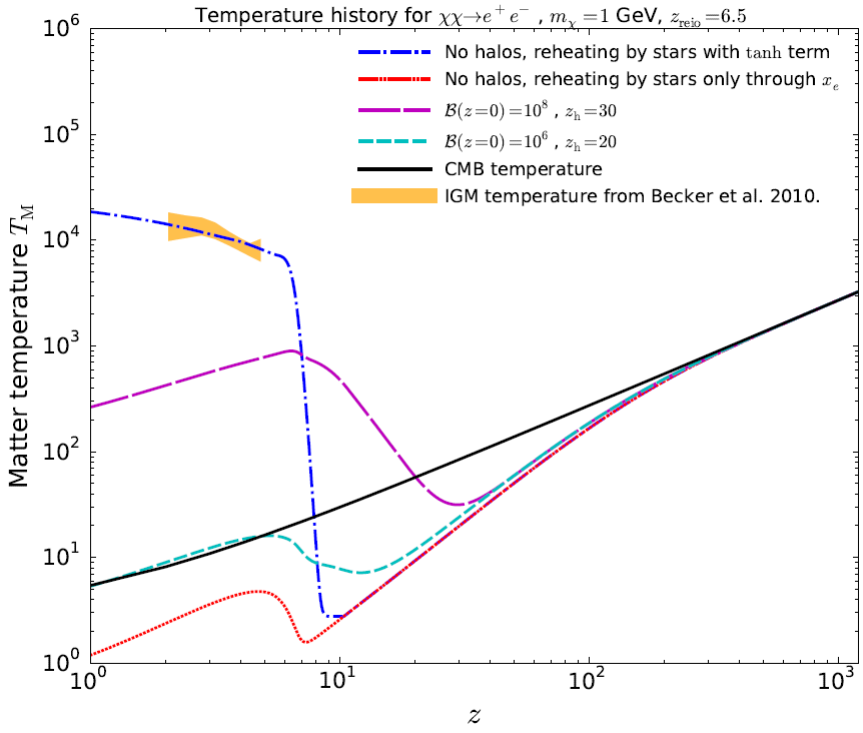

Figure 6.4: Figure from [184] showing the evolution of the matter temperature for various scenarios displayed on the plot.

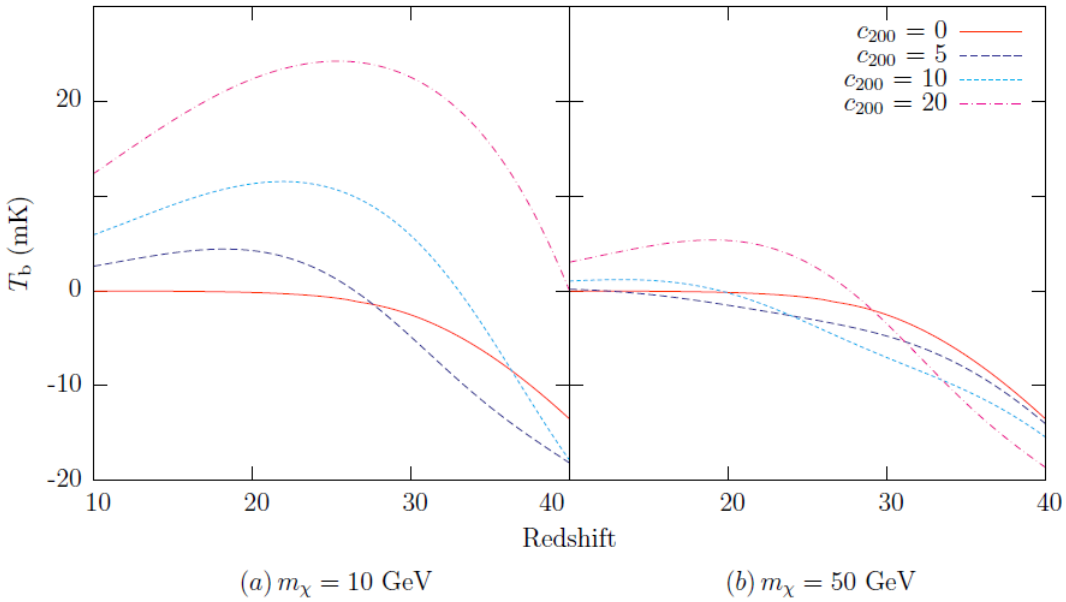

Figure 6.5: Figure from [191] showing the evolution of the differential 21-cm brightness temperature. The solid red line shows no DM heating, while the other lines show DM heating with various assumptions about the halo concentration parameter c_{200}. $\langle \sigma V \rangle$ is assumed to have the value 3×10^{-26} cm^3 s^{-1}.

sound horizon [26].

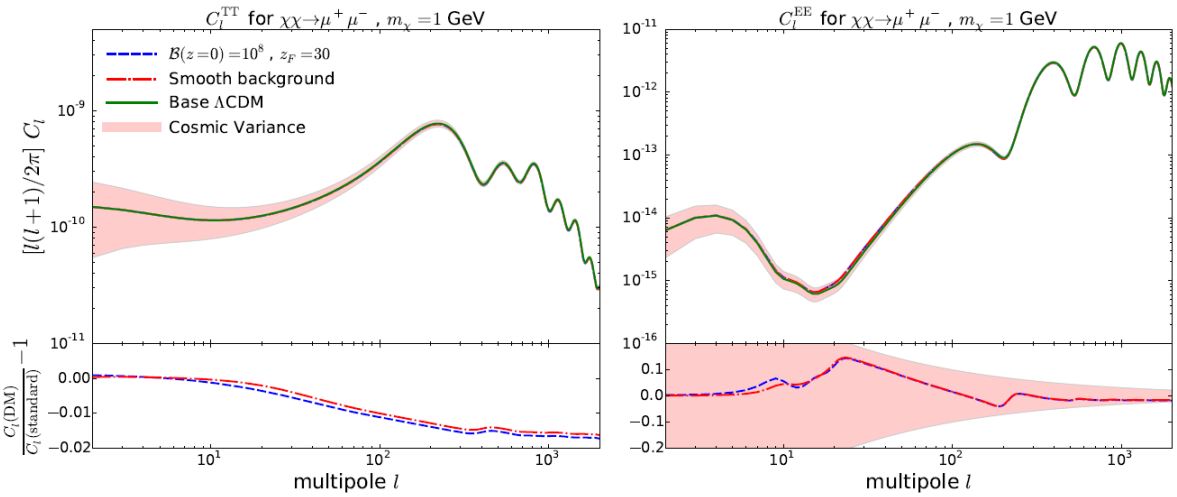

Figure 6.6: Figure from [184] showing the effect of DM energy injection on the CMB power spectrum. The lower panels show residuals against the ΛCDM model. All the displayed models agree with Planck data on reionisation optical depth and angular sound horizon [26].

Study of DM-induced modification of the 21-cm background would not only offer the chance to probe the nature of dark matter, but would be needed for a complete understanding of this background radiation in a universe that appears so strongly dominated by DM. The case for studying these phenomena can be motivated by the fact that it has been shown that DM annihilations can produce highly significant energy injections into the CDA [193] and that the 21-cm background will be more sensitive to the effects of virialised DM structures (halos) than CMB power spectra [184, 189, 190, 191].

This route of investigation is strongly motivated by upcoming projects to map 21-cm hydrogen emission, rather than analyse it statistically [194], particularly the Hydrogen Epoch of Reionisation Array (HERA), Precision Array for Probing the Epoch of Reionization (PAPER), and SKA. As seen in various figures shown here, this is needed to probe the redshifts required to differentiate between the various structure effects (β and z_h). Thus by studying the effects of dark matter on the 21-cm line, data from these projects can be utilised to greatly advance upon cosmological probes of DM, which have been mainly focussed upon the CMB [26]. Recent developments in the field [192] have also demonstrated that the effects of cooling by inverse-Compton scattering on DM-injected electrons had been underestimated in the past, and that this would lead to a suppression of DM-induced CMB distortions.

All of the preceding arguments suggest that cosmological dark matter searches need a more sensitive detection channel, if the effects of virialised structure in the CDA is to be detected, and that this can be provided by probes of the 21-cm background. The detection of dark matter effects on the 21-cm background is significant because it provides a window onto structure formation during the EOR and CDA, this being a major science goal of the SKA and vital to the testing of the standard ΛCDM cosmological paradigm.

Thus, an additional messenger channel for probing dark matter annihilation can be found through the study of the effects of dark matter on reionisation, allowing for the incorporation of yet another avenue of investigation into the efforts described here to employ multi-frequency techniques to constrain dark matter.

Chapter 7

Conclusions

In this work we have presented an argument for the use of a comprehensive multi-frequency strategy for the detection of neutralino dark matter, incorporating radio and X-ray observation in addition to the existing focus upon γ-ray detection. This was motivated by a wide-ranging study of the radio emission from dark matter halos, both in terms of the effect of the magnetic field and diffusion of the electrons themselves. This was conducted over a wide range of halo masses and red shifts in order to illustrate the power of radio telescopes, like the SKA, to locate dark matter halos via this emission, and to determine the optimal environments on which to focus radio dark matter searches. We demonstrated that the SKA, in particular, has the ability to target galaxy clusters out to redshifts $z \sim 1$ and local dwarf galaxies. These targets can produce limits on the dark matter cross-section between 3 and 6 orders of magnitude below the thermal relic level. This is greatly in excess of any existing experiment or observation set. This illustrates the competitive potential of the SKA even if it will be reduced by confusion limits and source subtraction processes. In fact when we incorporated confusion with background radio emissions in Chapter 5 we showed that the potential constraints from a galaxy cluster like Coma remain at least 2 orders of magnitude below the the thermal relic level.

We argued further that the polarimetry and rotation measure capability of the SKA is sufficient to resolve the magnetic field structure of target environments. Thus obviating the central uncertainty in the detection of dark matter radio emission. This was part of a broader plan illustrating the case for the detection of dark matter in radio as being an area in which the SKA can produce extremely valuable scientific data. This argument outlined the properties of the SKA that make it uniquely suited to this project. In particular, its high angular resolution allows it to distinguish between non-thermal astrophysical sources and dark matter emissions. Confusion limits in this regard are rapidly reached even in current instruments, thus the angular resolution of the SKA is needed, as it can employed in order to perform a source subtraction, utilising the long array baselines to locate small-scale sources. This allows SKA observation to overcome the confusion limit and put robust limits on possible dark matter models via radio observation. The proposed upgrade to SKA phase-2 is also argued to expand the reach of the SKA over the neutralino parameter space by granting it the power to observe inverse-Compton emission from electrons produced by neutralino annihilations, as well as increasing its sensitivity. We note that the performance in these observations is subject to the caveat that the effect of source subtraction on SKA sensitivity is as yet unknown. This is particularly important in dwarf galaxies where diffusion makes the radio emissions extended, increasing the effect of the confusion limit.

Our argument culminated in the demonstration of the effectiveness of multi-frequency analysis in constraining dark matter models. This was done by taking sources with observational limits in various regions of the spectrum and comparing the predictions of dark matter models suggested to be compatible with the AMS/Fermi/PAMELA (AFP) anti-particle excesses as well as the galactic centre γ-ray excess observed by Fermi-LAT. We demonstrated that neutralinos with masses above 10 GeV are in tension with existing measurements of the Coma cluster in particular. With the AFP models being ruled out in most

scenarios within the Draco dwarf galaxy as well. Furthermore, we cast doubt upon a dark matter interpretation of the excess seen by Fermi-LAT in the Reticulum-2 dwarf galaxy. Finally we examined the prospects of the ASTRO-H satellite mission to probe the dark matter parameter space. This analysis indicated that, in the soft X-rays, ASTRO-H has the potential to set very competitive limits on neutralino models, provided environments with favourable X-ray backgrounds can be found. Additionally, it is sensitive to regions of the Inverse-Compton spectrum which are strongly indicative of the neutralino mass and annihilation channel. These properties make X-ray observation by ASTRO-H an excellent compliment to the power of the SKA demonstrated earlier. Furthermore, these two experiments will serve as strong consistency checks on γ-ray and anti-particle detection methods.

Therefore, we have demonstrated the power of future experiments in the X-ray and radio regions of the spectrum to constrain the neutralino parameter space. The utilisation of these regions of the spectrum allow for powerful consistency checks that help to eliminate models that are only satisfactory in a particular environment or within a limited spectral region. Thus, the future of dark matter searches must be strongly oriented towards multi-frequency methodology, making use of the upcoming experiments like the SKA and ASTRO-H to compliment existing projects aimed at detecting dark matter in high energy products.

Appendix A

Bibliography

[1] Zwicky, F., 1933, Helvetica Physica Acta, **6**, 110-127.

[2] Dietrich, J. et al, 2012, Nature, **487**, Issue 7406, 202-204.

[3] Koopmans, L.V. & Treu, T., Astrophys. J., 2003, **583**, 606 [arXiv:astro-ph/0205281].

[4] Metcalf, R. B., Moustakas, L. A., Bunker, A. J. & Parry, I. R., 2003, arXiv:astro-ph/0309738.

[5] Hoekstra, H., Yee, H. & Gladders, 2002, M., New Astron. Rev., **46**, 767 [arXiv:astro-ph/0205205].

[6] Moustakas, L. A. & Metcalf, R. B., 2003, MNRAS, **339**, 607 [arXiv:astro-ph/0206176].

[7] Jungman, G., Kamionkowski, M. & Griest, K.,1996, J. Phys. Rep., **267**, 195.

[8] Bertone, G., Hooper, D. & Silk, J., 2005, J. Phys. Rep., **405**(5), 279.

[9] Moffat, J.W. et al., 2007, arXiv:0710.0364 [astro-ph].

[10] Duffy, L. D. & van Bibber, K., 2009, New J. Phys., **11**, 105008.

[11] Weinberg, S., 1978, Phys. Rev. Lett., **40**, 223.

[12] Wilczek, F., 1978, Phys. Rev. Lett., **40**, 279.

[13] Frampton, P., Kawasaki, M., Takahashi, F. & Yanagida, T., 2010, arXiv:1001.2308 [hep-ph].

[14] Feng, J., 2010, ARA & A, **48**, 495.

[15] Petraki, K. & Volkas, R., 2013, Int. J. Mod. Phys. A, **28**, 1330028.

[16] Gaitskell, R., 2004, Annu. Rev. Nucl. Part. Sci., **54**, 315.

[17] Carr, J. *et al*., 2006, Rep. Prog. Phys., **69**, 2475.

[18] Colafrancesco, S., 2010, arXiv:1004.3869 [astro-ph.CO].

[19] Bauer, D. *et al*.., 2013, arXiv:1305.1605 [hep-ph].

[20] Aartsen, M. *et al*. for the IceCube collaboration, 2013, Phys. Rev. D, **88**, 122001.

[21] Fraser, G., 2014, arXiv:1403.2436 [astro-ph.HE].

[22] Arik, M. et al. (CAST Collaboration), 2011, Phys. Rev. Lett., **107**, 261302.

[23] Ohta, R. *et al*., 2012, Nuclear Inst. and Methods in Physics Research A, pp. 73-78.

[24] Aprile, E. *et al*. for the Xenon100 collaboration, 2012, Astropart. Phys., **35**, 573-590.

[25] t Hooft, G., in: Recent Developments in Gauge Theories, Proc. NATO Advanced Summer Institute, Cargese, 1979, eds. t Hooft, G., et al. (Plenum, New York), 1980, 135.

[26] Ade, P. et al. for the Planck Collaboration, 2015, arXiv:1502.01589 [astro-ph].

[27] Bersanelli, M. *et al*., 2010, A& A, **520**, A4.

[28] Ackermann, M. et al. for the Fermi-LAT collaboration, 2014, Phys. Rev. D, **89**, 042001, arXiv:1310.0828 [astro-ph.HE].

[29] Drlica-Wagner, A. *et al*. for the Fermi-LAT collaboration & Abbott, T. *et al*. for the DES collaboration, 2015, arXiv: 1503.02632 [astro-ph].

[30] Atwood, W. B. *et al*. for the Fermi/LAT collaboration, 2009, Astrophys. J., **697**,1071, arXiv:0902.1089 [astro-ph].

[31] Regis, M., Colafrancesco, S., Profumo, S., de Blok, W. J. G., Massardi, M., Richter, L., 2014, JCAP, **10**, 016.

[32] Hooper, D. & Linden, T., 2011, Phys. Rev. D, **84**, 123005.

[33] Hooper, D., Linden, T. & Mertsch, P., 2015, JCAP, **03**, 021, arXiv:1410.1527 [astro-ph].

[34] Calore, F., Cholis, I., McCabe, C. & Weniger, C., 2015, Phys. Rev. D, **91**, 063003, arXiv:1411.4647 [astro-ph].

[35] O'Leary, R., Kistler, M., Kerr, M. & Dexter, J., 2015, arXiv:1504.02477 [astro-ph].

[36] Bartels, R., Krishnamurthy, S. & Weniger, C. , 2015, arXiv:1506.05104 [astro-ph].

[37] Lee, S. K. *et al*., 2015, arXiv:1506.05124 [astro-ph].

[38] Brandt, T. & Kocsis, B., 2015, arXiv:1507.05616 [astro-ph].

[39] Carlson, E., Linden, T. & Profumo, S., 2015, arXiv: 1510.04698 [astro-ph].

[40] Picozza, P. *et al*., 2007, Astropart. Phys., **27**(4), 296.

[41] Kounine, A. on behalf of the AMS collaboration, 2012, Int. J. Mod. Phys. E, **21**, 1230005.

[42] Cholis, I. & Hooper, D., 2013, Phys. Rev. D, **88**, 023013, arXiv:1304.1840 [astro-ph].

[43] Geringer-Sameth, A. *et al*., 2015, arXiv:1503.02320 [astro-ph].

[44] Bonnivard, V. *et al*., 2015, ApJ, **808**, L36.

[45] Di Mauro, M. & Vittino, A., 2015, PoS: *The 34th International Cosmic Ray Conference*, arXiv:1507.08680 [astro-ph.HE].

[46] `http://astro-h.isas.jaxa.jp/researchers/sim/sensitivity.html`.

[47] Pieri L. *et al*., 2011, Phys. Rev. D., **83**, 023518.

[48] Lamanna, G., Farnier, C., Jacholkowska, A., Kieffer, M., & Trichard, C. For The H.E.S.S. Collaboration, 2013, arXiv:1307.4918 [astro-ph.HE].

[49] Funk, S., 2013, arXiv:1310.2695 [astro-ph.HE].

[50] Conrad, J., 2012, arXiv:1210.4392 [astro-ph.CO].

[51] Morselli, A., Canadas, B. & Vitale, V. on behalf of the Fermi LAT collaboration, 2010, arXiv:1012.2292 [astro-ph].

[52] Bergström, L. & Kaplan, J., 1994, Astropart. Phys., **2**(3), 261.

[53] Gondolo, P., 1994, Nucl. Phys. B (Proc. Suppl.), **35**, 148.

[54] Gondolo, P. & Silk, J., 1999, Phys. Rev. D., **83**, 1719.

[55] Pieri, L. & Branchini, E., 2004, Phys. Rev. D., **69**, 043512.

[56] Colafrancesco, S., Profumo, S. & Ullio, P., 2006, A&A, **455**, 21.

[57] Siffert, B., Limone, A., Borriello, E., Longo, G. & Miele, G., 2011, MNRAS, **410**, 2463.

[58] Linden, T., Hooper, D. & Yusef-Zadeh, F., 2011, arXiv:1106.5493 [astro-ph.HE].

[59] Storm, E., Jeltema, T., Profumo, S. & Rudnick, L., 2012, arXiv:1210.0872 [astro-ph.CO].

[60] Spekkens, K., Mason, B., Aguirre, J. & Nhan, B., 2013, arXiv:1301.5306 [astro-ph.CO].

[61] Egorov, A. E. & Pierpaoli, E., 2013, Phys. Rev. D, **88**, 023504.

[62] Krause, M., Alexander, P., Bolton, R., et al., 2009, MNRAS, **400**, 646.

[63] Bogdanovic, T., Reynolds, C. S., Massey, R., 2011, ApJ, **731**, 7.

[64] Dewdney, P., Turner, W., Millenaar, R., McCool, R., Lazio, J. & Cornwell, T., 2012, *SKA baseline design document*, `http://www.skatelescope.org/wp-content/uploads/2012/07/SKA-TEL-SKO-DD-001-1_BaselineDesign1.pdf`.

[65] Colafrancesco, S., Marchegiani, P. & Beck, G., 2015, JCAP, **02**, 032C.

[66] Bottino, A., Donato, F., Fornengo, N. & Scopel, S., 2008, Phys. Rev. D, **77**, 127301.

[67] Ackerman, M. *et al.*, 2010, JCAP, **5**, 25.

[68] Colafrancesco , S. et al, arXiv:1502.03738 [astro-ph], to appear in Proceedings of Science.

[69] Beck, G. & Colafrancesco, S., 2015, arXiv: 1508.01386 [astro-ph.CO], accepted by JCAP.

[70] Rubin, V. & Ford, W., 1970, ApJ, **159**, 379.

[71] Brownstein, J. R. & Moffat, J. W., 2006, Astrophys.J., **636**, 721.

[72] Will, C. M., 2005, Living Rev. Rel., **9**, 3.

[73] Campbell, R. M. *et al.*, 1995, AJ, **110**, 2566.

[74] Porcas, R. W. *et al.*, 1979, Nature, **282**, 385.

[75] Wald, R. M., 1984, *General Relativity*, The University of Chicago Press (Chicago).

[76] Weisskopf, M. C., 1988, Space Science Reviews, **40**, 47.

[77] Weisskopf, M.C. *et al.*, 1987, Ap. Lett. Comm., **26**, 1.

[78] Markevitch, M. *et al.*, 2004, ApJ., **606** (2), 819.

[79] Clowe, D., Gonzalez, A. & Markevitch, M., 2004, ApJ, **604**, 596.

[80] Tyson, J. A., Kochanski, G. P. & DellAntonio, I. P., 1998, Astrophys. J. Lett., **498**, 107.

[81] Boggess, N.W., *et al.*, 1992, ApJ, **397**, 420.

[82] Hinshaw, G. *et al.* for the WMAP collaboration, 2012, arXiv: 1212.5226 [astro-ph].

[83] Sarkar, S., 1996, Rep. Prog. Phys., **59**, 1493.

[84] Schramm, D. N., & Turner, M., 1998, Rev, Mod. Phys. **70**, 303.

[85] Olive, K.A. & Thomas, D., 1997, Astropart. Phys., **7**, 27.

[86] Olive, K. A., 2000, arXiv:0009475 [astro-ph].

[87] Bahcall, N., Ostriker, J. P., Perlmutter, S. & Steinhardt, P. J., 1999, Science, **284**, 1481.

[88] Bergström, L., 2000, Rept.Prog.Phys., **63**, 793.

[89] Kashlinsky, A., 1998, Phys. Rep., **307**, 67.

[90] Bahcall, N. & Fan, X., 1998, ApJ, **504**, 1.

[91] Carlberg, R. G. *et al*., 1999, ApJ, **516**, 552.

[92] Holder, G. P.& Carlstrom, J. E., 1999, *Microwave Foregrounds, ASP Conference Series 181*, ed. de Oliveira-Costa, A. & Tegmark, M., p.199.

[93] Preskill, J., Wise, M. B. & Wilczek, F., 1983, Physics Letters B, **120**, 127.

[94] Ellis, J. *et al*., 1984, Nuclear Physics B, **238**, 453.

[95] Destri, C., de Vega, H. J. & Sanchez, N. G., 2013, New Astronomy, **22**, 39.

[96] Lovell, M. R., Frenk, C. S., Eke, V. R., Jenkins, A., Gao, L. & Theuns, T., 2014, MNRAS, **439**, 300.

[97] Frenk, C. S. & White, S. D. M., 2012, Ann. Phys., **524**, 507.

[98] Bardeen, J. M., Bond, J. R., Kaiser, N. & Sza- lay, A. S., 1986, ApJ, **304**, 15.

[99] Peebles, P. J. E., 1980, *Large-scale Structure of the Universe* (Princeton University Press).

[100] Navarro, J. F., Frenk, C. S. & White, S. D. M., ApJ, 1996, **462**, 563.

[101] Navarro, J. F. , Frenk, C. S. & White, S. D. M., 1996, ApJ, **462**, 563.

[102] Navarro, J. F. , Frenk, C. S. & White, S. D. M., 1997, ApJ, **490**, 493.

[103] Bullock, J.S. *et al*.., 2001, MNRAS, 321, 559.

[104] Muñoz-Cuartas, J. C., Macci, A. V., Gottlöber, S. & Dutton, A. A., 2010, arXiv:1007.0438 [astro-ph.CO].

[105] Prada, F. *et al*., 2012, MNRAS, **423** (4), 3018, arXiv:1104.5130 [astro-ph].

[106] Ng, K. *et al*., 2014, Phys. Rev. D, **89**, 083001, arXiv: 1310.1915 [astro-ph.CO].

[107] Einasto, J., 1968, Publications of the Tartuskoj Astrofizica Observatory, **36**, 414.

[108] Burkert, A., 1995, ApJ, **447**, L25.

[109] Walker, M. G., Mateo, M., Olszewski, E. W., Pearrubia, J., Evans, N. W. & Gilmore, G., 2009, ApJ, **704**, 1274.

[110] Adams, J. J. *et al*., 2014, arXiv:1405.4854 [astro-ph.GA].

[111] Gelato, S. & Sommer-Larsen, J., 1999, MNRAS, **303**, 321.

[112] Salucci, P., 2001, MNRAS, **320**, L1.

[113] de Blok, W. J. G., 2010, Advances in Astronomy, **2010**, Article ID 789293.

[114] Boylan-Kolchin, M., Bullock, J. S. & Kaplinghat, M., 2011, MNRAS, **415**, L40.

[115] Ogiya, G.& Burkert, A., 2015, MNRAS, **446**(3), 2363.

[116] Nagai, D. & Kravtsov, A. V., 2005, ApJ, 618, 557.

[117] Sanchez-Conde, M. & Prada, F., 2014, MNRAS, **442** (3), 2271, arXiv:1312.1729 [astro-ph].

[118] Lewin, J. & Smith, P, 1996, Astropart. Phys., **6**, 87.

[119] Marrodán Undagoitia, T. & Rauch, L., 2015, arXiv: 1509.08767 [physics.ins-det].

[120] Drukier, A., Freese, K. & Spergel, D., 1986, Phys. Rev. D, **33**, 3495.

[121] Spergel, D. N., 1988, Phys. Rev. D, **37**, 1353.

[122] Snowden-Ifft, D. P., Martoff, C. J., & Burwell, J. M., 2000, Phys. Rev. D, **61**, 101301, arXiv:astro-ph/9904064.

[123] Abe, K. *et al.*, 2013, Nucl. Instrum .Meth. A, **716**, 78, arXiv:1301.2815.

[124] Agnes, P. *et al.*, 2015, Phys. Lett. B, **743**, 456, arXiv:1410.0653.

[125] Aprile, E. *et al.*, 2012, Phys. Rev. Lett., **109**, 181301, arXiv:1207.5988.
cogent,dama2,crest2,cdms2,edelweiss2,xenon10,simple,zeplin3,coupp

[126] Aalseth, C. E. *et al.*, 2013, Phys. Rev. D, **88**, 012002.

[127] Savage, C. *et al.*, 2009, JCAP, **0904**, 010.

[128] Angloher, G. *et al.*, 2012, Eur. Phys. J. C, **72**,1971.

[129] Ahmed, Z. *et al.*, 2010, Science, **327**, 1619.

[130] Armengaud, E. *et al.*, 2011, Phys. Lett. B, **702**, 329.

[131] Angle, J. *et al.*, 2011, Phys. Rev. Lett., **107**, 051301.

[132] Felizardo, M. *et al.*, 2011, arXiv:1106.3014

[133] Akimov, D. *et al.*, 2012, Phys. Lett. B, **709**, 14.

[134] Behnke, E., *et al.*, 2012, arXiv:1204.3094.

[135] Akerib, D. *et al.*, 2013, Nucl.Instrum.Meth. A, **704**, 111, arXiv:1211.3788.

[136] Agnese, R. *et al.*, 2009, arXiv:0912.3592 [hep-ex].

[137] Agnese, R. *et al.*, 2013, arXiv:1309.3259

[138] Aprile, E. *et al.*, 2011, Phys. Rev. Lett., **107**, 131302.

[139] Ahmed, Z. *et al.*, 2001, Phys. Rev. Lett., **106**, 131302.

[140] Agnese, R. *et al.*, 2013, Phys. Rev. Lett., **111**, 251301.

[141] Bernabei, R. *et al.*, 2008, Eur. Phys. J. C , **56**, 333.

[142] Bernabei, R. *et al.*, 2008, Nucl. Instrum. Meth., **A592**, 297, arXiv:0804.2738.

[143] Green, A. M., 2010, JCAP, **1010**, 034, arXiv:1009.0916 [astro-ph.CO].

[144] McCabe, C., 2010, Phys.Rev. D, **82**, 023530, arXiv:1005.0579 [hep-ph].

[145] Pato, M., Baudis, L., Bertone, G., de Austri, R. R., Strigari, L. E. & Trotta, R., 2011, Phys.Rev. D, **83**, 083505.

[146] Feng, J. L. & Kumar, J., 2008, Phys.Rev.Lett., **101**, 231301, arXiv: 0803.4196.

[147] Askew, A., Chauhan, S., Penning, B., Shepherd, W. & Tripathi, M., 2014, International Journal of Modern Physics A, **29**, 1430041, arXiv: 1406.5662.

[148] Nath, P. *et al.*, 2010, Nucl. Phys. Proc. Suppl., **200-202**, 185, arXiv:1001.2693 [hep-ph].

[149] Bertone, G., Cerdeno, D. G., Fornasa, M., de Austri, R. R. & Trotta, R., 2010, Phys.Rev. D, **82**, 055008.

[150] Goodman, J., Ibe, M., Rajaraman, A., Shepherd, W., Tait, T. M. *et al.*, 2011, Phys.Lett. B, **695**, 185, arXiv: 1005.1286.

[151] Goodman, J., Ibe, M., Rajaraman, A., Shepherd, W., Tait, T. M. *et al.*, 2010, Phys.Rev. D, **82**, 116010, arXiv: 1008.1783.

[152] Busoni, G., De Simone, A., Morgante, E. & Riotto, A., 2014, Phys.Lett. B, **728**, 412, arXiv: 1307.2253.

[153] An, H., Wang, L.-T. & Zhang, H., 2013, arXiv: 1308.0592.

[154] DiFranzo, A., Nagao, K. I., Rajaraman, A. & Tait, T. M. P., 2013, JHEP, **1311**, 014, arXiv: 1308.2679.

[155] Buchmueller, O., Dolan, M. J. & McCabe, C., JHEP, **1401**, 025, arXiv: 1308.6799.

[156] Chang, S., Edezhath, R., Hutchinson, J. & Luty, M., 2014, Phys.Rev. D, **89**, 015011, arXiv: 1307.8120.

[157] Tech. Rep. CMS-PAS-EXO-12-048, 2013, CERN, Geneva.

[158] Profumo, S., Shepherd, W. & Tait, T., 2013, arXiv: 1307.6277.

[159] Della Negra, M., Petrilli, A., Herve, A. & Foa, L., 2006, *CMS Physics Technical Design Report Volume I: Software and Detector Performance*, `http://doc.cern.ch/ /archive/electronic/cern/preprints/lhcc/public/lhcc-2006-001.pdf`.

[160] CMS Collaboration, 2016, Phys. Lett. B, **755**, 102, arXiv:1410.8812 [hep-ex].

[161] Choi, K. *et al.*, 2015, arXiv: 1503.04858.

[162] Aartsen, M. *et al.*, 2016, JCAP, **04**, 022, arXiv:1601.00653 [hep-ph].

[163] Aad, G. *et al.*, 2008, JINST, **3**, S08003.

[164] Aad, G. *et al.*, 2015, Eur. Phys. J. C, **75**(7), 299, arXiv:1502.01518 [hep-ex]. [Erratum: 2015, Eur. Phys. J. C, **75**(9), 408].

[165] Fox, P. J., Harnik, R., Kopp, J. & Tsai Y., 2012, Phys. Rev. D, **85**, 056011, arXiv: 1109.4398.

[166] Ackermann, M. *et al.*, 2011, Phys.Rev.Lett., **107**, 241302, arXiv: 1108.3546.

[167] Sjöstrand, T., 1994, Comput. Phys. Commun., **82**, 74.

[168] Gondolo, P., Edsjo, J., Ullio, P., *et al.*. 2004, JCAP, **0407** ,008.

[169] Colafrancesco, S. & Blasi, S., 1998, Astropart. Phys., 9, 227.

[170] Baltz, E. A. & Edjso, J., 1999, Phys. Rev. D, **59**, 023511.

[171] Baltz, E. A. & Wai, L., 2004, Phys. Rev. D, **70**, 023512.

[172] Longair, M. S., 1994, *High Energy Astrophysics* (Cambridge University Press).

[173] Padmanabhan, T., 2000, *Theoretical Astrophysics, Volume 1* (Cambridge University Press).

[174] Hofmann, W., 1997, Proc. of the Workshop: *Towards a major atmospheric Cherenkov detector - V*, Kruger Park, O.C. de Jager (Ed.), p. 405.

[175] Abramowski, A. *et al*., 2014, Phys. Rev. D, **90**, 112012.

[176] Griest, K. & Seckel, D., Nucl. Phys. B, **283**, 681. [Erratum: 1988, Nucl. Phys.B, **296**, 1034].

[177] Aartsen, M. *et al*., 2013, Phys.Rev.Lett., **110**(13), 131302, arXiv:1212.4097 [astro-ph.HE].

[178] Heisig, J., Krämer, M., Pellen, M. & Wiebusch, C., 2016, Phys. Rev. D, **93**, 055029, arXiv: 1509.07867.

[179] Savage, C., Scaffidi, A., White, M. & Williams, A. G., 2015, Phys. Rev. D, **92**, 103519, arXiv:1502.02667.

[180] Akerib, D., *et. al*., 2014, Phys. Rev. Lett., **112**, 091303, arXiv:1310.8214.

[181] Cahill-Rowley, M. W., Hewett, J. L., Ismail, A., Peskin, M. E. & Rizzo, T. G., 2013, arXiv:1305.2419.

[182] Silverwood, H., Scott, P. *et al*., 2013, JCAP, **3**, 27, arXiv:1210.0844.

[183] Arina, C., Bertone, G. & Silverwood, H., 2013, Phys. Rev. D, **88**, 013002.

[184] Poulin, V., Serpico, P. & Lesgourges, J., 2015, arXiv: 1508.01370 [astro-ph.CO].

[185] Fan, X.-H., Strauss, M. A., Becker, R. H., White, R. L., Gunn, J. E. *et al*., 2006, Astron.J., **132**, 117.

[186] Schenker, M. A, Ellis, R.S., Konidaris, N. P. & Stark, D. P., 2014, ApJ., **795**(1), 20.

[187] McGreer, I., Mesinger, A. & DOdorico, V., 2015, MNRAS, **447**(1), 499.

[188] Liu, H., Slatyer, T. R. & Zavalaz, J., 2016, arXiv: 1604.02457 [astro-ph].

[189] Valdés, M., Ferrara, A., Mapelli, M. & Ripamonti, E., 2007, arXiv: 0701301 [astro-ph].

[190] Furlanetto, S., Peng Oh, S. & Pierpaoli, E., 2006, arXiv: 0608385 [astro-ph].

[191] Natarajan, A. & Schwarz, D. 2009, arXiv: 0903.4485 [astro-ph].

[192] Slatyer, T. R., 2015, arXiv: 1506.03812 [astro-ph.CO].

[193] Belikov, A. & Hooper, D., 2009, Phys. Rev. D, **80**, 035007.

[194] Mellema, G. *et al*, 2015, arXiv: 1501.04203, to appear in PoS: Advancing Astrophysics with the SKA.